
The Early Evolution of Solids in Protoplanetary Disks: Observational Constraints from Millimeter Interferometry

Luca Ricci



München 2011

The Early Evolution of Solids in Protoplanetary Disks: Observational Constraints from Millimeter Interferometry

Luca Ricci

Dissertation
an der Fakultät für Physik
der Ludwig–Maximilians–Universität
München

vorgelegt von
Luca Ricci
geboren am 17/12/1983 in Ravenna, Italien

München, den 11 August 2011

Erstgutachter: Prof. Dr. Andreas Burkert

Zweitgutachter: Prof. Dr. Jochen Weller

Tag der mündlichen Prüfung: September 29, 2011

Contents

Abstract	xv
Zusammenfassung	xvi
1 Introduction	1
1.1 The cradles of planets: young circumstellar disks	2
1.2 The “bottom-up” scenario: core accretion	6
1.3 The “top-down” scenario: disk instability	8
1.4 The early stages of planet formation and the role of this Thesis	9
2 Modelling the emission of protoplanetary disks	15
2.1 The disk continuum emission	15
2.1.1 The disk surface density	17
2.2 The dust model	20
2.2.1 The dust opacity	23
3 Dust properties of protoplanetary disks in Taurus-Auriga	25
3.1 Introduction	26
3.2 New 3mm observations and sample properties	28
3.2.1 New PdBI observations	28
3.2.2 Sample	28
3.2.3 Stellar properties	32
3.2.4 Mass accretion rates	33
3.2.5 Disks sub-mm and mm data from the literature	33
3.3 Disk models	36
3.3.1 Dust opacity	38
3.4 Results	39
3.4.1 Spectral slopes and dust opacity index	41
3.4.2 Grain growth	49
3.4.3 Dust mass	50

3.5	Summary	54
4	Dust grain growth in ρ-Ophiuchi protoplanetary disks	57
4.1	Introduction	57
4.2	New ATCA observations	59
4.3	Sample	60
4.3.1	Selection criteria	60
4.3.2	Completeness	60
4.3.3	Stellar properties	61
4.4	Analysis	62
4.4.1	Disk structure	62
4.4.2	Dust opacity	66
4.4.3	Method	67
4.5	Results	67
4.5.1	Grain growth	69
4.5.2	Disk mass	75
4.6	Summary	76
5	The (sub-)mm SED of disks in the Orion Nebula Cluster	79
5.1	Introduction	79
5.2	Observations	80
5.3	Results	85
5.3.1	Grain Growth	86
5.3.2	The case of 216-0939	87
5.3.3	Derived disk masses	87
5.4	Summary	88
6	The mm-colors of a young binary disk system in Orion	91
6.1	Introduction	91
6.2	Observations	92
6.2.1	EVLA	92
6.2.2	X-Shooter	95
6.3	Results	95
6.4	Discussion	96
6.4.1	Comparison of grain growth in the two disks	96
6.4.2	Testing the models of dust evolution	99
7	The effect of local optically thick regions in the long-wave emission of young circumstellar disks	101
7.1	Introduction	101
7.2	Sample	102
7.3	Analysis	103
7.3.1	Disk structure	103

7.3.2	Dust opacity	105
7.4	Results	105
7.4.1	Case of a constant f : the $F_{1\text{mm}}-\alpha_{1-3\text{mm}}$ diagram	106
7.4.2	Case of a constant f : requested masses in optically thick regions . .	107
7.4.3	Case of $f(r)$ as a step function: the $F_{1\text{mm}}-\alpha_{1-3\text{mm}}$ diagram	109
7.4.4	Case of $f(r)$ as a step function: requested overdensities	111
7.5	Discussion	112
8	Testing the theory of grain growth and fragmentation by millimeter observations of protoplanetary disks	117
8.1	Introduction	118
8.2	Model description	119
8.2.1	Disk model	119
8.2.2	Dust model	119
8.2.3	Comparison to observations	121
8.3	Results	122
8.3.1	Sub-mm fluxes and spectral indices	122
8.3.2	Radial profiles of the dust opacity index	123
8.4	Discussion and Conclusions	124
9	Trapping dust particles in the outer regions of protoplanetary disks	127
9.1	Introduction	127
9.2	Dust Evolution Model	129
9.3	Results	136
9.3.1	Density distribution of dust particles	136
9.3.2	Comparison to current observations	139
9.3.3	Future observations with ALMA	141
9.4	Conclusions	144
10	Conclusions	147

List of Figures

1.1	Classification scheme of YSOs and its evolutionary interpretation.	4
1.2	Image composition for five Orion proplyds observed under the HST Treasury Program on the Orion Nebula Cluster.	5
1.3	Scaling the size ladder from dust to planets.	7
1.4	Density map of a self-gravitating disk forming clumps through fragmentation.	9
2.1	Collection of disks imaged with CARMA at 1.3 mm.	19
2.2	Surface density radial profile constrained for disks in Ophiuchus through SMA observations at 0.88 mm.	21
3.1	Histograms of sub-mm fluxes and stellar properties of the selected sample in Taurus.	31
3.2	H-R diagram of the PMS stars in our Taurus sample.	34
3.3	Millimeter dust opacity for the adopted dust model.	41
3.4	Fits of the sub-mm/mm SEDs of the Taurus disks with the two-layer flared disk models.	42
3.5	Spectral index α between 1 and 3 mm vs flux at 1 mm from the model best fits for the Taurus disks.	45
3.6	Distribution of the dust opacity spectral index β for the Taurus disks.	47
3.7	Beta vs age plot for the Taurus sample.	48
3.8	Dust opacity spectral index β and maximum grain size a_{\max} vs disk mass in dust for the Taurus sample.	52
3.9	Disk mass in dust plotted against the stellar mass for the Taurus sample.	53
3.10	Disk mass in dust plotted against the mass accretion rate for the Taurus sample.	54
4.1	Histograms of sub-mm fluxes and stellar properties of our selected sample in Ophiuchus.	61
4.2	H-R diagram for the sources of the Ophiuchus sample.	65
4.3	Sub-mm/mm SED fits for the Ophiuchus disks with the two-layer flared disk models.	68

4.4	Spectral index α between 1 and 3 mm from the model best fits vs the observed flux at 3.3 mm for the Ophiuchus sample.	70
4.5	Distribution of the dust opacity spectral index β for the Ophiuchus disks. .	71
4.6	Dust opacity spectral index β versus age for Class 0, I, II YSOs.	73
4.7	SED spectral index between 1 and 3 mm vs indicators of grain growth from the 10- μ m silicate feature.	74
5.1	Location of the eight Orion disks overlaid on a JCMT-SCUBA map at 0.85 mm.	81
5.2	Flux density at 2.9 mm vs observing day for the calibrator source used during the CARMA observations in Orion.	83
5.3	Spectral index between 0.88 and 2.9 mm vs flux at 0.88 mm for the Orion sample.	85
5.4	Fit of the sub-mm/mm SED of the 216-0939 Orion disk with a two-layer passive flared disk model.	88
6.1	Location of the 253-1536 binary system overlaid on a JCMT-SCUBA map at 0.45 mm of the Orion region.	93
6.2	HST and EVLA maps of the 253-1536 binary system.	94
7.1	Flux density at 1mm vs spectral index between 1 and 3mm, with fluxes predicted by disk models with optically thick regions constant with radius.	108
7.2	Flux density at 1mm vs spectral index between 1 and 3mm, with fluxes predicted by disk models with optically thick regions confined in circular annuli.	110
8.1	Influence of the turbulence α_t -parameter, fragmentation velocity, disk mass, and grain porosity on the observed mm-fluxes and spectral indices.	123
8.2	Observed fluxes at mm-wavelengths of the Taurus and Ophiuchus star forming regions, and the areas covered by the simulation predictions.	124
8.3	Predicted profiles of the dust opacity index at mm-wavelengths for different variations of the fiducial model.	125
9.1	Dust density distribution for 1 Myr-old disks with different radial profiles of the pressure field.	130
9.2	Time evolution of the dust density distribution for disks with different radial profiles of the pressure field.	131
9.3	Time evolution of the dust-to-gas mass ratio for disks with different radial profiles of the pressure field.	134
9.4	Comparison of the observed fluxes at mm-wavelengths of disks in Taurus and Ophiuchus star forming regions with the results of the simulations at different times of the disk evolution.	137
9.5	Simulation of ALMA observations at 0.45 mm for a 2 Myr-old disk with pressure bumps.	138

9.6	Simulation of ALMA observations for a 1 and 2 Myr-old disks with different radial profile of pressure bumps.	142
9.7	Simulation of ALMA observations at different wavelengths for a 2 Myr-old disk with pressure bumps.	143
9.8	Map of the millimeter spectral index from simulations of ALMA observations for a disk with pressure bumps.	146

List of Tables

3.1	Summary of the new PdBI observations at 3 mm in Taurus.	29
3.2	Stellar properties of the selected sample in Taurus.	35
3.3	Literature sources for the sub-mm/mm data for the selected Taurus sample.	37
3.4	Adopted disks outer radii for the Taurus sample.	40
3.5	Derived disk properties for the Taurus sample.	43
4.1	Summary of the 3.3 mm ATCA observations in Ophiuchus.	63
4.2	Stellar properties of the considered sample in Ophiuchus.	64
4.3	Derived disk properties of the Ophiuchus sample.	77
5.1	Sub-Millimeter and Millimeter Flux Densities and Disk Sizes for the sample in Orion.	84
6.1	Disk fluxes and spectral indices of the two components in the 253-1536 binary system.	96
6.2	Derived parameters for the two disks in the 253-1536 binary system.	98
7.1	Requested dust overdensities in the added optically thick regions inside a ring between 10 and 20 AU from the central star.	112
7.2	Requested dust overdensities in the added optically thick regions inside a ring between 30 and 40 AU from the central star.	112
7.3	Requested dust overdensities in the added optically thick regions inside a ring between 50 and 60 AU from the central star.	112
7.4	Requested dust overdensities in the added optically thick regions inside a ring between 80 and 90 AU from the central star.	112
7.5	Summary of the CARMA observations at 102.5 GHz in Taurus.	115
8.1	Values of the input parameters of the models grid.	119
9.1	Values of the models input parameters	129
9.2	Information on some of the main parameters for the ALMA simulations.	140

Abstract

Young circumstellar disks around pre-Main Sequence stars are considered to be the cradles of planets. According to the core accretion scenario, the formation of planets involves a variety of physical mechanisms starting from the coagulation of sub- μm sized particles and going up to the gas-accretion phase leading to the build up of rocky planets and gas giants. The first stages of this process are characterized by collisional growth of tiny sub- μm sized grains, as those found in the interstellar medium. Observations in the millimeter can directly probe the existence of larger mm/cm-sized pebbles in young disks, i.e. the product of the first growth of smaller particles, and have the potential of constraining models of early growth of solids.

In this Thesis I obtained and analyzed new data in the millimetre for a sample of more than 50 young disks in three nearby star forming regions (Taurus, Ophiuchus, Orion); for all these sources I derived some of the main properties of dust particles, such as grain size and total mass. The results of my analysis indicate that nearly all the disks in the Class II evolutionary stage, no matter what their mass is or in which environment they are formed, contain dust grains with sizes of at least 1 mm in their outer regions. This shows that the formation of these large grains is very rapid, and also that these large solid particles are retained in the disk outer regions. These observations have the potential to test models of early evolution of solid particles in protoplanetary disks.

One of the strong aspects of my work has been the detailed comparison of the observations at millimetre wavelengths with the predictions of theoretical models for the evolution of solids in disks. In my Thesis I have produced the first statistically sound and well populated dataset to study the grain growth process in disks. These data have been used to highlight the successes and shortcomings of current dust evolution models in protoplanetary disks.

The results presented in this Thesis clearly identify the directions for future investigations in this area: on the observational side the next frontier is to resolve the distribution of large grains in disks at high angular resolution, to identify the process of grain growth in the earliest stages of disk formation and in the final stages of disk evolution, and to probe the presence of large grains in the extreme environments around young brown dwarfs and more massive Herbig AeBe young stars. The results of these observations, which are becoming possible with ALMA and EVLA, will guide the model development and ultimately constrain the initial phases of planetary systems formation.

Zusammenfassung

Junge zirkumstellare Scheiben um Vorhauptreihensterne werden gemeinhin als Geburtsort von Planeten angesehen. Im Zuge des *core accretion*-Szenarios entstehen Planeten durch das Verklumpen von sub- μm -großen Partikeln welche über die Gasakkretionsphase in die Bildung von Gesteinsplaneten und Gasriesen übergehen. Die erste Phase dieses Prozesses wird durch das kollisionsinduzierte Wachstum von winzigen sub- μm -großen Partikeln, wie man sie im interstellaren Medium findet, bestimmt. Mit Beobachtungen im Millimeterbereich kann man die Existenz größerer sog. *pebbles* (*engl.* "Kiesel") studieren. Dabei handelt es sich um mm bis cm-große Produkte der ersten Wachstumsphase kleiner Staubteilchen. Mit diesen Methoden lassen sich Modelle des frühen Staubwachstums testen.

Die vorliegende Arbeit behandelt die Beschreibung und Analyse neuer mm Beobachtungen von mehr als 50 jungen Scheiben in drei benachbarten Sternentstehungsgebieten (Taurus, Ophiuchus, Orion). Für alle Beobachtungsobjekte wurden die wichtigsten Eigenschaften der Staubteilchen ermittelt, unter anderem Korngröße und Gesamtmasse. Deren Analyse weist darauf hin, dass die Äußeren Bereiche fast aller Scheiben der Entwicklungsstufe II (*Class II*) Staubkörner von mindestens 1 mm Größe enthalten, unabhängig von ihrer Masse und Umgebungseinflüssen während der Entstehung. Die Beobachtungen sind geeignet um Modelle der frühen Entwicklung von Festkörperteilchen in protoplanetaren Scheiben zu testen.

Einer der wichtigsten Aspekte dieser Arbeit ist der detaillierte Vergleich von Beobachtungen im Millimeterbereich mit Vorhersagen theoretischer Modelle über die Entwicklung von Festkörperteilchen in Scheiben. Die Arbeit enthält den ersten statistisch fundierten, umfangreichen Datensatz um den Prozess des Teilchenwachstums in Scheiben zu untersuchen. Die Daten wurden dazu verwendet, die Stärken und Schwächen heutiger Staubenentwicklungsmodelle aufzudecken.

Die Ergebnisse dieser Arbeit weisen die Richtung für zukünftige Untersuchungen auf dem Gebiet: der nächste Schritt bezüglich Beobachtung ist die Bestimmung der Verteilung großer Partikel in Scheiben mittels hoher räumlicher Auflösung. So können sowohl das Staubwachstum in den Frühphasen der Scheibenentstehung und den Spätphasen der Scheibenentwicklung, als auch die Existenz von großen Teilchen unter den extremen Bedingungen, wie sie in der Umgebung von jungen Braunen Zwergen und den massereicheren Herbig AeBe Sternen herrschen, näher bestimmt werden. Die Ergebnisse dieser Beobachtungen, ermöglicht durch ALMA und EVLA, werden die Entwicklung von Modellen richtungsweisend beeinflussen und die ersten Phasen des Planetenentstehungsprozesses eingrenzen.

Chapter 1

Introduction

One of the most fascinating scientific achievements ever obtained by the observation of the sky has been the discovery of planets orbiting stars outside our Solar System. Since it is a planet, i.e. the Earth, the only habitat known to host life in the Universe, the detection and characterization of planets outside our Solar System, called “exo-planets”, have the potential to shed light on some of the most intriguing questions of mankind: “What is the origin of the Solar system?”, “Are planetary systems similar to the Solar system common in the Galaxy?”, “Are we alone in the Universe?”. The highly-improved capabilities of spectrographs in future astronomical facilities (e.g. ELTs, JWST) will allow us to characterize the chemical composition of exoplanets’ atmospheres. The detection of particular chemical elements (“bio-markers”) in the atmosphere of terrestrial planets inside the habitable zone of their host star would provide strong indication for the presence of extra-terrestrial life in those systems.

Since the first extrasolar planetary systems discovered around a millisecond pulsar in the early 1990s (PSR1257+12, Wolszczan & Frail, 1992), and around a Solar-type star three years later (51 Peg b, Mayor & Queloz, 1995), several hundred of exoplanets have been found. So far, most of the discovered exoplanets are giant gaseous planets, and only very recently we started to explore the Earth mass range. Other than being a clear demonstration of the outstanding technical development in the field of Astronomy, the ever growing number of discovered exoplanets is revealing a surprisingly vast variety of different orbital properties and planetary masses. This characteristic of the observed exoplanets is an indication that the planet formation process may have a variety of results.

Although understanding the origin of our planetary system has always been one of the overarching questions of science, important aspects of the whole process of planet formation are far from being understood. This is not too surprising if one considers the huge dynamical range involved in the making of planets: more than 12 order of magnitudes in the size of solids to go from tiny sub- μm sized particles, as those found in the interstellar medium (ISM, Mathis et al., 1977), to large planetary objects, with radii as large as at least thousands of km. This suggests that, in order to build planets, different physical mechanisms can play a role in growing particles in different size regimes.

Eminent natural philosophers of the 18th century already hypothesized that the Solar System was formed by the collapse of a primordial nebula made of gas and dust. Direct observational evidence supporting the general lines of this scenario had to wait until the last decade of the 20th century, when high angular resolution optical and millimeter images demonstrated the existence of gaseous and dusty disks rotating around young Solar-like stars. I briefly outline the general properties of these young circumstellar disks in Section 1.1.

In the second half of 20th century, two main theoretical frameworks have been proposed to explain the birth of planets. The first one is the core-accretion scenario, in which planets are formed through the assembly of initially small sub- μm to larger and larger particles all the way up to rocky cores (terrestrial planets). If some of these rocky cores become massive enough before the gas has dissipated in the disk, they can rapidly accrete a gaseous envelope (giant planets). The main steps invoked by this ‘solids grow first’ scenario are briefly described in Section 1.2.

The other main theoretical framework for planet formation is the disk instability paradigm. Circumstellar disks, especially at their very early stages of life, can be massive enough to have disk self-gravity play a crucial role in their dynamical evolution. In these cases, the disk self-gravity can trigger the development of spiral waves in the disk structure. The densest regions in such spiral arms can then be subject to fragmentation and gravitational collapse if the cooling rate of the fragment is faster than heating due to dissipation of energy during collapse. This mechanism has the potential to form very dense clumps of gas and dust, in which a planet can be formed very rapidly. This scenario is outlined in Section 1.3.

Finally, Section 1.4 provides a brief overview of the main concepts related to the early stages of planet formation, which represent the pivotal topic of this Thesis. The contribution of this Thesis to this field is also discussed, together with a short summary of the content of each Thesis’ chapter.

1.1 The cradles of planets: young circumstellar disks

The common birth places of planets are circumstellar disks orbiting young stars¹. It is in these systems that densities are high enough to form planetary systems according to the two main scenarios described in Sections 1.2 and 1.3.

Other than setting the stage for the birth of planets, young circumstellar disks are known to play a key role in the formation of stars. It is known that stars are formed

¹It is interesting to note that the formation of the first ever discovered planetary system, observed around a millisecond pulsar, cannot be explained through this scenario. A millisecond pulsar is a rapidly rotating neutron star formed during a supernova explosion. If the detected planets were present before the supernova event the significant mass loss during the explosion would have unbound the planetary system. The most likely scenario for the formation of such a planetary system is that this occurred in a disk of material captured by the neutron star after the supernova explosion. Note that subsequent surveys of pulsars aimed at detecting planets orbiting them have shown that this way of forming planets is a rare process.

through the gravitational collapse of dense cores in turbulent molecular clouds (Shu et al., 1987; Ballesteros-Paredes et al., 2007, top panel in Fig. 1.1). In order to go from a $\sim 10^{12}$ km sized core to a $\sim 10^6$ km sized star some of the core material has to lose angular momentum. This is done, at least in part, through the formation of a disk and its evolution (Terebey et al., 1984; Shu et al., 1987; Galli & Shu, 1993). Because of the conservation of angular momentum, the collapsing material carrying non-zero angular momentum cannot fall toward the center of the core and rains instead on the disk itself, making it more and more massive in these early stages of its evolution. Turbulence in the disk, and possibly also disk self-gravity induce torques which cause a redistribution of angular momentum and a radial spread of the disk material. In particular, part of the material drifts toward the innermost disk regions and gets accreted on the central protostar, whereas another part moves outward to conserve the total disk angular momentum.

From an observational perspective, young stellar objects (YSOs) with different Spectral Energy Distributions (SEDs) have been identified in several star forming regions (SFRs). These have been classified according to the slope of the SED, typically in the wavelength interval of $2.2 - 20 \mu\text{m}$ (Lada, 1987; Andre et al., 1993; Greene et al., 1994, see Fig. 1.1). “Class 0” YSOs are not visible at wavelengths shorter than $\sim 10 - 20 \mu\text{m}$, have a steeply rising spectrum in the mid-to-far IR and are bright in the sub-mm. “Class I” YSOs are visible in the near IR (but typically not in the optical), their SED show a rising spectrum in the mid-IR but not as steep as in the Class 0 YSOs. “Class II” YSOs are optically visible and have an IR SED which decreases with wavelength, but shows evidence for an “IR-excess” emission relative to a bare stellar black body. “Class III” YSOs are optically visible and show no or very little IR-excess. This classification scheme is thought to reflect an evolutionary sequence. In particular, Class 0 YSOs are considered to represent the earliest stages of the formation of a protostar, when this is still heavily embedded in its surrounding envelope which dominates the source emission. The deeply embedded Class 0 sources evolve towards Class I stage dissipating their circumstellar envelopes, and emission from the central protostar and from a young accretion disk can be often identified. In the Class II stage the circumstellar envelope has dissipated, the pre-Main Sequence (PMS) star becomes optically visible and is surrounded by a disk which is optically thick in the IR and optically thin in the sub-mm. Finally, Class III YSOs are more evolved PMS stars which can be surrounded by a planetary system and/or by a “debris disk”, made of asteroid/comet-sized objects, and of a population of smaller dust particles generated by the impacts between the larger bodies.

Observational evidence for the presence of gas and dust around young stars exists for many years from a variety of different tracers, like optical emission line spectra (e.g. Herbig, 1950), optical absorption of background emission (e.g. Ricci et al., 2008, see Fig. 1.2), continuum excess in the infrared (e.g. Ney et al., 1973), and sub-millimeter (e.g. Beckwith et al., 1990). However, it was only in the 1990s that the morphology of this circumstellar material could be really determined. In particular, high angular resolution imaging with the Hubble Space Telescope in the optical (O’Dell & Wong, 1996) and in the millimeter (Dutrey et al., 1996) typically revealed flattened structures, interpreted as disks seen in projection along the plane of the sky. In the few cases in which the disk is seen

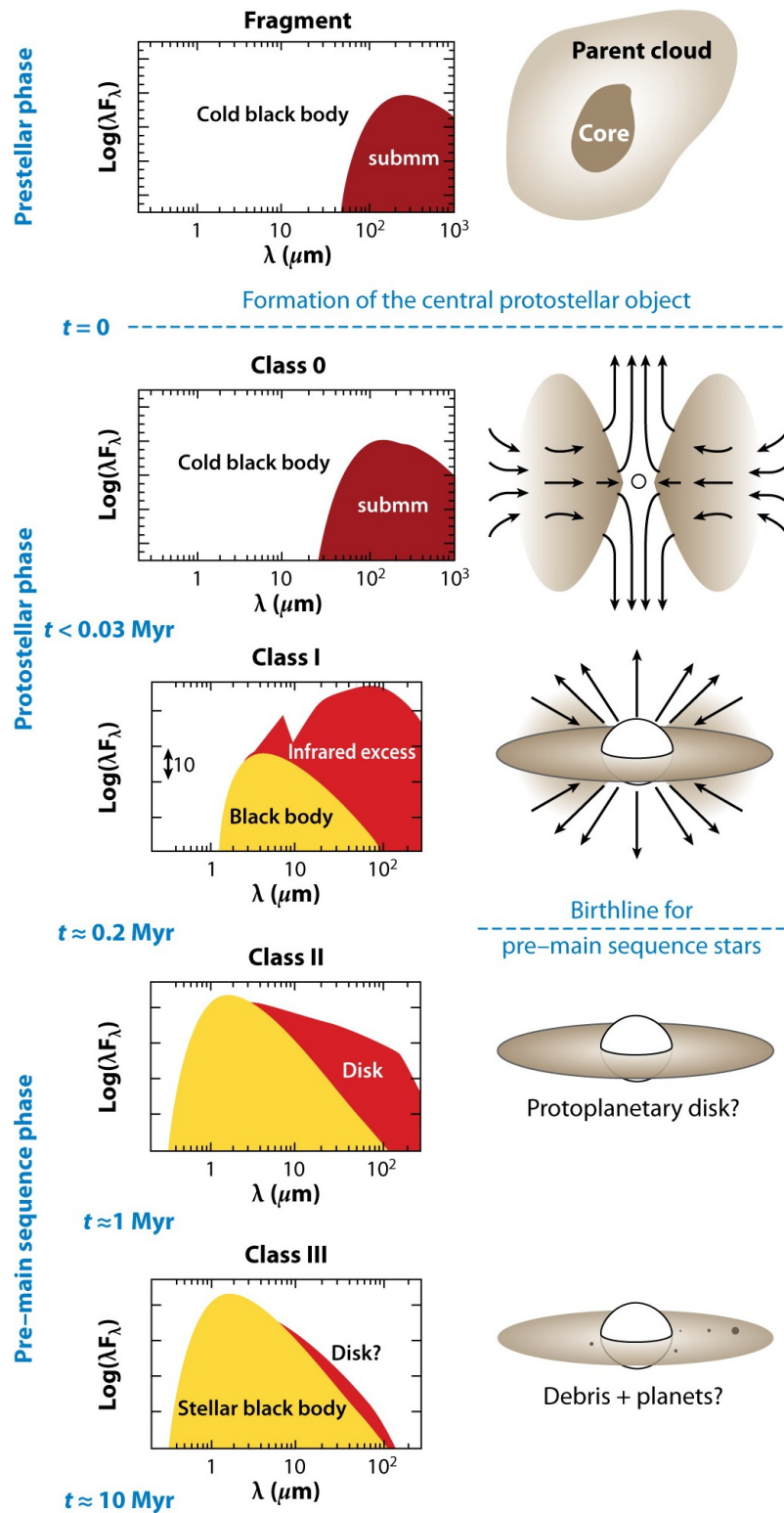


Figure 1.1: Classification scheme of YSOs and its evolutionary interpretation (adapted from Andre, 2002).



Figure 1.2: Image composition for five Orion proplyds observed under the HST Treasury Program on the Orion Nebula Cluster. The disks have been selected from the HST/ACS Atlas of protoplanetary disks in the Great Orion Nebula (Ricci et al., 2008). Credit: NASA/ESA and L. Ricci.

exactly as “face-on”, i.e. with the disk axis along the line of sight, its image appears as a circle, but more often the disk axis forms a non-zero angle with the line of sight, and the projected image is more flattened because of the disk inclination. Also, in some cases, high angular resolution observations of molecular lines, especially CO rotational transitions in the millimeter, provided evidence for velocity gradients along the disk. Data are generally consistent with emission from molecular gas in keplerian rotation (e.g. Simon et al., 2000), further strengthening the hypothesis of material in a disk rotating around the central star.

Multi-wavelength observations of disks have been used to derive some of the main properties of young circumstellar disks. In the optical, small ($< 1 \mu\text{m}$) particles in the disk scatter efficiently the radiation from the central star. Optical images at high angular resolution can be then used to investigate the geometrical structure of the disk surface layers. For disks seen as “edge-on” scattered light images have revealed a “flared” structure, where the ratio between the vertical scale height of the disk and the distance from the central star increases with radius (see the review by Duchene, 2008).

The disk thermal emission in the infrared is optically thick and therefore reflects the emitting temperature. By assuming a simple power-law for the temperature radial profile $T(r) \sim r^{-q}$, infrared SED of young T Tauri Stars are best-fitted typically with $q \approx 0.5$. This value of q is significantly lower than the one ($q = 0.75$) predicted both by models of accretion disks with internal heating due to viscous dissipation of gravitational energy, and by vertically thin disks heated by the radiation of the central star (see Natta et al., 2000, for a detailed discussion). The solution to this problem has been found by a class of models which considers flared disks (Kenyon & Hartmann, 1987) with an optically thin disk atmosphere directly heated by the stellar radiation (Chiang & Goldreich, 1997), consistently with what found later from optical images of edge-on disks. This class of models is described in the next Chapter, and it is used throughout the Thesis.

Whereas observations in the infrared probe the surface layers of the disk, the emission at longer millimeter wavelengths is optically thin and can be used to probe the cold and dense regions in the midplane of the outer disk, where planets are expected to form. Since these regions contain most of the disk mass, a measured integrated flux in the millimeter can be converted into an estimate for the disk mass. Furthermore high angular resolution imaging at these wavelengths can constrain the radial profile of the mass distribution in the

disk, which is a fundamental property for models of disk evolution and planet formation. Also, the spectral index of the (sub-)mm SED reflects the dependence on wavelength of the dust emissivity, which in turns, depends on the size of solid particles. All these topics are detailed in the next Chapter.

1.2 The “bottom-up” scenario: core accretion

The most widely accepted theory for the formation of planets is the so called core accretion - gas capture model. In this scenario planets are formed through the growth of solid particles starting from the microscopic grains found in the ISM (Mathis et al., 1977). This huge growth of solids can be divided in different steps, depending on the physical mechanism driving the dynamical evolution of the system.

The first stage of planetary formation starts with sub- μm grains which are well coupled to the gas in the protoplanetary disk via gas drag. In this phase grains grow via coagulation (sticking) in two-body collisions, sediment (in the vertical direction) toward the disk midplane, and drift radially toward the central star. These early stages of planet formation can be investigated through observations of protoplanetary disks, and represent the main topic of this Thesis. The main concepts are outlined in Section 1.4.

According to our current understanding of coagulation and motion of small solids in disk, sticking can produce solids not larger than roughly meter-sized rocks in the inner disk (< 10 AU from the central star) and cm-sized pebbles in the outer disk regions (~ 100 AU). Some mechanisms other than sticking of grains have to act in order to overcome these barriers and lead to the formation of planetesimals. Planetesimals are defined as bodies which are large and massive enough (sizes of the order of $1 - 100$ km) so that their gravity dominate the evolution and aerodynamic coupling to the gas in the disk is no longer significant. They play a crucial role in the core-accretion scenario because it is from the two-body inelastic collisions between planetesimals that “planetary embryos” are assembled.

Different mechanisms have been proposed in the literature to explain the formation of planetesimals (see Fig. 1.3 for a schematization). The most promising processes all involve the gravitational collapse of a dense region of small particles. The main driver for accumulating large masses of small particles in relatively small regions of the disk is what differentiate these models. In the classical model of Goldreich & Ward (1973), dust settles vertically into a thin layer in the disk midplane. If the dust density reached in this layer is high enough then this layer becomes unstable to its own gravity and form planetesimals directly. However, this concentration of particles in a thin layer is hampered by the development of Kelvin-Helmholtz instabilities expected in this process. These are caused by the vertical velocity shear between the dust layer rotating at Keplerian velocity and the gaseous disk regions above and below the dust-rich midplane rotating at sub-Keplerian velocities. Kelvin-Helmholtz instabilities generate turbulence which would stir up the dust particles, making the concentration of particles decrease below the threshold needed for gravitational collapse.

In this case gas turbulence hinders the concentration of particles, but recent numerical

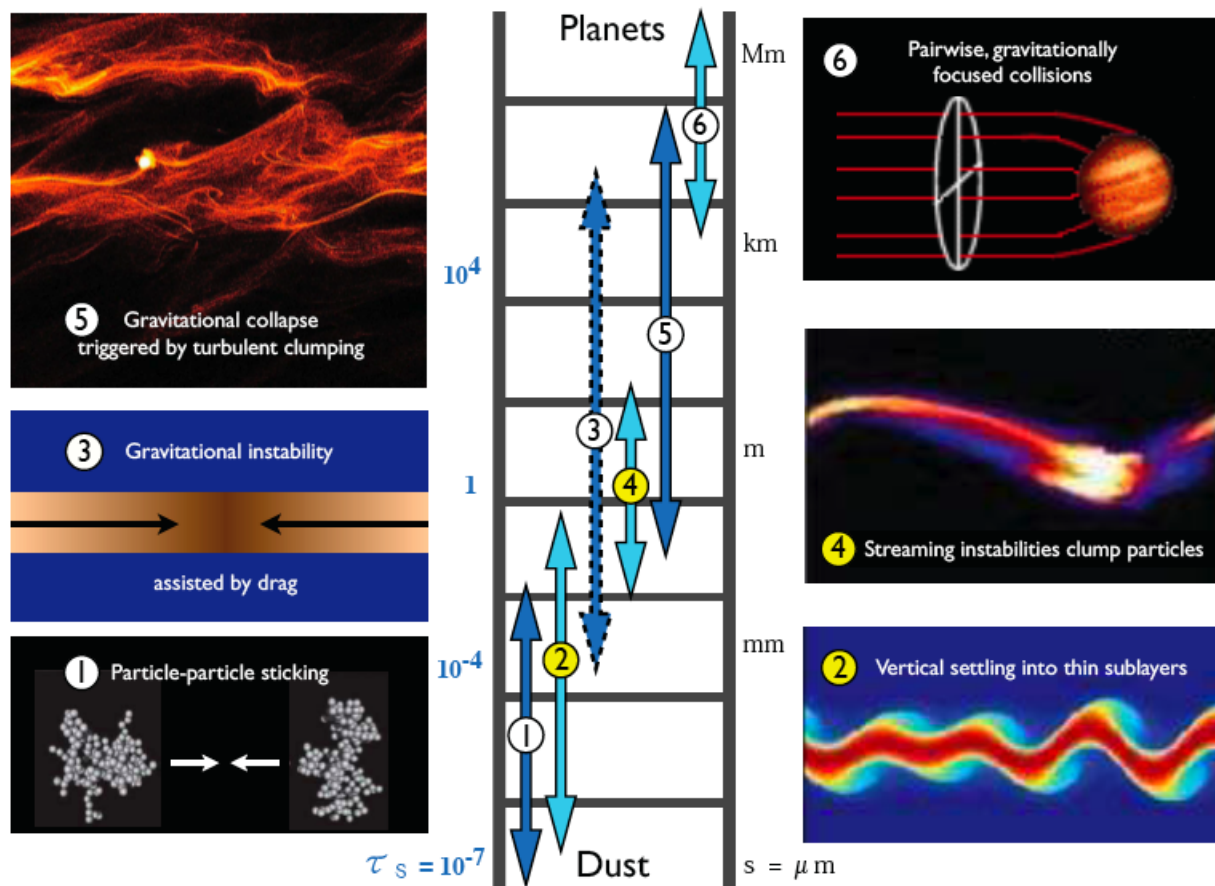


Figure 1.3: Scaling the size ladder from dust to planets. In the left and right panels different physical mechanisms which can potentially grow or concentrate solids are shown. The ranges of particle sizes on which each mechanism is expected to be relevant are indicated on the “size ladder” at the center of the figure (from Chiang & Youdin, 2010).

simulations of disks have shown that in some cases gas turbulence can also be very efficient in clumping particles. These simulations find that turbulence can lead to strong local overdensities of dust particles, and that solids $\sim 10 - 100$ cm in size gravitationally collapse in turbulent disks (see the review by Chiang & Youdin, 2010).

Once a population of planetesimals has formed in the disk, the subsequent evolution is dominated by gravitational interactions. In this stage, terrestrial planets can be formed together with the cores of giant planets. When a planet has grown to about 1 Earth mass, coupling between solids and gas in the disk becomes again important, although now it is gravity which drives the coupling rather than aerodynamical forces as in the early stages of grain growth. This causes exchange of angular momentum between the gaseous disk and planets, making them change their orbital major axis. This process, known as *planetary migration*, has been recently invoked to explain the existence of several “hot-Jupiters”, i.e. giant exoplanets orbiting very close (< 1 AU) their hosting star. Finally, when a rocky

planetary core reaches a mass of about 10 Earth masses, its gravity becomes so large that it can rapidly accrete a gaseous envelope from the parent disk, leading to the formation of a giant planet (see the review by Mordasini et al., 2010, and references therein).

1.3 The “top-down” scenario: disk instability

A competing scenario to form massive planets is the disk instability model. In this model, giant planets are thought to form from the collapse of a dense part of the gaseous circumstellar disk into a gravitationally bound clump. Contrary to the core-accretion scenario, in which planets are formed through the growth of smaller bodies, in the disk instability model planets are created at the final stages of the gravitational collapse of large and unstable disk regions.

It is known that a thin disk is unstable to the growth of axisymmetric gravitational disturbances if the stability Toomre-parameter

$$Q = \frac{c_s \kappa}{\pi G \Sigma} < 1, \quad (1.1)$$

where c_s is the sound speed, Σ is the disk surface density, G is the gravitational constant, and κ is the epicyclic frequency, equal to the angular velocity Ω for a disk with a Keplerian rotation curve (Toomre, 1964). Non-axisymmetric, spiral-like disturbances are generally more unstable, and thin disks can result unstable at considerably larger values of $Q \approx 3-4$. On the other hand, as described in Section 1.1 protoplanetary disks are not vertically thin, and a finite thickness of the disk has a stabilizing effect. Hydrodynamical simulations show that disks become unstable to spiral waves perturbations at Q values between about 1 and 2 (Mayer et al., 2004). From the definition of the Toomre-parameter (Eq. 1.1), it is clear that disks become unstable when they are cold ($c_s \propto T^{1/2}$) and massive (high Σ).

The criterion for instability is a necessary condition for having some dense parts of the disk collapsing into gravitational bound clumps, but is not sufficient. The other necessary condition is that during collapse disk cooling is faster than internal heating due to gravitational instabilities, which has a stabilizing effect on the disk. This effect can be simply quantified by considering the ratio ξ between the cooling timescale t_{cool} and the heating instability which is proportional to the dynamical timescale $\sim 1/\Omega$. Gammie (2001) showed that for a razor-thin disk there exists a critical ratio ξ_{crit} below which the disk cools down fast enough to have non-linear instabilities growing and driving collapse. For large enough cooling times ($\xi > \xi_{\text{crit}}$) the disk reaches a quasi-steady configuration, with the instability saturating at a finite amplitude such that the disk is kept close to marginal stability (Bertin & Lodato, 2001). Rice et al. (2005) carried out three-dimensional simulations using a Smoothed Particle Hydrodynamics (SPH) code and showed that the ξ_{crit} -parameter takes values between about 6 and 13 depending on the equation of state of the gas in the disk (see Fig. 1.4). However, a recent resolution study aimed at testing the convergence with increasing resolution of the ξ_{crit} parameter through 3D SPH simulations has shown that convergence is not clearly obtained even to very high values of particle numbers (~ 10

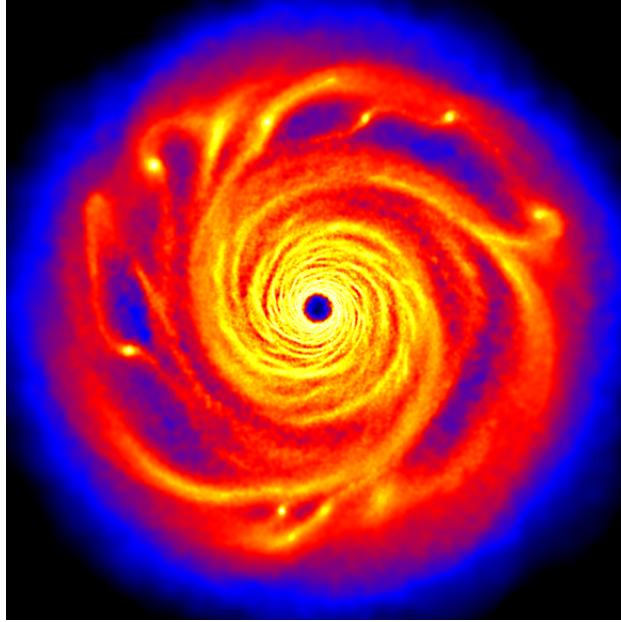


Figure 1.4: Equatorial density structure for $t_{\text{cool}} = 5\Omega^{-1}$ and for a disc mass of $0.25 M_{\odot}$. There are signs of fragmentation with the most massive fragment being gravitationally bound (from Rice et al., 2003).

million; Meru & Bate, 2011). Furthermore, different groups running hydrodynamic simulations which include radiation from the central star have found different results for disks with very similar initial conditions, e.g. fragmentation by Boss (2007) and no fragmentation by Cai et al. (2010).

Contrary to the core-accretion scenario, the disk instability scenario has the potential to form giant planets very quickly, on a dynamical timescale. However whether this model is a physically viable scenario for forming planets is still under debate. Higher resolution simulations properly accounting for the disk thermodynamics are needed to address this question. From an observational point of view, the spiral-wave structures expected for disks undergoing gravitational instabilities will be detectable and spatially resolvable through high angular resolution sub-mm interferometry with ALMA in nearby SFRs (Cossins et al., 2010a). Future observations of disks will therefore shed light on whether and to what extent the disk instability scenario is a channel used by nature for forming massive planets.

1.4 The early stages of planet formation and the role of this Thesis

The main subject of this Thesis is the early growth of solid particles in the disk. Tiny, sub- μm sized grains as those found in the ISM can grow in size by sticking after collision with other grains. In general, collisional growth requires a binding energy which is significant

compared to the kinetic energy of the collision, and a sufficient fraction of kinetic energy dissipation during the impact (Beckwith et al., 2000; Youdin, 2010). Other than by the mass of the colliding particles, the kinetic energy is determined by the relative velocity of the collision. Since at these stages the dynamics of solids is regulated by the aerodynamical coupling with the gas, different effects have to be considered by models of dust evolution in disks (Brauer et al., 2008a). These include brownian motion, vertical settling, azimuthal orbital motion, radial motion due to coupling with the accreting gas, radial drift, and turbulence mixing (Birnstiel et al., 2010a). As for the binding energy, in the regime of small particles gravity is irrelevant, whereas short-range van der Waals interactions can explain sticking of grains at speeds $\lesssim 1 - 10$ m/s (from both laboratory experiments and molecular dynamics simulations of collisions by Blum & Wurm, 2008; Dominik & Tielens, 1997, respectively). When grains collide with relative velocities which are larger than these “threshold velocities”, sticking is not efficient, and the grains fragment after the impact.

As described in Section 1.2, according to the core accretion scenario the process of grain sticking represents the first stage of planet formation. In principle, in the disk instability paradigm the whole growth of small solids to planetesimals occurs in a “single-step process” driven by the gravitational collapse of large portions of the (unstable) disk (Section 1.3). However, understanding which are the physical properties of dust grains at the beginning of the collapse is critical also for the disk instability model. Since radiative emission by dust grains plays a crucial role in the disk cooling, some knowledge of the typical grain sizes in the disk, on which dust emission depends, is fundamental to determine whether gravitational collapse can occur in real disks (Section 1.3; Cossins et al., 2010b). An investigation of the main properties of dust grains in disks is therefore fundamental for our understanding of the first stages of planet formation.

Observations of protoplanetary disks in nearby SFRs can constrain some key characteristics of the early evolution of solids in disks. For example, multi-wavelength observations of disks in the optical/infrared (Throop et al., 2001), and in the silicate feature at about $10 \mu\text{m}$ (e.g. Bouwman et al., 2001) imply that $\sim 1 - 10 \mu\text{m}$ -sized particles are present in the innermost regions of disks ($< 1 - 10$ AU from the central star). These grains are significantly larger than the sub- μm particles found in the ISM, providing evidence for the early growth of solids in disks. Furthermore, since at these disk radii dust coagulation is expected to be very rapid, the observational results indicate that small dust grains have to be replenished by collisional fragmentation (Birnstiel et al., 2009).

Two main limitations of the optical/infrared techniques in deriving information on the size of dust particles are: 1) only very small grains can be probed (with sizes of the order of the observing wavelength); 2) the observed dust lies in the surface layers of the disk, rather than in the disk midplane, where nearly all the process of planet formation is supposed to occur. In this Thesis I used dust continuum emission in the millimeter to constrain dust properties of disks in nearby SFRs. Compared with techniques in the infrared, the longer wavelengths allow to test the presence of larger, mm/cm-sized grains in the outer regions of the disk midplane.

As detailed in the next Chapters of this Thesis, at these long wavelengths the emission of the disk is mostly optically thin and as a consequence the spectral index α_{mm} of the

SED ($F_\nu \propto \nu^{\alpha_{\text{mm}}}$) carries the information on the spectral index β_{mm} of the dust opacity coefficient ($\kappa_\nu \propto \nu^{\beta_{\text{mm}}}$; see Beckwith & Sargent 1991). In particular, for the approximate case of completely optically thin emission in the Rayleigh-Jeans regime, $\alpha_{\text{mm}} = \beta_{\text{mm}} + 2$. Whereas tiny ISM-like particles are characterized by β_{mm} -values around 1.7 (and α_{mm} around 3.5), larger mm/cm-sized grains have lower values of β_{mm} and α_{mm} (Draine 2006). Therefore, multi-wavelength observations of young disks in the (sub-)millimeter can reveal the presence of mm/cm-sized pebbles in the disk outer regions (at radii ~ 100 AU), to which long-wavelength observations are most sensitive (e.g. Wilner et al., 2000; Testi et al., 2001, 2003; Wilner et al., 2005; Rodmann et al., 2006; Natta et al., 2007, and references therein).

Investigating the presence of mm/cm-sized grains in the disk outer regions is particularly relevant because models of dust evolution predict that these pebbles can be formed via coagulation only in the outer regions of relatively massive disks. Furthermore, solids orbiting at the Keplerian velocity in a laminar gas disk feel a constant head wind (caused by the gas rotating slightly sub-keplerian) which forces them to spiral inwards (Weiden-schilling, 1977). If this drag is as efficient as laminar theory predicts, mm/cm grains would quickly be removed from the outer disk regions (see Brauer et al., 2007). This “centimeter size” barrier for the growth of solids in the disk outer regions corresponds to the more famous meter barrier” for the formation of planetesimals at 1 AU, where the main difference is in the gas density (roughly 2 order of magnitudes) in the different regions of the disk. The investigation of mm/cm pebbles in the outer regions of disks with different properties (e.g. disk masses) and in different environments can therefore test the predictions of the models of dust evolution, in particular on the physics of dust coagulation and radial drift of solids.

In the following, I briefly summarize the content of all the next Chapters, with particular highlight for the original results of this Thesis.

Chapter 2 — I outline the main characteristics of the models adopted to calculate the sub-mm/mm emission of protoplanetary disks and derive constraints on the properties of dust grains;

Chapter 3 — I present a sensitive 3 mm survey of protoplanetary disks in the Taurus-Auriga SFR. By combining these new data with literature measurements at shorter sub-mm wavelengths, I constrained the dust properties (dust masses and grain sizes) for a sample of 21 isolated Class II disks. All the disks show evidence for dust grains with sizes of at least ~ 1 mm in their outer regions. Considering that the fainter disks are more representative of the bulk of the disk population than the brighter ones, for which some earlier information on grain growth was already obtained, this result has important consequences for our understanding of the early phases of planet formation: not only the few very massive disks can form and retain mm-sized pebbles in their outer regions, but also the more numerous less massive disks. I also derived in an homogeneous way the main stellar properties (stellar mass, age, luminosity, mass accretion rate) for the selected sample, and investigated any

correlation with dust properties without finding any significant trend;

Chapter 4 — I describe the results of a 3 mm survey of 27 disks in the Ophiuchus SFR. A sub-sample of 17 disks were selected using the same criteria adopted for the Taurus sample (Chapter 2). As for the disks in the Taurus SFR, an analysis of the disk emission in the sub-mm/mm indicates that mm/cm-sized pebbles are present in the disk outer regions. This shows that the formation of these large grains is very rapid, occurring before a young stellar object enters in the Class II evolutionary stage, and also that these large solid particles are retained in the disk outer regions. One or more physical mechanisms halting the radial drift of solids have to occur in the disk to explain this retention of pebbles in the outer disk;

Chapter 5 — I show new data at about 3 and 7 mm for 8 disks in the outer regions of the Orion Nebula Cluster (ONC). Evidence of grain growth to is found for all the disks, showing for the first time that the early stages of planet formation occur in disks in a clustered star forming region. In this sample, three disks are found to be more massive than about $0.05 M_{\odot}$. This confirms that massive disks are present in the outskirts of the ONC, contrary to what happens in the regions of the Nebula which are closer to the massive and UV-bright stars of the Trapezium.

Chapter 6 — I present new observations at 7 mm for a young binary disk system in the ONC. The measured fluxes were combined with data in the sub-mm to investigate the dust properties in both the disks of the system. The analysis indicates that the disk with lower density and higher temperature hosts larger grains than the companion disk, which is the opposite of what predicted by the dust evolution models. Ideas which can possibly reconcile models and observational results are discussed.

Chapter 7 — I investigate the effect of possible optically thick regions in the disk midplane on the disk SED at sub-mm/mm wavelengths. Compared with optically thin emission, the dependence on wavelength of optically thick emission is shallower in the millimeter and this might provide an alternative interpretation of the low values of the SED spectral indices measured for disks at long wavelengths. I investigate the physical properties that these regions would need to have to explain the observed mm-data of disks, and the physical processes that could lead to the formation of these optically thick regions in the disk. The main conclusion of this work is that, although the measured mm-fluxes can be explained by disks with very small optically thick and dense regions, for the vast majority of the observed disks no physical processes proposed so far are capable to reproduce the low mm-spectral indices via a strong enough concentration of small ISM-like particles. The result of this analysis further strengthen the scenario for which the measured low spectral indices of protoplanetary disks at long wavelengths are due to the presence of large mm/cm-sized pebbles in the disk outer regions.

Chapter 8 — I present the first calculations predicting the millimeter emission of disks based on a physical model of grain growth. The measured mm-wave fluxes for disks in Taurus and Ophiuchus (Chapter 3, 4) are used to constrain state-of-the-art models of the early evolution of solids in disks. Models can reproduce the observed mm spectral indices, meaning that mm/cm-sized pebbles can be formed in the outer disk regions, but

only for relatively bright, i.e. massive, disks. Two possible solutions to explain low mm spectral indices in fainter disks are 1) a reduction of dust particles due to radial drift, or 2) an efficient conversion of dust into larger, unseen bodies.

Chapter 9 — I show an investigation on the ability of disks to grow solids and trap them in the outer regions of disks, thus slowing down their radial drift. Models accounting for coagulation, fragmentation and motion of particles in a gaseous disk are used to simulate the evolution of solids, and trapping of particles is analyzed by considering a bumpy surface density profile. For different values of the amplitude and length scale of the bumps, I investigate the ability of these models to produce and retain large mm/cm-sized particles in the outer disk on Myr time scales. The predictions of these models are also compared with the observed mm-fluxes of real disks. Using the Common Astronomy Software Applications ALMA simulator, I show how ALMA observations in the near future will help to constrain the physics of dust evolution in protoplanetary disks.

Chapter 10 — I summarize the main findings of this Thesis and I discuss future prospects of this work which are planned or already in progress.

Modelling the emission of protoplanetary disks

Nearly all the information which can be extracted on the geometrical and physical structure of protoplanetary disks is derived from the analysis of the observed electromagnetic radiation. As outlined in the Introduction, the work presented in this Thesis is focused on the disk properties which can be constrained through observations at long (sub-)millimeter wavelengths. The aim of this Chapter is to describe the key physical ingredients which are relevant for the analysis of the sub-mm/mm spectral energy distribution (SED). In Section 2.1 I describe how the problem of converting the measured disk SED into constraints on the disk structure is typically tackled by disk models; in Section 2.1.1 I summarize the main observational findings for the disk surface density from sub-mm interferometry; in Section 2.2 the characteristics of the adopted dust model are presented, and the method to derive the dust opacity is finally described in Section 2.2.1.

2.1 The disk continuum emission

Whereas astronomical observations at different wavelengths can directly probe the SED of protoplanetary disks, in order to convert the information on the disk SED into constraints on the disk structure, modeling of the disk emission is necessary. Throughout this Thesis I will adopt the *two-layer passively irradiated* disk models (Chiang & Goldreich, 1997; Dullemond et al., 2001). These models have been extensively used to explain through a consistent picture a range of different observations (multi-wavelength photometry, spectral features, scattered light imaging, IR and sub-mm interferometric imaging) for disks around brown dwarfs, low-mass T Tauri stars, and intermediate mass Herbig AeBe stars (see Natta et al., 2007, and references therein).

The main input parameters of these models are the properties of the central star (luminosity, effective temperature, mass), the radial profile of the dust surface density $\Sigma(R)$, and the dust properties, which determine the dust opacity as described in Sect. 2.2, 2.2.1.

In these models, the vertical structure and temperature of the disk is computed under the assumptions of heating by the stellar radiation (i.e. the disk is *passive*, with no appreciable radiation arising from intrinsic luminosity in the disk), hydrostatic vertical equilibrium between the gas pressure and stellar gravity (disk self-gravity is neglected), thermodynamical equilibrium between gas and dust. The disk structure is determined by iterating the calculation of the vertical disk structure with an approximate solution to the radiative transfer problem. Because of the hypothesis of hydrostatic equilibrium, the disk has a flared geometry (Kenyon & Hartmann, 1987), with the opening angle (ratio between the scale height and orbital radius) increasing with the orbital radius. The vertical distribution of gas (and dust) is given by a Gaussian law with pressure scale height derived from the temperature in the disk midplane and the keplerian orbital frequency. At each iteration step, the radiative transfer problem is solved in an approximate way by splitting the disk structure in two layers: a *surface* layer defined as the locus of points in the disk with optical depth to the stellar radiation < 1 ; an *interior* layer, or disk *midplane*, characteristic of deeper disk regions. The disk surface layer absorbs the stellar radiation, it heats up, and re-emits half of the energy away from the disk, and the other half toward the disk interior. The interior layer absorbs a fraction of this re-emitted radiation, heats up, and in turn re-emits radiative energy away from the disk. The temperatures in the surface, T_s , and interior layers, T_i , are therefore calculated imposing thermal equilibrium. With this new midplane temperature T_i , a new vertical structure is calculated, and this process is repeated until convergence. Note that this method neglects the absorption of the midplane radiation by the disk surface layers, and, more in general, treats the exchange of energy along the vertical direction of the disk in an approximated way. However, more realistic (but more computationally expensive) 1 + 1D radiative transfer disk models have shown that the sub-mm SED computed through the two-layer approximation is accurate at the 10 – 20% level (see Dullemond & Natta, 2003).

Once the thermal structure of the disk is determined, the total continuum dust emission is derived by summing the contribution from the disk interior layer, i.e.

$$F_\nu^i = \frac{2\pi \cos i}{d^2} \int_{R_{\text{in}}}^{R_{\text{out}}} B_\nu[T_i(R)] \left[1 - e^{-\tau_\nu^i(R)}\right] R dR, \quad (2.1)$$

and from the disk surface

$$F_\nu^s = \frac{2\pi}{d^2} \int_{R_{\text{in}}}^{R_{\text{out}}} B_\nu[T_s(R)] \left[1 + e^{-\tau_\nu^i(R)}\right] \Delta\Sigma(R) \kappa_\nu^s R dR. \quad (2.2)$$

In Eq. (2.1) and (2.2)¹, ν is the frequency, i is the disk inclination, i.e. the angle between the disk axis and the line of sight, d is the distance, R_{in} and R_{out} are the inner and outer disk radii, respectively, $\Delta\Sigma$ is the dust surface density in the disk surface, κ_ν^s is the dust

¹The two terms in the sum in Eq. (2.2) come from the two surface layers of the disk: the one which is closer to the observer, for which no attenuation is present, and the one which is behind the midplane of the disk, which attenuates the radiation through the $e^{-\tau_\nu^i(R)}$ term.

opacity in the surface layer², τ_ν^i is the line-of-sight dust optical depth in the disk interior, i.e.

$$\tau_\nu^i = \frac{\Sigma(R)\kappa_\nu^i}{\cos i}, \quad (2.3)$$

where κ_ν^i is the dust opacity in the disk interior; finally, $B_\nu(T)$ is the Planck function at the temperature T :

$$B_\nu(T) = \frac{2h\nu^3}{c^2} \frac{1}{e^{\frac{h\nu}{k_B T}} - 1}, \quad (2.4)$$

where h is the Planck constant, c is the speed of light, k_B is the Boltzmann constant.

Eq. 2.1 can be interpreted as the sum of infinitesimal annuli, each emitting as a gray body at a local temperature $T_i(R)$. At long (sub-)millimeter wavelengths, most of the disk mass is contained in optically thin regions, i.e. with $\tau_\nu^i \ll 1$ (Sect. 2.2.1), and therefore the flux density from the disk midplane (Eq. 2.1, 2.3) can be approximated as

$$F_{\text{mm}}^i \approx \frac{2\pi}{d^2} \int_{R_{\text{in}}}^{R_{\text{out}}} B_{\text{mm}}[T_i(R)]\Sigma(R)\kappa_{\text{mm}}^i R dR, \quad (2.5)$$

Considering that at all radii $\Sigma(R) \gg \Delta\Sigma(R)$, the comparison between Eq. (2.2) and (2.5) shows that the disk midplane dominates the emission at (sub-)mm wavelengths. This is particularly relevant, since it means that (sub-)mm observations with high enough angular resolution have the potential to constrain the radial profile of the dust surface density, which is a crucial physical property for models of disk evolution and planet formation. This method has been used for interferometric observations in the sub-mm, as explained in the next section. Note that constraining the dust surface density is not possible through observations at shorter wavelengths: in the infrared the line-of-sight optical depth is typically larger than 1 because of the large IR dust opacities (see Sect. 2.2.1). For this reason only the surface layer, which contains a tiny fraction of the disk mass, can be probed at these wavelengths.

2.1.1 The disk surface density

As described in the last section, the low optical depths at sub-mm wavelengths allow to probe the midplane of the disk, which contains the bulk of disk mass. From Eq. (2.5) it follows that the surface brightness of the disk at these long wavelengths is given by

$$I_{\text{mm}}(R) \approx B_{\text{mm}}[T_i(R)]\Sigma(R)\kappa_{\text{mm}}^i. \quad (2.6)$$

Sub-mm observations which can spatially resolve the disk emission, in combination with a disk model which can derive the temperature profile $T_i(R)$ and dust opacity κ_{mm}^i ,

²Note that in these equations the dust opacity is taken to be radially constant.

can be used to constrain the radial profile of the dust surface density $\Sigma(R)$. The knowledge of the surface density profile $\Sigma(R)$ in protoplanetary disks is fundamental both for our understanding of planet formation (Mordasini et al., 2009; Boss, 2010), and of disk evolution (Hartmann et al., 1998).

Protoplanetary disks have typical diameters of a few hundreds AU, and angular sizes of the order of a few arcseconds at the distance of nearby star forming regions, e.g. Taurus and Ophiuchus (~ 150 pc). Therefore, sub-mm observations with angular resolutions of about 1 arcsec or less can probe the radial structure of the disk. To get to a diffraction-limited angular resolution of 1 arcsec at 1 mm, a telescope with an aperture size of 200 m is needed. Whereas this is not possible with a single-dish telescope, sub-arcsecond resolution can be easily achieved by interferometry, for which the angular resolution of the observations is defined by the longest separation between two antennas of the interferometric array, rather than by the aperture size of the single antenna.

The first extensive interferometric survey of protoplanetary disks in the millimeter was performed by Dutrey et al. (1996), who observed a sample of 33 young circumstellar disks in Taurus-Auriga with the Plateau de Bure Interferometer (PdBI) at 2.7 mm. In this survey the authors detected 2.7 mm dust continuum emission in 12 systems, and the angular resolution of the observations, of about 2-3'', allowed them to get first constraints on the physical size of disks. In particular, the surface density profile $\Sigma(R)$ was modeled as a simple truncated power law:

$$\Sigma(R) = \begin{cases} \Sigma(R_0) \times \left(\frac{R}{R_0}\right)^{-p} & \text{for } R \leq R_{\text{out}} \\ 0 & \text{for } R > R_{\text{out}} \end{cases} \quad (2.7)$$

where R_0 is an arbitrary radius in the disk. The constrained values of the disk outer radii R_{out} range between about 50 and 300 AU, with a peak at ~ 150 AU. However, since this value is close to the resolution limit of the observations (at the Taurus-Auriga distance an angular resolution of 2'' corresponds to a spatial resolution of about 280 AU in disk diameter, or 140 AU in disk radius), higher resolution observations were needed to confirm this result. For the same reason, i.e. limited resolution, the power-law exponent p of the surface density profile (Eq. 2.9) could not be constrained.

Kitamura et al. (2002) observed at 2 mm a sample of 13 young disks in Taurus-Auriga with an angular resolution of about 1'' using the Nobeyama Millimeter Array. For all these sources they constrained both the outer disk radius R_{out} and the power-law index p of the surface density profile. The central values of these two parameters span intervals of about 80 – 400 AU and 0 – 1.8 for R_{out} and p , respectively. Furthermore, other than fitting the observational data with the truncated power-law model (Eq. 2.9) they also adopted a more realistic and physically-motivated radial profile for the surface density with an exponential taper:

$$\Sigma(R) = \Sigma(R_c) \times \left(\frac{R}{R_c}\right)^{-\gamma} \exp\left[-\left(\frac{R}{R_c}\right)^{2-\gamma}\right], \quad (2.8)$$

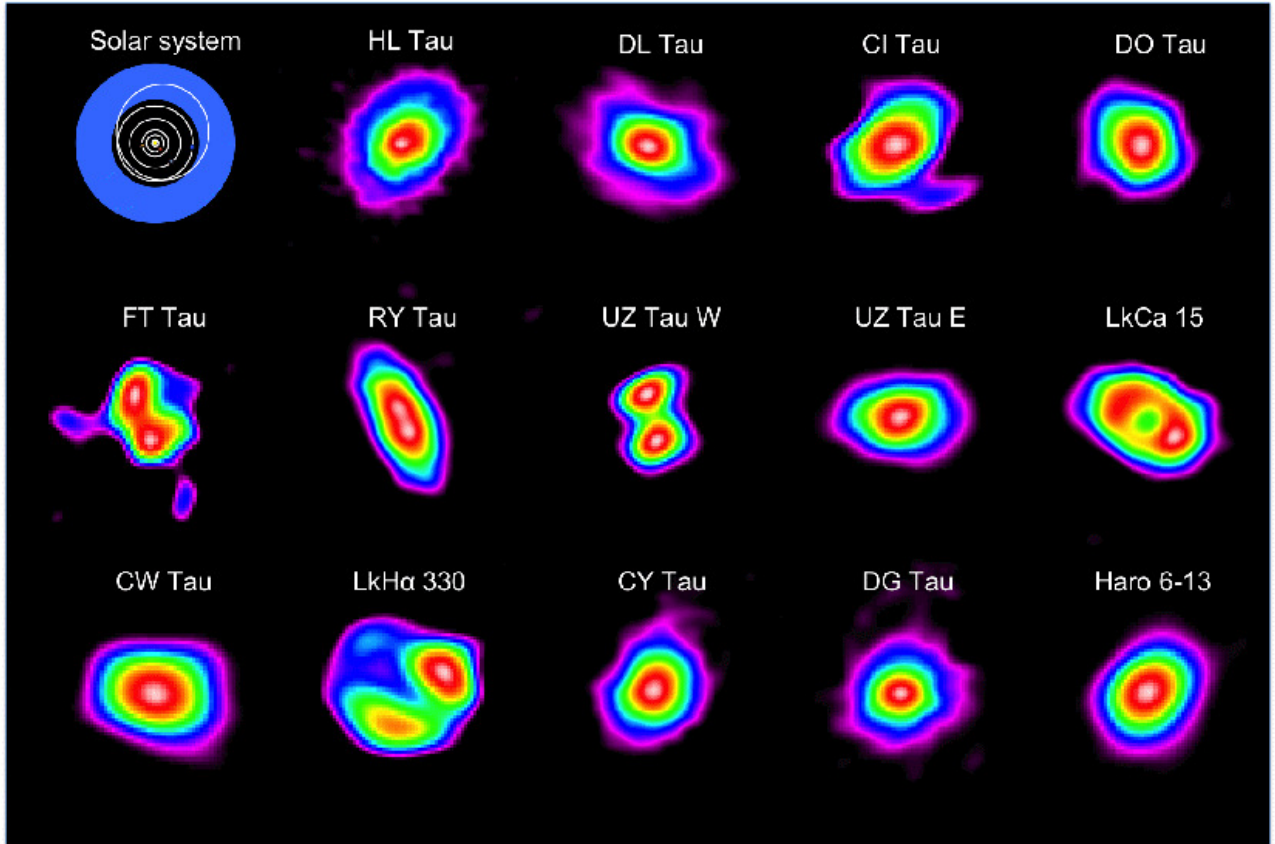


Figure 2.1: Collection of 14 disks in Taurus imaged at 1.3 mm with the Combined Array for Research in Millimeter-wave Astronomy (CARMA); the angular resolution of the observations is between $0.3''$ and $1.0''$; the top left panel shows the scale of the Solar System for comparison (work led by Laura Perez, Andrea Isella, and John Carpenter at Caltech, and Woojin Kwon at the University of Illinois; image available online at <http://www.mmarray.org>).

where R_c is a characteristic radial scale for this surface density profile, and γ controls the radial variation of the surface density itself. This surface density profile has the same form as in the similarity solution for viscous accretion disks (Lynden-Bell & Pringle, 1974; Hartmann et al., 1998), in which the radial dependence of the viscosity ν is a power-law function with index γ , i.e. $\nu(R) = \nu(R_c) \times (R/R_c)^\gamma$. A radial profile with an exponential taper as in Eq. (2.8) has also been invoked in the past to match the intensity profiles of disks seen in optical absorption in the Orion Nebula (McCaughrean & O’Dell, 1996), and, more recently, to reconcile the different disk radii obtained for the same disks from observations in continuum (probing the dust) and line (probing the molecular gas; see Hughes et al., 2008). By using this surface density profile to fit the data, Kitamura et al. (2002) derived γ -values in the range of 0 – 0.8.

In the following years, new sub-mm interferometers and improved capabilities of the existing facilities allowed to constrain the surface density of disks with higher precision.

Sub-mm observations with sub-arcsec angular resolution and high sensitivity became possible, and data were commonly interpreted with either sharply truncated power-law models or exponential tapered power-law ones. Isella et al. (2009) presented the first sub-arcsecond ($\sim 0.7''$ at 1.3 mm with CARMA) interferometric survey of disks, and found a relatively broad range of γ -values between about -0.8 and 0.8 for a sample of 14 disks, nearly all of them in Taurus (Fig. 2.1). In terms of the characteristic radii R_c , they constrained values $\sim 30 - 230$ AU when converted to the radial normalization shown in Eq. (2.8). This range for R_c is very similar to the one ($R_c \sim 14 - 198$ AU) derived by Andrews et al. (2009, 2010) through 0.88 mm observations with the SMA (angular resolution $\sim 0.3''$, or about 20 AU in terms of radial scale) for a sample of 16 disks in Ophiuchus. In terms of the γ parameter, however, they found a much narrower distribution ($\gamma \sim 0.4 - 1.1$) than the one derived by Isella et al. (2009) for another sample of disks. Further observations and analysis are needed to understand whether this discrepancy is really due to different properties of disks in Taurus and Ophiuchus or if it is instead due to the different disk models and/or methodologies adopted for fitting the data.

For most of the bright disks observed so far, the inferred surface density profiles are consistent with the expected distribution of mass in the early Solar Nebula. Fig. 2.2 shows the constrained surface density radial profiles for a sample of 12 disks in Ophiuchus Andrews et al. (2009, 2010) overlaid on the predicted surface density of the early Solar Nebula at the locations of Saturn, Uranus, Neptune planets according to the Minimum Mass Solar Nebula models (MMSN, Weidenschilling, 1977). In the last decades, different versions of the MMSN model have been proposed (Weidenschilling, 1977; Hayashi, 1981; Desch, 2007), but all of them are derived using the same basic procedure: augmenting the mass of heavy elements observed in planets with light elements (hydrogen and helium) to reach the element ratios for Solar composition, and spread these augmented masses into annuli around the Sun and centered on the (current) semi-major axes of the planets to derive the surface densities. Although the MMSN model is probably too simplistic to provide an accurate and detailed description of the distribution of matter in the early Solar Nebula, it can be considered as a useful order of magnitude guide. The fact that the observed disks show similar surface densities as those predicted from the MMSN models, confirm the idea that at least some of the observed disks have the potential to form planetary systems similar to our own.

2.2 The dust model

The last parameter appearing in Eq. (2.5) for the calculation of the (sub-)mm SED which has to be discussed is the monochromatic dust opacity in the disk midplane. In order to derive the dust opacity $\kappa(\lambda)$ a model for the emitting dust grains in the disk has to be considered. Specifying a dust model means defining the physical properties of the grains, like shape and size-distribution, and also the chemical composition. Therefore obtaining observational constraints on the dust opacity and its dependence on wavelength have the potential to infer the properties of dust grains in disks. Since as described in the first

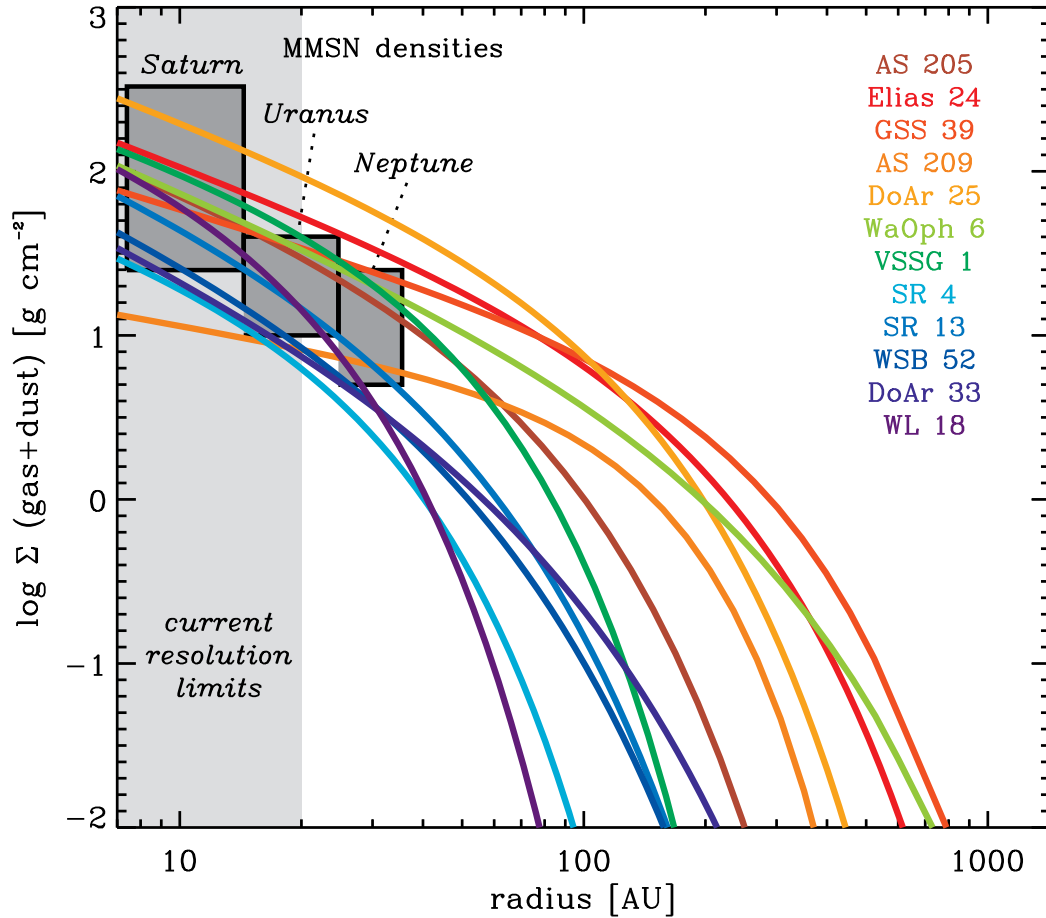


Figure 2.2: Total (gas+dust) surface density profile as constrained for 12 disks in Ophiuchus through SMA observations at 0.88 mm (Andrews et al., 2009, 2010). The density profiles inferred from dust tracers have been scaled up assuming a gas-to-dust mass ratio of 100. The angular resolution of the observations is $\sim 0.3''$, corresponding to a radial scale of about 20 AU at the Ophiuchus distance, as shown by the light gray shaded area in the plot. Dark gray boxes represent the surface densities extrapolated for Saturn, Uranus, and Neptune in the standard Minimum Mass Solar Nebula (Weidenschilling, 1977). Image from Williams & Cieza (2011).

Chapter the initial steps of planet formation involve the coagulation and growth of solid particles in the disk, observations of the dust emission from young disks can constrain the early stages of the formation of planetary systems. How this can be done through observations in the (sub-)mm, together with the limitations of this method, are the subjects of the following Chapters of this Thesis. In this Section, I describe the dust model that I'll adopt throughout the Thesis. In Section 2.2.1 I describe the method used to derive the monochromatic dust opacity.

The dust model adopted in this Thesis is a simplified version of the one proposed by Pollack et al. (1994), who estimated the composition and abundances of grains (and gases) in both molecular cloud cores and young circumstellar disks by considering the results of a wide range of astronomical data and theory, the composition of primitive bodies in the solar system, and solar elemental abundances³. In particular, the composition and abundances in disks are derived from the compositional model for molecular cloud cores, accounting for some chemical evolution expected in the shock interface between the cloud core and the disk, and at the physical conditions typical of disks. In this Thesis, I consider a simplified version of the Pollack et al. model, in which only the three most abundant species are considered. These are olivine, refractory organics, and water ice⁴. The adopted ratios for the abundances of these three species are close to those derived by Pollack et al. (1994) in the disk outer regions, which dominate the emission in the (sub-)mm (see next Chapters). The correspondent volume fractional ratios are 1 : 3 : 6 for olivine : organics : water ice. Also, the dust model considered in this Thesis accounts for the possibility of having some porosity in the grain by considering vacuum as an extra component. The impact of grain porosity onto the dust emission at sub-mm wavelengths is discussed in Chapter 8.

Since the evolution of dust grains involve frequent collisions of particles leading to either coagulation or fragmentation depending on the relative velocity of each encounter, it is reasonable to consider a dust population characterized by a distribution of grains with different sizes. Apart for Chapter 8 and XX, in which the grain size-distribution was calculated through physical models of dust evolution, in all other Chapters of the Thesis a truncated power-law is adopted:

$$n(a) = \begin{cases} a^{-q} & \text{for } a_{\min} < a < a_{\max} \\ 0 & \text{otherwise} \end{cases} \quad (2.9)$$

where a is the grain size, a_{\min} and a_{\max} are the minimum and maximum grain sizes present in the dust population, respectively, and q is the power-law index of the distribution. This simple formulation, which is nevertheless a good first approximation for the typical size-distributions derived by sophisticated models of dust evolution (see Birnstiel et al., 2011), is very useful to derive quick but significant constraints on some of the basic properties of the distribution of particle sizes through sub-mm observations of disks. This represents the main goal of this Thesis, and is the subject of the next Chapters.

³An implicit assumption of this model is that dust in protoplanetary disks have the properties as in the early Solar nebula.

⁴The other four, less abundant species considered in the Pollack et al. model are orthopyroxene, troilite, volatile organics, and metallic iron.

In terms of the shape of the grains I adopted spherical particles. Although small sub- μm sized aggregates are likely characterized by a fractal and fluffy (therefore non-spherical) geometry, the growth of these particles to larger grains with sizes of $0.1 - 1$ mm typically leads to more compact structures, which are closer to a simple spherical geometry (Beckwith et al., 2000; Blum & Wurm, 2008). Since, as detailed in the next Chapters, most of the (sub-)mm emission of disks is generated by mm-sized particles, the spherical approximation was adopted.

2.2.1 The dust opacity

Once a model for the dust grains in the disk is defined, the associated dust opacity law $\kappa(\nu)$ can be calculated. Grains in protoplanetary disks are composed of different chemical elements, and therefore a technique which combines the optical properties of the single constituents to derive the global properties of the composite grain is required. In this Thesis the Bruggeman effective medium theory (Bruggeman, 1935) was adopted for this purpose. After calculating the optical properties of the composite grain, the Mie theory provides an analytical solution of Maxwell's equations for the absorption of electromagnetic radiation by spherical particles, and it can be used to derive the absorption coefficient $Q_{\text{abs}}(a, \nu)$. This parameter can be in turn converted into a single-grain dust opacity $\kappa_1(a, \nu)$ and finally convolved with the grain size-distribution to get the opacity law $\kappa(\nu)$ of the dust population. In this Section, I describe the main steps of this procedure to derive the dust opacity for a given dust population.

The starting point is the knowledge of the (wavelength-dependent) optical constants (n_j, k_j) of each individual constituent of the grain, here labeled with the j -index. For the case of the dust model described in Sect. 2.2, the optical constants are taken from Weingartner & Draine (2001), Zubko et al. (1996), Warren (1984) for olivine, organics and water ice, respectively. The optical constants define the complex refractive index $m_j = n_j + k_j i$, and complex dielectric function $\epsilon_j = m_j^2$ of each component.

Once the complex dielectric functions $\{\epsilon_j\}_{j=1, \dots, n}$ are known, an effective dielectric function ϵ_{eff} for the composite grain can be computed using the Bruggeman effective medium theory and its mixing rule:

$$\sum_{j=1}^N f_j \frac{\epsilon_j - \epsilon_{\text{eff}}}{\epsilon_j + 2\epsilon_{\text{eff}}} = 0, \quad (2.10)$$

where N is the number of different constituents, including vacuum, in the grain, and f_j is the volume fraction of the j -th constituent ($\sum_{j=1}^N f_j = 1$). For vacuum, $\epsilon_{\text{vac}} = 1$. Eq. (2.10) is an implicit equation which can be solved for the effective dielectric function of the grain ϵ_{eff} . Mie theory can then be used to convert ϵ_{eff} (or the effective refractive index $m_{\text{eff}} = \sqrt{\epsilon_{\text{eff}}}$) into an absorption coefficient for a given grain size and frequency $Q_{\text{abs}}(a, \nu)$ (see e.g. Stratton, 1941, for a modern formulation of the Mie theory). The dust opacity for a

single grain is then easily calculated through

$$\kappa_1(a, \nu) = \frac{3}{4a\rho} Q_{\text{abs}}(a, \nu), \quad (2.11)$$

where “1” stands for “single grain” and ρ is the mean density of the grain:

$$\rho = \sum_{j=1}^N f_j \rho_j, \quad (2.12)$$

with ρ_j being the volume density of the j -th constituent.

Finally, the dust opacity $\kappa(\nu)$ of the dust population is calculated by convolving the single-grain opacity $\kappa_1(a, \nu)$ with the grain size distribution $n(a)$:

$$\kappa(\nu) = \frac{\int_0^\infty n(a) a^3 \kappa_1(a, \nu) da}{\int_0^\infty n(a) a^3 da}. \quad (2.13)$$

The reason for the factor a^3 in both the integrals of Eq. (2.13) can be easily understood by multiplying numerator and denominator by $(4\pi\rho/3)$: in the two integrals $(4\pi\rho a^3/3)$ is the mass of the particle of radius a , and since, by definition, $n(a)da$ is the number of particles with radii between a and $a + da$, the denominator gives the total mass of dust particles, whereas the numerator is the total cross section, and their fraction gives the dust opacity for the whole population of grains.

In the literature, the derivative of the dust opacity $\kappa(\nu)$ with respect to frequency is called “ β ”. This parameter plays a pivotal role in this Thesis because it is a proxy for the presence of millimeter/centimeter-sized pebbles in circumstellar disks, as detailed in Section 3.4 in Chapter 3. Whereas determining the absolute scale of the $\kappa(\nu)$ function in real disks is very hard through direct astronomical observations, its frequency-dependence, and therefore β , can instead be constrained by measuring how the flux-density of disks varies with frequency in the (sub-)mm (see Eq. 2.5).

Dust properties of protoplanetary disks in the Taurus-Auriga star forming region from millimeter wavelengths

Published as Ricci, Testi, Natta, Neri, Cabrit, & Herczeg, 2010, A&A 512, 15

Abstract

We present the most sensitive 3 mm-survey to date of protoplanetary disks carried out in the Taurus-Auriga star forming region (average rms of about 0.3 mJy), using the IRAM PdBI. With our high detection rate of 17/19 we provide the first detections at wavelengths longer than about 1 mm for 12 sources. This enables us to statistically study the mm SED slopes and dust properties of faint disks and compare them to brighter disks using a uniform analysis method. With these new data and literature measurements at sub-millimeter and millimeter wavelengths, we analyze the dust properties of a sample of 21 isolated disks around T Tauri stars in the Taurus-Auriga star forming region. Together with the information about the disks' spatial extension from sub/mm-mm interferometric studies, we derive from the observed sub-mm/mm spectral energy distribution constraints on the dust opacity law at these wavelengths, using two-layer flared disk models and a self-consistent dust model that properly takes into account the variation of the dust opacity with grain growth. We find evidence for the presence of dust particles in the disk midplane that have grown to sizes as large as at least 1 millimeter in all the disks of our sample, confirming what was previously observed on smaller brighter objects. This indicates that the dust coagulation from ISM dust to mm-sized grains is a very fast process in protoplanetary disks, which appears to occur before a young stellar object enters the class II evolutionary stage. The amount of these large grains in the disk outer regions is also found to be stationary throughout the whole class II evolutionary stage, which indicates that mechanisms slowing down the dust inward migration play an important

role in the Taurus-Auriga protoplanetary disks. Another result is that the spectral index between 1 and 3 mm for the six faintest disks in our sample is on average smaller than for the brighter disks, indicating either that these fainter yet unmapped disks are spatially much less extended than the brighter spatially resolved disks, or that fainter disks have typically larger dust grains in their outer regions. Considering that these fainter disks are more representative of the bulk of the disk population than the brighter ones, this may have important consequences for the theories of planetesimal formation and disk formation and evolution. Finally, we investigate the relations between the derived dust properties, namely dust mass and grain growth, and the properties of the central star, like its mass, age and mass accretion rate.

3.1 Introduction

Circumstellar disks play a fundamental role in the physical processes involved in star and planet formation. In these systems part of the material (gas and dust) loses angular momentum and accretes onto the central forming star, while another part of it may give birth to a planetary system. Although the content of dust is only a small fraction of the overall material in a circumstellar disk, dust grains are crucial elements in the early stages of planet formation. According to the core-accretion scenario (Safronov & Zvjagina, 1969; Pollack et al., 1996), growth from an initial ISM population of submicrometer-sized dust grains to planetesimals of 1 – 100 km sizes is believed to be the key mechanism of early planet formation. These planetesimals “embryos” then continue to grow leading to the formation of at least terrestrial planets and possibly the cores of giant planets.

Observational evidence of grain growth from the ISM dust has been obtained from a variety of techniques at different wavelengths. (Throop et al., 2001) observed in optical and near-infrared the translucent edge of the 114-426 protoplanetary disk in the Orion Nebula Cluster, and derived from the extinction curve of the background nebular emission a lower limit of a few microns for the dust grains in the very outer regions of the disk, about 500 AU away from the central star. Another method to probe the presence of large grains in the disk is through the shape and intensity of the 10- and 20- μm silicate features. The data indicate a large variety of silicate profiles, ranging from strongly peaked silicate bands and steeply rising spectral energy distributions (SEDs) to “boxy” silicate profiles and flatter SEDs (ISO, Spitzer Space Telescope, Malfait et al., 1998; Kessler-Silacci et al., 2006). The boxy features with low feature-to-continuum ratios are interpreted as grain growth to micron size (Bouwman et al., 2001).

However, the techniques outlined so far can only probe dust grains as large as some μm in the disk surface layers. They are not sensitive to larger grains in the disk midplane, the region in which planet formation is supposed to occur. In order to probe larger grains in the midplane, observations at millimeter wavelengths are needed. Beckwith & Sargent (1991) showed that T Tauri stars have shallow SEDs at sub-millimeter wavelengths. Under the assumption of optically thin emission at these frequencies, this implies a dust opacity dependence on wavelength ($\kappa_{\text{mm}} \propto \lambda^{-\beta}$) much flatter than in the ISM ($\beta_{\text{ISM}} = 1.7$),

which is naturally interpreted in terms of grain growth (see e.g. Draine, 2006). However, this interpretation of the disk SEDs is not unique, since the same data can be explained by very small optically thick disks. To break this degeneracy and sort out the effect of potentially large optical depth it is necessary to spatially resolve the disks to determine their actual sizes. Furthermore, in this context observations at millimeter wavelengths are very useful, since at these lower frequencies the impact of optically thick disk inner regions to the total emission is expected to be lower. Therefore, to actually probe the dust properties in protoplanetary disks, one needs to combine the determination of the sub-millimeter/millimeter SED with information on the disk extension from high-angular resolution interferometric observations (see e.g. Testi et al., 2001).

In the last years, several sub-mm/mm interferometric observations have been carried out to investigate dust grain growth in protoplanetary disks. Wilner et al. (2000) resolved the disk around the TW Hya pre-main-sequence (PMS) star at 7 mm using the Very Large Array (VLA). Extensive modelling of the SED of this source has shown that the dust grains in the outer parts of the TW Hya disk have grown to at least ~ 1 cm (Calvet et al., 2002). An analogous result has been obtained for the disk around CQ Tau (Testi et al., 2003). More recently, Rodmann et al. (2006) resolved 10 disks in the Taurus-Auriga star forming region and found clear evidence of grain growth in 4 of them. Lommen et al. (2007) resolved 1 disk in Chamaeleon and 4 in Lupus with the Submillimeter Array (SMA) at 1.4 mm and with the Australia Telescope Compact Array (ATCA) at 3.3 mm, and found clear evidence of dust grain growth to sizes of a few millimeter for 4 of them. Finally Schaefer et al. (2009) observed a sample of 23 low mass PMS stars (with spectral types of K7 and later) in Taurus-Auriga at 1.3 mm and 2.6 mm with the Plateau de Bure Interferometer (PdBI); they detected only 8 sources at 1.3 mm and 6 at 2.6 mm, and found evidence of grain growth for the 3 disks that they could spatially resolve.

In this paper we present our analysis on 21 protoplanetary disks around T Tauri stars in the Taurus-Auriga star forming region without stellar companions in the range $0.05'' - 3.5''$. For 11 of these objects, mainly faint disks with $F_{1.3\text{mm}} < 100$ mJy, we have obtained new data at ~ 3 mm with the Plateau de Bure Interferometer¹ (hereafter PdBI) with an average rms of about 0.3 mJy. Together with the data already present in the literature at sub/mm- and mm- wavelengths, and with the information obtained in the last years on the disks spatial extension from high-angular resolution interferometric observations at mm wavelengths, we investigate the dust properties in the disks, namely grain growth and dust mass, and their relation with the properties of the central star.

In Section 3.2 we present our new PdBI data, the properties of our sample, the method we used to estimate the main stellar physical quantities, and the data we used for our analysis. In Section 3.3 we describe the disk models adopted for the analysis of the disks sub-mm/mm SED. In Section 8.3 we show and discuss the results of our study in terms of dust grain growth and dust mass, whereas in Section 5.4 we summarize our main findings.

¹The Plateau de Bure Interferometer at IRAM is supported by INSU/CNRS (France), MPG (Germany) and IGN (Spain).

3.2 New 3mm observations and sample properties

3.2.1 New PdBI observations

We observed a total list of 19 targets; 16 of them were selected to be relatively faint, with $15 \text{ mJy} < F_{1.3\text{mm}} < 100 \text{ mJy}$ and with no known detections beyond about 1mm; the other 3 (HL, DO and DR Tau) are brighter sources that were observed for references purposes. The observations were carried out with PdBI between July and August, 2007. Owing to antenna maintenance work, all observations were carried out in a subarray of the six-element interferometer. The antennas were arranged in very compact configurations that provided sensitive baselines from 15 m to 80 m. The dual-polarization receivers, which were observing in the 3mm band, had typical receiver temperatures of about 35 K and were providing image sideband rejection values better than 10 dB. To achieve maximum sensitivity in the continuum, the spectral correlator was adjusted to cover a total effective bandwidth of about 2 GHz.

The observing procedures were set up to fill in gaps in the scheduling without any specific tuning wavelength within the 3mm band. Visibilities were obtained using on-source integration times of 22 min interspersed with 2 min calibrations on a nearby calibrator. Each star was observed on one or more occasions for a minimum of 40 min and a maximum of 2 hr on-source. The atmospheric phase stability on the baselines was always better than 40° , consistent with seeing conditions of $1''$ - $3''$, typical for summer. The absolute flux density scale was calibrated on 3C84, 0528+134, MWC349 and Mars, and was found to be accurate to 10%. The receiver passband shape was determined with excellent precision on a strong calibrator like 3C84.

We used the GILDAS package for the data reduction and analysis. The data were calibrated in the antenna based manner. The continuum visibilities were gridded with natural weighting and no taper to maximize the sensitivity. Since none of the target stars was found to be resolved in synthesized beams of $2''$ - $4''$, a point source model was fitted to the calibrated visibilities of each star to estimate the flux density of the continuum in the 3mm band. The results are summarized in Table 6.1. Among the 19 targets, 17 were detected, including 14 of the 16 faint sources, thanks to our good sensitivity; 12 of these are first detections longward of about 1mm, strongly expanding the available database of 3mm data towards fainter disks. The 2.6mm detections of LkHa 358 and GO Tau were recently published by Schaefer et al. (2009).

In Sections 7.2, 4.3.3 and 3.2.4 we describe the final sample used for our analysis of dust properties, the adopted method to estimate the stellar properties and mass accretion rates summarized in Table 7.5, whereas in 3.2.5 we report the sub-mm/mm data that we collected from the literature for our analysis.

3.2.2 Sample

Our final sample of 21 sources consists of all young stellar objects (YSO) in Taurus-Auriga catalogued in Andrews & Williams (2005) that fulfill the following criteria: (1) a Class II

Table 3.1: Summary of the new PdBI observations.

Object	α (J2000)	δ (J2000)	ν (GHz)	λ (mm)	F_ν (mJy)	rms (mJy)	Comments ¹
CW Tau	04:14:17.0	28:10:56.51	84.2	3.57	3.44	0.31	
CX Tau	04:14:47.8	26:48:11.16	86.2	3.49	1.01	0.13	
DE Tau	04:21:55.6	27:55:05.55	92.6	3.23	3.32	0.25	
DK Tau	04:30:44.3	26:01:23.96	84.2	3.57	4.70	0.20	2.5'' binary
DO Tau	04:38:28.6	26:10:49.76	84.2	3.57	13.80	0.29	
DP Tau	04:42:37.7	25:15:37.56	84.2	3.57	< 0.78	0.26	no sub-mm info
DR Tau	04:47:06.2	16:58:43.05	100.8	2.97	13.90	0.47	
DS Tau	04:47:48.6	29:25:10.96	100.8	2.97	2.96	0.21	
FM Tau	04:14:13.5	28:12:48.84	100.8	2.97	2.65	0.24	
FP Tau	04:14:47.4	26:46:26.65	100.8	2.97	11.80	0.26	no sub-mm info
FY Tau	04:32:30.5	24:19:56.69	100.8	2.97	1.90	0.28	no sub-mm info
FZ Tau	04:32:31.8	24:20:02.53	100.8	2.97	2.89	0.24	
GK Tau	04:33:34.6	24:21:06.07	100.8	2.97	< 0.96	0.32	2.5'' binary
GO Tau	04:43:03.1	25:20:17.38	86.2	3.49	4.05	0.34	
Haro 6-28	04:35:56.9	22:54:36.63	87.0	3.45	0.92	0.18	0.7'' binary
HL Tau	04:31:38.4	18:13:57.37	84.5	3.53	43.40	0.68	flat spectrum
HO Tau	04:35:20.2	22:32:13.98	87.0	3.45	2.03	0.53	
LkHa 358	04:31:36.2	18:13:43.20	84.5	3.53	2.46	0.22	no sub-mm info
SU Aur	04:55:59.4	30:34:10.39	84.5	3.53	2.88	0.19	

1) Reason why the source has not been considered in the analysis (see text for more details).

infrared SED, in order to avoid contamination of sub-mm fluxes by a residual envelope; (2) information on the central star through optical-NIR spectroscopic/photometric data, necessary to calculate self-consistent disk SED models; (3) one detection at ~ 3 mm (either from our new PdBI observations or from the literature) and at least one detection in the $0.45 \text{ mm} < \lambda < 0.85 \text{ mm}$ spectral region. This selection criterion was chosen in order to probe a broad enough spectral window to efficiently constrain the optically thin part of the sub-mm/mm spectral energy distribution (SED); (4) no evidence of stellar companions in the $0.05 - 3.5''$ range in angular separation. This range corresponds to about $5 - 500 \text{ AU}$ in projected physical separation at the Taurus-Auriga star forming region distance, here assumed to be 140 pc for all the sources of our sample (Bertout et al., 1999). The limit of 3.5 arcsec ensures that mm interferometric flux measurements, of typical resolution 1 arcsec , are not contaminated by the companion’s disk, while binaries closer than 5 AU should have outer disk properties similar to those of single stars on the scales probed by (sub-)mm data.

Only 21 sources catalogued by Andrews & Williams (2005) fulfill the above 4 criteria. They are listed in Table 7.5, and include 11 sources from our PdBI sample².

Figure 1 reports histograms that describe the completeness level of our final sample with respect to all Taurus-Auriga Class II YSOs catalogued in Andrews & Williams (2005), and fulfilling the “isolation” criterion (4). Our sample contains 63% of these “isolated” class II showing a flux at $\sim 0.85\text{mm}$ greater than 100 mJy , and 31% of the sources with lower 0.85mm fluxes. Therefore, our sample is not complete even for the brightest YSOs at 0.85mm . This is due to a lack of observations at $\sim 3\text{mm}$ for these sources. However, thanks to the high sensitivity of our new PdBI observations (see Section 7.5) our sample enables us to study statistically for the first time the dust properties of faint disks (i.e. with $F_{1.3\text{mm}} < 100 \text{ mJy}$, $F_{0.85\text{mm}} < 100 \text{ mJy}$) and compare them to the brighter ones using a uniform analysis method. In terms of the stellar properties, it is important to note that the Andrews & Williams (2005) catalogue includes only a few very low mass PMS stars: only stars with an estimated mass higher than about $0.2 M_{\odot}$ have been detected because of the sensitivity limits of the current facilities at sub-mm and mm wavelengths that make the detection of disks around very low mass YSOs very difficult. The sensitivity limitation is even more severe at 3mm , therefore our final sample includes 58% of all the class II isolated sample of Andrews & Williams (2005) with an estimated mass greater than $0.4 M_{\odot}$, but only two sources with $M_{\star} < 0.4 M_{\odot}$ (out of 10 in Andrews & Williams, 2005).

²The 8 sources dropped from the PdBI sample are HL Tau (a flat spectrum source that retains an envelope; Padgett et al., 1999); DP Tau, FP Tau, FY Tau and LkHa 358 that have no available submm detections for SED fitting; and DK Tau, GK Tau and Haro 6-28 which are binary systems with angular separations of $2.5''$ (Simon et al., 1992), $2.5''$ (Reipurth et al., 1993) and $0.7''$ (Leinert et al., 1993) respectively. We keep in our sample the wide binaries DS Tau and HO Tau (angular separations of $7.1''$ and $6.9''$ respectively, Mathieu, 1994); they do not show any emission from the companions from our new 3 mm interferometric observations. The other dropped multiple systems from the AW05 catalog are DH Tau ($2.3''$ binary, Itoh et al., 2005), GG Tau (quadruple system with a circumbinary ring of inner and outer radii of 180 and 260 AU respectively, Pinte et al., 2007), and UY Aur ($0.9''$ binary, Leinert et al., 1993).

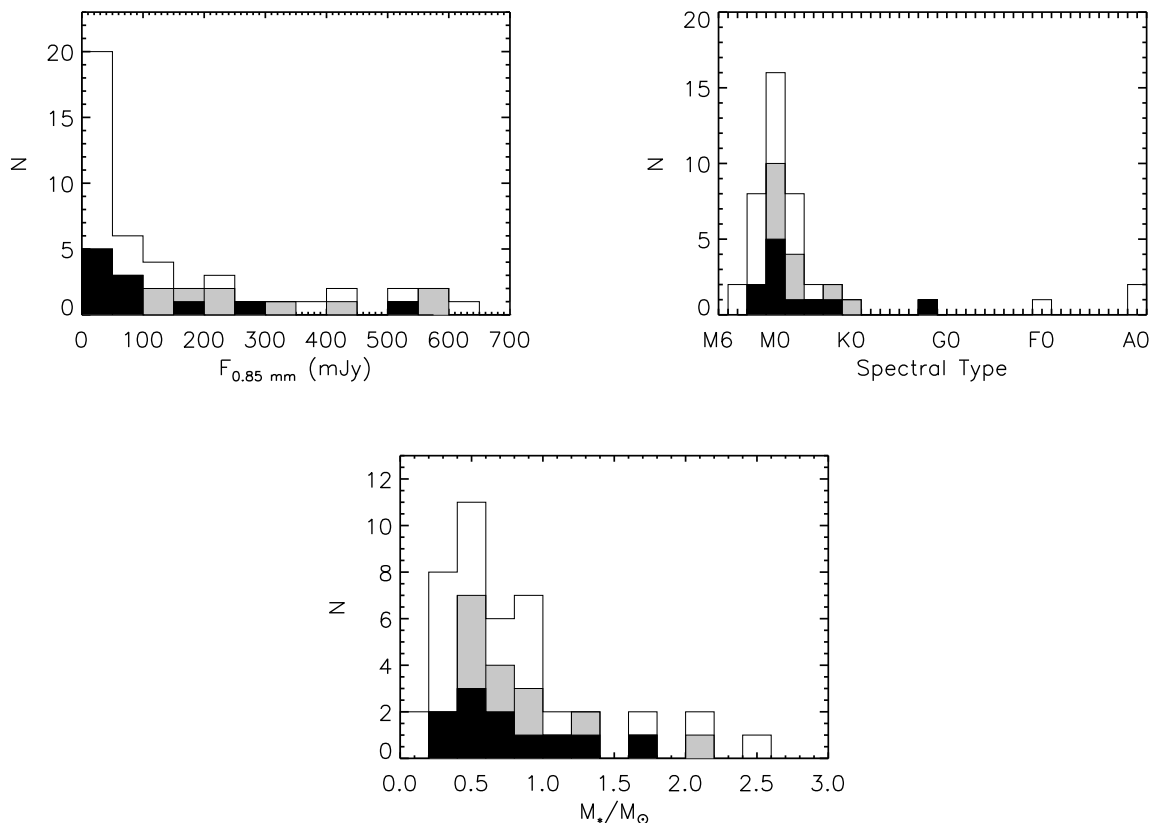


Figure 3.1: Histograms highlighting some properties of our selected sample. In all the histograms our sample is represented by black+grey columns, the black columns represent the disks in our sample for which we obtained new PdBI data at ~ 3 mm, while the total columns (black+grey+white) include all the class II YSOs from the Andrews & Williams (2005) catalogue with no evidence of stellar companions in the $0.05\text{--}3.5''$ interval in angular separation, from which our sample has been selected (see text). Upper left histogram represents the distribution of the ~ 0.85 mm fluxes, including upper limits, for all the sources but two, 04113+2758 and GM Aur, that have not been observed at ~ 0.85 mm. Upper right and bottom histograms show the distribution of stellar spectral type and estimated stellar mass (see Section 4.3.3) respectively. Four class II YSOs are not included in these histograms because for them an estimate of the stellar spectral type is not available. These are 04301+2608, FT Tau, Haro 6-39 and IC 2087.

3.2.3 Stellar properties

Spectral types for all the sources in our sample are taken from the literature (Kenyon & Hartmann, 1995; Briceño et al., 1998) and cover a range from G2 (SU Aur) to M2.5 (CX Tau). Spectral types of M0 and earlier have been converted to effective temperatures with the dwarf temperature scale of Schmidt-Kaler (1982), whereas for types later than M0 we adopted the temperature scale developed by Luhman (1999). Typical uncertainties for these sources are $\sim 1 - 1.5$ in spectral sub-types or $\sim 100 - 150$ K in temperature.

The stellar luminosities of all the pre-main-sequence (PMS) stars were computed from their J -band flux (2MASS All Sky Catalog of point sources, Cutri et al., 2003) to minimize contamination from UV and IR excess emission. For the bolometric corrections we adopted the dwarf values from Kenyon & Hartmann (1995) that are considered to be satisfactory approximations for these young sources in the J -band (Luhman, 1999).

In order to estimate the amount of extinction toward these young sources, we calculated the color excesses using intrinsic colors provided by Kenyon & Hartmann (1995) for G2–K7 spectral types and by Leggett et al. (1992) for M0–M2.5 types. To ensure that the color excess reflects only the effect of reddening, minimizing the emission due to accretion, the typical selected colors are between the R and H bands. Since for some of the objects at later spectral types in our sample $R - I$ measurements are not available, we dereddened the $J - H$ and $H - K_s$ colors from the 2MASS All Sky Catalog of point sources³ to the locus observed for classical T Tauri stars (CTTS) by Meyer et al. (1997), following the method described in Briceño et al. (2002). Extinctions are finally calculated adopting the extinction law of Rieke & Lebofsky (1985).

The computed photospheric luminosities cover a range from $0.16 L_{\odot}$ (HO Tau) to $10.6 L_{\odot}$ (SU Aur). Considering the uncertainties in the photometry, reddenings, bolometric corrections and distance, the typical errors in the bolometric luminosities are $\pm 0.08 - 0.13$ in $\log L_{\star}$. Slight differences from the values obtained by other authors are typically within the uncertainties and are not significant for the purposes of this paper.

Given the effective temperatures and photospheric luminosities, we placed the PMS stars on the H-R diagram and derived stellar masses and ages adopting the theoretical tracks and isochrones of Palla & Stahler (1999) (see Figure 4.2). One important source of uncertainty for stellar masses and ages is given by the spread of values obtainable by using different PMS evolutionary models. For example, if compared to the ones obtained with the Baraffe et al. (1998) models, our adopted values of stellar masses and ages are typically lower by a factor of ~ 1.5 and ~ 2 respectively. Our choice of using the Palla & Stahler (1999) models is uniquely due to the more complete coverage of the HR diagram plane, that allows us to use the same evolutionary models for all the sources of our sample. One should always bear in mind the high uncertainty associated to these quantities, especially to the stellar age (see Section 3.4.1 for a more detailed discussion about the estimates of YSO ages). According to the Palla & Stahler (1999) models the ranges spanned by our

³For this analysis the JHK_s magnitudes have been transformed from the 2MASS photometric system to the Johnson-Glass one using the color transformations reported in Carpenter (2001) and Bessell & Brett (1988).

sample go from about $0.3 M_{\odot}$ (CX Tau) to $2.2 M_{\odot}$ (RY Tau) in stellar masses and from about 0.1 Myr (UZ Tau E) to 17 Myr (DS Tau) in stellar ages.

The main stellar quantities described here are summarized in Table 7.5.

3.2.4 Mass accretion rates

Given the stellar luminosities and effective temperatures we calculated the stellar radii using the Stefan-Boltzmann law. Once the stellar mass M_{\star} and radius R_{\star} are set, the mass accretion rate \dot{M}_{acc} can be directly obtained from an estimate of the accretion luminosity L_{acc} by

$$\dot{M}_{\text{acc}} = 1.25 \frac{R_{\star} L_{\text{acc}}}{GM_{\star}}, \quad (3.1)$$

where G is the gravitational constant and the factor of ~ 1.25 is calculated assuming a disk truncation radius of $\sim 5 R_{\star}$ (Gullbring et al., 1998).

The estimates of L_{acc} were obtained from spectroscopic detections of excess Balmer continuum emission in the literature (see references in Table 7.5). These estimates are obtained primarily from measuring the excess flux in the Balmer continuum shortward of 3646 \AA . The luminosity is then obtained by applying a bolometric correction calculated from shock models (Calvet & Gullbring, 1998; Gullbring et al., 2000) or simplistic plane-parallel slabs (Valenti et al., 1993; Gullbring et al., 1998).

Two sources in our sample, FZ Tau and GO Tau, do not have literature estimates of accretion luminosity from the excess Balmer continuum emission. We obtained the accretion luminosity for these two sources from low-resolution spectra from $3200\text{--}8700 \text{ \AA}$ obtained with the Double Spectrograph at the 5m Hale Telescope at Palomar. The accretion luminosity was then calculated from the excess Balmer continuum emission, following the method described in Herczeg & Hillenbrand (2008).

3.2.5 Disks sub-mm and mm data from the literature

In order to probe the sub-millimetre and millimeter SED we collected data of the dust continuum emission between ~ 0.450 to $\sim 7 \text{ mm}$ from several works in the literature, listed in Table 3.3. These data, except for 7 mm measurements, have been used together with the new PdBI observations at $\sim 3 \text{ mm}$ to constrain the disk properties by fitting the sub-mm/mm SED with the models described in Section 3.3. The 7-mm data is excluded because free-free emission from ionized gas contaminates disk emission, with free-free emission typically contributing $\sim 20\%$ of the 7mm flux (Rodmann et al., 2006). Simultaneous cm observations are required to constrain the free-free emission at 7mm , which is variable on short timescales (\lesssim a few days, see Lommen et al., 2009). Only 2 disks in our sample (RY Tau and UZ Tau E) have been observed nearly simultaneously at centimeter and millimeter wavelengths (Rodmann et al., 2006), without which the 7mm fluxes should be considered only as upper limits for the dust emission. We therefore did not include the 7mm data in our analysis, although we included the available 7mm data from the literature in Figure

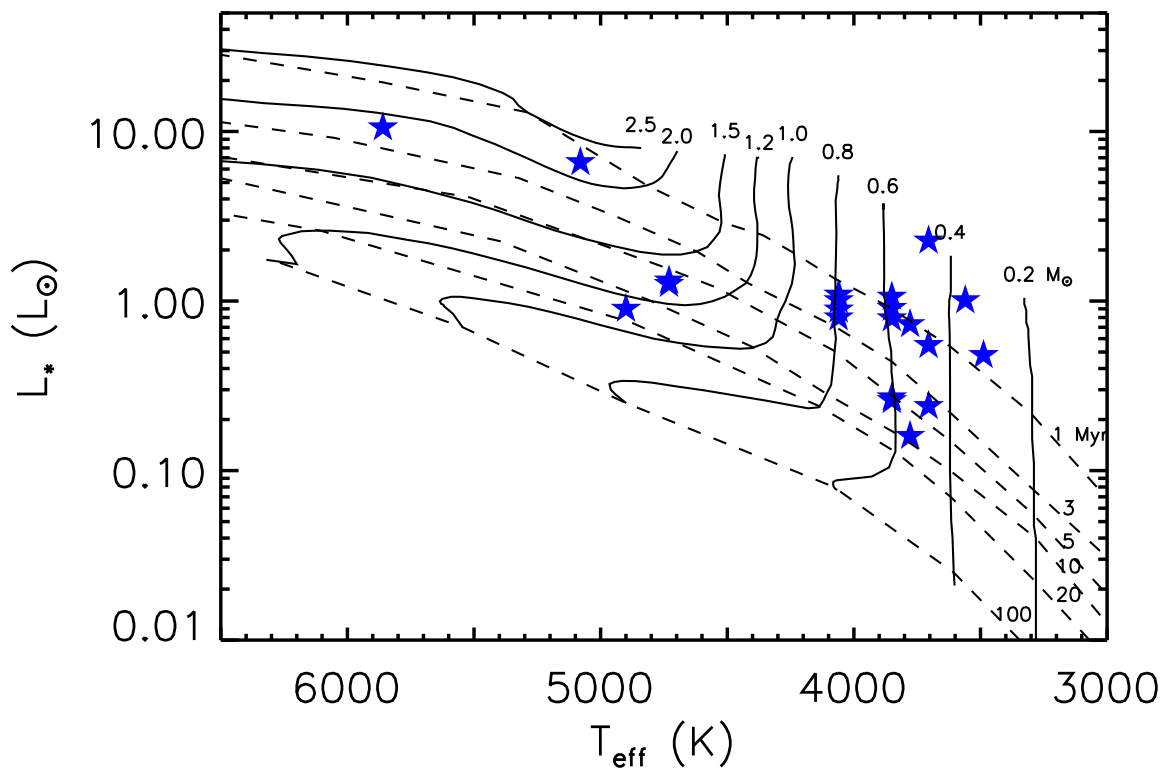


Figure 3.2: H-R diagram for the sources of our sample. The dashed lines correspond to the isochrones for ages in Myr as labeled at the right end of the lines from the Palla & Stahler (1999) PMS evolutionary models, while the solid ones represent the evolutionary tracks from the same models for PMS stars with masses as labeled at the top of the evolutionary track lines. In this diagram the evolutionary tracks start from an age of 0.1 Myr. The errorbars for the (T_{eff}, L_*) values of our objects are not shown, the uncertainties in the photometric parameters are typically $\sim 0.08 - 0.13$ in $\log L_*$ and $\sim 100 - 150$ K in temperature.

Table 3.2: Stellar properties.

Object	ST	T_{eff} (K)	L_{\star} (L_{\odot})	L_{acc} (L_{\odot})	Ref. (L_{acc}) ^a	R_{\star} (R_{\odot})	$\text{Log } \dot{M}_{\text{acc}}$ ($M_{\odot} \text{ yr}^{-1}$)	M_{\star} (M_{\odot})	Age (Myr)
AA Tau	K7	4060	0.80	0.03	1	1.8	-8.56	0.8	2.4
CI Tau	K7	4060	1.01	0.11	2	2.0	-7.95	0.8	1.7
CW Tau	K3	4730	1.32	0.05	2	1.7	-8.58	1.2	6.6
CX Tau	M2.5	3488	0.48	0.03	2	1.9	-8.18	0.3	0.8
CY Tau	M1	3705	0.55	0.04	1	1.8	-8.24	0.5	1.4
DE Tau	M2	3560	1.01	0.07	1	2.6	-7.69	0.4	0.2
DL Tau	K7	4060	0.89	0.23	2	1.9	-7.66	0.8	2.2
DM Tau	M1	3705	0.24	0.10	2	1.2	-7.99	0.5	3.6
DN Tau	M0	3850	0.91	0.02	1	2.2	-8.55	0.6	1.1
DO Tau	M0	3850	0.79	0.60	1	2.0	-7.10	0.6	1.3
DR Tau	K7	4060	1.09	0.72	2	2.1	-7.12	0.8	1.5
DS Tau	K2	4900	0.90	0.21	1	1.3	-8.00	1.1	17.0
FM Tau	M0	3850	0.26	0.10	2	1.2	-8.13	0.6	6.3
FZ Tau	M0	3850	1.06	0.46	3	2.3	-7.14	0.6	0.8
GM Aur	K3	4730	1.26	0.07	1	1.7	-8.44	1.2	7.2
GO Tau	M0	3850	0.27	0.01	3	1.2	-9.14	0.6	4.8
HO Tau	M0.5	3778	0.16	0.01	2	0.9	-9.13	0.5	8.7
IQ Tau	M0.5	3778	0.73	0.04	2	2.0	-8.24	0.6	1.2
RY Tau	K1	5080	6.59	1.60	4	3.3	-7.03	2.2	1.1
SU Aur	G2	5860	10.6	0.55	4	3.2	-7.52	1.7	2.2
UZ Tau E	M1	3705	2.27	0.31	2	3.7	-7.02	0.5	0.1

a) References. (1) Gullbring et al. (1998); (2) Valenti et al. (1993), these accretion luminosities have been multiplied by a factor $(140 \text{ pc}/160 \text{ pc})^2$ to account for the current estimate of 140 pc for the distance to the Taurus-Auriga star forming region; (3) Herczeg et al. (2009); (4) Calvet et al. (2004).

4.3 and verified a posteriori that the fluxes of our disk models for all sources are equal or less than the measured flux at 7mm. Simultaneous 7mm and cm-wavelength observations with the EVLA will extend the coverage of the disk SED to longer wavelengths, in order to better constrain the millimeter-wavelengths dust opacity and to provide information on dust grains larger than ~ 1 cm.

3.3 Disk models

We compare the observational sub-mm/mm data with the two-layer models of flared disks (i.e. in hydrostatic equilibrium) heated by the stellar radiation as developed by Dullemond et al. (2001), following the schematization of Chiang & Goldreich (1997). These models have been used in the analysis of CQ Tau by Testi et al. (2003) and of a sample of 9 Herbig Ae stars by Natta et al. (2004) and we refer to these papers for a more detailed description.

To completely characterize a model of the disk, we need to specify the stellar properties (i.e. the luminosity L_\star , effective temperature T_{eff} , mass M_\star and distance d , assumed to be 140 pc for all the sources in our sample), some characteristics of the disk structure, namely the inner and outer radius (R_{in} and R_{out} , respectively), the parameters Σ_1 and p defining the radial profile of the dust surface density assumed to be a power-law⁴ $\Sigma_{\text{dust}} = \Sigma_{\text{dust},1}(R/1 \text{ AU})^{-p}$, the disk inclination angle i (90° for an edge-on disk) and, lastly, the dust opacity. The millimeter SED is almost completely insensitive to some of the disk parameters, which cannot thus be constrained by our analysis. For example, the inner radius of the disk, R_{in} , affects the emission only at near and mid-infrared wavelengths.

The outer radius R_{out} is a parameter that can be probed by high-angular resolution interferometric observations. In our sample 13 disks have been spatially resolved, yielding an estimate for R_{out} . It is important to note that different interferometric observations performed on the same disk can lead to very different values of R_{out} (≥ 100 AU) because of differences in the observations angular resolution, sensitivity, and methods for deriving the radius. Given these uncertainties in the determination of R_{out} , we consider a range of possible values for R_{out} rather than a single-value estimate, as listed in Table 3.4. For the 8 objects in our sample that have not yet been mapped with angular resolutions smaller than a few arcseconds which may potentially resolve the disk, a fiducial interval of 100 – 300 AU has been assumed⁵. This adopted range for R_{out} comprises the vast majority of the

⁴As shown by Hughes et al. (2008) and Isella et al. (2009), a tapered exponential edge in the surface density profile, physically motivated by the viscous evolution of the disk, is able to explain the apparent discrepancy between gas and dust outer radii derived from millimeter observations of protoplanetary disks. Here we want to note that when fitting the sub/mm-mm SED with an exponential tail instead of a truncated power-law, the dust opacity spectral index β (defined in Section 3.3.1) is unchanged, and disk masses vary by less than a factor of 2, even if the outer disk radius becomes much bigger (see, e.g., Table 4 in Kitamura et al., 2002). So the simpler truncated power-law model is a justified approximation for the purposes of this paper.

⁵We will refer to these sources (CW, CX, DE, DS, FM, FZ, HO Tau, and SU Aur) as “unmapped” for the rest of the paper. Note that they are all faint with $F_{1\text{mm}} < 120$ mJy. This probably explains why for these objects no observations at high-angular resolution have been attempted yet: the sensitivity of the

Table 3.3: Literature sources for the sub-mm/mm data.

λ (mm)	Source References ^a
0.450	1
0.600	2, 3
0.624	4
0.769	4
0.800	2, 3
0.850	1, 5
0.880	5
1.056	4
1.100	2, 3
1.200	6
1.300	1, 7, 8, 9, 10
1.330	5
2.000	2, 11
2.700	7, 8, 12, 13
3.100	8
3.400	9, 14
7.000	15

a) References. (1) Andrews & Williams (2005); (2) Mannings & Emerson (1994); (3) Adams et al. (1990); (4) Beckwith & Sargent (1991); (5) Andrews & Williams (2007b); (6) Altenhoff et al. (1994); (7) Dutrey et al. (1996); (8) Jensen et al. (1996); (9) Koerner et al. (1995); (10) Isella et al. (2009); (11) Kitamura et al. (2002); (12) Mundy et al. (1996); (13) Schaefer et al. (2009); (14) Ohashi et al. (1996); (15) Rodmann et al. (2006).

disk outer radii distribution function as derived by Andrews & Williams (2007b) through $\sim 1''$ angular resolution sub-millimeter observations of 24 disks in Taurus-Auriga and ρ -Ophiucus. We will discuss the impact of the outer disk uncertainty on the results of our analysis in Section 8.3. Here we want to note that with these values of R_{out} the disk emission at sub-mm/mm wavelengths is dominated by the outer disk regions ($R > 30$ AU) which are optically thin to their own radiation. An effect of this is that the millimeter SED does not depend on the disk inclination angle i (for $i \lesssim 80^\circ$), thus decreasing the number of the model parameters used to fit the observational SED. This is certainly true for the spatially resolved disks for which we have an estimate for R_{out} . The 8 unmapped objects could have optically thick inner disks that contribute significantly to the sub-mm/mm emission. Since the disk outer radius cannot be constrained by the SED alone, interferometric imaging that spatially resolves these disks is the only way to get information on the exact value of R_{out} . Nevertheless, since the disks that have been spatially resolved so far show outer radii typically in the range 100 – 300 AU, we consider highly unlikely that a significant fraction of the unmapped disks have $R_{\text{out}} \lesssim 50$ AU, which would make the disk optically thick even at mm wavelengths.

3.3.1 Dust opacity

The last quantity that defines the disk model is the dust opacity, which depends on grain sizes, chemical compositions, and shapes (e.g. Miyake & Nakagawa, 1993; Pollack et al., 1994; Draine, 2006). In order to extract from the sub-mm/mm SED quantitative estimates for the dust grain sizes and the dust mass in the disks, assumptions on the chemical composition and shape of the dust grains have to be made.

For our discussion we considered porous composite spherical grains made of astronomical silicates, carbonaceous materials and water ice (optical constants for the individual components from Weingartner & Draine, 2001; Zubko et al., 1996; Warren, 1984, , respectively) adopting fractional abundances used by Pollack et al. (1994) (see caption of Figure 3.3). We considered a population of grains with a power-law size distribution $n(a) \propto a^{-q}$ between a minimum and a maximum size, a_{min} and a_{max} , respectively. In the ISM, a_{min} is a few tens of Å, $a_{\text{max}} \sim 0.1 - 0.2 \mu\text{m}$, and $q = 3.5$ (Mathis et al., 1977; Draine & Lee, 1984, , by analysing extinction and scattering of starlight from the interstellar dust). As discussed e.g. in Natta et al. (2004) in a protoplanetary disk, because of grain processing, one expects much larger values of a_{max} than in the ISM, and a variety of possible q values, depending on the processes of grain coagulation and fragmentation that occur in the disk. Experimental studies of fragmentation from a single target have found values of q ranging from ≈ 1.9 for low-velocity collisions to ≈ 4 for catastrophic impacts (Davies & Ryan, 1990), but the power-law index for fragments from shattering events integrated over a range of target masses need not be necessarily the same as in the case of a single target. In the disk, if the coagulation processes from the initial ISM-grains population dominate

current (sub-)mm interferometers would be not high enough to detect the low surface brightness of the outer disk regions.

over the fragmentation ones, then a value for q that is lower than the ISM one is expected (the opposite should occur in the case of fragmentation playing the major role).

In the adopted two-layer disk model, the disk is divided into the surface and midplane regions, and therefore two different opacity laws are considered. Because of the assumed vertical hydrodynamical equilibrium and dust settling, in a protoplanetary disk the content of mass in the midplane is much higher than in the surface. At millimeter wavelengths, where the disk is mostly optically thin to its own radiation, the midplane total emission dominates over the surface one (although the surface dust plays a crucial role for the heating of the disk). As a consequence, from our analysis we can extract information only on the dust opacity of the midplane, and for the rest of the paper when we consider the dust opacity we will mean only the midplane component.

For the dust grains in the disk surface we assumed the same chemical composition and shape as for the midplane grains, whereas for their size distribution we assumed for a_{\min} and a_{\max} values around $0.1 \mu\text{m}$ (the sub-mm SED is insensitive to these values as long as a_{\max} in the surface is much lower than a_{\max} in the midplane, as expected if dust settling is important).

Once the chemical composition and shape of the dust grains in the midplane are set, the dust opacity law depends on a_{\min} , a_{\max} and q . Considering a value of $0.1 \mu\text{m}$ for a_{\min} (the dependence of the millimeter dust opacity from this parameter turns out to be very weak), the models parameters for our analysis are the stellar parameters (L_{\star} , T_{eff} , M_{\star}), that have been set and listed in Table 7.5, plus the disk ones ($\Sigma_{\text{dust},1}$, p , R_{out} , q , a_{\max}), or equivalently (M_{dust} , p , q , a_{\max} , R_{out}) where M_{dust} is the mass of dust in the disk.

For reasons described in Section 8.3 it is convenient to approximate the millimeter dust opacity law discussed so far in terms of a power-law at millimeter wavelengths $\kappa = \kappa_{1\text{mm}}(\lambda/1 \text{ mm})^{-\beta}$, with $\kappa_{1\text{mm}}$ in units of cm^2 per gram of dust. At a fixed value of q the relations between $\kappa_{1\text{mm}}$, β and a_{\max} can be determined. These are shown in Figure 3.3 for $q = 2.5, 3, 3.5, 4$.

3.4 Results

The sub-mm/mm SED fits for all the objects in our sample are reported in Figure 4.3⁶. As discussed in Testi et al. (2003) and Natta et al. (2004), the only quantities that can be constrained by the sub-mm/mm SED are the millimeter dust opacity spectral index β (in this paper calculated between 1 and 3 mm) and the $M_{\text{dust}} \times \kappa_{1\text{mm}}$ product⁷. From the SED alone it is impossible to constrain the value of the surface density exponent p , since it is generally possible to fit the SED data with either very flat ($p = 0.5$) or

⁶We did not include existing NIR and mid-IR data in our analysis because at these shorter wavelengths the disk emission is optically thick and thus depends on the properties of the dust grains located in the surface layers of the inner disk regions. The aim of our analysis is instead to probe the optically thin disk emission in order to investigate the dust properties in the disk midplane.

⁷Note that, according to the adopted disk model, after fixing the stellar parameters, and these two quantities from the observed SED, the midplane temperature is well constrained.

Table 3.4: Adopted disks outer radii.

Object	$R_{\text{out}}^{\text{a}}$ (K02) (AU)	$R_{\text{out}}^{\text{a}}$ (AW07) (AU)	R_{g}^{b} (I09) (AU)	Adopted R_{out} -interval (AU)
AA Tau	214_{-51}^{+63}	400_{-75}^{+600}	...	200 – 400
CI Tau	...	225 ± 50	...	150 – 250
CW Tau	100 – 300
CX Tau	100 – 300
CY Tau	211 ± 28	...	230	230 – 330
DE Tau	100 – 300
DL Tau	152_{-27}^{+28}	175_{-25}^{+50}	...	150 – 250
DM Tau	220 ± 47	150_{-100}^{+250}	160	160 – 260
DN Tau	147 ± 469	100_{-25}^{+300}	125	125 – 225
DO Tau	98 ± 52	100 – 200
DR Tau	193 ± 141	100_{-25}^{+175}	90	90 – 190
DS Tau	100 – 300
FM Tau	100 – 300
FZ Tau	100 – 300
GM Aur	151_{-29}^{+63}	150 ± 25	270	270 – 370
GO Tau	...	350_{-175}^{+650}	160	160 – 260
HO Tau	100 – 300
IQ Tau	329_{-70}^{+403}	250 – 400
RY Tau	81 ± 128	150 ± 25	115	115 – 215
SU Aur	100 – 300
UZ Tau E	160	160 – 260

a) R_{out} listed here results from image fitting using a truncated power-law for the surface density profile. K02: Kitamura et al. (2002); AW07: Andrews & Williams (2007b). b) R_{g} is the radius within which the 95% of the source flux is observed, after fitting the visibility of the source with a gaussian; we used this value, when available, as a lower limit for our adopted R_{out} -interval. I09: Isella et al. (2009).

very steep ($p = 2$) surface density profiles. However, all available high angular resolution observations performed so far suggest that $p \leq 1.5$ (e.g. Dutrey et al., 1996; Wilner et al., 2000; Kitamura et al., 2002; Testi et al., 2003; Andrews & Williams, 2007b; Isella et al., 2009; Andrews et al., 2009).

The degeneracy of the SED on p and R_{out} has an impact onto the derived uncertainties for β and $M_{\text{dust}} \times \kappa_{1\text{mm}}$. Considering both this degeneracy and uncertainties of the observational data, the total absolute uncertainties are approximately 0.2 – 0.3 for β and a factor of ≈ 3 and ≈ 4 for $M_{\text{dust}} \times \kappa_{1\text{mm}}$ for the spatially resolved and unmapped disks respectively. These uncertainties are mainly due to the adopted ranges for R_{out} (listed in Table 3.4) and p between 0.5 and 1.5, whose values determine the impact of the optically thick regions of the disk to the total emission, as explained in Section 3.3.

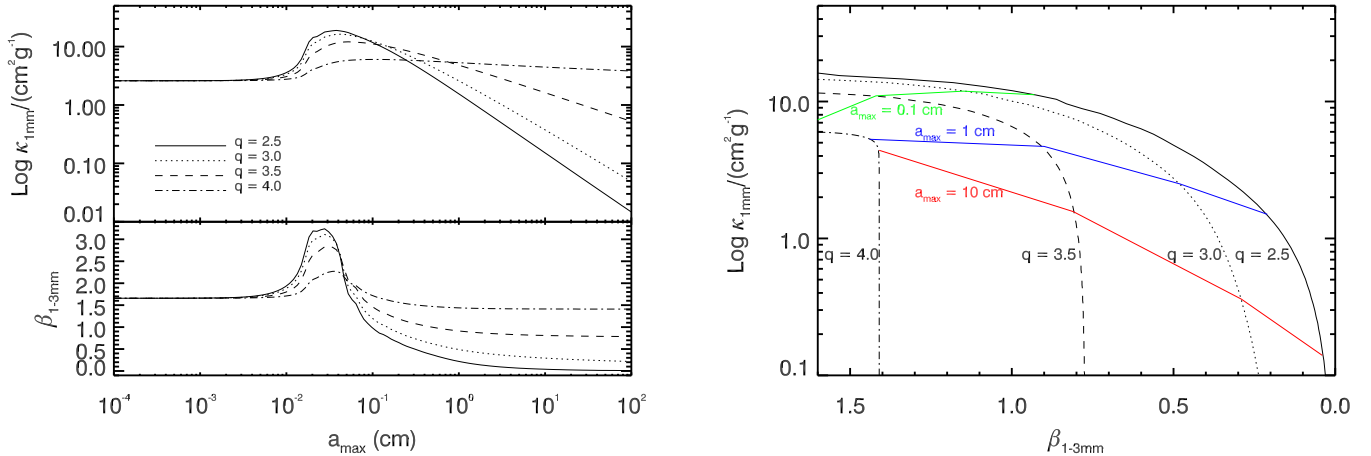


Figure 3.3: Millimeter dust opacity for the adopted dust model. Left top panel: dust opacity at 1 mm as function of a_{max} for a grain size distribution $n(a) \propto a^{-q}$ between $a_{\text{min}} = 0.1 \mu\text{m}$ and a_{max} . Different curves are for different values of q , as labelled. The dust grains adopted here are porous composite spheres made of astronomical silicates ($\approx 10\%$ in volume), carbonaceous materials ($\approx 20\%$) and water ice ($\approx 30\%$; see text for the references to the optical constants). Left bottom panel: β between 1 and 3 mm as a function of a_{max} for the same grain distributions. Right panel: dust opacity at 1 mm as function of β between 1 and 3 mm for the same grain distributions; different iso- a_{max} curves for $a_{\text{max}} = 0.1, 1, 10$ cm are shown. In the plots the unit of measure for the dust opacity is cm^2 per gram of dust.

The estimates for β and $M_{\text{dust}} \times \kappa_{1\text{mm}}$ obtained by our analysis are reported in Table 4.3.

3.4.1 Spectral slopes and dust opacity index

Before analysing the values of β , which provide information on the level of grain growth in the outer disk regions, it is important to check whether our results could be affected

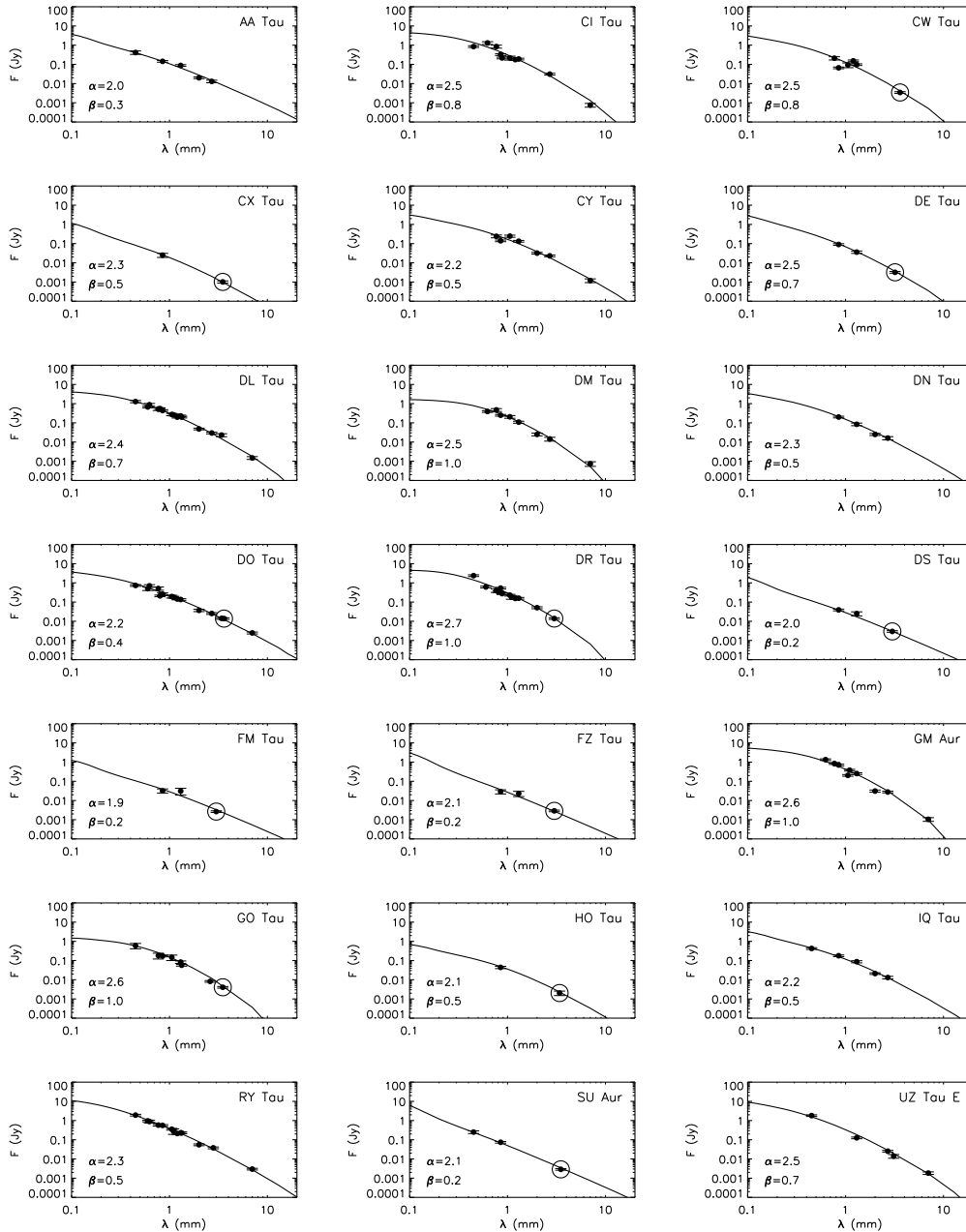


Figure 3.4: Fits of the sub-mm/mm SEDs with the two-layer flared disk models (solid lines). Note that even if the data at 7 mm, available only for 8 disks in our sample, are present in the plots, they have not been used in the fitting procedure (see Section 3.2.5). The errorbars in the plots take into account an uncertainty of 10% on the absolute flux scale, typical for flux measurements at these wavelengths. The circled data come from the new PdBI observations. The fitting values of the spectral index α and of the dust opacity spectral index β between 1 and 3 mm are indicated in the bottom left corner of each plot. The value of the surface density power-law index p adopted in these fits is 1, and the adopted value for the outer disk radius is listed in Table 4.3.

Table 3.5: Disk properties.

Object name ^a	$R_{\text{out}}^{\text{b}}$ (AU)	$F_{1\text{mm}}^{\text{c}}$ (mJy)	$\alpha_{1-3\text{mm}}$	$\beta_{1-3\text{mm}}$	$M_{\text{dust}} \times \kappa_{1\text{mm}}$ ($M_{\odot} \times \text{cm}^2\text{g}^{-1}$)	$M_{\text{dust}}^{q=2.5}$ (M_{\odot})	$M_{\text{dust}}^{q=3}$ (M_{\odot})	$M_{\text{dust}}^{q=3.5}$ (M_{\odot})
AA Tau	300	108	2.0	0.3	$2.8 \cdot 10^{-4}$	$1.5 \cdot 10^{-4}$	$1.5 \cdot 10^{-3}$...
CI Tau	200	314	2.5	0.8	$7.9 \cdot 10^{-4}$	$1.1 \cdot 10^{-4}$	$1.2 \cdot 10^{-4}$	$5.0 \cdot 10^{-4}$
<u>CW Tau</u>	200	129	2.5	0.8	$3.2 \cdot 10^{-4}$	$4.2 \cdot 10^{-5}$	$4.4 \cdot 10^{-5}$	$1.9 \cdot 10^{-4}$
<u>CX Tau</u>	200	19	2.3	0.5	$5.7 \cdot 10^{-5}$	$1.2 \cdot 10^{-5}$	$1.9 \cdot 10^{-5}$...
CY Tau	280	168	2.2	0.5	$6.0 \cdot 10^{-4}$	$1.3 \cdot 10^{-4}$	$2.0 \cdot 10^{-4}$...
<u>DE Tau</u>	200	69	2.5	0.7	$1.6 \cdot 10^{-4}$	$2.4 \cdot 10^{-5}$	$2.8 \cdot 10^{-5}$...
DL Tau	200	313	2.4	0.7	$8.4 \cdot 10^{-4}$	$1.3 \cdot 10^{-4}$	$1.5 \cdot 10^{-4}$...
DM Tau	210	209	2.5	1.0	$9.2 \cdot 10^{-4}$	$1.0 \cdot 10^{-4}$	$1.0 \cdot 10^{-4}$	$1.6 \cdot 10^{-4}$
DN Tau	175	153	2.3	0.5	$3.5 \cdot 10^{-4}$	$7.7 \cdot 10^{-5}$	$1.2 \cdot 10^{-4}$...
DO Tau	150	220	2.2	0.4	$4.9 \cdot 10^{-4}$	$1.4 \cdot 10^{-4}$	$3.1 \cdot 10^{-4}$...
DR Tau	140	298	2.7	1.0	$6.6 \cdot 10^{-4}$	$7.4 \cdot 10^{-5}$	$7.2 \cdot 10^{-5}$	$1.2 \cdot 10^{-4}$
<u>DS Tau</u>	200	28	2.0	0.2	$6.2 \cdot 10^{-5}$	$4.0 \cdot 10^{-5}$	$1.1 \cdot 10^{-3}$...
<u>FM Tau</u>	200	29	1.9	0.2	$6.5 \cdot 10^{-5}$	$6.0 \cdot 10^{-5}$	$1.7 \cdot 10^{-3}$...
<u>FZ Tau</u>	200	27	2.1	0.2	$5.0 \cdot 10^{-5}$	$3.2 \cdot 10^{-5}$	$9.0 \cdot 10^{-4}$...
GM Aur	320	423	2.6	1.0	$1.4 \cdot 10^{-3}$	$1.6 \cdot 10^{-4}$	$1.5 \cdot 10^{-4}$	$2.5 \cdot 10^{-4}$
GO Tau	210	151	2.6	1.0	$6.3 \cdot 10^{-4}$	$7.1 \cdot 10^{-5}$	$6.9 \cdot 10^{-5}$	$1.1 \cdot 10^{-4}$
<u>HO Tau</u>	200	36	2.1	0.5	$1.7 \cdot 10^{-4}$	$3.7 \cdot 10^{-5}$	$5.6 \cdot 10^{-5}$...
IQ Tau	325	118	2.2	0.5	$3.4 \cdot 10^{-4}$	$7.4 \cdot 10^{-5}$	$1.1 \cdot 10^{-4}$...
RY Tau	165	383	2.3	0.5	$5.1 \cdot 10^{-4}$	$1.1 \cdot 10^{-4}$	$1.7 \cdot 10^{-4}$...
<u>SU Aur</u>	200	50	2.1	0.2	$5.0 \cdot 10^{-5}$	$3.2 \cdot 10^{-5}$	$9.0 \cdot 10^{-4}$...
UZ Tau E	210	333	2.5	0.7	$6.1 \cdot 10^{-4}$	$9.6 \cdot 10^{-5}$	$1.1 \cdot 10^{-4}$...

a) Underlined objects are those that have not been mapped to date through high-angular resolution imaging. b) Central value of the adopted R_{out} -interval reported in Table 3.4. This is the value used to extract the other quantities listed in the Table. c) Source flux density at 1 mm from the best fit disk model described in Section 3.3.

by detection biases: indeed, for a given flux at $\sim 1\text{mm}$, a disk with large dust grains in the outer parts will produce a stronger emission at $\sim 3\text{mm}$ than a disk with a population of smaller-sized grains and be easier to detect. In Figure 5.3 the grey region of the plot indicates the area in the $(F_{1\text{mm}}, \alpha_{1-3\text{mm}})$ plane in which the observations carried out so far

are not sensitive, due to the sensitivity limits obtained at 1 and 3 mm. While we could investigate the dust properties for 4 disks with $15 \text{ mJy} < F_{1\text{mm}} < 30 \text{ mJy}$, the plot shows that a disk with a 1 mm flux in this same range, but with a spectral index $\alpha_{1-3\text{mm}} \gtrsim 3.2$, consistent with a disk model with ISM-like dust and an outer radius of $\sim 100 \text{ AU}$, would not be detected at 3 mm. Nevertheless, we want to point out that only 2 of our 16 targets with $F_{1\text{mm}} < 100 \text{ mJy}$ were not detected at 3mm, and both have very weak $F_{1.3\text{mm}}$ fluxes (upper limits of 27 mJy and 21 mJy for DP Tau and GK Tau respectively, Andrews & Williams, 2005), therefore the lack of disks with $\alpha \sim 3.2$ at $F_{1\text{mm}} > 30 \text{ mJy}$ does not seem to be due to our sensitivity limit but is most likely real. Furthermore, as evident from the same plot, the 6 faintest disks, with $F_{1\text{mm}} < 60 \text{ mJy}$, show a spectral index between 1 and 3 mm that is lower on average (2.08 ± 0.08) than for the brighter disks (2.40 ± 0.06). This is the reason of the discrepancy of the average value of the dust opacity spectral index $< \beta >$ between unmapped and resolved disks (see discussion below).

In Figure 3.3 we plot $\kappa_{1\text{mm}}$ and β as functions of a_{max} for different values of q . One interesting result is that the values of β obtained for the objects in our sample by the SED-fitting procedure are all less than or equal to 1, which can be explained only if dust grains with sizes larger than 1 mm are present in the disk. For the 9 sources with $\beta \leq 0.5$, the largest dust grains must have grown to sizes $\geq 1 \text{ cm}$ according to our dust model. If we let q assume values lower than 2.5, thus increasing the fractional number of the larger grains, the maximum grain size decreases, but $a_{\text{max}} \gtrsim 1 \text{ mm}$ for $\beta \lesssim 1$ is still needed.

The estimates of the maximum grain sizes a_{max} depend on the dust model that one adopts. If we consider for example the dust model adopted in Natta et al. (2004) (5% olivine, 15% organic materials, 35% water ice and 50% vacuum), the estimates for a_{max} are greater by about an order of magnitude than the ones obtained with our dust model. In general, no realistic dust grain models result in $\beta < 1$ for $a_{\text{max}} < 1 \text{ mm}$.

Here it is worthwhile to remember that, whereas for the 13 resolved disks in our sample β is well determined, for the 8 disks for which we do not have information on their spatial extension, the optically thick parts of a possible compact disk could significantly contribute to the emission. If that is the case, no conclusions on the dust grain properties could be drawn. In particular, for the 6 unmapped disks with $\alpha \approx 1.9 - 2.2$ (CX Tau, DS Tau, FM Tau, FZ Tau, HO Tau, SU Aur) a very compact disk with $R_{\text{out}} \approx 20 \text{ AU}$, a relative high inclination $i \approx 70^\circ$, and with ISM-like dust grains would fit the sub-mm/mm SED. For the other 2 unmapped sources, DE Tau ($\alpha \approx 2.4$) and CW Tau ($\alpha \approx 2.5$), ISM-like dust grains are consistent with the sub-mm/mm data using a disk model with $i \approx 70^\circ$ and $R_{\text{out}} \approx 30, 40 \text{ AU}$ respectively. For the faintest disks, the outer radius has to be small because if the disks were larger they would also need to be more massive in order to keep being optically thick, thus producing an α value close to 2 with all the possible dust properties. In that case, they would emit more sub-mm/mm-wave radiation than observed. Since, for an optically thick disk, decreasing the inclination angle has the effect of making the SED steeper (because the central, hotter parts are less obscured), for disks with $i < 70^\circ$ the outer radii would need to be even smaller to fit the SED. Since these disk outer radii are lower by factors of 2 – 4 than the smallest disks that have been spatially resolved so far, and since for all the 13 resolved disks the values of β have been found always much

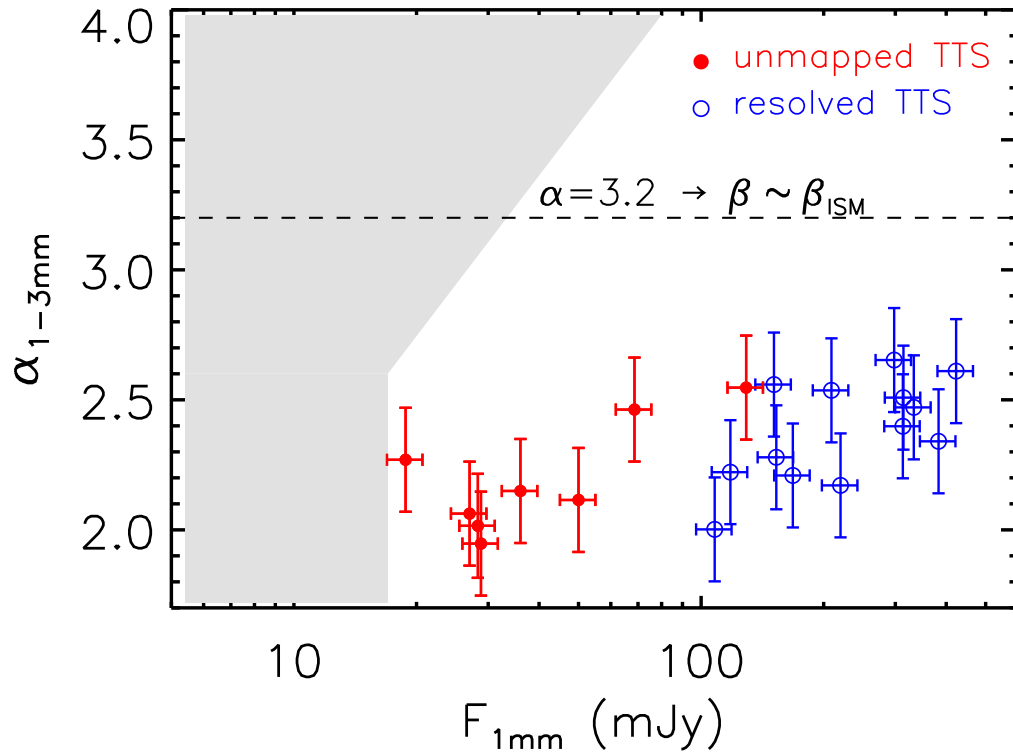


Figure 3.5: Spectral index α between 1 and 3 mm plotted against the flux at 1 mm from the model best fits shown in Figure 4.3. The points plotted here are listed in the first two columns of Table 4.3. Open blue points represent the spatially resolved disks, whereas the filled red points are for the unmapped ones. A value of α consistent with a disk model with ISM-like dust and an outer radius of ~ 100 AU is indicated as a dashed horizontal line. The grey region shows the area in the plot that is unexplored because of the 3σ sensitivity limits of our new and past millimeter observations (here considered as 15 mJy and 1.0 mJy at 1 and 3 mm respectively).

lower than in the ISM ($\beta_{\text{ISM}} \approx 1.7$, see Figure 3.6), thus showing clear evidence of grain growth, we consider very unlikely that many of the unmapped sources are compact, optically-thick disks with unprocessed ISM grains. For AA Tau, which is the faintest of the mapped sources ($F_{1\text{mm}} \approx 100$ mJy) and has a low spectral index of $\alpha \approx 2.0$ typical of fainter sources, the maps indicate a disk radius of 200 – 400 AU ruling out the possibility of optically thick disk regions dominating the total emission, and requiring a low β of 0.3 to explain the shallow slope.

Also, only for the disks with $\beta \gtrsim 0.8$, values of $q \gtrsim 3.5$ are consistent with the data (see right panel in Figure 3.3), in which case $a_{\text{max}} \geq 10$ cm. This is in good agreement with the following consideration using the approximated asymptotic formula $\beta \approx (q-3)\beta_{\text{RJ}}$, derived by Draine (2006), where β_{RJ} is the opacity spectral index of the solid material in the Rayleigh limit, and valid for a population of grains with $3 < q < 4$ and $a_{\text{min}} \ll a_c \ll a_{\text{max}}$, with a_c being a function of the real and imaginary parts of the complex dielectric function and wavelength (at millimeter wavelengths $a_c \sim 1$ mm). Since, at a fixed q , the function $\beta(a_{\text{max}})$ decreases when $a_{\text{max}} \gtrsim 1$ mm (see Figure 3.3), it follows that the approximated asymptotic value $(q-3)\beta_{\text{RJ}}$ gives a lower limit for β at a finite a_{max} . Adopting $\beta_{\text{RJ}} = 1.7$ from the small dust grains in the ISM, for $q \gtrsim 3.5$ we derive $\beta \gtrsim 0.85$, i.e. dust grains populations with $q \gtrsim 3.5$ cannot explain β -values lower than ≈ 0.85 ⁸.

In Figure 3.6 we report the histogram of the β -values derived by our analysis. The average value in our sample considering both unmapped and resolved disks, $\langle \beta \rangle = 0.6 \pm 0.06$, is not consistent with dust populations with q -values of 3.5, like for the ISM, or greater. Values of q lower than 3.5 have been obtained by, e.g., Tanaka et al. (2005) from simulations of grain growth in stratified protoplanetary disks which give vertically integrated size distributions with $q \approx 3$, plus a population of much larger bodies, to which however our observations would not be sensitive.

These considerations clearly suggest that the process of dust grain growth to mm-sizes has played a fundamental role in most, if not all, of the Taurus-Auriga protoplanetary disks whose sub-mm/mm SED has been sufficiently investigated.

From Figure 3.6 it is also evident that the two sub-samples made of unmapped and resolved disks separately have different averaged β values, with the β values being on average lower for the unmapped disks than for the resolved ones ($\langle \beta \rangle = 0.41 \pm 0.10$, 0.68 ± 0.06 for the unmapped and resolved disks respectively). Since the unmapped sample nearly coincides with the fainter disks with $F_{1\text{mm}} < 100$ mJy, and since β is correlated with the spectral index α , this is due to the trend already presented in Figure 5.3 between $F_{1\text{mm}}$ and $\alpha_{1-3\text{mm}}$. This trend agrees with simple expectations for grain growth: as the maximum grain size a_{max} increases, both β and $\kappa_{1\text{mm}}$ decrease, so disks with the same dust mass should become fainter as β gets smaller. Alternatively, the $F_{1\text{mm}}-\alpha_{1-3\text{mm}}$ trend could arise if the fainter disks are smaller, and then more optically thick, than the brighter, resolved ones, while their “true” β would be nearly the same.

In Figure 3.7 we show the β vs stellar age plot. No evidence of an evolutionary trend is present over the large range of stellar ages spanned by our sample. As already discussed the

⁸Note that β -values greater than ≈ 0.85 can be explained by both $q \lesssim 3.5$ and $q \gtrsim 3.5$.

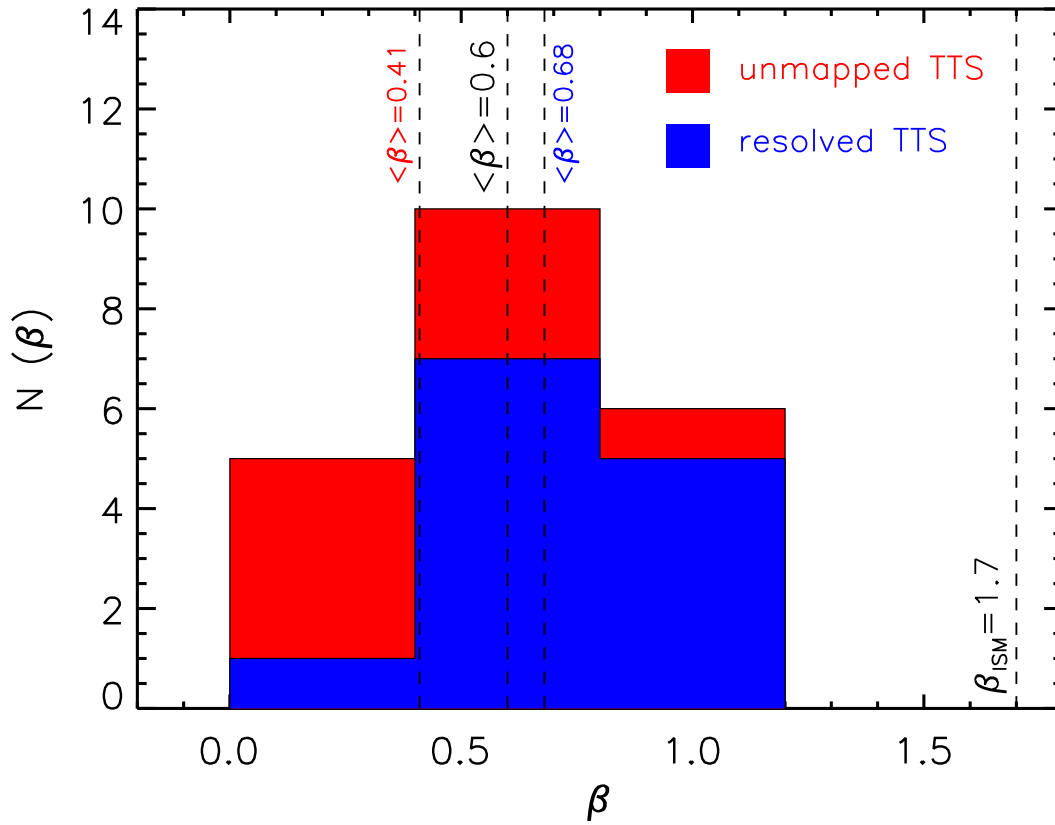


Figure 3.6: Distribution of the dust opacity spectral index β for the disks in our sample. In blue the values for the spatially resolved disks are indicated, whereas the red is for the unmapped ones. The average β value for all the sources in our sample (black), for the unmapped sources only (red), for the resolved sources only (blue), and the value of 1.7 for the ISM dust are indicated as dashed vertical lines.

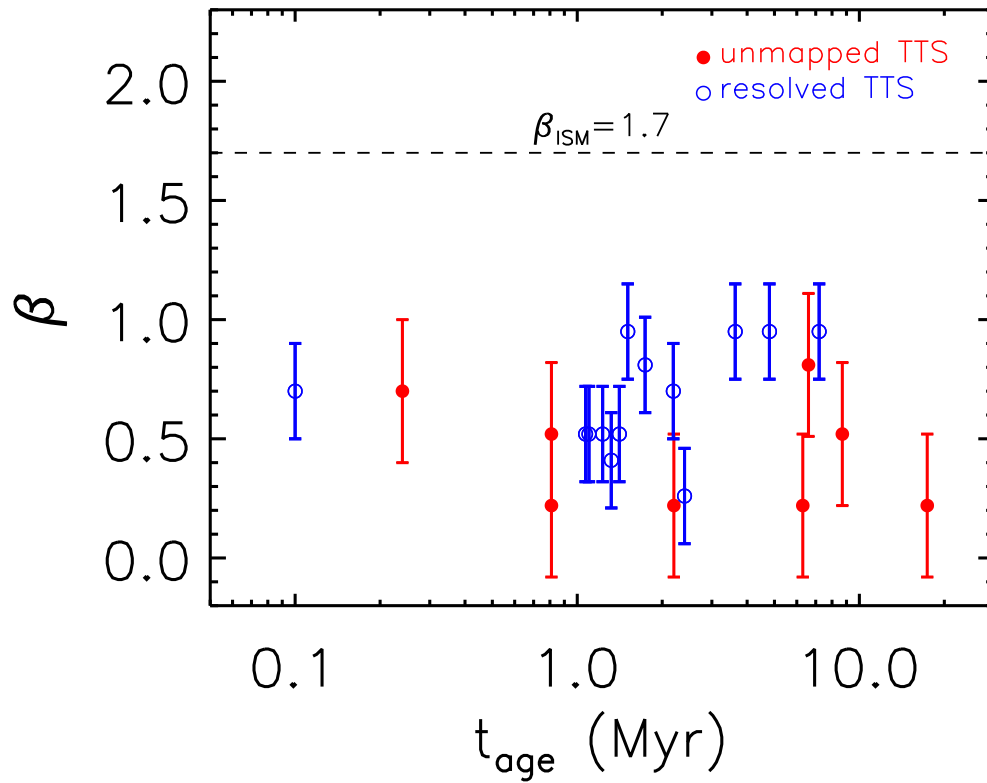


Figure 3.7: Beta versus age: relationship between the dust opacity spectral index β and the estimated stellar age obtained as in Section 4.3.3. Open blue points represent the spatially resolved disks, whereas the filled red points are for the unmapped ones. The β value for the ISM dust is indicated as a dashed horizontal line.

determination of the individual ages of PMS stars is very uncertain. Hartmann (2001) has shown that the large age spread deduced for T Tauri stars in Taurus may just be the result of uncertainties in the measurements towards individual members of a population with a very narrow age spread. Our most solid conclusion, not affected by the age determination uncertainties, is that most (if not all) of the Class II YSO in our sample show evidence of evolved grains in the disk outer regions.

3.4.2 Grain growth

These results confirm two statements that have been addressed in the last years. The first one is that the dust coagulation from ISM dust to mm/cm-sized grains is a fast process, that appears to occur *before* a YSO enters in the Class II evolutionary stage, i.e. when a dense envelope still surrounds the protostar+disk system. This is also consistent with the recent results by Kwon et al. (2009) who have found evidence of grain growth in 3 Class 0 YSOs in Perseus and Cepheus through CARMA observations at 1.3 and 2.7 mm.

The second statement is that the mm/cm-sized dust grains appear to stay longer in the outer disk if compared with their expected inward drift timescale due to the interaction with the gas component. In a circumstellar disk the gas experiences a pressure gradient force which cancels a part of the central star's gravity and induces a rotation slower than the Keplerian velocity. Dust grains, whose orbits are hardly affected by gas pressure, are assumed to be rotating with Keplerian velocity, and thus experience a headwind. They lose angular momentum and spiral inward to the central star (Adachi et al., 1976; Weiden-schilling, 1977). Takeuchi & Lin (2005) proposed as possible solutions to the drift problem that either the grain growth process from mm-sized to cm-sized grains is very long in the outer regions of the disk (timescales greater than 1 Myr, e.g. given by grains' sticking probability as low as 0.1) or that grains have already grown to 10 μ m or larger and they do not migrate rapidly anymore, and mm-sized particles are continuously replenished through collisions of these large bodies. However our analysis suggests that, unless the grain size distribution index is very low, i.e. $q < 2.5$, disks with $\beta \lesssim 0.5$ show evidence of grains as large as ~ 1 cm in the outer regions. Also, as already pointed out in Natta et al. (2004) and Brauer et al. (2007), a noteworthy amount of larger bodies, which would not contribute to the disk emission because of their negligibly small opacity coefficient, could significantly increase the disk masses. Since the typical orbital decay time for a cm-sized grain with a density of 0.1 g cm^{-3} at 50 AU is $\approx 10^5$ yr (10^4 yr for a more compact grain with a 1 g cm^{-3} density), to explain the presence of cm-sized grains in the older disks in our sample (with ages of few Myrs and up to $\sim 10^7$ yr) the reservoir of larger bodies would have to contain at least 100 times more mass than the observed dust mass. The total disk mass would then be comparable to or even exceeding the estimated stellar mass (using a standard gas-to-dust mass ratio of 100, see Section 3.4.3).

To solve the drift problem for very low and very high disk masses Brauer et al. (2007) proposed a significant reduction of the drag experienced by the dust due to a reduction of the gas-to-dust ratio in the disk from the canonical value of 100, and to possible collective effects of dust gathering in a thin midplane layer in the case of very-low turbulent disks.

For example, using a low value for the turbulence parameter $\alpha = 10^{-6}$ and a gas-to-dust ratio of 5, they find that cm-sized dust grains remain in the outer parts of the disk for more than 2 Myr if disk masses $< 0.05 M_\star$ or $> 0.2 M_\star$ are considered. In the range $M_{\text{disk}} \approx 0.05 - 0.2 M_\star$ the collective effects of dust are not efficient enough to retain cm-sized grains in the disk outer regions. If the disk is more turbulent, then more gas has to be removed in order to keep the particles in the outer parts for a longer period of time. To justify such small gas-to-dust ratios the authors suggest the process of photoevaporation as the main driver of gas removal. However, in this case, since photoevaporation is expected to manifest only in the later stages of disk evolution, then we would expect a strong evolutionary trend of β , which is instead not found by our analysis.

Another possibility is the presence in the disk of local gas pressure maxima that would block the inward drift of the dust grains. As shown by the dynamics calculation of Barge & Sommeria (1995) and Klahr et al. (1997) this mechanism may provide a solution also to the relative velocity fragmentation barrier that prevents meter-sized bodies to further grow in size in the inner regions of the disk.

3.4.3 Dust mass

From the sub-mm/mm SED fitting procedure we derived the quantity $M_{\text{dust}} \times \kappa_{1\text{mm}}$. To obtain the dust mass in the disks an estimate of $\kappa_{1\text{mm}}$ is needed. The choice of the dust opacity at 1 mm creates the largest uncertainty in the derivation of (dust) disk masses from millimeter observations. Estimates of $\kappa_{1\text{mm}}$ from different dust models in the literature span a range of a factor greater than 10. The most commonly used value in the literature is $\kappa_{1\text{mm}} \simeq 3 \text{ cm}^2$ per gram of dust (Beckwith et al., 1990) that, for simplicity, is supposed to be constant, i.e. independent of the dust grain properties, for all the disks. As noted in Natta et al. (2004) this is not realistic as grain growth affects both the frequency dependence of the dust opacity and its absolute value (e.g. Miyake & Nakagawa, 1993).

In this paper we use the dust model described in Section 3.3.1 to get an estimate of $\kappa_{1\text{mm}}$ that takes into account the dust physical properties, especially grain growth. As shown in the left top panel of Figure 3.3, at a fixed value of the grain size distribution index q , the value of $\kappa_{1\text{mm}}$ can be inferred from a_{max} which in turn can be derived from β through the relation plotted in the left bottom panel of the same figure. The relation between $\kappa_{1\text{mm}}$ and β is shown in the right panel. Therefore, from an estimate of β and $M_{\text{dust}} \times \kappa_{1\text{mm}}$ obtained by the sub-mm/mm SED fitting procedure we can get an estimate for $\kappa_{1\text{mm}}$ and then the dust mass M_{dust} for our dust model, after fixing the q parameter. In Table 4.3 we report the values of M_{dust} as obtained with this method for $q = 2.5, 3.0, 3.5$. It is important to bear in mind that, as for the estimate of the maximum grain size, also for $\kappa_{1\text{mm}}$, and thus for the dust mass, the estimates depend on the specific dust model that one adopts (see discussion in Natta et al., 2004). However, following Isella et al. (2009), we take into account the variation of the dust opacity with β using a well defined dust model to infer dust masses, and this approach is more accurate than considering a fixed $\kappa_{1\text{mm}}$ as often done in previous studies.

In general, for our specific dust model, when $\beta < 1$ then $M_{\text{dust}}^{q=2.5} < M_{\text{dust}}^{q=3} < M_{\text{dust}}^{q=3.5}$, the

amount of variation of M_{dust}^q for the different q values being dependent on β . In particular, when $\beta \simeq 0.8 - 1$ $M_{\text{dust}}^{q=2.5}$ and $M_{\text{dust}}^{q=3}$ are nearly coincident and $M_{\text{dust}}^{q=3.5}$ is greater than $M_{\text{dust}}^{q=2.5}$ by factors of $\sim 2 - 4$. For $\beta \lesssim 0.7$ a grain size distribution with $q = 3.5$ cannot explain the observational data and the discrepancy between $M_{\text{dust}}^{q=2.5}$ and $M_{\text{dust}}^{q=3}$ increases up to a factor of ~ 15 when $\beta \simeq 0.2$. This is due to the increase of the distance between the $\kappa_{1\text{mm}}(\beta)$ curves at fixed q -values, when β decreases, as shown in the right panel of Figure 3.3

As already mentioned in Section 3.4.1, from the value of β it is impossible to disentangle a_{max} and q . Nevertheless, only the disks showing $\beta \geq 0.8$ can be explained by a grain size distribution index $q = 3.5$. For this reason, for the rest of our analysis we will consider separately only the cases in which the dust grain size distribution is characterized by $q = 2.5$ or 3. The value of q in protoplanetary disks is unknown and it is not observationally constrainable, and so it is in principle possible that it can vary substantially from one disk to the other. For our discussion we will use the assumption that q is the same for all the disks.

Once the dust mass is estimated, this is commonly converted into an estimate of the total disk mass (dust+gas) using the standard ISM gas-to-dust ratio of 100. However, if the dust and gas components have different evolutionary timescales, this ratio is a function of time and the standard ISM value would be inappropriate for estimating the disk mass at the present time. Physical processes that are likely to alter this ratio during the evolution of a protoplanetary disk are gas photo-evaporation, which would lead to a decrease of the gas-to-dust ratio (unless a significant amount of dust is dragged away by the gas flow), and dust inward migration, which instead would increase it. Natta et al. (2004) suggested that the standard ISM ratio provides a correct estimate of the “original” disk mass, when the disk composition reflected that of the parent cloud. However, this is true only if a negligible amount of dust has migrated with respect to the gas and accreted onto the central star, otherwise the ISM ratio would provide only a lower limit to the original disk mass. Because of our ignorance on the gas-to-dust ratio evolution in this paper we will not convert the dust mass into a total disk mass. Also, it is important to note that since millimeter observations are insensitive to the emission of bodies much larger than 1 cm, including planetesimals and planets, the dust mass we are referring to in this paper does not include the contribution from these larger objects. The dust mass is intended to be the mass in “small grains” only, and is a lower limit to the total mass in dust.

Figure 3.8 shows the β vs M_{dust} plots for q equal to 2.5 and 3. The plot with $q = 2.5$ does not show any significant relation. In the $q = 3$ case an anticorrelation between these two quantities may be present, with the more massive dust disks being associated to the ones showing today the largest grains in their outer parts, with a_{max} up to ~ 10 cm. This possible anticorrelation is clearly an effect of the choice of a physical model for the dust that takes into account the variation of the dust opacity normalization factor with the size-distribution of the dust grains (Section 3.3.1). If we had made the unrealistic assumption of a constant value for the dust opacity at, say, 1 mm, we would have found an opposite result, i.e. disks with *less* mass in dust would have shown on average larger grains, as can be derived from Figure 5.3, since α is approximately proportional to β and $F_{1\text{mm}}$ would be approximately proportional to the dust mass, in the constant $\kappa_{1\text{mm}}$ case. More realistically,

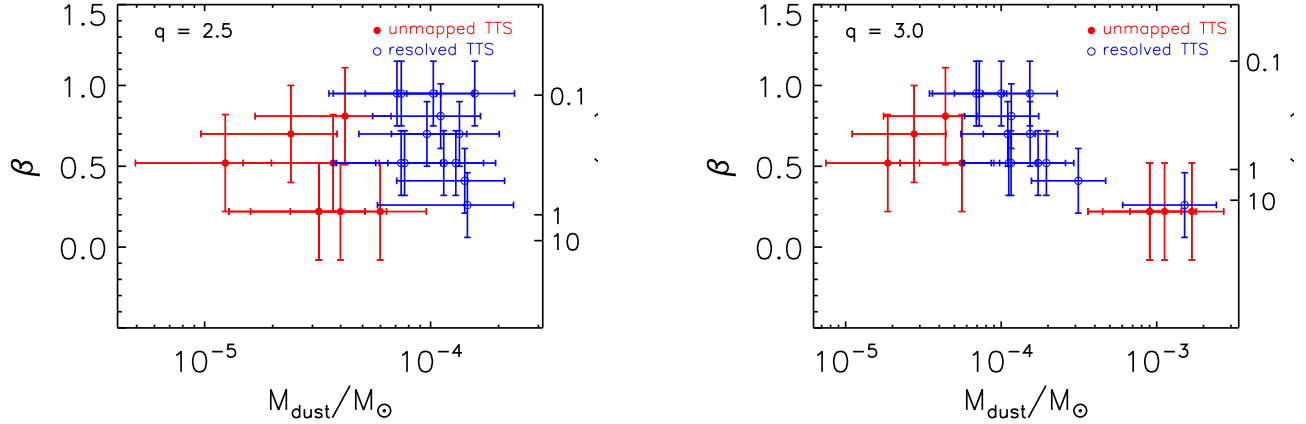


Figure 3.8: Dust opacity spectral index β and maximum grain size a_{\max} plotted against the disk mass in dust for the sources in our sample. In the left and right panels the dust mass has been obtained adopting a value of 2.5 and 3 respectively for the power index q of the dust grains size distribution. Open blue points represent the spatially resolved disks, whereas the filled red points are for the unmapped ones. The errorbars in the dust mass estimates do not take into account our uncertainty on the real value of q .

lower values of β imply low absolute values of the dust millimeter opacity (see right panel of Figure 3.3), so that, for a fixed observed flux and disk temperature, the corresponding dust mass must be larger. The reason why the plot with $q = 2.5$ does not show signs of anticorrelation is that at a fixed β a lower q value is associated to a smaller dust grain maximum size. The β range spanned by the disks in our sample translates into a range in $\kappa_{1\text{mm}}$ that is narrower for $q = 2.5$ than it is for $q = 3$ (see right panel of Figure 3.3), thus leading to smaller correction factors with respect to the constant $\kappa_{1\text{mm}}$ case. Note that among the 5 disks showing the smallest β ($\approx 0.2 - 0.3$) and the highest dust masses (about $10^{-3} M_{\odot}$ for $q = 3$) only one (AA Tau) has been mapped and spatially resolved. High angular resolution and high sensitivity imaging of these disks together with other ones are needed to test the robustness of the $\beta - M_{\text{disk,init}}$ anticorrelation in the $q = 3$ case.

Figure 3.9 and 3.10 plot the disk mass in dust against the estimated mass of the central star (dust mass obtained with q -values of 2.5 and 3) and mass accretion rate (dust mass with $q = 3$ and stellar ages smaller and greater than 2 Myr) respectively. In the $0.3 - 2 M_{\odot}$ range in stellar mass the dust mass does not show any trend (for $q = 2.5$: $3 \cdot 10^{-5} < M_{\text{dust}} < 2 \cdot 10^{-4} M_{\odot}$; for $q = 3$: $4 \cdot 10^{-5} < M_{\text{disk,init}} < 2 \cdot 10^{-3} M_{\odot}$). The two YSOs with $M_{\star} \lesssim 0.3 M_{\odot}$ have lower dust masses than all the other YSOs for both $q = 2.5$ and 3. However, the range in stellar mass spanned by our sample is rather limited, and particularly biased toward YSOs with late-K and early-M spectral types. From the upper limits obtained at 1.3 mm by Schaefer et al. (2009) for 14 T-Tauri stars with spectral types later than $\approx M2$ ($F_{1.3\text{mm}} \lesssim 5 - 20$ mJy), and from the detection of very low disk masses

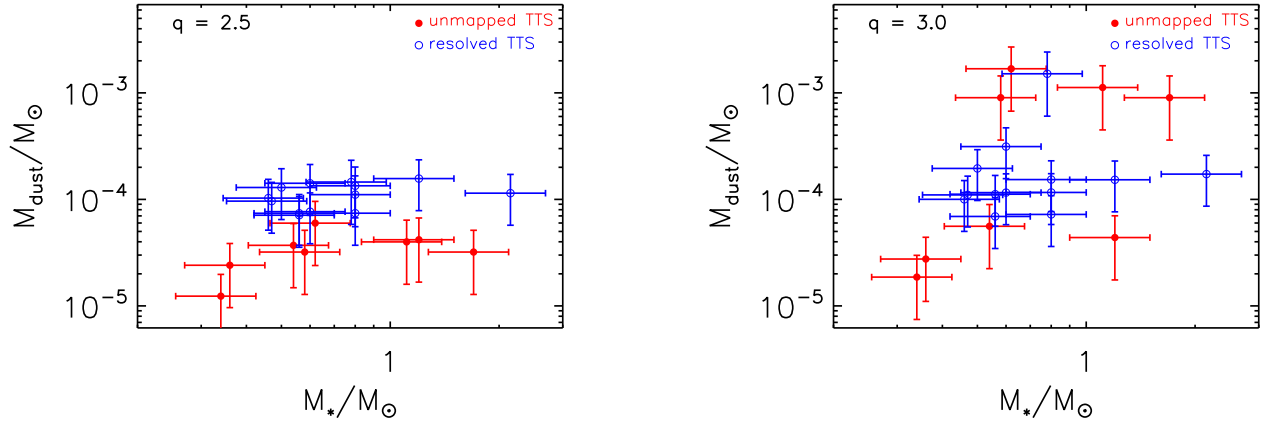


Figure 3.9: Disk mass in dust plotted against the stellar mass for the sources in our sample. In the left and right panels the dust mass has been obtained adopting a value of 2.5 and 3 respectively for the power index q of the dust grains size distribution. The stellar mass has been estimated as described in Section 4.3.3, and the errorbars take into account the range of values given by different PMS stars evolutionary models. Open blue points represent the spatially resolved disks, whereas the filled red points are for the unmapped ones. The errorbars in the dust mass estimates do not take into account our uncertainty on the real value of q .

around sub-stellar objects in Taurus-Auriga (Klahr et al., 2003; Scholz et al., 2006), it is likely that a correlation between the disk mass in dust and the mass of the central star exists. High sensitivity millimeter observations are needed to constrain the disk masses in dust around very low mass PMS stars. In Figure 3.10 a trend of higher mass accretion rates for the more massive disks in dust may be present in the data but still the scatter is very large (a similar result is obtained for the $q = 2.5$ case). Other relations between the dust properties (β , dust mass) and the stellar ones (e.g. stellar luminosity, effective temperature) have been investigated but no significant correlations have been found.

Finally, we have compared the values of β obtained in this paper with the ones derived in Natta et al. (2004) for a sample of 6 intermediate mass Herbig Ae stars and 3 lower mass T Tauri stars. From the two-sided Kolmogorov-Smirnov test, the probability that the β values from the two samples come from the same distribution is about 88%, indicating that the disks in the two samples have similar dust properties in terms of grain growth. (in the Natta et al., 2004, sample only one object, the Herbig Ae star HD150193, has a relatively high $\beta = 1.6 \pm 0.2$, compatible with non-evolved ISM-like dust grains).

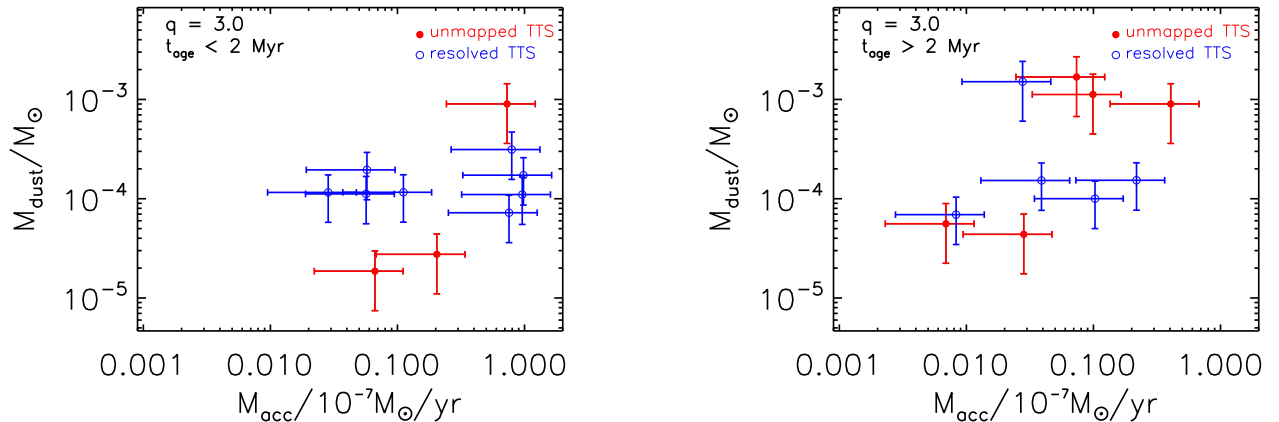


Figure 3.10: Disk mass in dust plotted against the mass accretion rate for the sources in our sample. In the left and right panels we included the objects with estimated ages of less and more than 2 Myr respectively. The dust mass has been obtained adopting a value of 3 for the power index q of the dust grains size distribution. The stellar mass accretion rate has been estimated following the method described in Section 3.2.4. Open blue points represent the spatially resolved disks, whereas the filled red points are for the unmapped ones. The errorbars in the mass accretion rate take into account the typical intrinsic time-variability of the accretion rates. The errorbars in the dust mass estimates do not include our uncertainty on the actual value of q .

3.5 Summary

We have analysed the sub-mm/mm SED out to 3mm of a sample of 21 Class II T-Tauri stars in the Taurus-Auriga star forming region. This sample comprises about the 60% of the “isolated” class II YSOs with an estimated stellar mass greater than $\approx 0.4 M_{\odot}$. It also comprises approximately 1/3 of the isolated class II which have been observed at 0.85mm to have a flux less than 100 mJy, for which we provide first 3mm detections thanks to sensitive PdBI observations. Our main findings are summarized below:

1. For all the sources in our sample the millimeter opacity spectral index β is significantly lower than the value obtained for the dust in the ISM. For the 13 spatially resolved disks this is a clear evidence of the presence in the outer disk regions of dust grains as large as at least 1 mm. For the 8 unmapped sources, assuming disk outer radii comparable to the resolved sources low β values are found as well, suggesting that even for these fainter sources 1 mm-sized grains are in the disk outer regions. This confirms, over a larger sample and less massive disks, the results obtained by past observations on T-Tauri stars (e.g. Rodmann et al., 2006, and references therein).
2. No significant evidence of an evolutionary trend for the millimeter opacity spectral

index β has been found. This indicates that the dust grain growth to ~ 1 mm-sizes is a very fast process in a protoplanetary disk, that appears to occur before a YSO enters in the Class II evolutionary stage. Also, the amount of these large grains in the disk outer regions does not appear to decline throughout all the Class II evolutionary stage.

3. Only for 9 sources in our sample a power law index for the grain size distribution of the ISM, $q_{\text{ISM}} \approx 3.5$, is consistent with the sub/mm-mm SED. Instead, most of the disks show evidence of a smaller q -value.
4. We have not found any significant correlation between the dust properties, namely grain growth and dust mass in the disk outer regions, and the properties of the central star, including the mass accretion rate onto the stellar surface. However, our sample contains mostly YSOs with a narrow range in spectral types, namely between late-K and early-M, and it is possible that a correlation between the disk mass in dust and the stellar mass will become apparent when considering also disks around late-M spectral types.
5. The 6 faintest sources in our sample, with $F_{1\text{mm}} < 50$ mJy, show a spectral index between 1 and 3 mm that is on average lower than the spectral index of the brighter sources. This may indicate either that for these fainter, yet unmapped disks the emission from the optically thick inner disk is much more significant than for the brighter sources or that the dust grains in the outer regions of these fainter disks are even larger than in the brighter YSOs, possibly up to 10 cm if $q = 3$. The latter hypothesis would imply on average a lower absolute value for the millimeter opacity coefficient for these fainter disks. Taking into account this effect through a physical model for the dust properties, we found, in the case of a value for the power index of the grain size distribution $q = 3$, an anticorrelation between β and the disk dust mass, that would indicate that larger dust grains are found in the outer parts of the more massive disks (in dust).

In the next future, with the advent of the next sub-mm/mm facilities (both new interferometers like ALMA and technical improvements in the existent arrays, like for example the E-VLA) it will be possible to extend the investigation of the dust properties to fainter circumstellar disks around the lowest mass PMS stars and brown dwarfs. Furthermore, thanks to the great enhancements in both high angular resolution and sensitivity that these facilities will provide, it will be possible to determine their spatial extension.

Dust grain growth in ρ -Ophiuchi protoplanetary disks

Published as Ricci, Testi, Natta, & Brooks, 2010, A&A 521, 66

Abstract

We present new ATCA observations at 3.3 mm of 27 young stellar objects in the ρ -Oph young cluster. 25 of these sources have been detected. We analyze the sub-millimeter and millimeter SED for a subsample of 17 isolated class II protoplanetary disks and derive constraints on the grain growth and total dust mass in the disk outer regions. All the disks in our sample show a mm slope of the SED which is significantly shallower than the one observed for the ISM at these long wavelengths. This indicates that 1) class II disks in Ophiuchus host grains grown to mm/cm-sizes in their outer regions; 2) formation of mm/cm-sized pebbles is a fast process and 3) a mechanism halting or slowing down the inward radial drift of solid particles is required to explain the data. These findings are consistent with previous results in other star forming regions. We compare the dust properties of this sample with those of a uniformly selected sample in Taurus-Auriga and find no statistical evidence of any difference in terms of grain growth between the two regions. Finally, in our sample the mm slope of the SED is not found to correlate with indicators of grain growth to micron sizes in the surface layers of the inner disk.

4.1 Introduction

Circumstellar disks around pre-main sequence (PMS) stars are the common birth places of planetary systems. In order to build up large bodies such as giant planets a huge growth of solid particles by more than 12 orders of magnitude in size has to occur starting from submicron-sized microscopic dust grains as those typically found in the interstellar

medium (ISM; Mathis et al., 1977). The first stages of this process of grain growth are characterized by the dynamical interaction between gas and dust, leading to collisions between the solid particles and finally coagulation (see Beckwith et al., 2000; Dominik et al., 2007; Natta et al., 2007).

Evidence for the presence of micron-sized dust grains in protoplanetary disks has been provided by the inspection of ISO and Spitzer spectra for the silicate feature at about 10 μm (e.g. Bouwman et al., 2001; Van Boekel, 2003; Kessler-Silacci et al., 2006). However infrared observations can only probe the uppermost surface layers of the disk, while to investigate the properties of dust in the disk midplane, where planet formation is expected to take place, observations at longer wavelengths are needed. If the long-wave emission is optically thin the spectral index of the SED at these wavelengths can be related to the spectral index of the dust opacity β ($\kappa_{\text{dust}} \propto \lambda^{-\beta}$), and β -values lower than ~ 1 are naturally interpreted in terms of grain growth (Draine, 2006). Beckwith & Sargent (1991) were the first to show that T Tauri Stars (TTS) have SEDs at submillimeter wavelengths which are typically shallower than what found for the ISM, suggesting that dust grains as large as at least 1 mm are present in the disk midplane. However these single-dish observations did not have a good enough angular resolution to spatially resolve the disks, and the same data could in principle be explained also by optically thick emission from compact disks with unprocessed, ISM-like grains.

Wilner et al. (2000) and Testi et al. (2003) resolved the disks around TW Hya and CQ Tau PMS stars at 7 mm with the Very Large Array (VLA), confirming that the long-wave emission from these disks reveals the presence of cm-sized pebbles in the disk midplane. Rodmann et al. (2006) and Lommen et al. (2007) found evidence of grain growth to \sim mm/cm-sized pebbles for about ten T Tauri stars in the Taurus-Auriga, Chamaeleon and Lupus star forming regions (SFRs). Lommen et al. (2010) have combined new and literature data for disks from five different SFRs (Taurus-Auriga, Lupus, Chamaeleon, Corona Australis and Serpens) and reported a tentative correlation between the mm slope of the SED and the strength of the 10- μm silicate feature, possibly suggesting that inner and outer disk evolve simultaneously in terms of dust grain growth.

So far, most of the observations carried out at long wavelengths have targeted the brightest sources. Ricci et al. (2010a, hereafter R10) have started to probe fainter disks with new sensitive data at 3 mm obtained with the Plateau de Bure Interferometer in Taurus and analyzed a sample of 21 isolated class II Young Stellar Objects (YSOs) in this SFR. For all the disks in this sample they found neither evidence for time evolution of dust grain growth nor significant relations between dust properties and stellar ones were found.

In this paper we perform the same analysis presented in R10, but on a sample of disks in another SFR, i.e. ρ -Ophiuchi. In Sect. 2 we present new 3 mm data for 27 ρ -Oph YSOs obtained with the Australia Telescope Compact Array (ATCA¹) and its new Compact Array Broadband Backend (CABB). In Sect. 3 we describe the properties of the sub-sample used for the analysis. The method adopted for deriving the dust properties,

¹The Australia Telescope Compact Array is part of the Australia Telescope which is funded by the Commonwealth of Australia for operation as a National Facility managed by CSIRO.

namely grain growth and dust mass, is the same used in R10 and it is described in Sect. 4. The results of the analysis are described in Sect. 5, whereas Sect. 6 summarizes the main findings of our work.

4.2 New ATCA observations

We observed 27 YSOs in the ρ -Oph star forming region at 3.2944 mm with ATCA and the new CABB digital filter bank. Targets were chosen by being class II (most of them) or “flat spectrum” YSOs, with a detected flux at 1.3mm higher than 20 mJy in order to have good chances for detection at ~ 3.3 mm with a few hours at most of integration time on-source.

The observations were carried out between the end of April and the beginning of July 2009, with the ATCA array in the H168 and H75 configurations respectively. The obtained FWHM of the synthesized beam of $\sim 3 - 7''$ did not allow us to spatially resolve any of our sources, and so a 2D-gaussian model was used to estimate the flux density in the continuum at 3.3 mm. To obtain the best sensitivity in the continuum we set the correlator to cover the full 2-GHz CABB effective bandwidth on all the five antennas available at ~ 3 mm. Each source has been observed one or more times, with a total integration time on-source ranging between about 40 minutes and 3 hours.

The complex gain calibration was done on the calibrators 1622-297 and 1730-130, and science targets were typically observed for 10 minutes and then spaced out with 2 minutes on the gain calibrator. The absolute calibration was done with Uranus except for a few times in which 1921-293 was used and then its flux was always cross-calibrated with Uranus the day after. In general, the baselines that resolved out Uranus were not used for flux calibration². In this work, we assume a 1σ -uncertainty on the calibrated flux of about 25%.

The results of the observations are reported in Table 6.1. In particular we have detected 25 out of 27 targeted YSOs. The detected sources have fluxes ranging from about 1.5 and 48.8 mJy at 3.3 mm. For the two undetected sources, IRS 33 and GY 284, we obtained an upper limit for the flux at 3.3 mm of 1.2 mJy. These sources have been previously detected by Motte et al. (1998) using the IRAM 30m single-dish telescope at 1.3 mm. Although their reported fluxes are relatively large (105 ± 20 mJy and 130 ± 10 mJy for IRS 33 and GY 284 respectively) the emission for both the sources appears to be spatially resolved by a beam with a FWHM of about 11 arcsec. This indicates that a significant fraction of the collected flux at 1.3 mm comes from an extended envelope surrounding the circumstellar disk. In order to get a reliable estimate for the flux at ~ 1 mm from the circumstellar disk only, interferometric observations at ~ 1 mm are needed to filter out the contaminating emission from the envelope. Since these are not available in the literature we do not include IRS 33 and GY 284 in our sample discussed in the next section.

²For the data reduction we used the MIRIAD package.

4.3 Sample

In this section we describe some properties of the sample considered for our analysis³. In Sect. 4.3.1 we outline the selection criteria adopted to select our sample, Sect. 4.3.2 describes the sample completeness level, and finally in Sect. 4.3.3 we derive the stellar parameters.

4.3.1 Selection criteria

We used the same selection criteria adopted in R10:

1. class II YSOs as catalogued in Andrews & Williams (2007a) from the infrared SED to avoid contamination of (sub-)mm fluxes by a residual envelope;
2. central stars need to be well characterized through optical-NIR spectroscopic/photometric data to obtain self-consistent disk SED models;
3. YSOs with at least one detection in the $0.45 \leq \lambda \leq 1.3$ mm spectral range⁴ other than being observed through the new ATCA observations described in Sect. 2, to have a good sampling of the (sub-)mm SED;
4. no evidence of stellar companions with projected physical separation between 5 and 500 AU to avoid tidal interactions that may alter the outer disk structure; adopting for all the YSOs in our sample the current estimate of ~ 130 pc for the distance to the ρ -Oph star forming region (Wilking et al., 2008; Lombardi et al., 2008), the range in projected physical separation translates into a range in angular separation of $\sim 0.05 - 4''$.

Among the 25 YSOs detected with ATCA at 3.3 mm, 17 satisfy these selection criteria and they constitute the sample of our analysis. They are listed in Table 7.5.

4.3.2 Completeness

The two histograms in Fig. 4.1 show the distribution of the “isolated”, i.e. satisfying the selection criterion (4) in Sect. 4.3.1, class II YSOs from the Andrews & Williams (2007a) catalogue. The histogram on the left side shows that our sample comprises all the isolated class II YSOs with $F_{1.3\text{mm}} > 75$ mJy, while for the fainter objects the completeness level reduces to 22% (8/36).

³Note that the final sample used in the analysis does not comprise all the targets of the new ATCA observations described in Sect. 7.5.

⁴Note that in R10 a slightly narrower spectral range of $0.45 \leq \lambda \leq 0.85$ mm was chosen. We adopted a broader spectral range to include in our sample the sources YLW 16c and WSB 52, for which no observations at $\lambda < 1.3$ mm have been carried out so far. The different uncertainties for the spectral slopes of these sources, due to a shorter spectral leverage, are properly taken into account in the analysis.

In terms of the stellar properties, our sample includes 53% (16/30) of the isolated PMS stars with stellar types equal to or earlier than M1, correspondent to a stellar mass larger than $\sim 0.5 M_{\odot}$ for a ~ 1 Myr old PMS star according to the Palla & Stahler (1999) models⁵ (see Fig. 4.2). Our sample is much less complete for PMS stars with later spectral types (or smaller stellar mass): only 7% of the known PMS stars with a mass smaller than $\sim 0.4 M_{\odot}$ is in our sample (1/15), and this has to be considered as an upper limit since the Andrews & Williams (2007a) catalogue does not comprise class II YSOs with spectral types later than M5. This is due to the sensitivity limits of the current (sub-)mm facilities to detect emission from circumstellar material around very-low mass PMS stars.

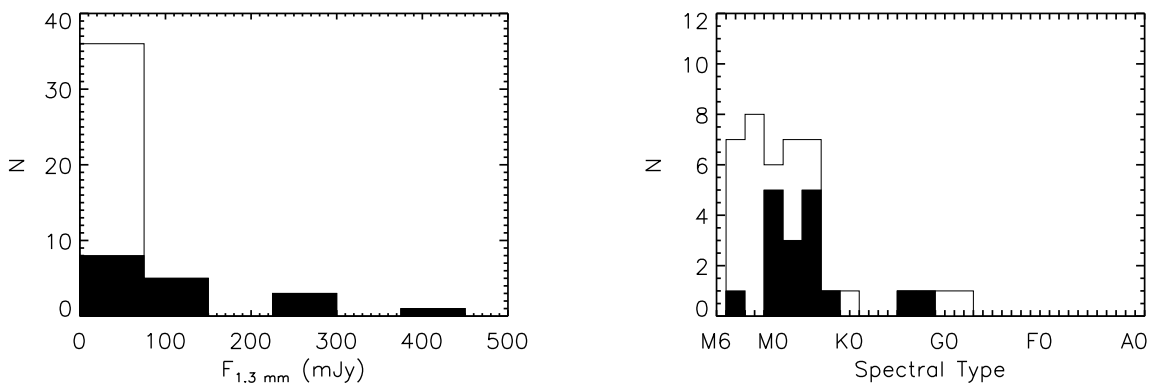


Figure 4.1: Histograms highlighting some properties of our selected sample. In both the histograms our sample is represented by black columns, while the total columns (black+white) include all the class II YSOs from the Andrews & Williams (2007a) catalogue with no evidence of stellar companions in the $0.05 - 4.0''$ interval in angular separation, from which our sample has been selected (see Sect. 4.3.1). Left) Distribution of the fluxes at 1.3 mm, including upper limits; Right) Distribution of stellar spectral type (see Sect. 4.3.3).

4.3.3 Stellar properties

To constrain the stellar properties we used the same method as described in R10. We estimated the stellar effective temperatures by converting the adopted spectral types (from Andrews & Williams (from Andrews & Williams, 2007a, and references therein)⁶ with the dwarf temperature scale of Schmidt-Kaler (1982) for spectral types earlier than M0 and the intermediate temperature scale of Luhman (1999) for spectral types equal to or later than M0.

⁵Note that this completeness level is very close to the one obtained in R10 in the Taurus-Auriga star forming region, i.e. $\sim 58\%$ of the isolated class II YSOs with stellar masses larger than $\sim 0.4 M_{\odot}$.

⁶For only two cases in our sample, i.e. EL 20 and IRS 41, the spectral types are not available in Andrews & Williams (2007a). For these PMS stars we adopted the stellar types from Natta et al. (2006) which are based on near infrared broad band photometry.

Stellar luminosities were computed from the 2MASS J -band flux (Cutri et al., 2003) after calculating the extinction of each object by dereddening the $J - H$ and $H - K_s$ colors to the locus observed for Classical T Tauri stars (Meyer et al., 1997), and adopting the Cardelli et al. (1989) extinction law with $R_V = 4.2$, which is appropriate for ρ -Oph⁷.

Luminosities and effective temperatures were converted into stellar masses and ages by using the Palla & Stahler (1999) models of PMS stars, as done in R10 (see Fig. 4.2). According to these models the ranges spanned by our sample go from about $0.2 M_\odot$ (WSB 60) to $1.9 M_\odot$ (SR 21) in mass and from about 0.7 Myr (GSS 26, EL 24, YLW 16c) to 6.6 Myr (SR 21) in age.

The stellar parameters are reported in Table 7.5.

4.4 Analysis

In order to constrain the dust properties in the disk outer regions we fitted the sub-mm/mm SED with two-layer (i.e. disk surface and midplane) models of flared disks heated by the radiation of the central star (Chiang & Goldreich, 1997; Dullemond et al., 2001). In Sect. 7.3.1 and 7.3.2 we describe the parameters which are needed to define a two-layer disk model. In Sect. 4.3 we then discuss which are the physical quantities of these models that can be constrained by our analysis.

4.4.1 Disk structure

In order to characterize a model of the disk estimates for some stellar physical quantities (bolometric luminosity L_\star , effective temperature T_{eff} and mass M_\star), plus some information on the disk structure and on the dust opacity are needed. As for the stellar parameters we used the values listed in Table 7.5. Regarding the disk structure the only relevant parameters for our analysis are the disk outer radius R_{out} and the parameters $\Sigma_{\text{dust},1}$ and p which define a power-law surface density for the dust component:

$$\Sigma_{\text{dust}}(R) = \Sigma_{\text{dust},1} \left(\frac{R}{1 \text{ AU}} \right)^{-p}, \quad (4.1)$$

radially truncated at R_{out} . For the disk outer radii we adopted the intervals listed in Column (3) of Table 4.3. For the seven disks in our sample which have been mapped by high angular resolution observations at sub-mm/mm wavelengths presented in Andrews & Williams (2007b) we considered intervals roughly centered on their best-fit values. Three sources (EL 20, WSB 52, DoAr 44) have been observed and spatially resolved by recent observations carried out by Andrews et al. (2009) with the SMA at 0.87 mm: these disks show evidence of an outer radius larger than 100 AU, but an accurate estimate of the outer radius R_{out} could not be derived, since in order to fit the interferometric visibilities they

⁷For IRS 41, for which the 2MASS J -band flux is not available, we adopted the luminosities as derived by Natta et al. (2006), after correcting them by a multiplicative factor $(130 \text{ pc}/150 \text{ pc})^2$ to account for the different adopted distance of 150 pc in the Natta et al. paper.

Table 4.1: Summary of the 3.3 mm ATCA observations.

Object	α (J2000)	δ (J2000)	F_ν (mJy)	rms (mJy)	Comments ^b	Ref.	Other names
AS 205A	16:11:31.4	-18:38:26.0	27.2	1.2	triple (1.5", sb)	1	HBC 254
SR 4	16:25:56.1	-24:20:48.3	4.4	0.4			AS 206
GSS 26	16:26:10.3	-24:20:54.9	24.2	0.9			
EL 20	16:26:18.9	-24:28:20.2	7.3	0.5			VSSG 1
LFAM 1	16:26:21.7	-24:22:50.8	17.5	0.6	flat spectrum	2	
DoAr 24E	16:26:23.4	-24:21:00.7	8.3	0.4	binary (2.0")	1	GSS 31
DoAr 25	16:26:23.7	-24:43:14.1	25.0	0.6			WSB 29
EL 24	16:26:24.1	-24:16:14.0	48.8	0.7			WSB 31
EL 27	16:26:45.0	-24:23:08.2	38.7	0.6			GSS 39
WL 18	16:26:49.0	-24:38:25.7	3.1	0.5	binary (3.6")	3	GY 129
SR 24S	16:26:58.5	-24:45:37.1	26.6	0.8	flat spectrum, triple (5.2", 0.2")	2,4,5	HBC 262
SR 21	16:27:10.2	-24:19:12.9	4.2	0.4			EL 30
IRS 33 ^a	16:27:14.5	-24:26:46.1	< 1.2	0.4			GY 236
IRS 41	16:27:19.3	-24:28:44.4	6.2	1.2			WL 3
CRBR 85	16:27:24.7	-24:41:03.2	1.5	0.3	envelope	6	
YLW 16c	16:27:26.5	-24:39:23.4	6.5	0.4			GY 262
GY 284 ^a	16:27:30.8	-24:24:56.0	< 1.2	0.4			
IRS 49	16:27:38.3	-24:36:58.8	4.4	0.4			GY 308
DoAr 33	16:27:39.0	-23:58:19.1	3.7	0.3			WSB 53
WSB 52	16:27:39.5	-24:39:15.9	10.2	0.5			GY 314
IRS 51	16:27:39.8	-24:43:15.0	12.7	0.8	binary (1.6")	3	GY 315
WSB 60	16:28:16.5	-24:36:58.0	15.3	0.5			YLW 58
SR 13	16:28:45.3	-24:28:19.2	10.0	0.6	binary (0.4")	3	HBC 266
DoAr 44	16:31:33.5	-24:27:37.7	10.4	0.5			HBC 268
RNO 90	16:34:09.2	-15:48:16.9	7.6	0.5			HBC 649
Wa Oph 6	16:48:45.6	-14:16:36.0	10.3	0.4			HBC 653
AS 209	16:49:15.3	-14:22:08.6	17.5	0.5			HBC 270

a) For this undetected source the (α, δ) coordinates are from 2MASS (Cutri et al., 2003);

b) Reason why the source has not been considered in the analysis (see Sect. 4.3.1); enclosed in parenthesis there are the angular separation(s) between the stellar companions ("sb" = spectroscopic companion);

c) References: (1) McCabe et al. (2006); Andrews & Williams (2007a); (3) Ratzka et al. (2005); (4) Reipurth et al. (1993); (5) Simon et al. (1995); (6) McClure et al. (2010).

Table 4.2: Stellar properties of the considered sample.

Object	ST	T_{eff} (K)	L_{\star} (L_{\odot})	R_{\star} (R_{\odot})	M_{\star} (M_{\odot})	Age (Myr)
SR 4	K5	4350	2.17	2.58	1.14	1.07
GSS 26	M0	3850	1.39	2.64	0.56	0.54
EL 20	M0	3850	0.93	2.16	0.62	1.07
DoAr 25	K5	4350	1.43	2.10	1.12	2.09
EL 24	K6	4205	2.58	3.01	0.96	0.58
EL 27	M0	3850	0.78	1.98	0.58	1.23
SR 21	G3	5830	11.38	3.29	1.97	2.21
IRS 41	K7	4060	1.61	2.55	0.80	0.76
YLW 16c	M1	3705	1.11	2.55	0.48	0.54
IRS 49	M0	3850	1.02	2.26	0.64	1.00
DoAr 33	K4	4590	1.81	2.12	1.44	2.88
WSB 52	K5	4350	0.95	1.71	1.04	4.17
WSB 60	M4	3270	0.23	1.49	0.20	0.93
DoAr 44	K3	4730	1.55	1.85	1.29	5.13
RNO 90	G5	5770	10.24	3.19	1.87	2.32
Wa Oph 6	K6	4205	2.32	2.86	0.98	0.71
AS 209	K5	4350	2.11	2.55	1.18	1.23

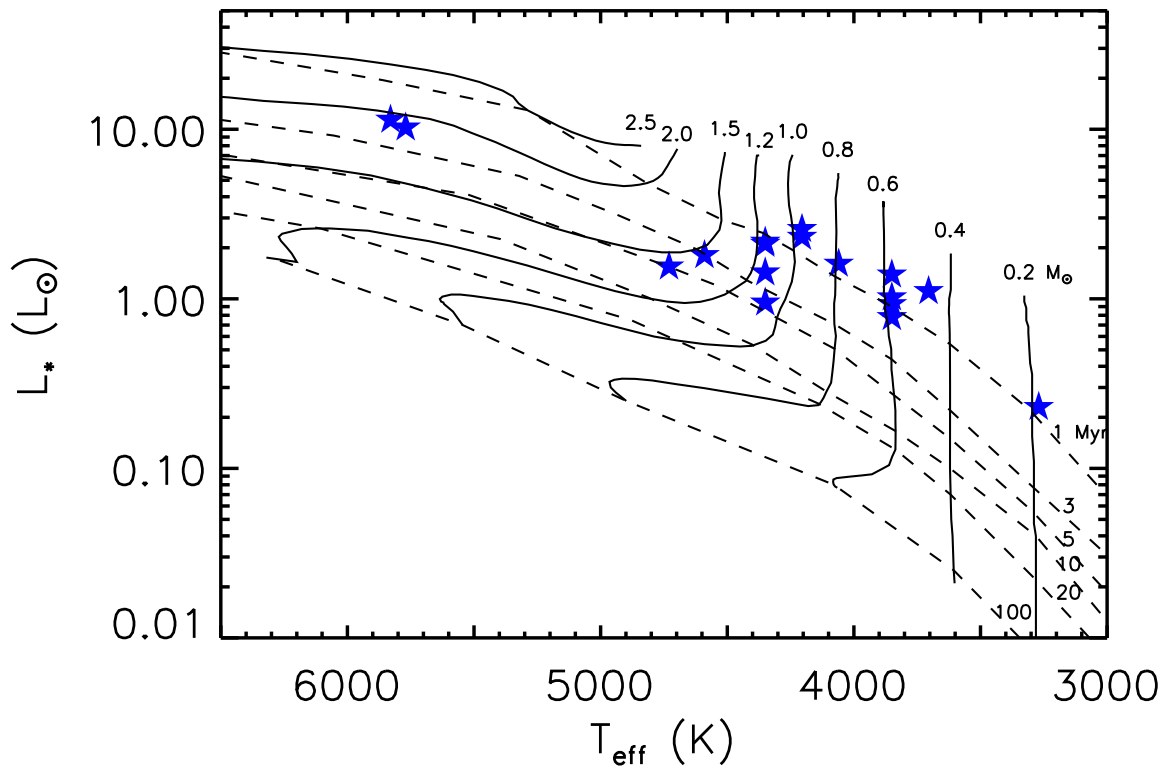


Figure 4.2: H-R diagram for the sources of our sample. The dashed and solid lines represent the isochrones and evolutionary tracks respectively from the Palla & Stahler (1999) PMS evolutionary models. In this diagram the evolutionary tracks start from an age of 0.1 Myr. The uncertainties, not shown in the plot, are typically $\sim 0.08 - 0.13$ in $\log L_*$ and $\sim 100 - 150$ K in temperature.

adopted the self-similar solution for a viscous disk (Lynden-Bell & Pringle, 1974) rather than a truncated power-law disk. For the seven sources in our sample which have not been mapped yet we adopted a fiducial interval for R_{out} of 100 – 300 AU, which comprises nearly all the disks outer radii as found for the 24 Taurus and Ophiucus circumstellar disks in Andrews & Williams (2007b). Based on the results of this same work we adopt for all the sources in our sample an interval for the surface density power-law index p which goes from 0.5 to 1.5.

An important thing to keep in mind here is that with these values for the outer radius of the disk the dust emission at the long wavelengths considered in this paper turns out to be dominated by the optically thin outer disk regions. This has two important consequences for our discussion. The first one is that constraints on dust properties such as dust grain sizes and dust mass can be derived from the continuum emission at sub-mm/mm wavelengths. If a disk is much more compact than the ones which have been commonly mapped so far, i.e. if $R_{\text{out}} \lesssim 20 - 30$ AU, then its emission would be dominated by the denser inner regions which are optically thick even at these long wavelengths, and no information on the dust properties could be inferred by the observed continuum. The second consequence is that the disk inclination is not a relevant parameter for our analysis, except only for the case of a nearly edge-on disk that however would make the central PMS star invisible in the optical.

4.4.2 Dust opacity

To calculate the dust opacity we adopted the same dust grain model taken in R10, i.e. porous composite spherical grains made of astronomical silicates (optical constants from Weingartner & Draine, 2001), carbonaceous materials (Zubko et al., 1996) and water ices (Warren, 1984) with fractional abundances from a simplification of the model used in Pollack et al. (1994) and a volume fraction for vacuum of $\approx 30\%$. In the disk surface and midplane we consider a dust grain population with a grain size number density throughout all the disk

$$n(a) \propto a^{-q} \quad (4.2)$$

between a_{min} and a_{max} (a here is the grain radius). In this paper we adopt two different grain size distributions in the disk surface and midplane, since both observations and theory predict larger grains in the midplane. In particular, although we consider in both the surface and midplane a small value of $a_{\text{min}} \approx 0.1 \mu\text{m}$, for the maximum grain size a_{max} in the disk surface we consider a value only slightly larger than a_{min} ⁸, whereas a_{max} has been left free to vary in the disk midplane. As done in R10 we consider in this work four possible values for the q -parameter: 2.5, 3.0, 3.5, 4.0.

⁸We also consider the same value of q for both the surface and the midplane. However, contrary to the dust in the midplane where q is a relevant parameter, in the disk surface the adopted q -value is practically non influential since a_{max} is only slightly larger than a_{min}

4.4.3 Method

After having set the disk outer radius R_{out} and the power-law index p of the surface density profile, the two-layer models can be used to fit the sub-mm/mm SED of circumstellar disks to constrain dust properties in the disk midplane⁹, in particular the spectral index of the dust opacity β between two mm-wavelengths (1 and 3 mm in the case of this paper) and the product $M_{\text{dust}} \times \kappa_{1\text{mm}}$ between the mass in dust and the dust opacity at 1 mm. Except for very low values of β , which cannot be explained by large values of the power-law index q of the grain size number-density (see discussion in Sect. 5.1), every β -value can be reproduced by different (q, a_{max}) couples. Furthermore, at a fixed q , the precise value of the maximum grain size a_{max} correspondent to a certain derived β depends strongly on the model that one adopts for the dust. The only robust conclusion which is valid for all the reasonable models of dust analyzed so far is that β -values lower than the value found for the ISM ($\beta_{\text{ISM}} \sim 1.7$) can be obtained only with dust populations in which grains as large as at least ~ 1 mm are present (see e.g. Natta et al., 2007). For these reasons in the rest of the paper we will rarely refer to the maximum grain size a_{max} , whereas we will more frequently use β as our proxy for grain growth.

In order to derive an estimate for $\kappa_{1\text{mm}}$ and thus constrain the dust mass M_{dust} , one has to adopt a certain model for the dust grain which provide a family of functions $\kappa_{1\text{mm}}(\beta)$ labeled with the q -parameter. The $\kappa_{1\text{mm}}(\beta)$ functions considered in this paper have been obtained using the dust model presented in Sect. 7.3.2 and they are the same shown in Figure 3 in R10.

Figure 4.3 reports the best fit flared disk model overplotted to the sub-mm/mm data for each disk in our sample¹⁰. Since as explained in Sect. 4.1 for each disk we have adopted, instead of a single value, an interval of possible values for R_{out} and p , the uncertainty on these parameters translates into an uncertainty on the quantities derived by fitting the sub-mm/mm SED, i.e. β and $M_{\text{dust}} \times \kappa_{1\text{mm}}$. Adding this contribution to the uncertainties in the observational data, the total absolute uncertainties are approximately 0.4 for β and a factor of $\approx 3 - 4$ for $M_{\text{dust}} \times \kappa_{1\text{mm}}$.

4.5 Results

The results of the SED-fitting procedure are listed in Table 3. Here we discuss them in terms of dust grain growth (Sect. 5.1) and mass in dust (Sect. 5.2) for our sample of protoplanetary disks.

⁹Note that this is true only in the case in which the dust emission at long wavelengths comes mostly from the optically thin disk outer regions, as described at the end of Sect. 7.3.1

¹⁰Note that for a few disks (SR 4, EL 20, RNO 90) the flux at ~ 1 mm falls below the model line. Although this could be due to problems in the observations, another possible reason is that the 3 mm-flux for these sources is contaminated by free-free emission. If this was the case, the derived β -values for these disks would be only lower-limits. Observations at longer wavelengths, where free-free dominates the emission, are needed to constrain its possible contribution at 3 mm.

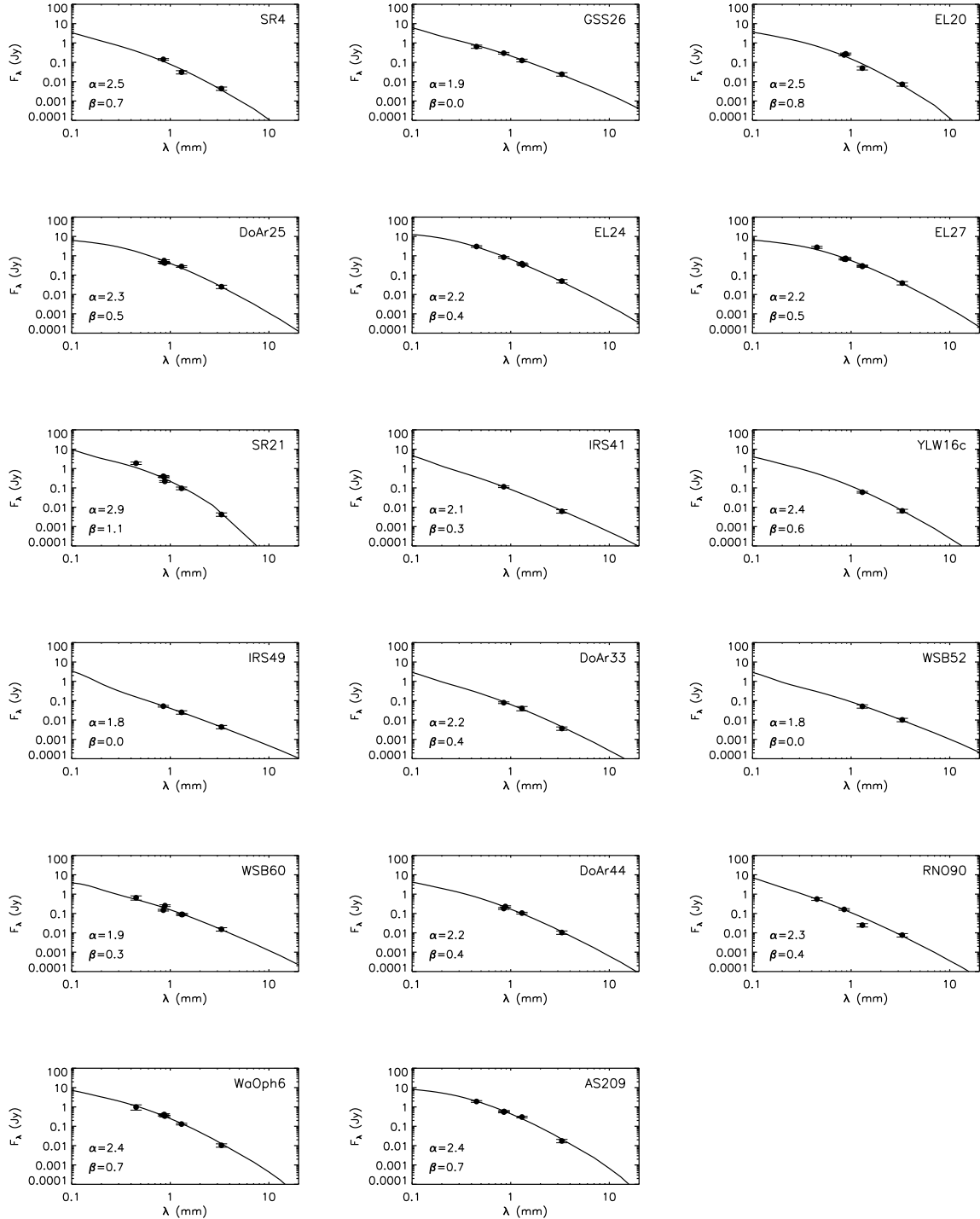


Figure 4.3: Sub-mm/mm SED fits for the 17 sources in our sample with the two-layer flared disk models (solid lines). The errorbars in the plots take into account an uncertainty of 10% on the absolute flux scale at wavelengths shorter than 3 mm, and of 25% at 3 mm. The fitting values of the spectral index α and of the dust opacity spectral index β between 1 and 3 mm are indicated in the bottom left corner of each plot. The value of the adopted surface density power-law index p is 1, the adopted value for the outer disk radius is the central value of the R_{out} -interval listed in Table 4.3, whereas the value for the power-law index of the initial dust density is $\beta_{\text{init}} = 0$ for all disks (GSS 26, YLW 16, IRS

4.5.1 Grain growth

Information on the level of dust grain growth in the outer regions of protoplanetary disks comes from the analysis of the spectral index of the dust opacity at (sub-)millimeter wavelengths β , which reflects the spectral index of the disk SED at these long wavelengths α . In particular for a completely optically thin disk in the Rayleigh-Jeans regime $\beta = \alpha - 2$, whereas if emission from the optically thick disk inner regions (i.e. $R \lesssim 20 - 30$ AU) and deviations of the emitted spectrum from the Rayleigh-Jeans regime are taken into account, as done for our analysis, $\beta \gtrsim \alpha - 2$. In the limit case of a completely optically thick disk even at these long wavelengths the SED spectral index α becomes independent on β and so no information on grain growth would be obtainable. In Columns (5) and (6) of Table 3 the constrained values of α and β between 1 and 3 mm are reported¹¹.

Figure 4 shows the SED spectral index $\alpha_{1-3\text{mm}}$ plotted against the observed flux at 3.3 mm for all the sources in our sample. The spanned range in $\alpha_{1-3\text{mm}}$ is 1.8 – 2.9, and there is no clear evidence of any correlation between the two plotted quantities. The fact that all the disks in our sample show a (sub-)mm spectral index which is shallower than the one found for the ISM, i.e. $\alpha < \alpha_{\text{ISM}}$, brings evidence of grain growth from an initial ISM-like dust population for all the disks in our sample¹².

In Figure 5 we report the histogram of the derived distribution of β -values. All the disks show $\beta < \beta_{\text{ISM}} \sim 1.7$, indicative of dust grain growth to at least mm-sizes. Note that for 9 out of the 17 disks $\beta \lesssim 0.8$ (considering a 1σ -uncertainty on β of about 0.4) and for them the data are not consistent with the MRN-value of 3.5 for the power-law index q of the dust grain size distribution in the ISM (Mathis et al., 1977): for these disks q -values as low as 2.5 – 3 are needed (see discussion in R10).

The mean value is $\langle \beta \rangle = 0.46 \pm 0.08$, which is consistent within 1σ with the one obtained for the Taurus sample discussed in R10 ($\langle \beta \rangle_{\text{Tau}} = 0.6 \pm 0.06$). In order to make a statistical comparison of the dust grain growth between the Taurus sample and the one presented in this paper in the ρ -Oph star forming region we performed a two-sample KS test. The probability that the two samples have β -values drawn from the same distribution is $\approx 22\%$. The hypothesis that the samples in Taurus and Ophiuchus have the same β -distribution cannot thus be rejected at the 95% of confidence level.

In Figure 6 we plot the (sub-)mm spectral index of the dust opacity β against the stellar age for YSOs in different evolutionary stages: the 38 class II disks in Ophiuchus and Taurus presented here and in R10 respectively, and a sample of 15 less evolved class 0 YSOs¹³ in Taurus, Perseus, and isolated from the PROSAC survey (Joergensen et al., 2007) and from Kwon et al. (2009). Contrary to the class II disks, for all the class 0

¹¹Note that the difference $\alpha - \beta$ turns out to be in the range 1.6 – 1.9. This (small) discrepancy from the value of 2 is primarily due to the low temperature of the outer disk midplane and the consequent deviation from the Rayleigh-Jeans regime of the mm-wave emission.

¹²This sentence is strictly valid for the ten disks in our sample which have been mapped so far; for the seven disks which have not been mapped yet this sentence is valid only if the underlying assumption that their spatial extension is not so small that most of the mm emission is optically thick ($R_{\text{out}} \lesssim 20 - 30$ AU) holds true.

¹³Note that for these objects there are no robust age-estimates.

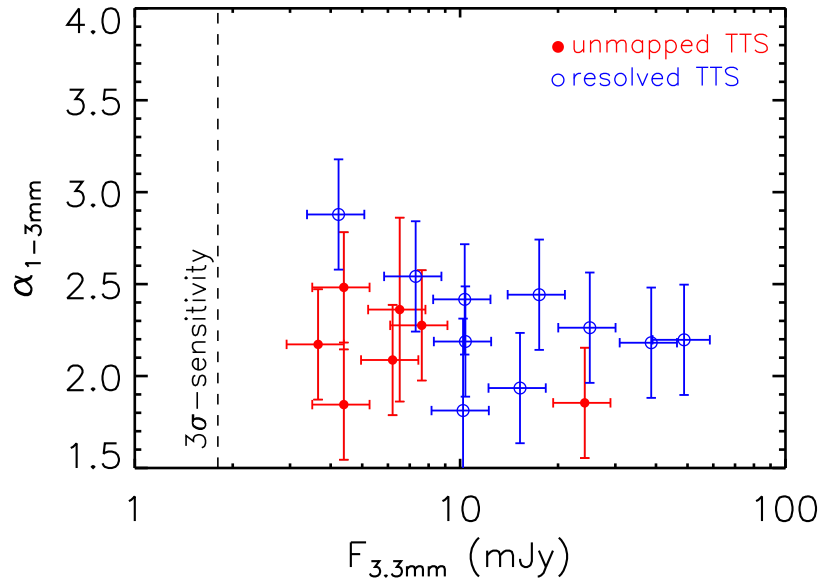


Figure 4.4: Spectral index α between 1 and 3 mm from the model best fits shown in Figure 3 plotted against the observed flux at 3.3 mm. Open blue points represent the spatially resolved disks, whereas the filled red points are for the unmapped ones. The dashed vertical line shows the mean 3σ -sensitivity of our ATCA observations, i.e. about 1.8 mJy.

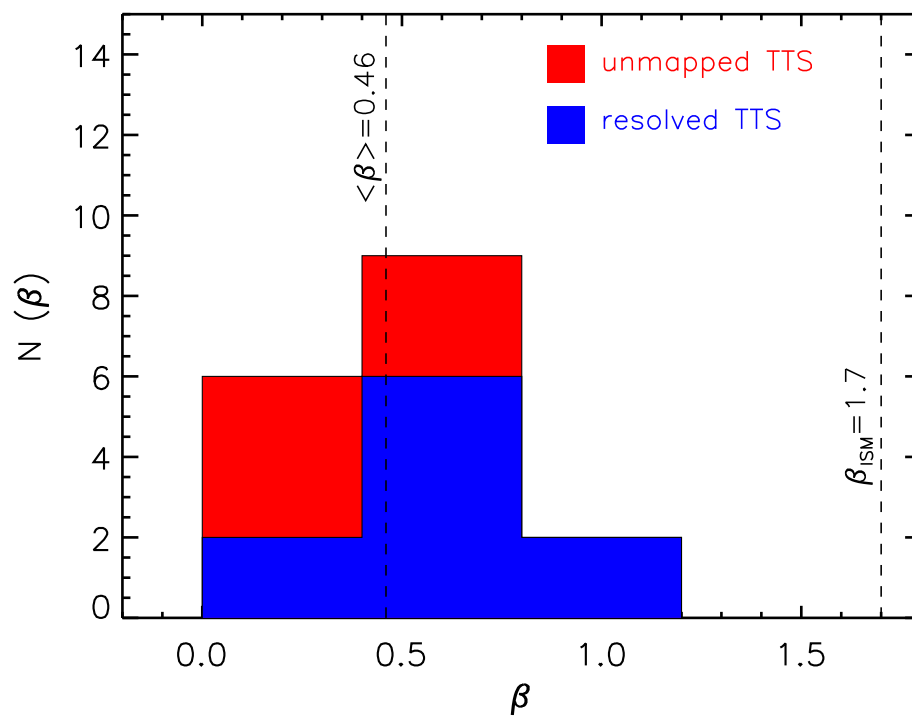


Figure 4.5: Distribution of the dust opacity spectral index β for the disks in our sample. In blue the values for the spatially resolved disks are indicated, whereas the red is for the unmapped ones. The average β value for all the sources in our sample and the value of ~ 1.7 for the ISM dust are indicated as dashed vertical lines.

objects the values of β have been obtained using the approximated $\beta = \alpha - 2$ relation (see caption of Figure 6). As described before, this relation gives only a lower-limit for β , and this probably explains why for many of these sources the derived β is negative. A more sophisticated analysis is needed to get more robust estimates of β by taking into account self-consistently deviations from the above relation as due to departures from the Rayleigh-Jeans regime of the emission (especially for these cold sources) and to marginally optically thick emission typically associated to the compact structure forming the disk. However, the low values of β obtained for nearly all these sources appear to show evidence for dust grain growth to \sim mm-sizes (see Figure 3 in R10) already in the earliest stages of star formation. Ormel et al. (2009) have recently investigated the effects of dust coagulation and fragmentation onto the dust size distribution in molecular cloud cores. They found that grain sizes close to ~ 1 mm can be formed if cloud lifetimes are not restricted to free-fall times but rather support mechanisms like e.g. ambipolar diffusion are present and if freeze-out of ice has commenced. According to their simulations ice-coated grains can grow to sizes of $\sim 0.3 - 8$ mm in one ambipolar diffusion timescale at densities of $n = 10^5 - 10^7 \text{ cm}^{-3}$, which are typical of the inner regions of molecular cores. Dust grain growth to \sim mm-sizes can thus be a process accompanying the very first phases of star formation.

Figure 6 shows also that there is no relation between the dust opacity spectral index and the stellar age for the class II disks: grains as large as ~ 1 mm appears to be present in the outer regions of disks throughout all the class II evolutionary stage. This is in contrast with the short timescales of inward radial drift expected for \sim mm/cm-sized grains in the outer disk as a consequence of the dust interaction with the gas component. In order to explain the retention of large dust grains in these outer regions some mechanisms which may halt the drift of solid particles, e.g. local pressure maxima due to turbulent vortices or spiral density waves, have been invoked. Birnstiel et al. (2010b) have compared the observed fluxes at millimeter wavelengths for the disks samples described in R10 and in this paper with predictions of dust evolution models accounting for coagulation and fragmentation. They showed that, if radial drift of solid particles is completely suppressed, a grain size distribution at the steady-state (due to a balance between coagulation and fragmentation) can explain the mm-wave emission of the brightest disks. The observed flux of the fainter disks are instead typically overpredicted even by more than one order of magnitude. These discrepancies may be explained by considering in the disk models a dust reduction due to radial drift at a reduced rate¹⁴ or during an earlier evolutionary time or due to efficient conversion of dust into larger, unseen bodies (see Birnstiel et al., 2010b, for more details). Observations of these faint disks can thus help us to determine which mechanisms play a major role for the dynamics and evolution of large grains in the outer regions of disks.

Figure 7 shows the spectral index between 1 and 3 mm in Taurus (left) and Ophiuchus (right) plotted against two indicators of dust processing from the silicate feature observed

¹⁴The radial drift, other than decreasing the amount of dust in the disk and thus decreasing the flux at millimeter wavelengths, is more efficient for mm/cm-sized pebbles than for smaller grains in the outer disk. For this reason, if one wants to explain the low values of the mm-spectral indices only a reduced rate of radial drift (from that expected theoretically) can be invoked.

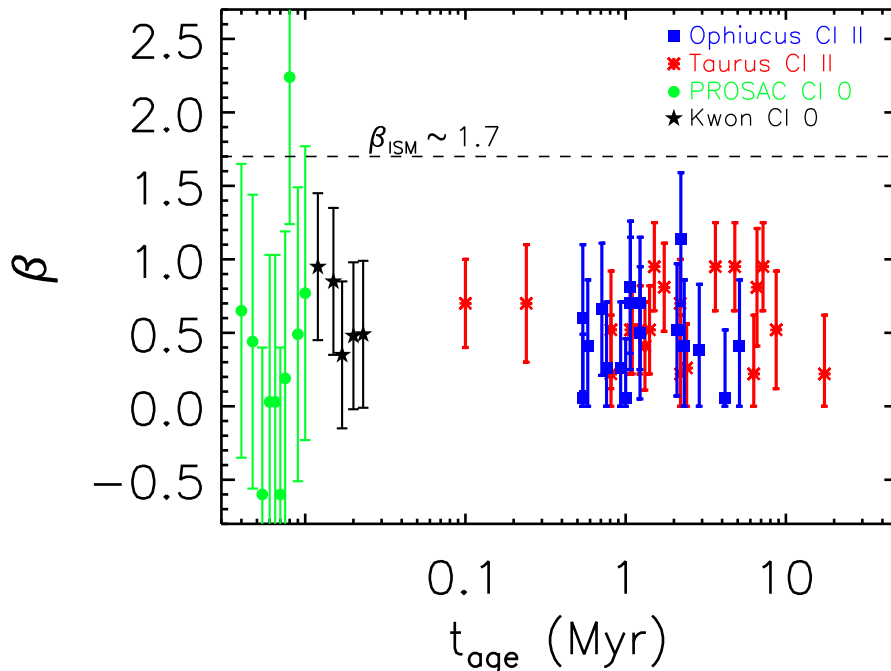


Figure 4.6: Dust opacity spectral index β versus age: relationship between the dust opacity spectral index β and the estimated stellar age obtained as in Sect. 3.3 for the class II YSOs. Note that for the class 0 YSOs (green circles and black stars) the position in the x-axis of the plot is only indicative, since no robust age estimates can be derived for these sources. Blue squares represent the sample of class II YSOs presented in this paper, red asterisks are the Taurus-Auriga class II disks from R10, green circles are the class 0 YSOs from the PROSAC survey (Joergensen et al., 2007), black stars are class 0 YSOs from Kwon et al. (2009). The β -value for the ISM dust is indicated as a dashed horizontal line. For all the class 0 YSOs the values of β have been obtained using the $\beta = \alpha - 2$ relation, where α is the spectral index between the CARMA total fluxes at 1.3 and 2.7 mm for the Kwon et al. sample, and between the fluxes collected at 0.85 and 1.3 mm with the SMA array at baselines longer than 40 k λ for the PROSAC sample. This criterion was chosen by the authors to minimize the contribution from the extended envelope to the total emission.

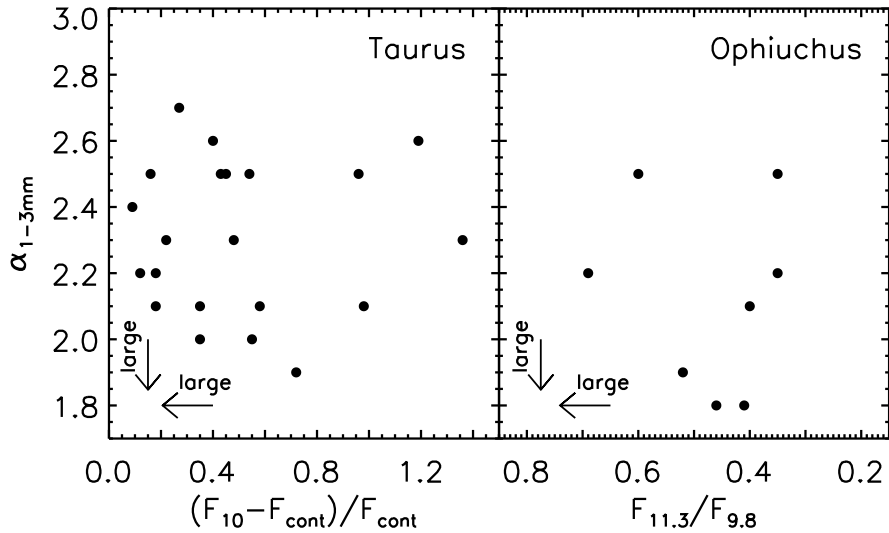


Figure 4.7: SED spectral index between 1 and 3 mm versus indicators of grain growth from the 10- μm silicate feature. Left) SED slope between 1 and 3 mm vs the ratio between the 10- μm line flux and the continuum as derived from Spitzer/IRS observations by Furlan et al. (Furlan et al. (2006)) for the sample of Taurus-Auriga class II YSOs described in R10. Right) SED slope between 1 and 3 mm vs the ratio between the flux at 11.3 and 9.8 μm as derived from Spitzer/IRS observations by McClure et al. (2010); the plotted points are all the class II YSOs described in this paper with a value of $F_{11.3}/F_{9.8}$ reported in McClure et al.. In the two plots the arrows in the lower left corners show toward which direction the values of the plotted quantities are indicative of the presence of largest grains.

at about $10\ \mu\text{m}$ (see e.g. Kessler-Silacci et al., 2006). Data for the $10\ \mu\text{m}$ silicate feature for the two samples in Taurus and Ophiuchus come from the literature and refer to different indicators (see caption of Figure 7) since we could not find the same indicator for both the regions. However Lommen et al. (2010) showed that these two indicators correlate well and so they can be both used to probe the growth of grains from interstellar, submicron sizes to sizes of several microns in the disk surface layers. In particular low values of the ratio between the $10\ \mu\text{m}$ line flux and the continuum, $(F_{10} - F_{\text{cont}})/F_{\text{cont}}$, and large values of the ratio between the fluxes at 11.3 and $9.8\ \mu\text{m}$, $F_{11.3}/F_{9.8}$, are interpreted in terms of grain growth to micron sizes (Bouwman et al., 2001; Kessler-Silacci et al., 2006). Very recently Lommen et al. (2010) have found a tentative correlation between these quantities for a sample of about 30 TTS and Herbig-Ae/Be systems spread over five different star forming regions, including Taurus-Auriga. Since the mm slope of the SED probes grains in the disk outer regions whereas the $10\text{-}\mu\text{m}$ silicate feature is sensitive to grains in the inner regions, the tentative correlation may indicate a parallel evolution of the inner and outer disk in terms of dust grain growth. However, in this work we do not find any correlation neither for the sample in Taurus nor for the one in Ophiuchus. Note that in the case of Ophiuchus the sample with literature data for the $10\text{-}\mu\text{m}$ silicate feature is limited to eight disks only. In Taurus our sample comprises nine of the eleven disks considered by Lommen et al., and for two of them (AA Tau and GM Aur) our derived values of $\alpha_{1-3\text{mm}}$ are not consistent with and lower than the values used by Lommen et al.¹⁵. Note also that the absence of such a correlation would not be too surprising since the physical mechanisms which are responsible for the observed values of the grain growth indicators are different: the presence of mm/cm-sized pebbles in the midplane of the outer disk is mainly due to coagulation processes and mechanisms which trap these pebbles in the outer disk, whereas the presence of μm -sized grains in the surface layers of the inner disk is probably regulated by fragmentation of larger solid particles and a balance between settling and turbulence mixing which keeps these relatively small grains in the uppermost layers of the disk. Further observations with more sensitive telescopes in the future are needed to provide necessary the necessary statistics to better investigate the possible relation between dust grains in the outer and inner disk regions and to possibly constrain the processes of radial mixing and vertical settling.

4.5.2 Disk mass

Table 3 lists the derived dust masses for our sample of disks detected at $3\ \text{mm}$. As already discussed in R10, the inferred dust mass depends, at a given chemical composition and porosity for the dust grain, on the assumed value of the power-law index q of the grain size distribution. This dependence, which is due to the different millimeter dust opacities obtained for different values of q (see R10), is particularly strong for relatively low values of β . For example, in the case of WSB 60, with $\beta \approx 0.3$, $M_{\text{dust}}^{q=3}$ is larger than $M_{\text{dust}}^{q=2.5}$ by a

¹⁵This discrepancy is probably due to a different choice of the literature data used for the derivation of α . In the case of R10 all the data obtained at sub-mm and mm wavelengths have been used.

factor of about 10.

Even if the estimate for M_{dust} depends on the value of q , the range spanned by our sample for $q = 2.5$ and $q = 3$ turns out to be very similar¹⁶, namely $\sim 2 \cdot 10^{-5} - 3 \cdot 10^{-3} M_{\odot}$, corresponding to roughly $6 - 1000 M_{\oplus}$. By defining a planetesimal as a rocky body with a radius of 10 km and a density similar to the one adopted for our dust grain model (i.e. $\rho \sim 1 \text{ g/cm}^3$), the maximum number of planetesimals which can be potentially formed out of this reservoir of small grains (see discussion below) is $\sim 10^{10} - 10^{12}$.

These numbers have to be taken with great caution mainly because of the large uncertainty for the inferred dust mass of a factor as large as 10 (see e.g. the discussion in Natta et al., 2004).

Here it is important to remember that observations at (sub-)mm wavelengths are completely insensitive to pebbles/stones much larger than $\sim 1 - 10$ cm, since the dust opacity decreases as the a_{max} of the dust population increases at sizes larger than the wavelengths of the observations. For this reason the dust masses presented here have to be interpreted as lower limits for the real total mass in solids, since in principle large pebbles/stones or even larger rocky bodies like planetesimals may be already present in the disk.

Finally we have investigated relations between dust properties in disks (i.e. β , M_{dust}) and the stellar ones (listed in Table 2) but we did not find any significant correlation, similarly to the case of Taurus (R10). No significant correlation was found neither between grain growth and dust mass.

4.6 Summary

We have presented new observations at ~ 3 mm obtained with the ATCA array and the new CABB digital filter bank for 27 protoplanetary disks in the ρ -Oph star forming region. Among these we selected the 17 isolated class II YSOs with well characterized stellar properties (see selection criteria in Sect. 3.1). Our sample comprises all the ρ -Oph isolated class II YSOs with an observed flux at 1.3 mm larger than ~ 75 mJy, and $\sim 50\%$ of the isolated PMS stars with mass larger than $\sim 0.5 M_{\odot}$. We have analyzed the (sub-)millimeter SED of our disk sample and here is the summary of our main findings:

1. The spectral index β of the millimeter dust opacity turns out to be lower than the typical value found for the ISM for all the 17 disks detected at 3 mm. The mean value is $\langle \beta \rangle \approx 0.5$. For the ten disks which have been observed and spatially resolved through past high-angular resolution continuum imaging at sub-mm wavelengths this represents evidence for the presence of dust grains as large as at least ~ 1 mm in the disk outer regions. For the seven disks which have not been mapped yet the observations could in principle be consistent also with very compact ($R_{\text{out}} < 20 - 30$ AU) disks, significantly different from those mapped so far.

¹⁶Note however that for the four disks with the lowest value of β (≈ 0) $M_{\text{dust}}^{q=3}$ cannot be obtained. The reason for this is that these very low β -values cannot be explained with $q = 3$ (see discussion in Sect. 5.1). For the same reason only two disks have an estimate for the dust mass with $q = 3.5$.

Table 4.3: Disk properties.

Object name	R_{out} (AW07)	R_{out} -interval	α	β	$M_{\text{dust}} \times \kappa_{1\text{mm}}$	$M_{\text{dust}}^{q=2.5}$	$M_{\text{dust}}^{q=3}$	$M_{\text{dust}}^{q=3.5}$
(1)	(AU)	(AU)	(4)	(5)	($M_{\odot} \times \text{cm}^2 \text{g}^{-1}$)	(M_{\odot})	(M_{\odot})	(M_{\odot})
(1)	(2)	(3)	(4)	(5)	(6)	(7)	(8)	(9)
<u>SR 4</u>	...	100–300	2.5	0.7	$1.3 \cdot 10^{-4}$	$2.1 \cdot 10^{-5}$	$2.4 \cdot 10^{-5}$...
<u>GSS 26</u>	...	100–300	1.9	0.0	$3.5 \cdot 10^{-4}$	$2.3 \cdot 10^{-3}$
EL 20	...	100–300	2.5	0.8	$3.2 \cdot 10^{-4}$	$4.3 \cdot 10^{-5}$	$4.5 \cdot 10^{-5}$	$1.9 \cdot 10^{-4}$
DoAr 25	200	100–300	2.3	0.5	$8.0 \cdot 10^{-4}$	$1.8 \cdot 10^{-4}$	$2.6 \cdot 10^{-4}$...
EL 24	175	75–275	2.2	0.4	$9.9 \cdot 10^{-4}$	$2.9 \cdot 10^{-4}$	$6.3 \cdot 10^{-4}$...
EL 27	275	175–375	2.2	0.5	$1.5 \cdot 10^{-3}$	$3.5 \cdot 10^{-4}$	$5.6 \cdot 10^{-4}$...
SR 21	600	500–700	2.9	1.1	$5.3 \cdot 10^{-4}$	$4.9 \cdot 10^{-5}$	$4.5 \cdot 10^{-5}$	$5.5 \cdot 10^{-5}$
<u>IRS 41</u>	...	100–300	2.1	0.3	$1.3 \cdot 10^{-4}$	$6.6 \cdot 10^{-5}$	$6.8 \cdot 10^{-4}$...
<u>YLW 16c</u>	...	100–300	2.4	0.0	$2.3 \cdot 10^{-4}$	$4.3 \cdot 10^{-5}$	$5.6 \cdot 10^{-5}$...
<u>IRS 49</u>	...	100–300	1.8	0.0	$3.9 \cdot 10^{-5}$	$2.2 \cdot 10^{-3}$
<u>DoAr 33</u>	...	100–300	2.2	0.4	$1.2 \cdot 10^{-4}$	$3.4 \cdot 10^{-5}$	$9.9 \cdot 10^{-5}$...
WSB 52	...	100–300	1.8	0.0	$1.4 \cdot 10^{-5}$	$2.6 \cdot 10^{-3}$
WSB 60	350	250–450	1.9	0.3	$5.6 \cdot 10^{-4}$	$2.9 \cdot 10^{-4}$	$3.0 \cdot 10^{-3}$...
DoAr 44	...	100–300	2.2	0.4	$3.0 \cdot 10^{-4}$	$8.8 \cdot 10^{-5}$	$1.9 \cdot 10^{-4}$...
<u>RNO 90</u>	...	100–300	2.3	0.4	$1.1 \cdot 10^{-4}$	$3.1 \cdot 10^{-5}$	$7.1 \cdot 10^{-5}$...
Wa Oph 6	275	175–375	2.4	0.7	$4.9 \cdot 10^{-4}$	$8.0 \cdot 10^{-5}$	$9.8 \cdot 10^{-5}$...
AS 209	200	100–300	2.4	0.7	$7.9 \cdot 10^{-4}$	$1.2 \cdot 10^{-4}$	$1.4 \cdot 10^{-4}$...

1) Underlined objects are those which have not been mapped to date through high-angular resolution imaging. The objects which have been mapped but do not have an estimate for the outer disk radius as reported in Column (2) have been spatially resolve by Andrews et al. (2009). Contrary to Andrews & Williams (2007a), they modeled the disk surface brightness by using a self-similar profile instead of a truncated power-law. For this reason no estimate for R_{out} could be extracted for these sources (see footnote in Sect. 4.1). 2) Best-fit estimate of the disk outer radius by fitting the observed visibilities at sub-millimeter wavelengths using a truncated power-law for the surface density profile. AW07: Andrews & Williams (2007a). 3) Interval of the disk outer radius adopted for our analysis. 4) Best-fit estimate of the spectral index of the SED α between 1 and 3 mm derived by considering for the outer disk radius the central value of the interval reported in Column (3), and for the power-law index of the surface density profile $p = 1$. 5) Best-fit estimate of the spectral index of the dust opacity β between 1 and 3 mm. 6) Product between the dust mass and the dust opacity at 1 mm from the best-fit two-layer disk model. 7) Dust mass obtained with a power-law index for the grain size distribution $q = 2.5$. 8) Like Column (7) but with $q = 3$. The sources without an estimate of the dust mass have a β -value (reported in Column (6)) which cannot be reproduced with $q = 3$. 9) Like Column (8) but with $q = 3.5$.

2. From a comparison between the results found for our sample in ρ -Oph and an homogeneously selected sample of 21 isolated class II disks in Taurus-Auriga (R10), there is no statistical evidence of any difference between the distribution of β -values found in the two star forming regions. This may suggest that environmental effects do not play an important role in the first phases of planet formation.
3. There is no evidence for any evolution of the dust spectral index: dust grains appear to be present in the outer regions of protoplanetary disks throughout all the class II evolutionary stage of YSOs, confirming what previously found in Taurus. In order to explain the retention of large dust grains in the outer disk some mechanisms which may halt the inward drift of solid particles, e.g. local pressure maxima due to turbulent vortices or spiral density waves, have to be invoked. Since evidence for grain growth to millimeter sizes appears to be present in some class 0 YSOs the formation of the \sim mm-sized grains seen in class II disks may already occur in the densest inner regions of molecular cloud cores (Ormel et al., 2009).
4. The mm slope of the SED does not correlate with indicators of dust processing from the silicate feature observed at about $10 \mu\text{m}$, which are sensitive to grain growth to micron sizes in the surface layers of the inner disk; further observations at (sub-)mm wavelengths are needed to extend the investigation to a larger sample.
5. The spanned range in dust mass contained in grains with sizes $\lesssim 1 \text{ cm}$ as derived with the dust model described in Sect. 4.2 is about $2 \cdot 10^{-5} - 3 \cdot 10^{-3} M_{\odot}$ or roughly $6 - 1000 M_{\oplus}$. This reservoir of small grains is capable of forming about $10^{10} - 10^{12}$ 10 km-sized planetesimals with a mean density of $\sim 1 \text{ g/cm}^3$.

The (sub-)millimeter SED of protoplanetary disks in the outskirts of the Orion Nebula Cluster

Published as Ricci, Mann, Testi, Williams, Isella, Robberto, Natta, & Brooks, 2011, A&A 525, 81

Abstract

We present the sub-mm/mm SED for a sample of eight young circumstellar disks in the outer regions of the Orion nebula cluster (ONC). New observations were carried out at 2.9 mm with the CARMA array and for one disk, 216-0939, at 3.3 and 6.8 mm with ATCA. By combining these new millimeter data with literature measurements at sub-millimeter wavelengths we investigate grain growth and measure the dust mass in protoplanetary disks in the ONC. These data provide evidence for dust grain growth to at least millimeter-sizes for the first time in a high-mass star-forming region. The obtained range in sub-mm/mm spectral index, namely 1.5-3.2, indicates that for disks in the outskirts of the ONC (projected distance from the cluster center between about 0.4 pc and 1.5 pc) grain growth to mm sizes occurs in the same manner as disks in regions where only low-mass stars form. Finally, in our sample three disks are more massive than about $0.05 M_{\odot}$, confirming that massive disks are present in the outer regions of the Orion nebula.

5.1 Introduction

Disks around young Pre-Main Sequence (PMS) stars are thought to be the cradles of planets, and for this reason they are often called “proto-planetary disks”. Evidence for the very early stages of planet formation in protoplanetary disks has been obtained by a

variety of different techniques, ranging from the optical to the millimeter-wave spectral domain. Compared to observations at shorter wavelengths the inspection of the sub-mm and mm emission of disks provides two key advantages for the investigation of the physical processes related to planet formation. First, except for the very inner regions of the disk, the dust optical depth at these long wavelengths is sufficiently low that the disk midplane can be probed. Second, since the maximum grain size to which a particular technique is sensitive to is of the order of the observational wavelength, the (sub-)millimeter spectral regime offers the chance to investigate grain growth up to mm/cm sizes (see Rodmann et al., 2006).

So far nearly all the information we have on the dust grain properties in protoplanetary disks has been derived from systems in low-mass Star Forming Regions (SFRs). Little information on the dust grains in young disks is present for high-mass SFRs. The analysis of dust in high-mass SFRs is particularly compelling since about 75% of the observed Young Stellar Objects (YSOs) formed in a clustered environment, where high-mass stars form (Bressert et al., 2010).

Some evidence for dust grain growth in protoplanetary disks in the Orion Nebula Cluster (ONC) has been obtained at optical and infrared wavelengths. Throop et al. (2001) and Shuping et al. (2003) observed in optical and NIR the largest ONC silhouette disk (114-426). From the extinction curve of the background nebular emission they found that the NIR opacity of the disk is dominated by grains as large as about 10 μm , larger than the typical sub-micron sized grains found in the ISM (Mathis et al., 1977). Using low-resolution spectroscopy in the mid-IR, Shuping et al. (2006) found evidence for grain growth to a few μm in the surface layers of eight disks in the Trapezium Cluster.

During the last 15 years several ONC disks have been surveyed by interferometric observations at mm-wavelengths (e.g. Wilner et al., 2005; Eisner et al., 2008; Mann & Williams, 2009b). However, the targeted disks were quite close to the main ionizing source of the cluster, the O6-type Trapezium star θ^1 Ori C (typical projected distances lower than 0.2 pc by assuming a distance to the ONC of 400 pc, Menten et al., 2007; Sandstrom et al., 2007; Kraus et al., 2009). As a consequence, the high levels of free-free emission by ionized gas swamped the dust emission from the disks, making estimates of grain growth almost impossible to derive from multi-wavelength dust measurements in the millimeter spectral window.

In this work we present new mm-wave interferometric observations for a sample of eight disk systems in the outskirts of the ONC. Because of their location relatively far from θ^1 Ori C (projected distances between 0.4 and 1.5 pc, see Figure 5.1), information on grain growth can be derived from mm-wave observations. This allows us to probe the dust properties in these ONC disks over the entire sub-mm/mm SED.

5.2 Observations

We describe here new mm-wave observations of eight young circumstellar disks in the ONC. The disks were selected for being detected within the SMA survey of protoplanetary disks

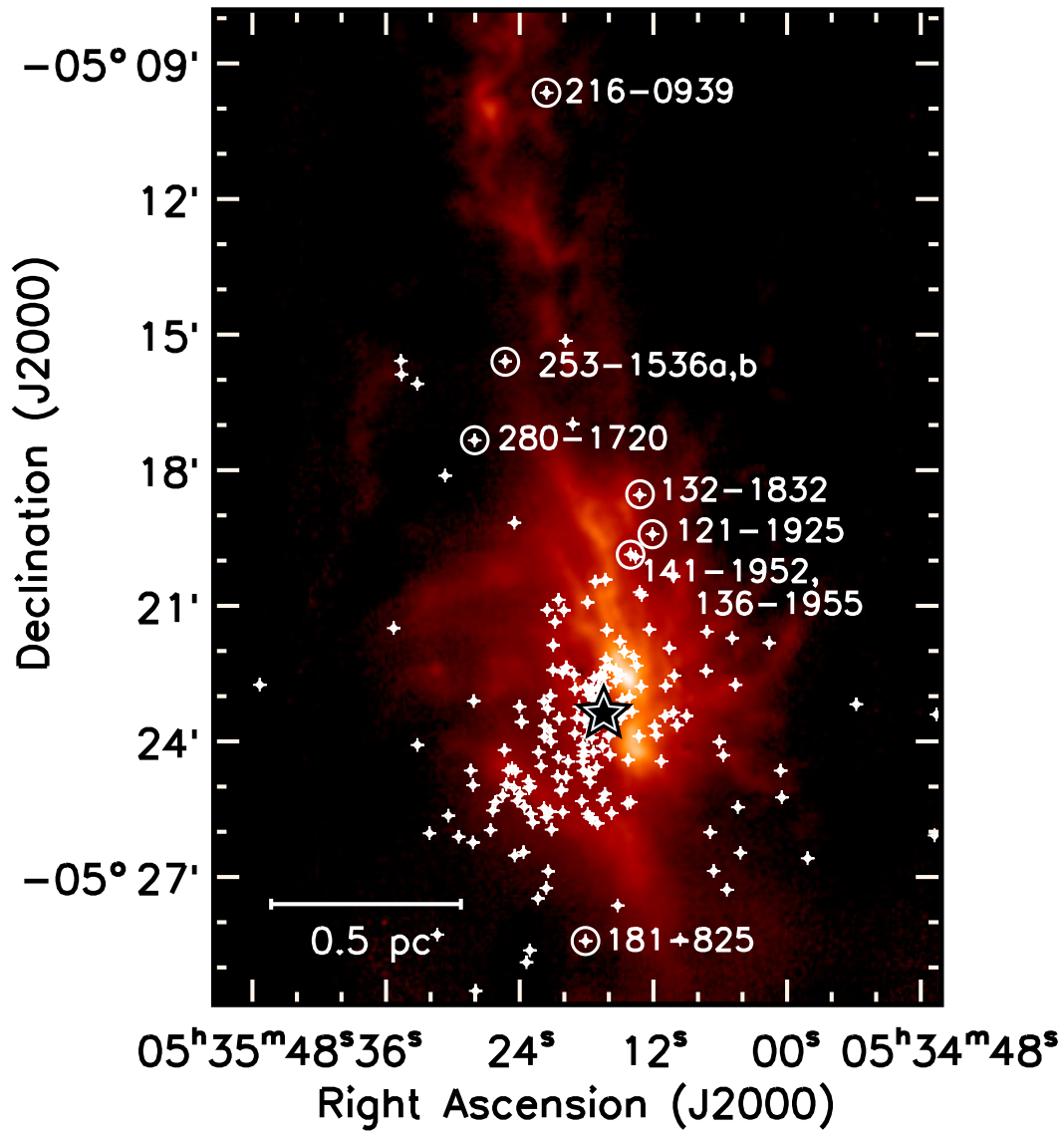


Figure 5.1: Location of the eight disks in our sample (within white circles) overlaid on a JCMT-SCUBA 850 μm image of the ONC (Johnstone & Bally, 1999). The black and white star near the bottom of the image marks the position of the θ^1 Ori C star. White crosses represent the positions of proplyds identified by HST observations.

in Orion (Mann & Williams, 2010) with a 0.88 mm-flux density larger than about 15 mJy, and by being located in the outer regions of the ONC (i.e. projected distance from the Trapezium Cluster larger than 3 arcmin). This latter selection criterion was chosen to avoid contamination at mm-wavelengths from the non-uniform background emission and free-free emission from ionized gas typically observed in the inner ONC. The disks in our sample are listed in Table 6.1.

The dust thermal emission toward our sample of eight young disk systems in the ONC was observed with the Combined Array for Research in Millimeter Astronomy (CARMA) between 2010 Mar 26 and Apr 01. The array was in C configuration which provides baselines between 30 and 350 m. Observations were carried out at a central frequency of 102.5 GHz (2.92 mm), with a total bandwidth of 4 GHz.

The raw visibilities for each night were calibrated and edited using the MIRIAD software package. Amplitude and phase calibration were performed through observations of the QSO J0607-085. Passband calibration was obtained by observing the QSO 0423-013. Mars and Uranus were used to set the absolute flux scale. The uncertainty on CARMA flux calibration is typically estimated to be $\sim 15\%$ and is due to uncertainties in the planetary models and in the correction for atmospheric effects and hardware instabilities. Figure 5.2 shows the measured 2.9 mm-flux density of the QSO J0607-085 during the period covered by the CARMA observations. Both in the case that the QSO flux was slowly fading during the week of observations (with a light curve shown by the dotted line in the plot, which represents a linear fit of the data), and in the case that the QSO had a constant 2.9 mm flux density (equal to the weighted mean of the measured fluxes), the repeatability of our flux measurements is within the adopted 15%-level. 15% is therefore a conservative estimate since part of the scatter may be due to intrinsic variability of the QSO on 1-day timescale.

Maps of the dust continuum emission were obtained by standard Fourier inversion adopting natural weighting, and photometry was obtained in the image plane. The resulting FWHM of the synthesized beam is about 2 arcsec.

One of our disks, 216-0939, was also observed with the Australia Telescope Compact Array (ATCA) and the new CABB digital filter bank, which provides a total continuum bandwidth of 2 GHz. Observations were carried out at a central frequency of 91.000 GHz (3.294 mm) on 2009 Oct 13, and of 44.000 GHz (6.813 mm) on 2009 Oct 14. The ATCA array was in the hybrid H168 configuration, providing an angular resolution of about 3 arcsec at 3.3 mm and 6.3 arcsec at 6.8 mm.

The gain was calibrated with frequent observations of 0529+075. The passband was calibrated using 1921-293, and the absolute flux scale was determined through observations of Uranus. The uncertainty on the calibrated flux is about 30% at 3.3 mm and 20% at 6.8 mm. The MIRIAD package was used for visibilities calibration, Fourier inversion, deconvolution and imaging.

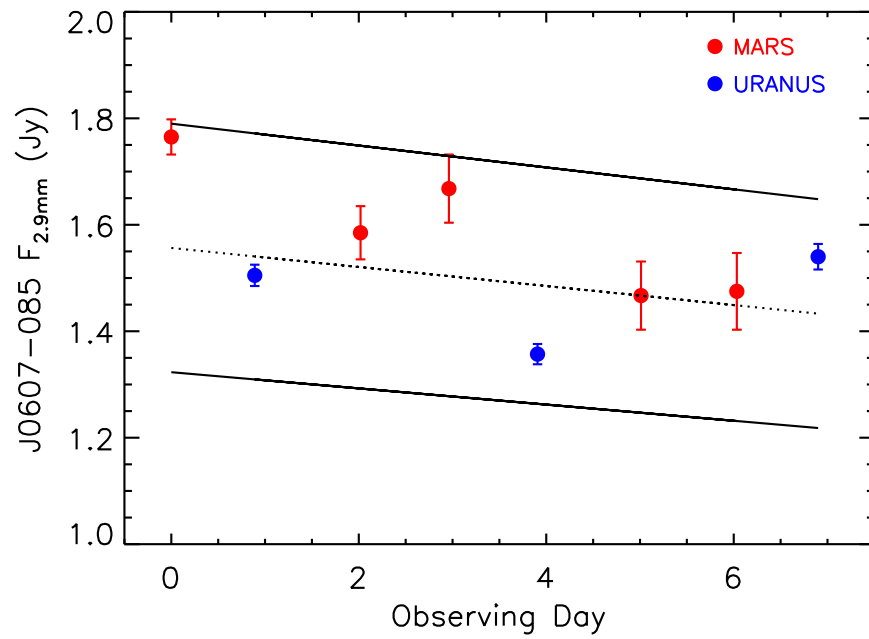


Figure 5.2: Flux density at 2.9 mm versus observing day for the QSO J0609-085 used as the phase and amplitude calibrator during the CARMA observations. Red circles represent fluxes obtained using Mars as the flux calibrator, whereas blue circles have been obtained using Uranus. The dotted line represents a linear fit of the data, and the two continuous lines refer to the $\pm 15\%$ -levels from the linear fit.

Table 5.1: Sub-Millimeter and Millimeter Flux Densities and Disk Sizes

Object	$F_{0.88\text{mm}}$ (mJy)	$F_{2.9\text{mm}}$ (mJy)	$F_{3.3\text{mm}}$ (mJy)	$F_{6.8\text{mm}}$ (mJy)	α	SMA Size (arcsec)	HST Size (arcsec)	$\kappa_{2.9\text{mm}}^{q=2.5}$ (cm^2g^{-1})	$M_{\text{disk}}^{q=2.5}$ (M_{\odot})
(1)	(2)	(3)	(4)	(5)	(6)	(7)	(8)	(9)	(10)
121-1925	15.0±1.5	2.4±0.4	1.5±0.4	Unresolved	0.8	0.003	0.1
132-1832	16.5±1.7	<2.7	>1.5	1.1±0.4	1.3
136-1955	77.6±1.2	1.8±0.4	3.2±0.5	0.5±0.1	...	0.02	0.006
141-1952	30.6±1.2	1.9±0.4	2.3±0.5	0.4±0.1	0.7	0.02	0.003
181-825	54.8±1.0	4.4±0.5	2.1±0.4	Unresolved	0.7	0.01	0.05
216-0939	91.9±1.3	3.5±0.6	2.5±0.3	0.34±0.05	2.7±0.2	1.6±0.1	2.6	0.04	0.02
253-1536 ^a	134.2±1.0	7.9±0.7	2.6±0.4	1.5±0.1	1.5	0.04	0.05
280-1720	21.8±0.7	<1.8	>2.1	Unresolved	0.8

1) Object name. 2) 0.88 mm-flux density (from Mann & Williams 2010, in press). 3) 2.9 mm-flux density. 4) 3.3 mm-flux density. 5) 6.8 mm-flux density. 6) Sub-mm/mm spectral index derived by fitting with a power-law the data shown in the table. The errors account for the uncertainty on the flux scale at each waveband. 7) FWHM along the disk major axis from a gaussian fit in the SMA images. 8) Disk diameter from HST images (Smith et al., 2005; Ricci et al., 2008). 9) 2.9 mm-dust opacity derived by the SED-fitting procedure (and the adopted dust model) assuming $q = 2.5$. 10) Disk mass derived by the SED-fitting procedure assuming $q = 2.5$ (see Sect. 5.3.3). a) The SMA observations of 253-1536 show a weaker secondary component ($F_{0.88\text{mm}} = 37.6 \pm 1.0$ mJy). The spectral index of this system has been calculated by using for $F_{0.88\text{mm}}$ the sum of the SMA fluxes separately measured for the two circumstellar disks. For this reason the derived spectral index and disk mass are descriptive of the whole system rather than of the two disks separately.

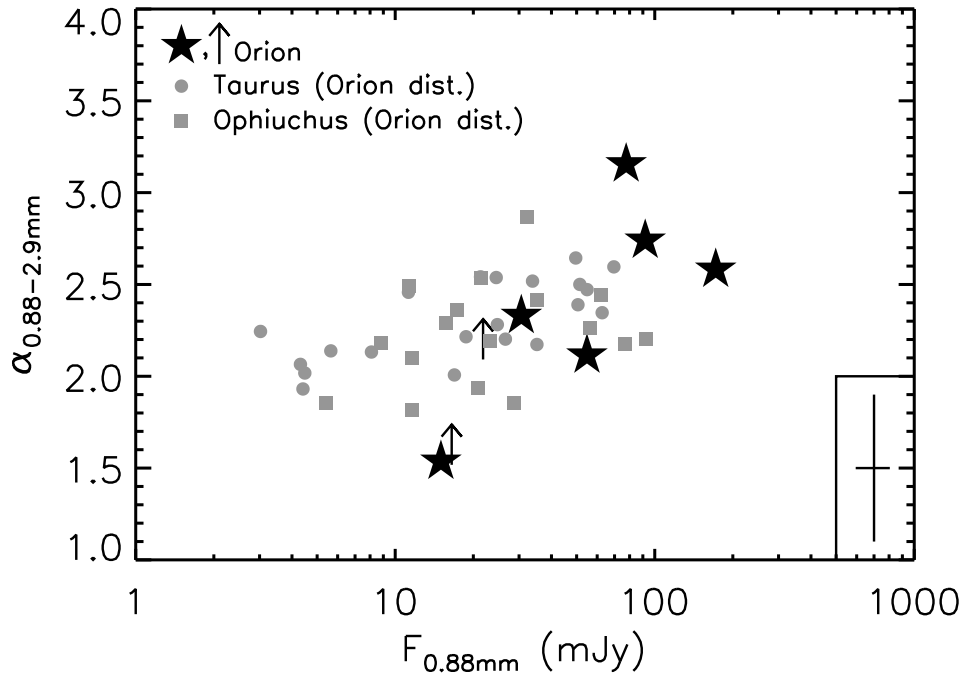


Figure 5.3: Spectral index between 0.88 and 2.9 mm plotted against the flux at 0.88 mm. Black stars and lower-limits are for the ONC disks, whereas grey circles and squares are for class II disks in Taurus (Ricci et al., 2010a) and Ophiuchus (Ricci et al., 2010b), respectively. The fluxes of the Taurus and Ophiuchus disks have been scaled to the ONC-distance adopted in this work (400 pc) to allow a comparison with the ONC disks. In the lower-right corner of the plot, the typical errorbars of the plotted quantities are shown.

5.3 Results

Table 6.1 reports the sub-mm/mm flux densities obtained for our sample of eight young circumstellar disks in the outskirts of the ONC. Column (6) lists the sub-mm/mm spectral index α ($F_\nu \sim \nu^\alpha$) as derived from the results of our observations. Whereas all the eight disks in our sample have been detected with the SMA at 0.88 mm (Mann & Williams, 2010), we detected six of them at 2.9 mm with CARMA. For the two undetected disks, 132-1832 and 280-1720, the upper-limits in the 2.9 mm-flux density translate into lower-limits for the sub-mm/mm spectral index. The range in sub-mm/mm spectral index spanned by our sample, i.e. ~ 1.5 -3.2, is very close to what observed for class II YSOs in low-mass SFRs (see Figure 5.3). This indicates that the properties of dust grains for disks in the outskirts of the ONC are very similar to those found in disks in low-mass SFRs. Furthermore we did not find any clear trend between spectral index α , HST size, disk mass, or distance from θ^1 Ori C.

5.3.1 Grain Growth

Information on the grain-size distribution of dust in the outer regions of protoplanetary disks can be obtained by analyzing the disk SED at sub-mm/mm wavelengths (e.g. Draine, 2006)). More specifically, for a disk whose sub/mm-mm flux is entirely due to optically thin dust emission in the Rayleigh-Jeans regime, a very simple relation between the measurable spectral index α of the sub-mm/mm SED and the spectral index β of the dust opacity¹ holds, namely $\beta = \alpha - 2$.

Values of β lower than the value found for the unprocessed ISM dust population ($\beta_{\text{ISM}} \sim 1.7-2$) can be obtained only with dust population where grains as large as at least ~ 1 mm are present (see e.g. Natta et al., 2007). Deviations from the aforementioned relation between α and β can be accounted for by using physical disk models to fit the disk SED together with the knowledge of the spatial extension of the disk, which is needed to estimate the impact of the inner optically thick regions on the long-wave spectrum (see Testi et al., 2001)). By doing this for 38 class II disks around low-mass PMS stars in the Taurus-Auriga and Ophiuchus SFRs, Ricci et al. (2010a,b) found $\alpha - \beta = 1.8 \pm 0.1$. All disks in our sample have outer radii larger than ~ 100 AU (Table 6.1, col. 7 and 8), all the model fits have only a minimal contribution from optically thick emission (see discussion in Ricci et al., 2010a). Applying the α - β relation to the Orion disks, we obtain values for the dust opacity spectral index β ranging between about 0 for 121-1925 and 1.4 for 136-1955. Apart for the case of 136-1955 whose 1σ -interval of β is consistent with β_{ISM} , for all the other five disks detected with CARMA the constrained β -values are significantly lower than β_{ISM} , and thus we found firm evidence of grain growth to \sim mm-sized pebbles for the first time in the ONC, and, more generally, in the cluster environment of a high-mass SFR.

Note that, to derive the results described so far, we assumed that all the measured sub-mm/mm flux comes from dust emission only. At mm-wavelengths some contribution to the measured flux from ionized gas has been found in the literature. This contribution can be constrained from observations at longer cm-wavelengths, where free-free emission from ionized gas dominates over the dust emission. For disks in low-mass SFRs the presence of ionized gas is probably induced by the ionizing flux from the central star, and it has been found to contribute typically for 25% or less at 7 mm and a few percent at most at 3 mm (?Rodmann et al., 2006; Lommen et al., 2009). For disks in the inner ONC at angular separations lower than about 1 arcmin from the main ionizing source of the entire region, θ^1 Ori C (projected separations lower than about 0.1 pc), free-free emission has been typically found to dominate the emission at wavelengths close to 3 mm and longer (Wilner et al., 2005; Eisner et al., 2008; Mann & Williams, 2009b). In order to get accurate estimates for dust grain growth from multi-wavelengths observations in the millimeter, it is important to consider disks which are further away from θ^1 Ori C, for which the free-free emission does not swamp the mm-wave emission from dust. Our sample is made of sources which are at projected distances between about 0.4 and 1.5 pc. Since our disks are much further away in terms of projected distance to θ^1 Ori C than the disks observed in the literature, in the rest of the paper we will assume that no contribution from free-free emission is present for

¹At long wavelengths the dust opacity law is well represented by a power law $\kappa_\nu \propto \nu^\beta$.

the disks in our sample. This is supported by the fact that the derived spectral slope α for our sources do not correlate with the projected distance to θ^1 Ori C, as one may expect if significant contamination from free-free emission was present in our data. Furthermore, in the case of 216-0939 for which new data at 3 mm and 7 mm have been obtained, the sub-mm/mm SED does not show any change of the spectral slope (Figure 5.4), as it would be expected if free-free emission was significant at these wavelengths (see e.g. Wilner et al., 2005). However, future observations at longer cm-wavelengths are needed to really constrain the impact of free-free emission and test this assumption.

5.3.2 The case of 216-0939

Figure 5.4 shows the fit of the sub-mm/mm SED of 216-0939, which is the best characterized disk in our sample, with two-layer (surface+midplane) models of flared disks heated by the radiation of the central star (Chiang & Goldreich, 1997; Dullemond et al., 2001). For the stellar parameters we considered a PMS star with a K5-spectral type (from Hillenbrand, 1997), which we converted into an effective temperature of 4350 K using the temperature scale of Schmidt-Kaler (1982). We then derived a stellar mass of about $1.2 M_{\odot}$ and a stellar luminosity of $2.5 L_{\odot}$ by placing the PMS star onto a 1 Myr-isochrone from the Palla & Stahler (1999) PMS evolutionary models. For the disk we adopted a truncated power-law mass surface density with an exponent of 1 (as found by ?, from disks in Taurus and Ophiuchus) and an outer radius of about 290 AU from the size of the mm-emission in the SMA map (Table 6.1). A disk inclination of 75° has been taken from an analysis of optical HST images (Smith et al., 2005). From the SED-fitting procedure (Fig. 5.4) we derived $\beta = 1.0 \pm 0.3$, which is indicative of grain growth in the 216-0939 disk.

By using the same dust model discussed in Ricci et al. (2010a,b), i.e. spherical porous grains made of silicates, carbonaceous materials and water ice (abundance of each species from Semenov et al., 2003), we could get information on the grain-size distribution, here assumed to be a truncated power-law with index q and maximum grain size a_{\max} . A good fit of the SED could be obtained only for $q \lesssim 3.5$. Grain-size distributions with q -values of 3 and 2.5 fit equally well the sub-mm/mm SED but with different a_{\max} -values, namely about 2.5 and 2 mm, respectively, but here it is important to note that the precise estimate for the maximum grain size a_{\max} can strongly depend on the adopted dust model.

5.3.3 Derived disk masses

Other than providing information on the grain-size distribution, the SED-fitting procedure described in the last section returns estimates for the dust mass in the disk, and, by assuming the ISM-value of about 100 for the gas-to-dust mass ratio, for the total disk mass. Column (9) in Table 6.1 reports the derived disk masses for the six disks detected at millimeter wavelengths, for which information on the dust properties could be inferred. For these estimates we considered a q -value of 2.5 because for the two disks showing the lowest mm-spectral indices, 121-1925 and 181-825, models with $q \gtrsim 3$ cannot reproduce the data. This shows that the grain size distribution in these disks is shallower than found

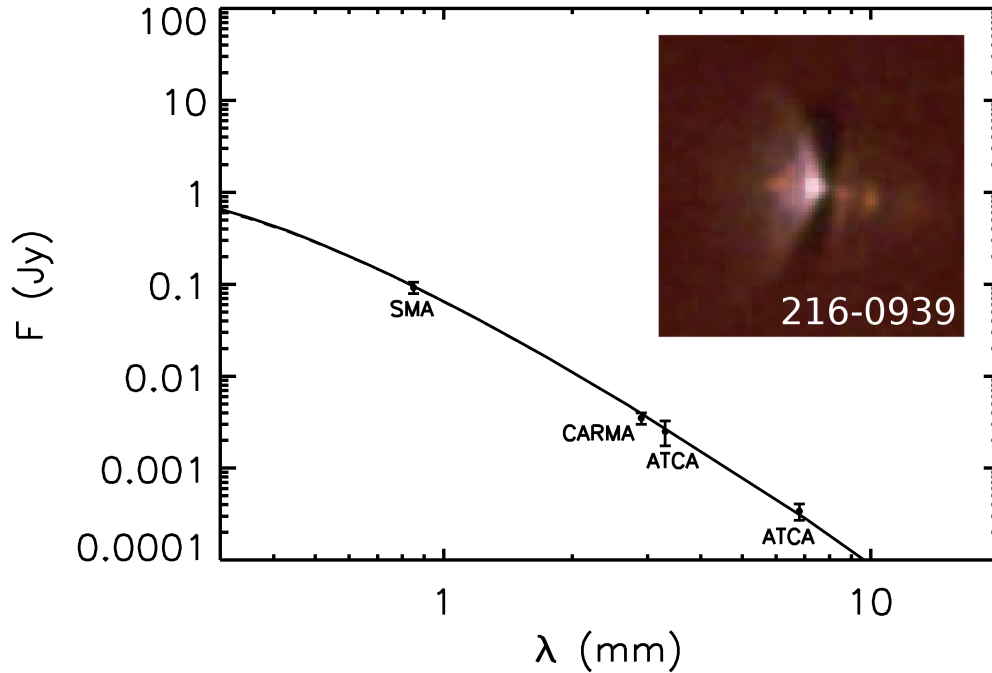


Figure 5.4: Fit of the sub-mm/mm SED of the 216-0939 Orion disk with a two-layer passive flared disk model. The parameters of the model shown here are described in Sect. 5.3.2. The uncertainties in the data points account for the uncertainty on the flux-scale. The color image of the 216-0939 disk is from HST observations by Smith et al. (2005).

for the ISM ($q_{\text{ISM}} \approx 3.5$, Mathis et al., 1977). This result, which, as described in Ricci et al. (2010a) does not depend on the adopted dust model, is another indicator for dust processing in these disks.

The range in disk mass covered by our sample is $0.003\text{--}0.1 M_{\odot}$. This shows that massive disks are present in the outer regions of the ONC, confirming recent results by Mann & Williams (2009a). Note that 121-1925 is the faintest disk at 0.88 mm but is nevertheless detected at 0.88 mm. We thus derive a very low value for α . In our analysis, this implies a very low value for β , and a very significant inferred grain growth, suggesting a very low value for the dust opacity coefficient at 2.9 mm (see col. 9 in Table 6.1), and consequently a large disk mass.

5.4 Summary

We present new millimeter interferometric observations of eight disks in the outskirts of the ONC. Together with sub-mm data in the literature, these new data allow us to study dust properties, like grain growth and disk mass, from the entire sub-mm/mm SED. Except for one disk, 136-1955, whose emission is consistent within the errorbars with a ISM-like dust

population, we found evidence, for the first time in cluster environment in a high-mass SFR, of grain growth to at least mm-sized pebbles for 5 out of the 6 detected disks at mm-wavelengths. As for the disk masses, estimated by using a dust model which accounts for grain growth in the calculation of the dust opacities, our results confirm that massive disks ($M \geq 0.05 M_{\odot}$) can be found in the outskirts of the ONC.

The mm-colors of a young binary disk system in the Orion Nebula Cluster

From Ricci, Testi, Williams, Mann, & Birnstiel, accepted for publication in the ApJ Letters Special Issue on the first EVLA results

Abstract

We present new EVLA continuum observations at 7 mm of the 253-1536 binary disk system in the Orion Nebula Cluster. The measured fluxes were combined with data in the sub-mm to derive the millimeter spectral index of each individual disk component. We show how these observations can be used to test the models of dust evolution and early growth of solids in protoplanetary disks. Our analysis indicates that the disk with lower density and higher temperature hosts larger grains than the companion disk. This result is the opposite of what predicted by the dust evolution models. The models and observational results can be reconciled if the viscosity α -parameter differs by more than a factor of ten in the two disks, or if the distribution of solids in the disks is strongly affected by radial motions. This analysis can be applied to future high-angular resolution observations of young disks with EVLA and ALMA to provide even stronger observational constraints to the models of dust evolution in protoplanetary disks.

6.1 Introduction

Young circumstellar disks around pre-Main Sequence (PMS) stars are thought to host the birth of planets. According to the core accretion scenario, the formation of planets involves a variety of physical mechanisms from the coagulation of sub- μm sized particles up to the gas-accretion phase leading to the build up of gas giants. One of the most critical steps which is left to be explained is how this growth of solids proceeds from mm/cm-sized dust grains to km-sized rocks, called planetesimals. This is crucial because it is

from the gravitational-driven collision of these planetesimals that both the rocky Earth-like planets and the rocky cores of giant planets are ultimately supposed to be formed. Different mechanisms have been proposed in the literature to explain the formation of planetesimals. In general, these mechanisms induce the local accumulation of particles with sizes of $\sim 1 - 100$ mm at densities which are high enough to make these clumps unstable to gravitational collapse (Chiang & Youdin, 2010). It is therefore very important to well characterize the early phases of coagulation of small dust grains in order to set the right initial conditions for the mechanisms governing the formation of planetesimals.

Recently, sophisticated models of dust evolution in disks including several effects like dust coagulation, fragmentation and radial motions, have been built (Birnstiel et al., 2010a). Continuum observations in the (sub-)millimeter constrain fundamental parameters of the dust population in the disk, e.g. the total dust mass, the radial-dependent dust surface density, and the size distribution of dust grains at sizes of about $\sim 0.1 - 10$ mm (see Williams & Cieza, 2011). These observational constraints can be used to test the models of dust evolution and shed light onto the first stages of planetesimal formation (Birnstiel et al., 2010b).

The recent initial upgrades of the Very Large Array into the Expanded Very Large Array (EVLA; Perley et al., 2011) allowed a significant increase in continuum sensitivity at long wavelengths. We present new EVLA observations at about 7 mm of the 253-1536 binary system in the Orion Nebula Cluster (Fig. 6.1). The projected angular separation of the two PMS stars is about $1.1''$ which corresponds to a projected physical separation of 460 AU at the ONC distance of ~ 420 pc (Kraus et al., 2009). Optical images with the Hubble Space Telescope (HST) has revealed the presence of a large disk seen in absorption around the east companion, 253-1536a. Mann & Williams (2009a) observed the binary at 0.88 mm with the Sub-Millimeter Array (SMA) and estimated for the 253-1536a disk a mass of about $0.07 M_{\odot}$ which makes this disk the most massive ever observed in the ONC. They also detected a fainter disk around the other PMS star, 253-1536b, and found a ratio for the two disk masses of about 4.

6.2 Observations

6.2.1 EVLA

We obtained new EVLA data under the project 10B-102, with a total observing time of 6 hours. At the time of observations the EVLA was in the C configuration, and provided a total bandwidth of 256 MHz, that we centered at the frequency of 43.280 GHz (6.9 mm) in the Q-band.

Passband and absolute flux calibration was performed through observations of the QSO 3C147 (J0542+4951). Amplitude and phase calibration was obtained by observing the QSO J0607-0834. The measured 6.9 mm-flux density of J0607-0834 range from about 1.9 Jy to 2.1 Jy during the three observing runs, thus showing a discrepancy in the fluxes which is within the $\sim 10\%$ -uncertainty on the absolute flux, as typically estimated for EVLA

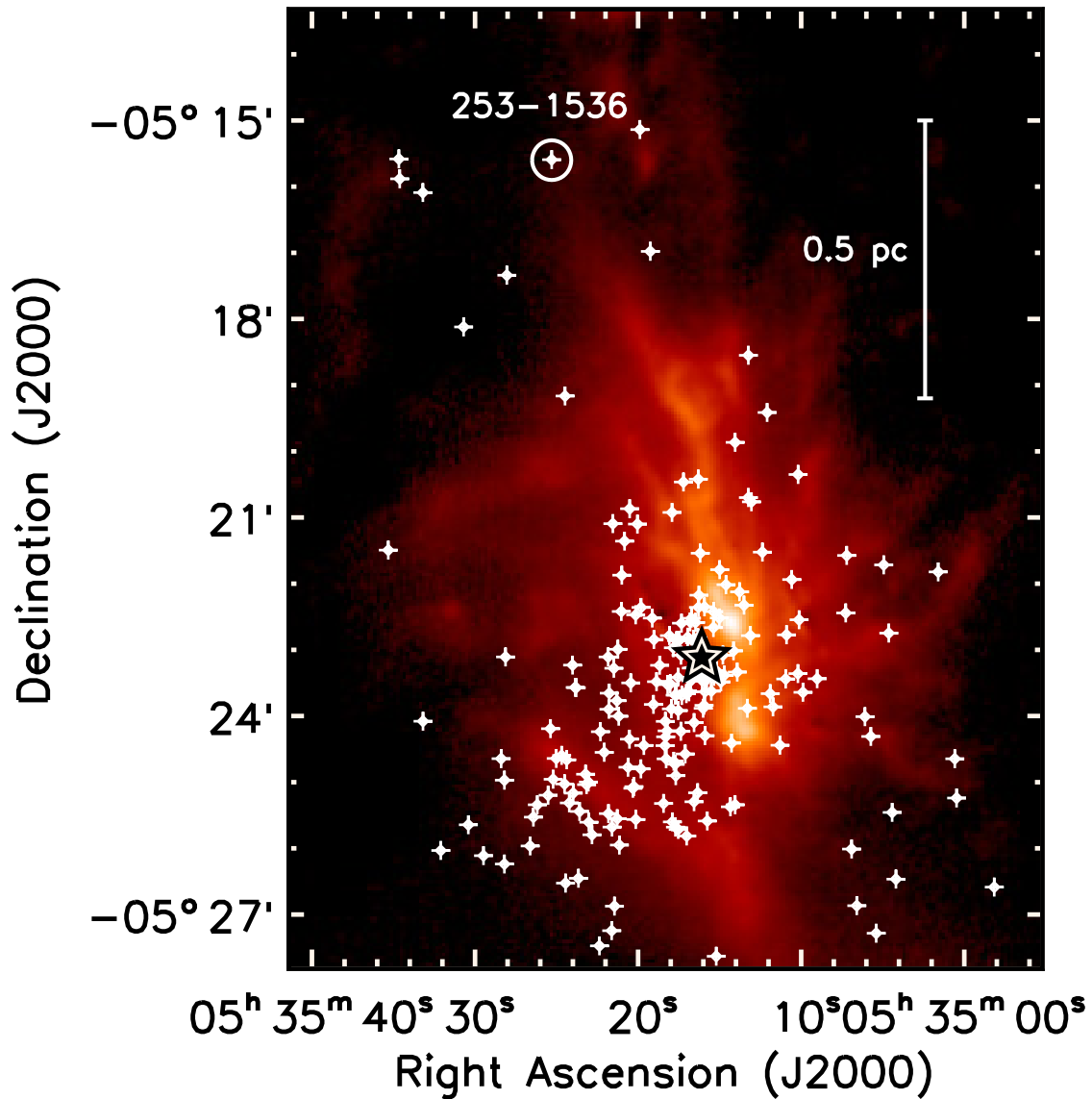


Figure 6.1: ONC map at 450 μm with SCUBA/JCMT (Johnstone & Bally, 1999). White crosses indicate the HST-identified proplyds, whereas the star marks the location of θ^1 Ori C. The location of the 253-1536 binary system is shown.

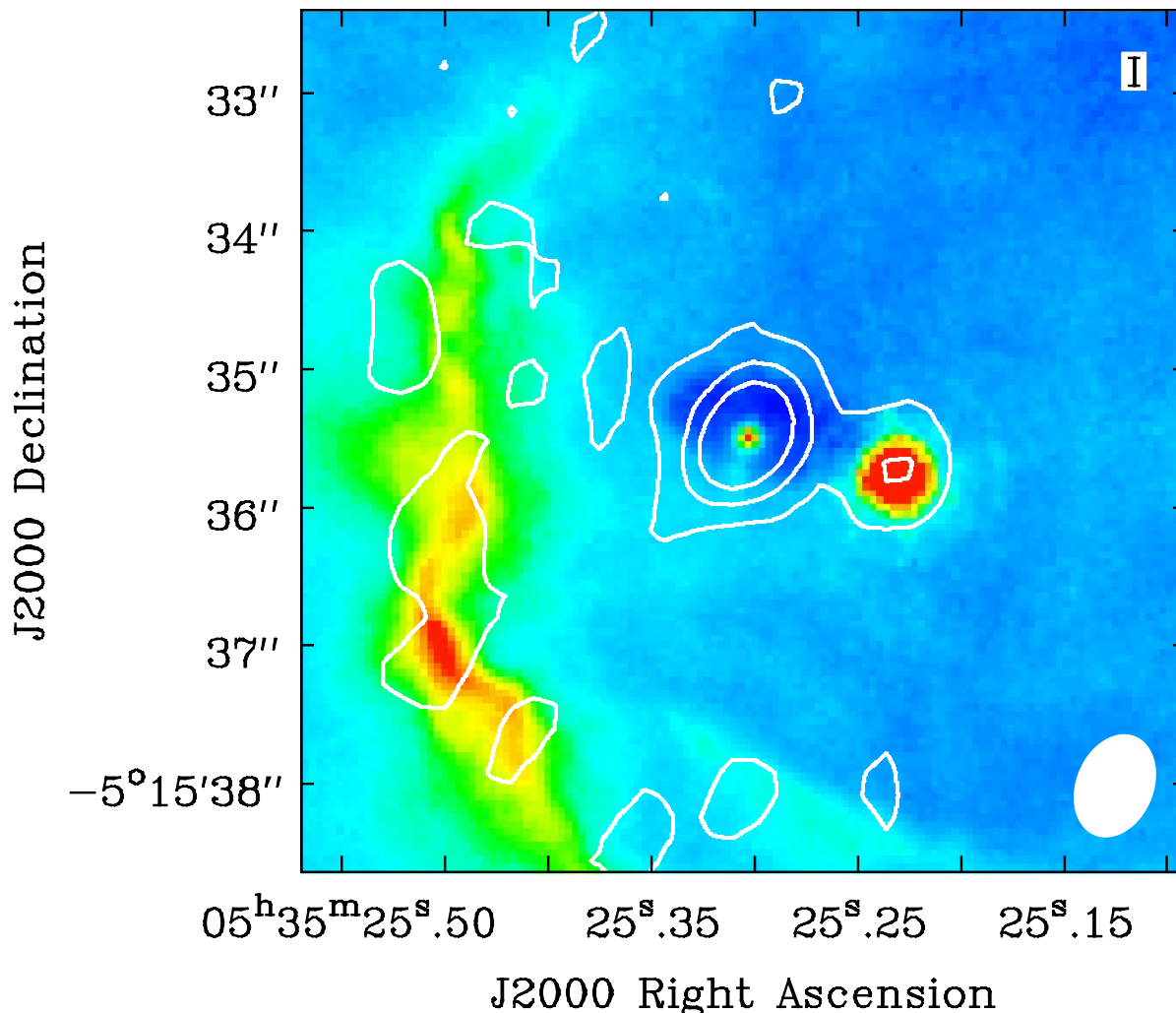


Figure 6.2: Map of the 253-1536 binary system. In color the HST image in the $H\alpha$ F658N filter (Ricci et al., 2008), whereas white contours represent the EVLA continuum data at 6.9 mm. Contour lines are drawn at $3, 6$ and 9σ , where $\sigma = 0.035$ mJy/beam. The white ellipse in the lower right corner indicates the size of the EVLA synthesized beam.

observations in the Q-band.

The raw visibilities were calibrated using the Common Astronomy Software Applications (*CASA*) package. Maps of the continuum emission were derived by adopting natural weighting to maximize the observations sensitivity, and photometry was obtained through Gaussian fitting in the image plane using the *imfit* task in *CASA*. The resulting synthesized beam has sizes of about $0.77'' \times 0.55''$. The measured rms-noise of the final map is about $35 \mu\text{Jy}$.

6.2.2 X-Shooter

We observed 253-1536 with XShooter at the ESO-VLT on September 27, 2010. We obtained complete spectra from 330 through 2500 nm at a spectral resolution in the range 5000-9000. We aligned the $\sim 11 \times 1.0$ arcsec slit along the binary position angle to observe the two components simultaneously. We performed an on-slit dithering pattern with 8 exposures of 190s each, to avoid saturation on the brightest component and to efficiently remove sky emission, bad pixels and cosmic ray hits. We reduced the data using the standard XShooter pipeline recipes, and IRAF for extraction of the 1D spectra and subsequent analysis. We used spectra of LTT 1020 and Hip 025028 (B3V) to correct for instrumental response and telluric absorption. The spectrum of the bright component is detected with very high signal-to-noise across the whole spectral range, while the faint component of the binary system is only detected at K and H bands and cannot be easily separated from the glow of the other component at shorter wavelengths.

We detect numerous absorption and emission features in the two spectra. Nevertheless, for the purpose of this Letter we just analysed the spectra to attempt a spectral classification of the two components of the binary. We compared our spectra with those from the spectral libraries of Allen & Strom (1995) and Wallace & Hinkle (1997). We find that the bright stellar component of the binary, i.e. 253-1536b, is consistent with previous classification as an M2 star both based on the optical and near infrared spectrum. The faint component, 253-1536a, does not show prominent absorption lines. In particular, it is lacking CO, Fe, Al and Ca features that are commonly observed in K-band spectra of late type dwarfs. Overall the spectrum seems to be consistent with heavily veiled and extincted late F and G types. In this paper we will consider a spectral type of G2 for the 253-1536a PMS star.

6.3 Results

The contours in Figure 6.2 show the EVLA map at 6.9 mm superimposed to the HST image in H α . Both the disks are clearly detected at 6.9 mm, and the measured fluxes are listed in Table 6.1, together with the ones measured with the SMA array at 0.88 mm (?). Continuum observations of young circumstellar disks in the sub-mm probe the emission from dust particles. At longer millimeter wavelengths the dust emission can be contaminated by ionized gas, with ionization driven by X-ray/UV-radiation generated either by nearby young massive stars, e.g. in the Trapezium Cluster (Wilner et al., 2005), or by the PMS star at the center of the disk, as seen for disks in low mass SFRs (Rodmann et al., 2006).

In the case of the 253-1536 system, the distance to the θ^1 Ori C massive star, i.e. ~ 1 pc in projection (see Fig. 6.1), is too large to make the gas in the disks being significantly ionized by the θ^1 Ori C UV-radiation. This is indicated by the lack, in these ONC peripheral regions, of photoevaporating proplyds with bright ionization cusps pointing toward the direction of θ^1 Ori C in the HST images (Ricci et al., 2008). At the same time, a bright rim of ionized gas is visible in both the HST and EVLA maps on the east side of the binary

Table 6.1: Disk fluxes and spectral indices.

Source	$F_{6.9\text{mm}}$ (mJy)	$\text{rms}_{6.9\text{mm}}$ (mJy)	$F_{0.88\text{mm}}$ (mJy)	$\text{rms}_{0.88\text{mm}}$ (mJy)	$\alpha_{0.88-6.9\text{mm}}$
253-1536a	1.10	0.035	135.0	1.0	2.34 ± 0.16
253-1536b	0.34	0.035	38.4	1.0	2.30 ± 0.19

Column 6: Spectral index between 0.88 and 6.9 mm; reported errors take into account a 10 %-uncertainty on the absolute flux scale at both 0.88 and 6.9 mm.

system (Fig. 6.2). The star which is causing this feature is probably NU Orionis, an early B-type star located toward the direction of the bright rim, which is also responsible for the excitation of the M43 HII region (Smith et al., 2005).

To evaluate the relative impact of dust and ionized gas emission at a given frequency, the slope of the SED can be used: dust thermal emission presents a steep spectrum, with values of the spectral index α_{mm} ($F_\nu \propto \nu^\alpha$) between about 2 and 3, whereas the ionized gas emission is characterized by a much more shallow dependence on frequency, e.g. $\alpha \lesssim 1$ for a symmetric, ionized, optically thick wind (Panagia & Felli, 1975), and $\alpha \lesssim 0$ for optically thin emission (Mezger et al., 1967). For the 253-1536 system, Ricci et al. (2011) measured a spectral index of 2.6 ± 0.4 between 0.88 and 2.9 mm. Since the observations at 2.9 mm did not spatially resolve the binary system, this value is descriptive of the whole system rather than of the two disks separately. By adding up the 6.9 mm-flux densities for the two disks, the spectral index of the whole system is 2.0 ± 0.5 between 2.9 and 6.9 mm and 2.3 ± 0.2 between 0.88 and 6.9 mm. Both the measured absolute values of the spectral indices, and the fact that no statistically-significant changes are seen in the slope of the spectrum between 0.88 and 6.9 mm suggest that the dust dominates the total sub-mm/mm emission. This is consistent with what found also for 216-0939, another HST-identified disk in the northern outskirts of the ONC (Ricci et al., 2011). In the following we will therefore assume that the measured sub-mm/mm fluxes are only due to thermal emission from dust particles in the disks.

6.4 Discussion

6.4.1 Comparison of grain growth in the two disks

Since the dust emission of disks at these long wavelengths is mostly optically thin, the spectral index α of the (sub-)mm SED is a proxy for the spectral index β of the dust opacity coefficient ($\kappa_\nu \propto \nu^\beta$), which in turn carries the information on grain growth in the disk. For example, in the Rayleigh-Jeans regime for a completely optically thin emission, $\beta = \alpha - 2$. However, since the hypotheses of completely optically thin emission in the Rayleigh-Jeans regime are not always realized even at these long wavelengths, modelling of the disk emission is required.

We modelled the measured disk sub-mm SED of the 253-1536 binary system by using a modified version of the two-layer passively irradiated disk models (Chiang & Goldreich, 1997; Dullemond et al., 2001), as described in Ricci et al. (2010a,b). The effective temperature of the two stellar companions were derived by converting the spectral types adopted in Section 6.2.2 with the temperature scale of Luhman et al. (2003). By using the Palla & Stahler (1999) PMS evolutionary tracks and new multi-band optical photometry and spectroscopy, Da Rio et al. (2010) recently derived a new estimate for the ONC mean age of about 2 Myr. With these same PMS evolutionary tracks and age, the values for the stellar masses and luminosities are about $2 M_{\odot}$, $12 L_{\odot}$ for 253-1536a and about $0.3 M_{\odot}$, $0.2 L_{\odot}$ for 253-1536b, respectively.

The angular resolutions of the EVLA and SMA observations do not allow us to properly constrain the radial profile of the dust surface density in the two disks. For this reason, we consider in this analysis disks with truncated power-law surface densities ($\Sigma_{\text{dust}} \propto r^{-p}$ for $r < R_{\text{out}}$ and $\Sigma_{\text{dust}} = 0$ for $r > R_{\text{out}}$) with possible p -values between 0 and 1.5, as obtained through high-angular resolution sub-mm imaging of disks in nearby SFRs (Andrews & Williams, 2007b). As for the disk outer radius R_{out} , the HST and SMA observations constrained a value of $R_{\text{out}} \approx 280$ AU for the 253-1536a disk and derived an upper limit of 60 AU for the unresolved 253-1536b disk. Since the R_{out} of the 253-1536b disk is not determined by the observations, in the following analysis we will consider two different possibilities, namely $R_{\text{out}} = 40$ and 60 AU. Smaller disks with $R_{\text{out}} \lesssim 30$ AU always fail to reproduce the measured (sub-)mm fluxes of 253-1536b. This is due to the fact that the emission of such small and dense disks becomes optically thick and, as a consequence, underestimates the relatively large (sub-)mm fluxes of 253-1536b (Testi et al., 2001). Note that these possible values for the outer radius of the 253-1536b disk are all significantly lower than the estimated radius of the Roche lobe, i.e. $\gtrsim 100$ AU (from Paczyński, 1971, using our estimates for the stellar masses, and the projected physical separation as a lower limit for the binary semi-major axis). This means that the material in the disk lies well inside the stable zone in the Roche lobe.

Another important parameter is the disk inclination, defined as the angle between the disk axis and the line-of-sight. By taking the ratio of the two projected disk axes in the HST images, we estimated an inclination $i \sim 55^{\circ}$ for the 253-1536a disk. This procedure cannot be applied to the smaller 253-1536b disk, which has not been detected by HST. The X-Shooter spectra show that the 253-1536b star is significantly less extinguished than its stellar companion. This indicates that the 253-1536b disk is likely less inclined than the companion. For this disk we considered a range of possible inclinations between 0° and 50° .

With the parameters outlined above we determined the spectral index β of the dust opacity coefficient by fitting the long-wave SED with the two-layer disk models (see Ricci et al., 2010a). Table 6.2 shows the constrained β -values for the possible different R_{out} and i for the 253-1536b disk, and in the $p = 1$ case. The difference between the estimated β -values for the 253-1536b disk is given by the different contribution of the inner optically thick regions to the total emission. The decrease of R_{out} , or the increase of i , which increases the line-of-sight optical depth of the disk, makes this contribution more important. As

Table 6.2: Derived parameters for the two disks in the 253-1536 binary system.

Disk parameters in the $p = 1$ case.

Source	R_{out} (AU)	i ($^{\circ}$)	β	$\Sigma_{\text{gas,outer}}$ (g/cm^2)	$T_{\text{dust,outer}}$ (K)
253-1536a	280	55	0.5 ± 0.2	1.5 – 4	18 – 29
253-1536b	40	0	1.0 ± 0.2	30 – 60	18 – 25
	40	30	1.4 ± 0.2	50 – 100	18 – 25
	40	50
	60	0	0.7 ± 0.2	10 – 20	15 – 20
	60	30	0.8 ± 0.2	11 – 22	15 – 20
	60	50	0.9 ± 0.2	12 – 24	15 – 20

Columns 5,6: ranges of gas surface densities and dust temperatures constrained in the disk outer regions (Section 8.3). These values have been obtained by adopting the dust model described in Ricci et al. (2010a). However, note that for our analysis, only the ratio of the surface densities and dust temperatures in the two disks is relevant. A model with $R_{\text{out}} = 40$ AU and $i = 50^{\circ}$ cannot reproduce the observed fluxes for 253-1536b.

a consequence, β becomes larger, i.e. the spectrum of the dust emissivity steepens, to compensate for the opposite effect given by optically thick emission. To better quantify the value of β for the 253-1536b disk, high-angular resolution imaging is needed to directly constrain its outer radius, and therefore the impact of the optically thick inner regions to its total emission. The important point to be noticed here is that for all the possible values of the disk parameters (this result is unchanged for possible other p -values between 0 and 1.5), the β -value constrained for 253-1536b is larger than for 253-1536a.

The β -index carries information on the size a_{max} of the largest grains in the dust population of the outer disk (e.g. Natta et al., 2007). β -values lower than about 1 – 1.5 can only be explained with the presence of grains as large as at least 0.1 – 1 mm. Converting an estimate for β into one for a_{max} is particularly difficult because of our ignorance on the physical/chemical properties of the probed dust. However, for all the dust models considered in the literature, a general anticorrelation between β and a_{max} is generally obtained for $\beta \lesssim 1.5$. Under the assumption that the chemistry/shape of the dust grains in the two disks is the same and considering that the dust evolution models in disks with the constrained physical properties predict a slope q which is nearly identical (Birnstiel et al., 2011), this means that the observational data indicate that the 253-1536a disk, with a lower β , contains larger grains in its outer regions than 253-1536b. By considering the same dust model adopted in Ricci et al. (2010a,b, 2011), and varying the assumed q -value between 2 and 3 (see Ricci et al., 2010a), the inferred a_{max} in the 253-1536a disk is larger than in the companion disk by factors of about 2 – 10, depending on the values for R_{out} and i for the 253-1536b disk.

6.4.2 Testing the models of dust evolution

Recent physical models of dust evolution which include coagulation and fragmentation of dust grains predict a local relation

$$a_{\max} = \frac{\Sigma_{\text{gas}}}{\pi \alpha_{\text{visc}}} \frac{u_f^2}{c_s^2 \rho_s}, \quad (6.1)$$

between the maximum grain size allowed by fragmentation, the gas surface density Σ_{gas} , the viscosity α_{visc} -parameter (Shakura & Sunyaev, 1973), the thermal speed c_s , the critical velocity u_f above which two grains fragment after colliding, and the grain density ρ_s (see Birnstiel et al., 2010a,b).

By assuming that the chemical composition and shape of dust grains in the two disks of the binary system is the same, the highly uncertain term u_f^2/ρ_s in Eq. 6.1 cancels out when taking the ratio of a_{\max} in the two disks:

$$\frac{a_{\max,1}}{a_{\max,2}} \approx \frac{\Sigma_{\text{gas},1}}{\Sigma_{\text{gas},2}} \frac{c_{s,2}^2}{c_{s,1}^2} \frac{\alpha_{\text{visc},2}}{\alpha_{\text{visc},1}} \approx \frac{\Sigma_{\text{gas},1}}{\Sigma_{\text{gas},2}} \frac{T_{\text{dust},2}}{T_{\text{dust},1}} \frac{\alpha_{\text{visc},2}}{\alpha_{\text{visc},1}}, \quad (6.2)$$

where T_{dust} is the dust temperature in the disk midplane. This means that observational constraints on the ratio of a_{\max} in different disks allow to test models of dust evolution in disks without basing the whole analysis on parameters whose values are very uncertain.

Equations 6.1 and 6.2 are valid locally in the disk. However, as noted above, our observations do not have enough angular resolution to properly resolve the disk structure and directly constrain the radial dependence of quantities like e.g. the dust surface density. The estimates obtained above on the dust properties in the two disks are referred to the disk regions which dominate the emission at long wavelengths, i.e. the outer regions. We can therefore attempt a comparison between the predictions of the dust evolution models and our observational results in the disk “outer regions”, which have to be properly defined.

Since the two disks have very different outer radii, the spatial regions probed by their (sub-)mm SED are different. According to the two-layer disk models, more than 50% of the total sub-mm emission from 253-1536a comes from regions with stellocentric radii $r > 100$ AU, whereas for 253-1536b the same fraction of emission comes from $r > 20 - 30$ AU. As shown in Table 6.2 for the $p = 1$ case, in these regions the 253-1536b disk is denser than 253-1536a by a factor of about 10 – 30, and colder by a factor of about 1.2-1.4. By including these values in Eq. 6.2, and assuming the same α_{visc} -value in the two disks, it is evident that the models of dust evolution would predict significantly larger grains in the 253-1536b disk, which is contrary to what was derived in the last section. This result does not change even when considering other possible p -values for the power-law index of the disk surface density between 0 and 1.5.

To reconcile the prediction of the models of dust evolution with the ratios of a_{\max} reported in Section 6.4.1, the viscosity α_{visc} -parameter in the 253-1536b disk has to be larger than in the companion disk by more than a factor of 10. Physically, this is because to explain the smaller grains observed in the outer regions of the 253-1536b disk, the

turbulence velocity, which is roughly proportional to $\sqrt{\alpha_{\text{visc}}}$, has to be very high to increase the relative velocities between solid particles thus making fragmentation more efficient.

Although different α_{visc} -values could in principle be present in the two disks, magneto-rotational simulations of protoplanetary disks predict that larger values of α_{visc} are typically obtained in environments with lower densities (Gammie, 1996), which is the opposite of what requested by the dust evolution models to explain the observational results for the 253-1536 binary system. The fact that larger grains are seen in environments with lower densities probably suggests that radial motion of particles in the disks, a phenomenon which is not included when deriving this prediction, plays a fundamental role in the redistribution of solid particles in protoplanetary disks. This is also what Birnstiel et al. (2010b) suggested to reconcile the predictions of these same models with the measured sub-mm fluxes of isolated disks in Taurus and Ophiuchus SFRs.

High angular resolution and high sensitivity observations with ALMA and EVLA will allow us to test the dust evolution models locally in the disk, and possibly to probe viscosity with high spectral and spatial resolution observations of gas.

The effect of local optically thick regions in the long-wave emission of young circumstellar disks

From Ricci, Testi, Natta, Trotta, Isella, & Wilner, to be submitted to A&A

7.1 Introduction

Planets around solar-like stars are thought to originate from the material contained in a circumstellar “protoplanetary” disk. Observations of protoplanetary disks around pre-main sequence (PMS) stars at optical and infrared wavelengths have provided evidence for the presence of dust grains as large as at least a few μm in many of these systems. Since these grains are larger than the submicron-sized grains found in the interstellar medium (ISM), these observational results have been interpreted in terms of dust grain growth from an original ISM-like dust population in the disk. These are the first steps of the huge process of growth of solid particles which may potentially lead to the formation of planetesimals and then planetary bodies.

In order to investigate the presence of larger grains in the disk, observations at longer wavelengths are needed. Furthermore, since the dust opacity decreases as the wavelength increases, whereas infrared observations are sensitive to emission from the disk surface layers, observations in the millimeter probe the denser disk midplane, where the whole process of planetesimal formation is supposed to occur.

In the last two decades several authors measured relatively shallow slopes α of the Spectral Energy Distribution (SED; $F_\nu \sim \nu^\alpha$ with $\alpha \sim 2 - 3$) at sub-mm and mm wavelengths for class II young stellar objects (YSOs). Under the assumption of completely optically thin emission and if the emitting dust is warm enough to make the Rayleigh-Jeans approximation hold true at these wavelengths, the SED spectral index α is directly linked to the

spectral index β of the dust opacity coefficient κ_ν ¹ through $\beta = \alpha - 2$. In this way, the measured low values of α translate into values of $\beta \lesssim 1$ which are significantly lower than the value of $1.5 - 2$ associated to the ISM (Mathis et al., 1977). For all the reasonable models of dust analyzed so far the obtained values of β for class II disks can be interpreted only if grains have grown to sizes of at least a few millimeters (see e.g. Natta et al., 2007).

Another *a priori* possible scenario for the interpretation of the measured low values of the mm-spectral indices is that a significant fraction of emission at these wavelengths come from optically thick regions in the disk. In this case, the spectral index of the SED would reflect only the spectral index of the Planck function, which is 2 for emission in the Rayleigh-Jeans regime. This value is consistent with what measured for a large population of young circumstellar disks (e.g. Rodmann et al., 2006; Ricci et al., 2010a). Furthermore, in the last years several different physical processes with the potential of concentrating particles in disks have been proposed as possible triggering mechanisms for the formation of planetesimals (see Chiang & Youdin, 2010). These all lead to a local increase of the particles density in some regions of the disk. If this density gets high enough, these regions might become optically thick even at long wavelengths. Note that if this scenario was viable, the spectral index of the SED would not carry out the information on the grain sizes (through β) and so no constraints on that property could be derived from the observations.

Therefore it is important to investigate the potential effect of optically thick disk regions on the disk total emission at millimeter wavelengths. With this work we want to answer questions like: 1) could the observed low values of the (sub-)millimeter spectral indices of disks be explained by local concentrations of small, ISM-like particles *instead of* by the presence of mm/cm-sized pebbles? 2) if yes, which characteristics do they need to have? 3) are these local concentrations of small particles in disks physically plausible?

7.2 Sample

We describe here the sample of Class II YSOs that we will consider in the following analysis. This is made of the samples of low-mass YSOs uniformly selected in the Taurus, Ophiuchus and Orion Nebula SFRs by (Ricci et al., 2010a,b, 2011, respectively). These sources have been selected (1) by being low-mass Class II YSOs with no evidence of extended emission from a parental envelope, (2) by having known sub-mm/mm SED and stellar properties, (3) as well as no evidence of any stellar companion at spatial separations of about $10 - 500$ AU that would likely affect the structure of the disk outer regions, to which observations at sub-mm/mm wavelengths are most sensitive to. For a more detailed discussion on the properties of the selected samples we refer to the (Ricci et al., 2010a,b, 2011) papers.

In addition to these 46 sources, we consider here also the three low-mass Class II YSOs BP Tau, DQ Tau, V836 Tau for which we obtained new CARMA observations and satisfy the selection criteria described above, as detailed in the Appendix.

¹At these long wavelengths κ_ν is well approximated by a power-law.

7.3 Analysis

In this Section we present the method adopted to explore the impact of optically thick regions in the total emission of a disk at sub-mm/mm wavelengths. Section 7.3.1 describes the disk model used in our analysis and how the optically thick regions are included in the disk structure. Section 7.3.2 describes the main properties of the dust models used to derive the dust opacities.

7.3.1 Disk structure

We start by defining an “unperturbed” disk structure on the top of which we will add the contribution of optically thick disk regions to the total flux density of the disk. For a disk with midplane temperature $T_{\text{mid}}(r)$ and dust mass surface density $\Sigma(r)$ between an inner and outer radius R_{in} and R_{out} , respectively, the sub-mm/mm SED can be modelled as the sum of the contribution by infinitesimal annuli with radius r (in cylindrical coordinate system):

$$F_{\nu}^{\text{unp}} = \frac{\cos i}{d^2} \int_{R_{\text{in}}}^{R_{\text{out}}} B_{\nu}(T_{\text{mid}}(r)) (1 - e^{-\tau_{\nu}(r)}) 2\pi r dr, \quad (7.1)$$

where i is the disk inclination, i.e. the angle between the disk axis and the perpendicular to the plane of the sky², d is the distance of the disk from the observer, and B_{ν} is the Planck function. In Eq. 7.1 the optical depth $\tau_{\nu}(r)$ is defined as

$$\tau_{\nu}(r) = \frac{\kappa_{\nu} \Sigma_{\text{dust}}(r)}{\cos i}, \quad (7.2)$$

where κ_{ν} is the dust opacity coefficient³ given by the dust model described in Section 7.3.2, and $\Sigma_{\text{dust}}(r)$ is the dust surface density.

In this work we adopted a modified version of the two-layer models of passively irradiated flared disks developed by Dullemond et al. (2001) (following the schematization by Chiang & Goldreich, 1997) to derive the disk structure. In order for these models to calculate the temperature of the disk midplane, a surface density profile has to be given as input.

For the radial profile of the dust surface density we consider here the self-similar solution for a viscous disk (Lynden-Bell & Pringle, 1974):

$$\Sigma_{\text{dust}}(r) = \Sigma_0 \left(\frac{r}{r_c} \right)^{-\gamma} \exp \left[- \left(\frac{r}{r_c} \right)^{2-\gamma} \right], \quad (7.3)$$

²This parameter does not affect the sub-mm/mm significantly as long as the emission at these wavelengths is dominated by the optically thin disk regions. However this is not true anymore when emission from optically thick regions becomes important. In this paper we have adopted a value of 30° for the disk inclination of all the modelled disks.

³Note that here we have implicitly assumed that the dust opacity does not change within the disk.

with values of the Σ_0 , γ , r_c parameters lying in the ranges observationally constrained by sub-arcsec angular resolution imaging of young protoplanetary disks in the sub-mm (Isella et al., 2009; Andrews et al., 2009, 2010, see Section 8.3).

After setting the dust surface density, the properties of the dust grains and of the central star (see below), the temperature profile $T_{\text{mid}}(r)$ is derived by balancing the heating due to the reprocessed stellar radiation by the disk surface layers with cooling due to the dust thermal emission. Here we consider disks around a PMS stars with a mass of $0.5 M_{\odot}$, bolometric luminosity of $0.9 L_{\odot}$ and effective temperature of 4000 K, which are typical values for the sample of low-mass PMS stars studied in Ricci et al. (2010a,b, 2011) in the Taurus, Ophiuchus and Orion Nebula Cluster forming regions.

On the top of the “unperturbed” disk structure just defined, we add the contribution of optically thick regions in the disk, i.e. regions where the optical depth $\tau_{\nu} \gg 1$ even at sub-mm and mm wavelengths. By noticing that for a completely optically thick disk the Eq. 7.1 for the flux density reduces to

$$F_{\nu}^{\text{opt.thick}} = \frac{\cos i}{d^2} \int_{R_{\text{in}}}^{R_{\text{out}}} B_{\nu}(T_{\text{mid}}(r)) 2\pi r dr, \quad (7.4)$$

we modify Eq. 7.1 by adding at each radius r a fraction f of optically thick material so that the total flux density becomes:

$$F_{\nu}^f = \frac{\cos i}{d^2} \int_{R_{\text{in}}}^{R_{\text{out}}} B_{\nu}(T_{\text{mid}}(r)) [f + (1 - f) (1 - e^{-\tau_{\nu}(r)})] \times \\ \times 2\pi r dr \quad (7.5)$$

The “filling factor” f can thus be read as the fraction of area in the disk which is optically thick at all the wavelengths considered in the analysis. In general $f = f(r)$, i.e. the filling factor is a function of radius. If $f = 0$ at all radii, Eq. 7.5 reduces to Eq. 7.1, i.e. no optically thick regions are added to the flux density of an unperturbed disk. If $f = 1$ at all radii, Eq. 7.5 reduces to Eq. 7.4 for the flux density of a completely optically thick disk.

We will treat first the simplest case of $f(r)$ which is constant with radius in Sect. 7.4.1, then we will consider for $f(r)$ a family of step functions which are non-zero only within specified regions in the disk in Sect. 7.4.3.

Note that since for nearly all the disks imaged at high angular resolution in the sub-mm the constrained values of γ turned out to be larger than 0 (Andrews et al., 2009, 2010; Isella et al., 2009), Eq. 7.3 implies that the dust surface density typically decreases with distance from the central star. This means that even the innermost regions of unperturbed disks can be dense enough to be optically thick at long wavelengths, as it was recognized since the very first analyses of sub-mm observations of YSOs (e.g. Beckwith et al., 1990). Testi et al. (2001) quantified the impact of optically thick emission from inner disk regions by showing how the predicted mm-fluxes change when considering different parameters for the disk structure. To visualize their main results, they used the F_{mm} vs α_{mm} diagram,

where F_{mm} is the flux-density at a given mm-wavelength and α_{mm} is the mm-spectral index. In this paper we will extensively use this diagram. The main difference with this and other previous works is that our attention will mostly focus on the impact of possible optically thick regions throughout the disk, rather than only on the optically thick inner regions in the unperturbed disk structure. A parametric study of the effect of these local optically thick regions on the mm-SED, and of their properties is presented in Section 8.3. Physically, these optically thick regions might be caused by an increase of the optical depth as due to local concentration of particles (see Eq. 7.2). Different physical processes with the potential of concentrating particles have been proposed in the literature with the aim of investigating the formation of planetesimals (see Chiang & Youdin, 2010). These are discussed in Section 7.5.

7.3.2 Dust opacity

The only physical quantity present in Eq. 7.1, 7.2, 7.5 which is left to be described is the frequency-dependent dust opacity coefficient κ_{ν} . This term, which at long wavelengths represents the level of emissivity of the disk per unit dust mass, can be specified only when a model for the dust grain chemical composition, porosity, shape and size is considered (see e.g. Natta et al., 2004).

In this paper we adopt the same dust grain model as in Birnstiel et al. (2010a); Ricci et al. (2010a,a), i.e. porous composite spherical grains made of astronomical silicates, and water ice (optical constants from Weingartner & Draine, 2001; Zubko et al., 1996; Warren, 1984, respectively⁴). We use the ratio between the fractional abundances estimated by Semenov et al. (2003). After setting the chemical composition, porosity and shape of the grain, a grain size distribution $n(a)$ has to be specified in order to determine the dust opacity coefficient κ_{ν} of the dust model. We adopt a power-law grain size distribution with power-law exponent q

$$n(a) \propto a^{-q} \quad (7.6)$$

truncated between the minimum and maximum grain sizes a_{min} and a_{max} , respectively. Since in this work we want to investigate the impact of local optically thick regions in the outer disk on the slope of the mm-SED *without invoking the presence of large mm-sized grains*, we consider here a size distribution which has been proposed by Mathis et al. (1977) to fit extinction measurements of the interstellar medium. For this ISM-like dust $a_{\text{max}} \approx 0.1 \mu\text{m}$, $a_{\text{min}} \ll a_{\text{max}}$, and $q \approx 3.5$.

7.4 Results

In this section we present the results of our analysis. In particular, in Sect. 7.4.1 and 7.4.3 we compare the mm-flux densities as derived by our disk models for different values of

⁴The refractive indices of the different species have been combined by using the Bruggeman mixing theory.

parameters related to the disk structure, with those measured by Ricci et al. (2010a,b, 2011) for 49 disks in Class II YSOs in the Taurus, Ophiuchus and Orion star forming regions.

7.4.1 Case of a constant f : the $F_{1\text{mm}}-\alpha_{1-3\text{mm}}$ diagram

We start by considering a $f(r)$ -function which is constant for stellocentric radii lower than 300 AU⁵ and equal to 0 outside 300 AU. Each panel in Figure 7.1 shows the prediction of our disk models for different values of the filling factor f and of the dust mass for a given couple of the (γ, r_c) parameters for the disk unperturbed structure⁶. The values of the parameters considered in this work for the unperturbed disk, i.e. $\gamma = 0, 0.5, 1$ and $r_c = 20, 200$ AU (see equation 7.3), lay at the limits of the ranges for these parameters as recently constrained by a high-angular resolution survey of about 30 protoplanetary disks in the sub-mm (Isella et al., 2009; Andrews et al., 2009, 2010).

In each panel the points with $f = 0$ represent the emission of the unperturbed disk only, i.e. without any addition of optically thick regions. The dependence of the flux density at 1 mm on the dust mass is due to the fact that the bulk of the material reside in the outer disk regions where the surface density is relatively low and the emission optically thin. In terms of the spectral index $\alpha_{1-3\text{mm}}$ the points with $f = 0$ lay at relatively large values of about 3 – 3.5. This is due to the adopted ISM-like dust models, for which the value of the spectral slope β of the dust opacity coefficient is about 1.5. The slight decrease of $\alpha_{1-3\text{mm}}$ with increasing dust mass is given by the fact that for disks that are massive enough the innermost disk regions ($r < 10 - 20$ AU) are so dense that the emission from these regions can become optically thick also in the sub-mm, and this has the effect of making the SED shallower.

Note however that the points with $f = 0$ do not get into the area in the $F_{1\text{mm}}-\alpha_{1-3\text{mm}}$ diagram which contains the bulk of the observational data. In particular the models presented here with $f = 0$ overpredict the observed spectral index $\alpha_{1-3\text{mm}}$. In the literature, the commonly adopted interpretation for this discrepancy between models and data is that the assumption of a ISM-like distribution of particle sizes in disks is wrong. By considering in the optically thin outer disk dust particles larger than about 1 mm, the spectral index $\alpha_{1-3\text{mm}}$ gets lower because of a decrease in the spectral index β of the dust opacity coefficient as compared with the value for the ISM-like dust. In this work, we investigate the feasibility of an alternative scenario in which the measured low spectral indices are due to optically thick regions in the outer disk rather than to the presence of large grains in the outer disk, as detailed in the last Section.

The effect of increasing the filling factor f of optically thick regions has always the same kind of signature in the $(F_{1\text{mm}}, \alpha_{1-3\text{mm}})$ -plane: the absolute flux in the (sub-)mm increases because more and more optical depth is added into the system, whereas the spectral index

⁵For all the disks considered in this work, more than 80% of the unperturbed disk mass is contained within 300 AU.

⁶The value of the normalization factor in equation 7.3, i.e. Σ_0 , is set after fixing the (unperturbed) dust mass in the disk.

tends to decrease and approach the value of about 2, as expected for completely optically thick emission in the Rayleigh-Jeans regime⁷.

The main result shown in Figure 7.1 is that, for most of the unperturbed disk structures, relatively low values of the filling factor ($f \lesssim 0.05$) are required to explain the bulk of the data. The most significant variation of the mm-fluxes with the properties of the unperturbed disk comes when the characteristic radius changes from 20 to 200 AU (see left and right panels, respectively). With $r_c = 20$ AU the surface density is more concentrated in the inner disk than in the $r_c = 200$ AU case. As a consequence of this the impact of the optically thick inner regions to the total emission is more evident (see e.g. the low $\alpha_{1-3\text{mm}}$ -value of the model with $f = 0$ and a dust mass of $10^{-3} M_\odot$ for the unperturbed disk structure). However, the fluxes of the disks with $f > 0$ do not dramatically depend on the structure of the unperturbed disk. This is due to the fact that in most of the cases already for $f \approx 0.05$ the total disk emission becomes dominated by the added optically thick regions.

What varies strongly with the unperturbed disk structure at a given f is the mass which has to be included in these added regions in order to make them optically thick. This is discussed in the next section.

7.4.2 Case of a constant f : requested masses in optically thick regions

So far we have considered the emission of our modelled disks without considering how much mass has to be added to the disk in order to make a fraction of the disk surface optically thick even at millimeter wavelengths. A simple way to do this is to calculate the surface density which has to be present in the added regions to give them an optical depth of about 1 at the longest wavelength considered in this work, i.e. 3 mm, and then integrate over the disk area covered by the filling factor f . This represents actually a lower limit for the mass which has to be present in the added regions to make them optically thick: if more mass is put onto those regions this does not have a significant effect onto the SED.

Therefore, the surface density of dust in the optically regions Σ_{dust}^f is given by the condition

$$\tau_{3\text{mm}} \approx \Sigma_{\text{dust}}^f \kappa_{3\text{mm}} \approx 1 \rightarrow \Sigma_{\text{dust}}^f \approx 1/\kappa_{3\text{mm}}, \quad (7.7)$$

which implies that Σ_{dust}^f does not depend on the stellocentric radius. As a consequence of this the total amount of dust in these regions

$$M_{\text{dust}}^f = f \int_{R_{\text{in}}}^{R_{\text{out}}} \Sigma_{\text{dust}}^f 2\pi r dr \approx f \Sigma_{\text{dust}}^f \pi R_{\text{out}}^2, \quad (7.8)$$

⁷Note that in some cases the disk models predict values for the spectral index $\alpha_{1-3\text{mm}}$ which are lower than 2. This is because the Rayleigh-Jeans regime is not completely reached at these wavelengths in our disks.

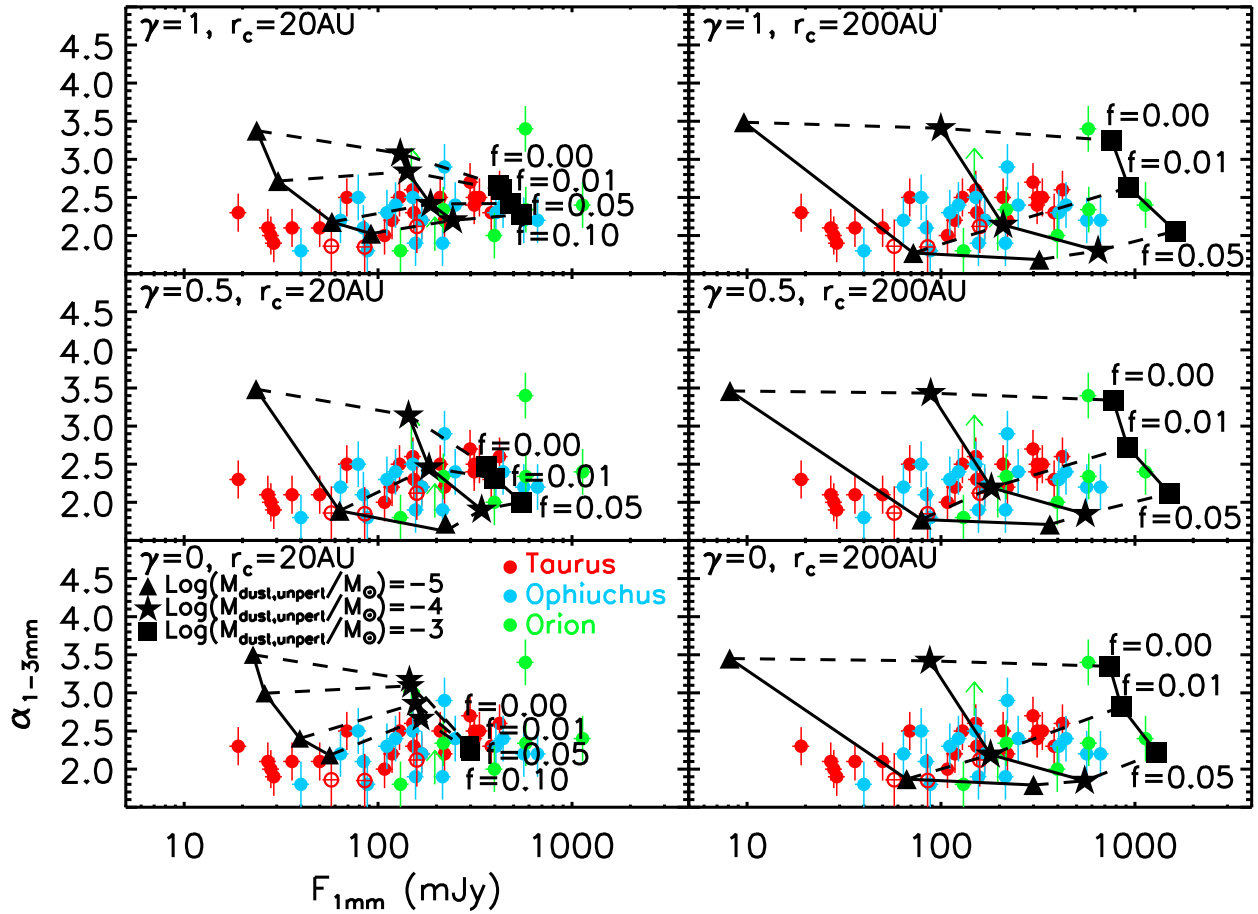


Figure 7.1: Flux density at 1mm vs spectral index between 1 and 3mm. In each panel red, blu and green points represent observational data of Class II YSOs in Taurus (Ricci et al., 2010a), Ophiuchus (Ricci et al., 2010b), and Orion Nebula Cluster (Ricci et al., 2011). Red empty circles are the three Class II YSOs observed with CARMA and discussed in the Appendix. Black symbols show the models predictions for different unperturbed dust mass: triangles for $10^{-5} M_\odot$, stars for $10^{-4} M_\odot$, and squares for $10^{-3} M_\odot$. Solid lines connect disk models with the same unperturbed dust mass, whereas dashed lines connect models with the same constant filling factor f for the optically thick regions, with values indicated in the bottom right side of each panel. In each panel a given couple of the (γ, r_c) -parameters has been assumed for the unperturbed disk structure, with values indicated in the top left corner.

i.e. the total dust mass in the optically regions depends quadratically on the largest radius in which these regions are present in the disk, namely 300 AU in this simulation. For the dust considered in Section 7.3.2, $\kappa_{3\text{mm}} \approx 0.45 \text{ cm}^2/\text{g}$ and $M_{\text{dust}}^f \approx f \times 0.07 M_{\odot}$. This means that even in the case of the the model with the largest unperturbed mass in dust ($10^{-3} M_{\odot}$) and with the lowest value of the filling factor f considered here (0.01), the dust mass in the optically thick regions have to contain already the 70% of the mass in the unperturbed disk. This ratio then increases linearly with both f and the dust mass of the unperturbed disk. This argument clearly shows that in order to have optically thick regions of the kind discussed so far in the outer disk a very strong redistribution of dust particles has to occur in the disk (see Section 7.5).

As shown in Eq. 7.8, the dust mass in the optically thick regions depends quadratically on the disk outer radius. An idea to reduce the amount of dust which is requested in these optically thick regions is therefore to reduce the area in the disk where these are located. This is the topic of the next section.

7.4.3 Case of $f(r)$ as a step function: the $F_{1\text{mm}}-\alpha_{1-3\text{mm}}$ diagram

We consider here the possibility of having optically thick regions which are localized in smaller areas of the disk. In particular, we discuss four cases in which $f(r)$ is a step function with values greater than 0 between 10 and 20 AU, 30 and 40 AU, 50 and 60 AU, 80 and 90 AU. The four panels in Fig. 7.2 show the model predictions on the $F_{1\text{mm}} - \alpha_{1-3\text{mm}}$ diagram for disks with such localized optically thick regions and an unperturbed disk structure with $\gamma = 0.5$ and $r_c = 60 \text{ AU}$, which are about the median values for disks imaged at high-angular resolution.

The optically thick regions can have a significant impact onto the global mm-SED even if they are concentrated in rings with a relatively small width of 10 AU. The effect is stronger for the disk with lower masses because of the higher contrast in optical depth between the unperturbed disk and the optically thick regions. For the same reason, i.e. the contrast with the unperturbed disk structure, and for the fact that the area of an annulus of a given width scales linearly with the central radius of the annulus, at a given filling factor f inside the ring, the effect of the optically thick regions is the largest in the ring which is the furthest from the star, i.e. between 80 and 90 AU. Note however that to reproduce the bulk of the data, larger fractions f are needed than in the $f(r) = \text{const}$ case. This is because in the case of optically thick emission, apart for the temperature, it is the surface area of the emitting material that determines the amount of its emission. Therefore, if these regions are distributed over a smaller area of the disk, they need to occupy a larger fraction of that area, which is what found by our analysis. This argument justifies our choice of dealing with very simple structures for the optically thick regions: even if optically thick regions in real disks would likely have more complex structures than modelled here, our analysis is meaningful in terms of the fractional area covered by such regions throughout the disk.

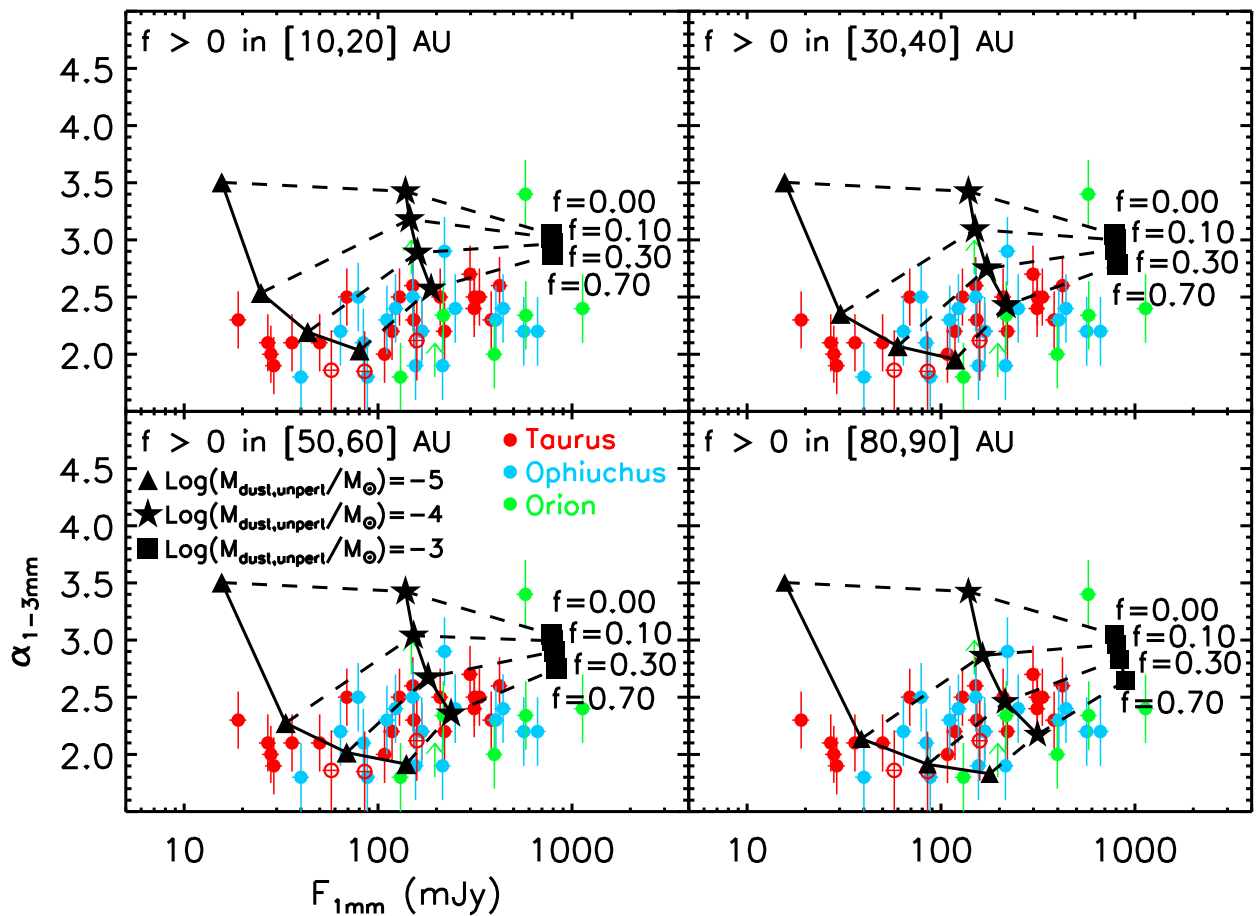


Figure 7.2: As in Fig. 7.1, but with optically thick regions localized in annuli of 10 AU-width, with inner and outer radii indicated in the top left corner of each panel.

7.4.4 Case of $f(r)$ as a step function: requested overdensities

As done in Section 7.4.2 for the case of a constant f within 300 AU, we analyze here the dust mass which has to be present in the optically thick regions. This can be calculated by using the first equality in Eq. 7.8 with the inner and outer radii of the ring for R_{in} and R_{out} , respectively.

For the case of the ring between 10 and 20 AU the total dust mass in the optically thick regions is $M_{\text{dust}}^f \approx f \times 0.00024 M_{\odot}$, and rises to $\approx f \times 0.00055 M_{\odot}$, $\approx f \times 0.00087 M_{\odot}$ and $\approx f \times 0.0013 M_{\odot}$ when the ring is moved outward to 50-60 AU and 80-90 AU, respectively, because of the increased area of the ring itself. Considering filling factors $f \gtrsim 0.1$ on the top of the lowest mass disk ($M_{\text{dust,unpert}} = 10^{-5} M_{\odot}$), which would explain the left end of the $F_{1\text{mm}}-\alpha_{1-3\text{mm}}$ diagram (Fig. 7.2), the mass in the optically thick regions overcome the one in the unperturbed structure for all the rings considered here. This would require an extremely strong concentration of particles in those regions which are not seen in the results of the numerical simulations run so far (see discussion in Section 7.5). For the disk with $M_{\text{dust,unpert}} = 10^{-4} M_{\odot}$ a significant decrease of the spectral index $\alpha_{1-3\text{mm}}$, i.e. down to about 2.5 and lower is obtained only for $f \gtrsim 0.3$ (Fig. 7.2). These filling factors require dust masses in the optically thick regions as large as at least 70% of the unperturbed disk mass. Finally, the added optically thick regions in the most massive disk considered here, with $M_{\text{dust,unpert}} = 10^{-3} M_{\odot}$, contain relatively low dust mass as compared with the unperturbed disk mass. For example, in the case of $f = 0.5$ the ratio among the former and latter masses is about 12%, 28%, 44%, 65% for the optically thick regions inside rings with radii of 10-20 AU, 30-40 AU, 50-60 AU and 80-90 AU, respectively.

Tables 7.1-7.4 report, for models with different unperturbed disk structures in terms of total dust mass, γ and r_c , the requested overdensities in the optically thick regions. These are defined as the ratio between the dust surface density Σ_{dust}^f in the optically thick regions and the surface density in the unperturbed disk structure evaluated at the center of the ring. Since Σ_{dust}^f is always the same (i.e. $1/k_{3\text{mm}} \approx 2.2 \text{ cm}^2/\text{g}$), the requested overdensities depend only on the value that the dust surface density of the unperturbed disk assumes in the ring, and therefore on the $(M_{\text{dust,unpert}}, \gamma, r_c)$ parameters which define such surface density⁸. The lowest values for the overdensities are found for the most massive disk in the case of the innermost radius. The low values of order of unity indicate that this disk is massive enough to have the unperturbed structure at radii of $\sim 10\text{-}20$ AU marginally optically thick by itself, i.e. without the addition of any artificial optically thick region.

⁸Note that the values of these overdensities do not depend on the adopted value for the dust opacity $\kappa_{3\text{mm}}$. This is because both the surface density in the optically thick regions, and the surface density in the optically thin unperturbed disk structure at a given flux depend on the dust opacity as $\kappa_{3\text{mm}}^{-1}$.

Table 7.1: Requested dust overdensities in the added optically thick regions inside a ring between 10 and 20 AU from the central star.

	$\gamma = 1$		$\gamma = 0.5$		$\gamma = 0$	
	$r_c = 20$ AU	$r_c = 200$ AU	$r_c = 20$ AU	$r_c = 200$ AU	$r_c = 20$ AU	$r_c = 200$ AU
$M_{\text{dust,unp}} = 10^{-5} M_{\odot}$	~ 100	~ 520	~ 70	~ 1200	~ 55	~ 3200
$M_{\text{dust,unp}} = 10^{-4} M_{\odot}$	~ 10	~ 52	~ 7	~ 120	~ 5.5	~ 320
$M_{\text{dust,unp}} = 10^{-3} M_{\odot}$	~ 1	~ 5.2	~ 0.7	~ 12	~ 0.55	~ 32

Table 7.2: Requested dust overdensities in the added optically thick regions inside a ring between 30 and 40 AU from the central star.

	$\gamma = 1$		$\gamma = 0.5$		$\gamma = 0$	
	$r_c = 20$ AU	$r_c = 200$ AU	$r_c = 20$ AU	$r_c = 200$ AU	$r_c = 20$ AU	$r_c = 200$ AU
$M_{\text{dust,unp}} = 10^{-5} M_{\odot}$	~ 630	~ 1300	~ 530	~ 2000	~ 680	~ 3300
$M_{\text{dust,unp}} = 10^{-4} M_{\odot}$	~ 63	~ 130	~ 53	~ 200	~ 68	~ 330
$M_{\text{dust,unp}} = 10^{-3} M_{\odot}$	~ 6.3	~ 13	~ 5.3	~ 20	~ 6.8	~ 33

Table 7.3: Requested dust overdensities in the added optically thick regions inside a ring between 50 and 60 AU from the central star.

	$\gamma = 1$		$\gamma = 0.5$		$\gamma = 0$	
	$r_c = 20$ AU	$r_c = 200$ AU	$r_c = 20$ AU	$r_c = 200$ AU	$r_c = 20$ AU	$r_c = 200$ AU
$M_{\text{dust,unp}} = 10^{-5} M_{\odot}$	~ 2700	~ 2300	~ 5700	~ 2700	~ 62000	~ 3400
$M_{\text{dust,unp}} = 10^{-4} M_{\odot}$	~ 270	~ 230	~ 570	~ 270	~ 6200	~ 340
$M_{\text{dust,unp}} = 10^{-3} M_{\odot}$	~ 27	~ 23	~ 57	~ 27	~ 620	~ 34

Table 7.4: Requested dust overdensities in the added optically thick regions inside a ring between 80 and 90 AU from the central star.

	$\gamma = 1$		$\gamma = 0.5$		$\gamma = 0$	
	$r_c = 20$ AU	$r_c = 200$ AU	$r_c = 20$ AU	$r_c = 200$ AU	$r_c = 20$ AU	$r_c = 200$ AU
$M_{\text{dust,unp}} = 10^{-5} M_{\odot}$	~ 19000	~ 4100	~ 370000	~ 3800	$\sim 2.4 \cdot 10^9$	~ 3700
$M_{\text{dust,unp}} = 10^{-4} M_{\odot}$	~ 1900	~ 410	~ 37000	~ 380	$\sim 2.4 \cdot 10^8$	~ 370
$M_{\text{dust,unp}} = 10^{-3} M_{\odot}$	~ 190	~ 41	~ 3700	~ 38	$\sim 2.4 \cdot 10^7$	~ 37

7.5 Discussion

To understand whether the optically thick regions discussed in this paper are physically plausible in real protoplanetary disks, one has to compare the requested filling factors and overdensities of regions with small, sub-micron sized grains discussed in the last section with the outcome of the numerical simulations which investigate different mechanisms leading to the concentration of solid particles. These mechanisms are often invoked in the literature for their potential of halting locally the otherwise fast radial drift of solids (Brauer et al., 2007) and of forming planetesimals in the disk (see a recent review by Chiang & Youdin,

2010).

A promising mechanism to concentrate solid particles is through the development of streaming instabilities, in which the gas and solid components are mutually coupled by drag forces in a turbulent disk. Johansen & Youdin (2007) showed that overdensities of particles even larger than 1000 can be formed. Looking at Tables 7.1-7.4 this indicates that these overdense regions would probably be optically thick also in the millimeter for most of the disk models considered here. However, in terms of the impact to the global disk SED, the filling factor f of these regions is probably not large enough to be really significant: the fraction of particles in overdense regions at level of the order of 100 or above is only about 1% or less (see Fig. 11 in Johansen & Youdin, 2007). This means that the filling factor f of disk area occupied by such regions is much lower than that, as the mean distance between particles decreases with increasing density. Furthermore, all these highly-overdense regions are obtained for solid particles which are only marginally coupled to the gas, with values for the Stokes parameter⁹, $St \sim 1$. Sub-micron sized grains, as those considered in this analysis, are instead very well coupled to the gas ($St \ll 1$). In the case of streaming instabilities Johansen & Youdin (2007) showed that already for particles with $St \sim 0.1$, the level of overdensity is decreased by a factor of 10. For these reasons, we argue that, although streaming instabilities may potentially form overdense regions which are optically thick at millimeter wavelengths, the low spectral indices found in the mm-SED of young disks cannot be explained by the concentration of sub-micron sized particles through this kind of mechanism.

Another possible mechanism which has been proposed to trap solids involves the presence of large anticyclonic vortices in the disk. These structures can be the result of baroclinic instability (Klahr & Bodenheimer, 2003), the Rossby wave instability (Lovelace et al., 1999), or magneto-rotational instability (Fromang & Nelson, 2005). Recent 2D numerical simulations of circumstellar disks have shown that, although overdensities larger than 2-3 order of magnitudes can be obtained in vortices covering a significant fraction of the disk surface area, the solids that are trapped are larger than about 10 cm, whereas smaller ISM-like dust is not significantly affected by such structures (Lyra et al., 2009).

Long-lived axisymmetric pressure bumps have been obtained in simulations of magneto-rotational turbulent disks (Johansen et al., 2009). These pressure bumps have the potential of trapping solids which are marginally coupled to the gas, like mm-cm sized pebbles, but the obtained overdensities in gas are not large enough ($\lesssim 10 - 20\%$) to redistribute more gas-coupled small grains at the levels required for the optically thick regime (Tables 7.1-7.4).

Finally, some concentration of dust particles can occur in disks undergoing gravitational instabilities. In these disks, the non-linear evolution of these instabilities lead to the formation of spiral waves with local overdensities in the gas component as high as about 100 (Rice et al., 2004; Boss, 2010). Since sub-mm sized particles are well coupled to the gas, the same

⁹The Stokes parameter is an adimensional parametrization for the particle size in a gaseous disk. In the Epstein regime, which is relevant for the conditions in the disks treated in this work, $St = \pi a \rho_s / (2 \Sigma_{\text{gas}})$, where a and ρ_s are the particle size and density, respectively.

level of overdensity is expected for small grains as well. Considering that spiral waves are characterized by very extended structures, the results presented in this work show that the overdense regions in spiral waves can be optically thick even at mm-wavelengths and can even dominate the emission of a young disk at these wavelengths. This means that for gravitational unstable disks the measured low values of the mm-spectral index ($\alpha_{1-3\text{mm}} \lesssim 3.0$) can be potentially explained by the optically thick emission of small ISM-like grains from overdense regions in spiral waves. However, in order for disks to develop these instabilities, they need to be rather massive. Recent numerical simulations of Boss (2010) have shown that more than about $0.04 M_{\odot}$ inside 20 AU are needed around a $1 M_{\odot}$ protostar, or about $0.02 M_{\odot}$ around a $0.5 M_{\odot}$ protostar as considered in this work. By assuming a standard ISM-like value of 100 for the gas-to-dust ratio, this lower-limit corresponds to $2 \cdot 10^{-4} M_{\odot}$ of dust mass inside 20 AU from the central protostar. Therefore, only the mm-fluxes of disks in the bright tail of the $F_{1\text{mm}} - \alpha_{1-3\text{mm}}$ diagram can be explained by accumulation of unprocessed ISM-like grains via gravitational instabilities. High sensitivity and angular resolution imaging with ALMA in the sub-mm will soon constrain the occurrence of these instabilities in real disks (Cossins et al., 2010a).

The main conclusion of this work is that for the vast majority of disks no physical processes proposed so far are capable to reproduce the measured low mm-spectral indices via a concentration of small ISM-like particles in optically thick regions. The result of this analysis further strengthens the scenario for which the measured low spectral indices of protoplanetary disks at long wavelengths are due to the presence of large mm/cm-sized pebbles in the disk outer regions.

Appendix: New CARMA observations at 3mm

We describe here new mm-wave observations of nine YSOs in the Taurus-Auriga star forming region (SFR). The sources were selected for being relatively bright at sub-mm/mm wavelengths, namely with a flux density at 0.85 mm greater than 100 mJy and/or a 1.3 mm-flux density greater than 30 mJy. This criterion was chosen to have high chances to detect our sources at about 3 mm with the Combined Array for Research in Millimeter Astronomy (CARMA). The observed YSOs are listed in Table 1.

The dust thermal emission toward our sample of nine young disk systems in Taurus-Auriga was observed with CARMA between 2010 March 2 and April 6. The array was in C configuration which provides baselines between 30 and 350 m. Observations were carried out at a central frequency of 102.5 GHz (2.92 mm), with a total bandwidth of 4 GHz. The raw visibilities for each night were calibrated and edited using the MIRIAD software package. Amplitude and phase calibration were performed through observations of the QSOs 0336+323 (for 04113+2758, V892 Tau, FN Tau), 3C 111 (for IC 2087, AB Aur, BP Tau, V836 Tau), 0449+113 (for DQ Tau). Passband calibration was obtained by observing the QSO 3C 84. Mars and Uranus were used to set the absolute flux scale. The uncertainty on CARMA flux calibration is typically estimated to be $\sim 15\%$ and is due to uncertainties in the planetary models and in the correction for atmospheric effects and

Table 7.5: Summary of the CARMA observations at 102.5 GHz in Taurus.

Object	RA	DEC	F_ν	rms	Comments
	(J2000)	(J2000)	(mJy)	(mJy)	
(1)	(2)	(3)	(4)	(5)	(6)
AB Aur	04:14:47.8	26:48:11.1	10.0	0.9	Herbig Ae/Be
V892 Tau	04:21:55.6	27:55:05.5	54.9	1.0	Herbig Ae/Be
BP Tau	04:30:44.3	26:01:23.9	10.1	0.6	
DQ Tau	04:38:28.6	26:10:49.7	14.9	0.6	
FN Tau	04:47:06.2	16:58:43.0	4.1	0.8	extended envelope emission
IC 2087 ^a	04:39:55.8	25:45:02.0	< 2.7	0.9	Class I
V836 Tau	04:14:13.5	28:12:48.8	6.6	0.5	
MHO 1	04:14:17.0	28:10:56.5	50.5	1.1	no sub-mm info
MHO 2	04:14:47.8	26:48:11.1	30.2	1.1	no sub-mm info

Notes. ^(a) For this undetected source the (RA,DEC) coordinates are from 2MASS (Cutri et al., 2003).

Column (6) reports the reason why the source has not been considered in the analysis (see Appendix).

hardware instabilities (see Ricci et al., 2011, for an analysis of the repeatability of 3mm-flux measurements with CARMA on observations performed in the same time period of the ones presented here). Maps of the dust continuum emission were obtained by standard Fourier inversion adopting natural weighting, and photometry was obtained in the image plane. The resulting FWHM of the synthesized beam is about 2".

Among the nine observed YSOs, we considered the three sources (BP Tau, DQ Tau, V836 Tau) which satisfy the selection criteria adopted in this work and listed in Sect. 7.2. We instead did not include the other observed sources for the following reasons:

- AB Aur and V892 Tau, since they are Herbig Ae/Be stars, and therefore with a central PMS star more massive than the sample of T Tauri stars considered in this paper;
- FN Tau shows evidence of spatially resolved nebulosity in near-infrared scattering light (Kudo et al., 2008), likely due to a leftover protostellar envelope. Furthermore, Momose et al. (2010) showed how disk models fail to reproduce at the same time SMA 0.88 mm observations at high-angular resolution and single dish data at

1.3 mm, confirming that an extended “halo” component is present in the FN Tau system.

- IC 2087, which is an embedded Class I YSO (Luhman et al., 2010), and therefore, a significant contribution from an extended envelope to the sub-mm/mm emission is expected to occur;
- MHO 1 and MHO 2, which are part of a binary system with angular separation of $4.0''$ (or about 560 AU at the Taurus distance Duchene et al., 2004) and no interferometric observations which can separate the two components have been carried out so far in the sub-mm.

As for the three selected sources, according to Luhman et al. (2010), and references therein, BP Tau is a K7-spectral type PMS star, DQ Tau is a double lined spectroscopic binary which consists of two PMS stars with similar spectral type in the range of K7 to M1, and V836 Tau is a K7. Andrews & Williams (2005) reported fluxes for BP Tau of 130 ± 7 mJy and 47 ± 0.7 mJy at about 0.85 and 1.3 mm, respectively, whereas for V836 Tau $F_{0.85\text{mm}} = 74 \pm 3$ mJy, $F_{1.3\text{mm}} = 37 \pm 6$ mJy. The other selected source, DQ Tau, is a circumbinary disk which is known to undergo recurring millimeter flares due to star-star magnetic reconnection events (see Salter et al., 2010, and references therein). By measuring the light curve in the millimeter Salter et al. (2010) estimated a quiescent level of the emission at about 1.3 mm of 97 mJy, and of 17 mJy at 2.7 mm, which is roughly consistent with the measured flux of 14.9 ± 0.6 mJy at 3.2 mm presented in this work. By combining these data with the new ones obtained at 3.2 mm with CARMA (Table 7.5) for the three selected sources, we obtained the mm-spectral index shown as red empty circles in Fig. 7.1,7.2.

Testing the theory of grain growth and fragmentation by millimeter observations of protoplanetary disks

Published as Birnstiel, Ricci, Trotta, Dullemond, Natta, Testi, Dominik, Henning, Ormel, & Zsom, 2010, A&A Letters 516, 14

Abstract

Observations at sub-millimeter and mm wavelengths will in the near future be able to resolve the radial dependence of the mm spectral slope in circumstellar disks with a resolution of around a few AU at the distance of the closest star-forming regions. We aim to constrain physical models of grain growth and fragmentation by a large sample of (sub-)mm observations of disks around pre-main sequence stars in the Taurus-Auriga and Ophiuchus star-forming regions. State-of-the-art coagulation/fragmentation and disk-structure codes are coupled to produce steady-state grain size distributions and to predict the spectral slopes at (sub-)mm wavelengths. This work presents the first calculations predicting the mm spectral slope based on a physical model of grain growth. Our models can quite naturally reproduce the observed mm-slopes, but a simultaneous match to the observed range of flux levels can only be reached by a reduction of the dust mass by a factor of a few up to about 30 while keeping the gas mass of the disk the same. This dust reduction can either be caused by radial drift at a reduced rate or during an earlier evolutionary time (otherwise the predicted fluxes would become too low) or due to efficient conversion of dust into larger, unseen bodies.

8.1 Introduction

Circumstellar disks play a fundamental role in the formation of stars as most of the stellar material is believed to be transported through the disk before being accreted onto the star (Lynden-Bell & Pringle, 1974). At the same time circumstellar disks are thought to be the birth places of planets. Understanding the physics of circumstellar disks is therefore the key to some of the most active fields of astrophysical research today.

However, observing these disks in order to learn about the physical processes taking place in their interior is a challenging task. Strom et al. (1989) and Beckwith et al. (1990) were the first to use observations at mm-wavelengths to confirm that many of the observed pre-main sequence (PMS) stars showed excess radiation above the spectrum of a T Tauri star. While these single dish observations provided valuable insight in dust masses (since mm observations probe not only the thin surface layers, but the bulk of the dust mass in the mid-plane), recent developments in the field of (sub-)mm interferometry grant the possibility to constrain models of disk structure and evolution of protoplanetary disks by fitting parametric models to the observed radial profiles (e.g., ??). Spatially resolving the disks is important since it ensures that low millimeter spectral slopes are not just an artifact of high optical depth.

Today, mm spectral slopes are known for quite a number of disks and spatially resolved observations indicate that the low values measured in these samples are related to grain growth (e.g., Testi et al., 2003; Natta et al., 2004; Rodmann et al., 2006). Grains are believed to collide and stick together by van der Waals forces, thus forming larger and larger aggregates (Dominik & Tielens, 1997; Poppe et al., 2000; Blum & Wurm, 2008). Due to this loose binding, collisions with velocities in excess of a few m s^{-1} may lead to fragmentation of the aggregates.

Larger samples of radially resolved mm spectral slopes are expected in the near future, but still no study so far interpreted mm observations using simulated grain size distributions but rather used simple parametric power-law distributions with an upper size cut-off. In this work, we use a state of the art dust grain evolution code (similar to Brauer et al., 2008a; Birnstiel et al., 2010a) to derive steady-state grain distributions where grain growth and fragmentation effects balance each other. We self-consistently solve for the grain size distributions and the disk structure to predict fluxes at mm wavelengths and the radial dependence of the mm spectral index. Comparing these results to observed values in the Taurus and Ophiuchus star-forming regions allows us to test predictions of the theory of grain growth/fragmentation and to infer constraints on grain properties such as the critical collision velocity and the distribution of fragments produced in collision events.

Grains orbiting at the Keplerian velocity in a laminar gas disk feel a constant head wind (caused by the gas rotating slightly sub-keplerian) which forces them to spiral inwards (Weidenschilling, 1977). If this drag is as efficient as laminar theory predicts, all dust particles which are necessary to explain the observed spectral indices, would quickly be removed (see Brauer et al., 2007). In this Letter, we therefore assume that radial drift is halted by an unknown mechanism. Under this assumption, we find that low values of the mm spectral index can be explained by the theory. We show that in order to explain the

Table 8.1: Parameters of the model grid: M_{disk} is the total disk mass, α_t is the turbulence parameter, u_f is the critical collision velocity, f_{vac} is the grain volume fraction of vacuum and ξ is the index of the distribution of fragments (see Eq. 8.3). The parameters of the fiducial model are highlighted in bold face.

parameter		values			
M_{disk}	$[M_{\odot}]$	5×10^{-3}	1×10^{-2}	5×10^{-2}	1×10^{-1}
α_t		5×10^{-4}	1×10^{-3}	5×10^{-3}	-
u_f	$[\text{m/s}]$	1	3	10	-
f_{vac}	$[\% \text{ vol.}]$	10	30	50	-
ξ		1.0	1.5	1.8	-

observed flux levels, the amount of observable¹ dust needs to be reduced by either reducing the dust-to-gas ratio (perhaps by radial drift at an intermediate efficiency or during an earlier evolutionary epoch) or by dust particle growth beyond centimeter sizes.

8.2 Model description

8.2.1 Disk model

We consider disks around a PMS star with a mass of $0.5 M_{\odot}$, bolometric luminosity of $0.9 L_{\odot}$ and effective temperature of 4000 K, at a distance of 140 pc, which are typical values for the sample of low-mass PMS stars studied in Ricci et al. (2010a). To derive the disk structure we adopted a modified version of the two-layer models of passively irradiated flared disks developed by Dullemond et al. (2001) (following the schematization by Chiang & Goldreich, 1997), in which we have relaxed the common assumption that dust grain properties are constant throughout the disk. For the disk surface density we adopted the self-similar solution for a viscous disk (see Lynden-Bell & Pringle, 1974) with parameters lying in the ranges observationally constrained by Andrews et al. (2009). The surface density gradient γ and the characteristic radius R_c (for the definitions, see Hartmann et al., 1998) are assumed to be $\gamma = 1$ and $R_c = 60 \text{ AU}$, respectively. Throughout this work we assume a constant dust-to-gas mass ratio of 1%.

8.2.2 Dust model

We use a coagulation/fragmentation code as described in Brauer et al. (2008a) and Birnstiel et al. (2010a) to simulate the growth of dust particles. Particles grow due to mutual collisions (induced by Brownian motion and by turbulence, see Ormel et al., 2007a) and

¹by “visible” or “observable” dust we mean the dust particles which are responsible for most of the thermal continuum emission at (sub-)mm wavelengths which are typically smaller than a few centimeter in radius.

subsequent sticking by van der Waals forces. We assume the dust particles to be spheres of internal density ρ_s and vary ρ_s to account for porosity effects. However, we do not treat a dynamic porosity model (see Ormel et al., 2007b; Zsom & Dullemond, 2008).

With increasing collision velocity Δu , the probability of sticking decreases and fragmentation events start to become important. In this Letter, we use the fragmentation probability

$$p_f = \begin{cases} 0 & \text{if } \Delta u < u_f - \delta u \\ 1 & \text{if } \Delta u > u_f \\ 1 - \frac{u_f - \Delta u}{\delta u} & \text{else} \end{cases} \quad (8.1)$$

where u_f is the collision velocity above which particles are assumed to fragment and δu is the transition width between coagulation and fragmentation (taken to be $0.2 u_f$). Recent studies of collision experiments (Güttler et al., 2010) and numerical simulations (Zsom et al., 2010) indicate that there is also a regime in which particles may bounce. However, since this topic is still not well understood, we will omit these effects in this work.

Radial drift is an, as yet, unsolved problem (Brauer et al., 2007; Birnstiel et al., 2009). However there are several effects such as spiral wave structure (e.g., Cossins et al., 2009), density sinks (e.g., Brauer et al., 2008b) or zonal flows (e.g., Johansen et al., 2009) which may reduce the effectiveness of radial drift. In this paper we assume that radial drift is ineffective since we focus on the question whether observations can be explained through the physics of grain growth and fragmentation. The question to answer in this case is not, how to retain particles at these radii, but rather how to create them there in the first place.

To investigate this problem, we simulate the physics of particle growth and fragmentation until a steady state between both processes develops. Since the relative velocities for particles typically increase with grain radius, we can relate the fragmentation velocity to a certain grain size (which defines the “fragmentation barrier”, see Birnstiel et al., 2009)

$$a_{\max} \simeq \frac{2\Sigma_g}{\pi\alpha_t\rho_s} \cdot \frac{u_f^2}{c_s^2}, \quad (8.2)$$

above which particles fragment (with Σ_g , α_t and c_s being the gas surface density, the turbulence parameter and the sound speed, respectively). u_f and α_t are assumed to be radially constant with α_t values within a range expected from theoretical (see Johansen et al., 2005) and observational works (see Andrews et al., 2009). Grains which reach a_{\max} will experience high velocity collisions causing them to be eroded or even completely fragmented. The resulting fragments can again contribute to growth processes at smaller sizes and the grain size distribution will at some point reach a steady state where gain and loss terms caused by coagulation and by fragmentation cancel out at all sizes.

Particles will need a certain time to grow to the fragmentation barrier. The time to reach the steady state will therefore be a few of these growth time scales. Depending on the distance to the central star, the steady state is typically reached after a few thousand years at 1 AU up to about 1 Myr at 100 AU. The mean ages of the sources in our sample are ≈ 2 Myr and $\approx 0.5 - 1$ Myr for the Taurus and Ophiuchus PMS stars, respectively. Since radii around 40 – 80 AU dominate the observed emission at (sub-)mm wavelengths, we expect most of the samples to be in or at least close to a steady state.

If the highest collision velocity that turbulent motion induces (depending on α_t and c_s) is smaller than the critical collision velocity u_f , then (at least some) particles do not fragment (i.e. the break through the fragmentation barrier) and a steady state is never reached. Due to this scenario, some of the possible combinations of the parameter values (see Table 8.1) do not reach a steady state and are therefore not included in the results.

The shape of the steady state grain size distributions is influenced mainly by five parameters: the previously mentioned α_t , u_f , Σ_g , the temperature T (through the sound speed c_s), and by the prescription of fragmentation. In our models, we assume the distribution of fragments to follow a power-law number density distribution,

$$n(m) \propto m^{-\xi}, \quad (8.3)$$

with an upper end at m_f . We consider fragmentation and cratering, as described in Birnstiel et al. (2010a). Recent experiments suggest ξ values between 1.07 and 1.37 (see Güttler et al., 2010). In this work, we consider ξ values between 1.0 and 1.8.

To calculate the dust opacity of a given grain size distribution we adopted the same dust grain model taken in Ricci et al. (2010a), i.e. porous composite spherical grains made of astronomical silicates, carbonaceous materials and water ices (see Ricci et al., 2010a, for the references to the optical constants). The ratio between the fractional abundance of each species comes from Semenov et al. (2003) and models with three different porosities have been considered in this Letter (see Table 8.1). We used the Bruggeman mixing theory to combine the refractive indices of the different materials and to calculate the dust opacity of the composite grains. The opacity induces probably the largest uncertainties in our calculations as grain composition, grain structure and temperature effects may lead to largely different opacities (see, for example Henning & Stognienko, 1996).

8.2.3 Comparison to observations

We compare the (sub-)mm SED generated by our models with observational data of Ricci et al. (2010a) and Ricci et al. (2010b), more specifically the flux at 1 mm ($F_{1\text{mm}}$) and the spectral index between 1 and 3 mm ($F(\lambda) \propto \lambda^{-\alpha_{1-3\text{mm}}}$). The samples considered include all the class II disks in the Taurus-Auriga and ρ -Oph star-forming regions respectively for which both the central PMS star and the disk are observationally well characterized through optical-NIR spectroscopy/photometry and (sub-)mm photometry/interferometry. To calculate the dust opacity as a function of wavelengths and radius, and the temperature in the disk mid-plane, we iterated the two-layer disk model (keeping the profile of Σ_g constant in time) with the dust model described above until convergence is reached. Once the physical structure of the disk is determined, the two-layer disk models return the disk SED which can be compared to the observations.

The influence of the different parameters on the calculated $\alpha_{1-3\text{mm}}$ values can mostly be understood by a simple model for a dust distribution, as used in Ricci et al. (2010a) (cf. Fig. 3 in Ricci et al., 2010a): for maximum grain sizes much smaller than the observed wavelengths, the spectral index of the dust opacity $\beta_{1-3\text{mm}}(\kappa(\lambda) \propto \lambda^{-\beta_{1-3\text{mm}}})$ is constant,

while it decreases for a_{max} values larger than sub-mm sizes. In between (at a few tenth of a mm), there is a peak which is caused by an increased opacity of grains with sizes similar to the observed wavelength. The relation between α_{1-3mm} and β_{1-3mm} depends on the emitting spectrum and the optical depth. For a completely optically thin disk in the Rayleigh-Jeans regime $\beta_{1-3mm} = \alpha_{1-3mm} - 2$. However, if the emitted spectrum deviates from the Rayleigh-Jeans limit, then $\beta_{1-3mm} \gtrsim \alpha_{1-3mm} - 2$. In our models, $\alpha_{1-3mm} - \beta_{1-3mm}$ turns out to be typically between 1.4 and 1.7 if a_{max} is outside of the peak of opacity.

8.3 Results

8.3.1 Sub-mm fluxes and spectral indices

For all possible combinations of the parameters shown in Table 8.1, we solved for the steady-state grain size distributions and derived the α_{1-3mm} and F_{1mm} values. As noted before, some of the models do not result in a steady state and are, therefore, not shown here.

The top left panel of Fig. 8.1 shows the influence of the turbulence parameter α_t . According to Eq. 8.2, the maximum grain size increases if α_t decreases. Depending on where a_{max} lies with respect to the opacity peak (see Ricci et al., 2010a, , Fig. 3), α_{1-3mm} can increase or decrease with increasing α_t . In the simulations presented here, a_{max} is typically so large that increasing α_t predicts larger spectral slopes.

a_{max} is more sensitive to u_f (cf. top right panel in Fig. 8.1): the maximum grain size a_{max} is proportional to u_f^2 , therefore a change of u_f by a factor of about 3 significantly changes α_{1-3mm} by increasing the grain size by about one order of magnitude. However many models with a fragmentation velocity of 10 m/s never reach a steady state. It is therefore not possible to explain lower α_{1-3mm} values by a further increase of u_f alone.

The way that M_{disk} influences F_{1mm} and α_{1-3mm} is twofold. Firstly, a decrease in M_{disk} (assuming a constant dust-to-gas ratio and a fixed shape of the disk surface density, i.e. not varying R_c and γ , see Section 8.2.1), reduces the amount of emitting dust and thus F_{1mm} . Secondly, such a reduction in gas mass also reduces a_{max} (Eq. 8.2), which tends to increase α_{1-3mm} . This combined trend is seen in Fig. 8.1. Hence, in order to explain faint sources with low α_{1-3mm} , the amount of emitting dust has to be reduced while the disk gas mass stays large. This effect could be achieved in two ways: the amount of dust could be reduced by radial drift at a reduced rate (full radial drift would quickly remove all mm-sized grains, see Brauer et al., 2007) or only the “visible” amount of dust is reduced if some of the dust is already contained in larger bodies. This latter case is predicted by our non-steady-state distribution models and will be discussed in more details in a forthcoming paper.

In general, lower values of ξ translate to shallower grain-size distribution, which result in lower values of β_{1-3mm} (see Draine, 2006). The lower right panel in Fig. 8.1 does not seem to indicate a strong dependence on ξ , however lower values of ξ (around 1) seem to be closer to the observations especially at large fluxes.

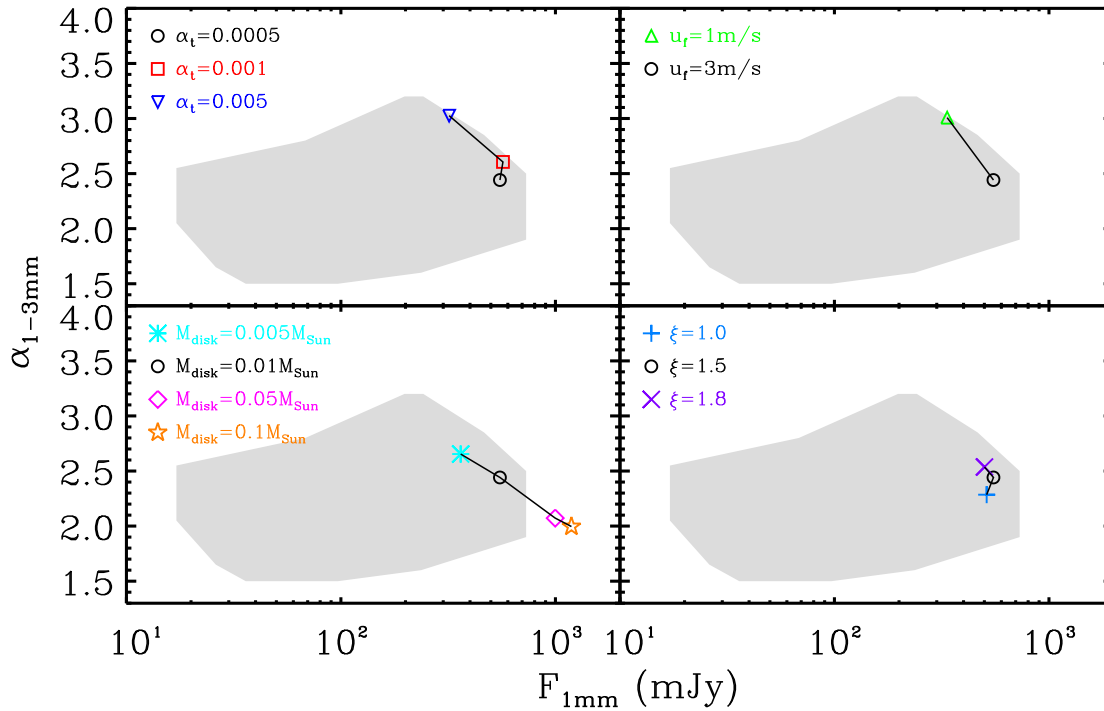


Figure 8.1: Influence of the parameters α_t (top left), fragmentation velocity (top right), disk mass (bottom left) and grain porosity (bottom right) on the observed fluxes and spectral indices. The black circle denotes the fiducial model whose parameters are given in Table 8.1. The grey area represents the region in which the observed sources lie (see Fig. 8.2).

Figure 8.2 shows the areas which are covered by our sets of simulations for different porosities in comparison to the observational samples. It can be seen that only the brightest sources are covered by the simulations. The trend of larger $\alpha_{1-3\text{mm}}$ for larger vacuum fraction seems to be in contradiction with Eq. 8.2, since smaller grain volume density leads to larger a_{max} . However in this case, the opacity is much more affected by changing the grain structure: reducing the grains vacuum fraction increases the spectral index at sub-mm while it is reduced for longer wavelength. Therefore opacity effects outweigh the smaller changes in a_{max} . A more thorough analysis of opacity effects is beyond the scope of this letter, however it seems implausible that the large spread in the observations can be explained by different kinds of grains alone (see Draine, 2006).

8.3.2 Radial profiles of the dust opacity index

The presented models also compute $\alpha_{1-3\text{mm}}$ as function of radius. From the point of view of comparison to observations, this is somewhat premature since observational methods are not yet able to provide reliable radial profiles of $\alpha_{1-3\text{mm}}$ (e.g., Isella et al., 2010; Banzatti et al., 2011). However, the predicted radial dependence of $\beta_{1-3\text{mm}}$ (shown in Fig. 8.3) agrees

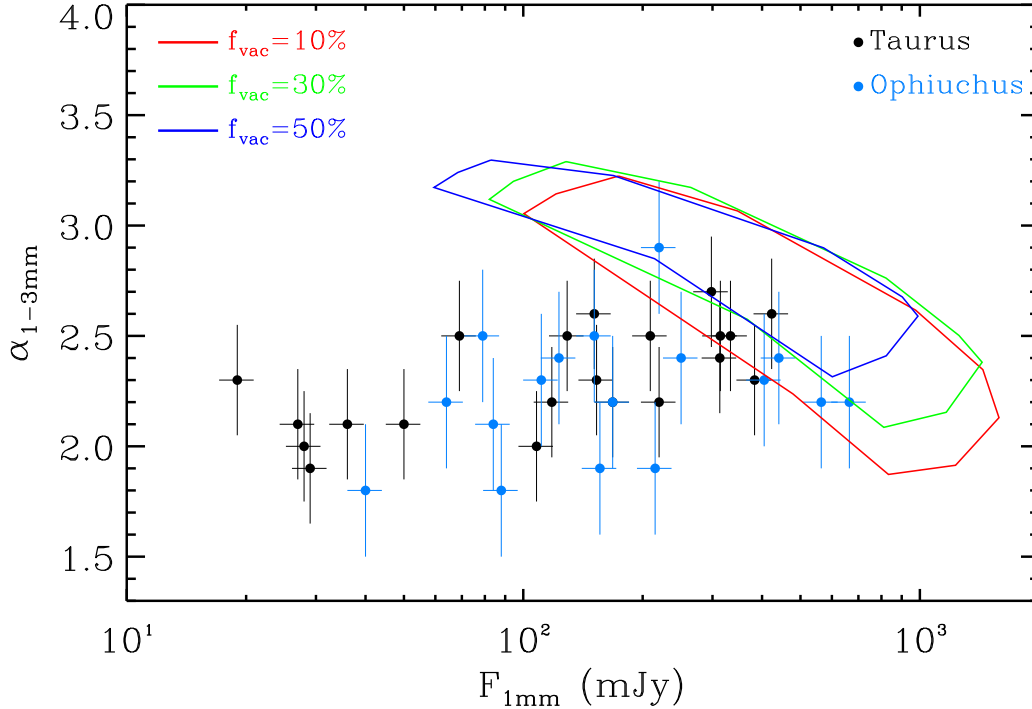


Figure 8.2: Observed fluxes at mm-wavelengths of the Taurus (black dots) and the Ophiuchus (blue dots) star-forming regions (see Ricci et al., 2010a,b) and the areas covered by the simulation results for different vacuum fractions of the grains (varying all other parameters according to Table 8.1).

with the observations so far. It can be seen that the shape of most models looks similar, slightly increasing from $\beta_{1-3\text{mm}}$ -values around 0.5 at 10 AU up to around 1.5 at 100 AU. The reason for this is that a_{max} depends on the ratio of surface density over temperature. Under typical assumptions, a_{max} will decrease with radius. An upper grain size which is decreasing with radius and stays outside the peak in the opacity results in $\beta_{1-3\text{mm}}$ increasing with radius (cf. Fig. 3 in Ricci et al., 2010a). If the radially decreasing upper grain size a_{max} reaches sizes just below mm, then the peak in opacity will produce also a peak in the radial profile of $\beta_{1-3\text{mm}}$ (the size of which depends much on the assumed opacity), which can be seen in Fig. 8.3. Thus, even though a_{max} is monotone in radius, $\beta_{1-3\text{mm}}$ does not need to be monotone.

8.4 Discussion and Conclusions

In this Letter, we present the first in-depth comparison of simulated grain size distributions and observed mm spectral indices of YSOs in the Taurus and the Ophiuchus star-forming

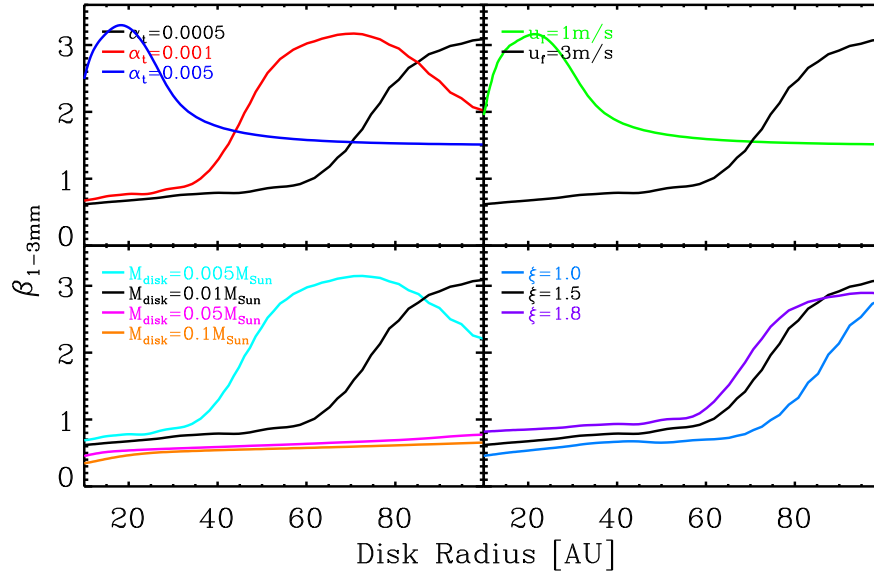


Figure 8.3: Predicted profiles of the dust opacity index at mm-wavelengths for different variations of the fiducial model. The colors correspond to the parameters shown in Fig. 8.1.

regions. Additionally we present the first predictions of the radial profile of the dust opacity index at mm wavelength which are consistent with the limits set by Isella et al. (2010).

Low values of the observed mm-slopes are quite naturally reproduced by our models, favoring low values of ξ and α_t as well as fragmentation threshold velocities above 1 m s^{-1} . However, a simultaneous match to the observed range of flux levels requires a reduction of the dust mass by a factor of a few up to about 30. This over-prediction of fluxes cannot be fixed by simply reducing the disk mass since the predicted $\alpha_{1-3\text{mm}}$ would be too large for smaller disk masses. Opacities induce a large uncertainty in the flux levels. However, considering the results of Draine (2006), it seems implausible that the large spread in observed fluxes for different disks with similar $\alpha_{1-3\text{mm}}$ (which is probably even larger as very faint disks are not contained in the sample) can be explained by different grain mineralogy alone.

The aforementioned reduction of observable dust could be due to radial drift at a reduced rate or during an earlier epoch (drift has been artificially suppressed in this work in order to explain the low values of $\alpha_{1-3\text{mm}}$ by $\gtrsim 1 \text{ mm}$ sized grains). Another possible explanation is grain growth to even larger sizes as these bodies have a small opacity coefficient per unit mass.

Finally, a different dependence between $\alpha_{1-3\text{mm}}$ and the observed flux $F_{1\text{mm}}$ might also

originate from disk surface densities profiles that differ from what we have assumed in this work. This possibility, as well as the effect of a different dust composition, will be considered in a future work. Future work will also consider different opacity and composition of the grains as well as time dependent simulations of the gas surface density and the dust evolution.

Trapping dust particles in the outer regions of protoplanetary disks

From Pinilla, Birnstiel, Ricci, Dullemond, Testi, & Natta, to be submitted to A&A

Abstract

During the early stages of planet formation when dust particles grow by coagulation, they acquire high relative velocities that lead to destructive collisions. Additionally, when the dust particles grow to some maximum value, they move quickly to the star due to the radial drift. In order to explain grain growth to mm sized objects, as observed in protoplanetary disks at sub-mm and mm wavelengths, we investigate whether strong inhomogeneities in the gas density profiles cause pressure bumps that allow to reduce the radial drift. We use coagulation/fragmentation and disk-structure models, to simulate the evolution of dust in a bumpy surface density profile which we mimic with a sinusoidal disturbance. For different values of the amplitude and length scale of the bumps, we investigate the ability of this model to produce and retain large particles on megayears time scales. Using the Common Astronomy Software Applications ALMA simulator, we study how future observations with ALMA help to constrain the physics of dust evolution in protoplanetary disks. We present the favorable conditions to trap dust particles and the corresponding calculations predicting the spectral slope in the mm-wavelength range, to compare with current observations. In addition, we present simulated images using different antenna configurations of ALMA at different frequencies, to show that the ring structures are detectable at approximately distances of the Taurus Auriga or Ophiucus star forming regions.

9.1 Introduction

The study of planet formation is an important field in astronomy with an increasing research since the middle of the twentieth century, however there are still countless unanswered questions. One of these questions is the observed grain growth to mm sized particles

in the outer disk regions (Andrews & Williams, 2005; Isella et al., 2009; Guilloteau et al., 2011) that suggests a mechanism operating that prevents the rapid inward drift (Klahr et al., 1997; Brauer et al., 2007; Johansen & Youdin, 2007). Different efforts are aimed to explain theoretically the growth from small dust particles to planetesimals, which have led to the development of different numerical models (e.g. Nakazawa et al., 1981; Dullemond & Dominik, 2005; Brauer et al., 2008a; Zsom & Dullemond, 2008; Okuzumi, 2009; Birnstiel et al., 2010a). Due to the fact that circumstellar disks exhibit a wide range of temperatures, they radiate from micron wavelengths to millimeter wavelengths, which is why they can be observed with infrared and radio telescopes. With the construction of different kinds of these telescopes, e.g. Spitzer, Herschel, SMA, EVLA or ALMA, astronomers can observe with more details the material inside accretion disks around young stars. The parallel development of theory and observations have allowed astronomers to study the different stages of planet formation, making this topic one of the most active fields in astrophysics today.

The first stage of planet formation, the growth from sub-micron sized particles to larger objects is a complex process that contains many physical challenges. Owing to the fact that the gas moves with sub-keplerian velocity due to the gas pressure gradient, the dust particles must drift inwards. Before a large object can be formed, the radial drift causes solid particles to move towards the star. Moreover, fragmentation due to high relative velocities does not allow dust particles to form larger bodies. The combination of these two problems is called “meter-size barrier” because if we have one meter sized object at one AU, after around 100 years, due to the radial drift the object moves towards the star, preventing that any larger object could be formed. In addition, if we do not take into account the radial drift in our models and we force the particles to stay in the outer regions of the disks (Birnstiel et al., 2010a), the solid particles reach high relative velocities that lead to fragmentation collisions.

The observations in the inner regions of the disk, where planets like Earth should be formed, are very difficult because these regions are so small on the sky that few telescopes can spatially resolve them and also these regions are optically thick. However, what amounts to the meter-size barrier in the inner few AU is a “millimeter-size barrier” in the outer regions of the disk. These outer regions are much easier to spatially resolve. Moreover, one can use millimeter observations, which probe precisely the grain size range of the millimeter-size.

Observations of protoplanetary disks at sub-millimeter and mm wavelengths show that the disks remain dust-rich during several million years (Andrews & Williams, 2005; Isella et al., 2009; Hernández et al., 2007; Ricci et al., 2010a; Banzatti et al., 2011). However, it is still not clear how to prevent the inward drift and how to explain theoretically that mm-sized particles are observed in the outer regions of the disk. Different mechanisms of planetesimal formation have been proposed to resist the rapid inwards drift like: gravitational instabilities (Youdin & Shu, 2002), the presence of zonal flows (Johansen et al., 2009) or Rossby wave instabilities (RWI) of viscously accumulated gas which form vortices (Regaly et al., submitted to A&A). With the model presented here, we want to imitate these mechanisms by artificially adding pressure bumps onto a smooth density profile.

Table 9.1: Parameters of the model

Parameter	Values
A	0.1
	0.3
f	1.0
	3.0
α	10^{-3}
$R_{\star}[R_{\odot}]$	2.5
$T_{\star}[K]$	4300
$M_{disk}[M_{\odot}]$	0.05
$\rho_s[gr/cm^3]$	1.2
$v_f[m/s]$	10

We add a sinusoidal function to the gas density profile as an arbitrary approximation of pressure bumps. These pressure bumps have same strength as the ones added to the density, following a simple equation of state for the pressure in the disk $P = \rho c_s^2$. Depending on the size of the particle, the dust grains will be nearly perfectly trapped in the pressure peaks, because a positive pressure gradient can causes that dust particles move outwards. Nevertheless, the problem is very challenging because turbulence can mix part of the dust particles out of the bumps, so that overall there may still be some net radial inward drift, or more importantly, dust fragmentation may convert part of the large particles into smaller dust particles, which are less easily trapped and thus drift more readily inward.

The purpose of this paper is to model the combination of three processes: the radial drift, the radial turbulent mixing and the dust coagulation/fragmentation cycle in a bumpy surface density profile. With the intention of finding out how the presence of pressure bumps can help to explain the retainment of dust pebbles in the outer regions of protoplanetary disks, as is observed. In addition, we show simulated images using different antenna configurations of the complete stage of ALMA, to study if it is possible to detect these kind of inhomogeneities with future ALMA observations. This paper is ordered as follows: Sect. 2 will describe the coagulation/fragmentation model and the sinusoidal perturbation that we take for the perturbation. Section 3 will describe the results of the simulations, the comparison with current observations and the future observations with ALMA. Finally, section 4 will summarizes our results and the conclusions of this work.

9.2 Dust Evolution Model

To simulate the growth of dust particles, we use a coagulation/fragmentation code (?). This model combine disk-evolution and dust-evolution model which includes: radial drift, relative azimuthal velocities, radial dependence of fragmentation critical velocities and viscous resistance for Stokes-drag regime.

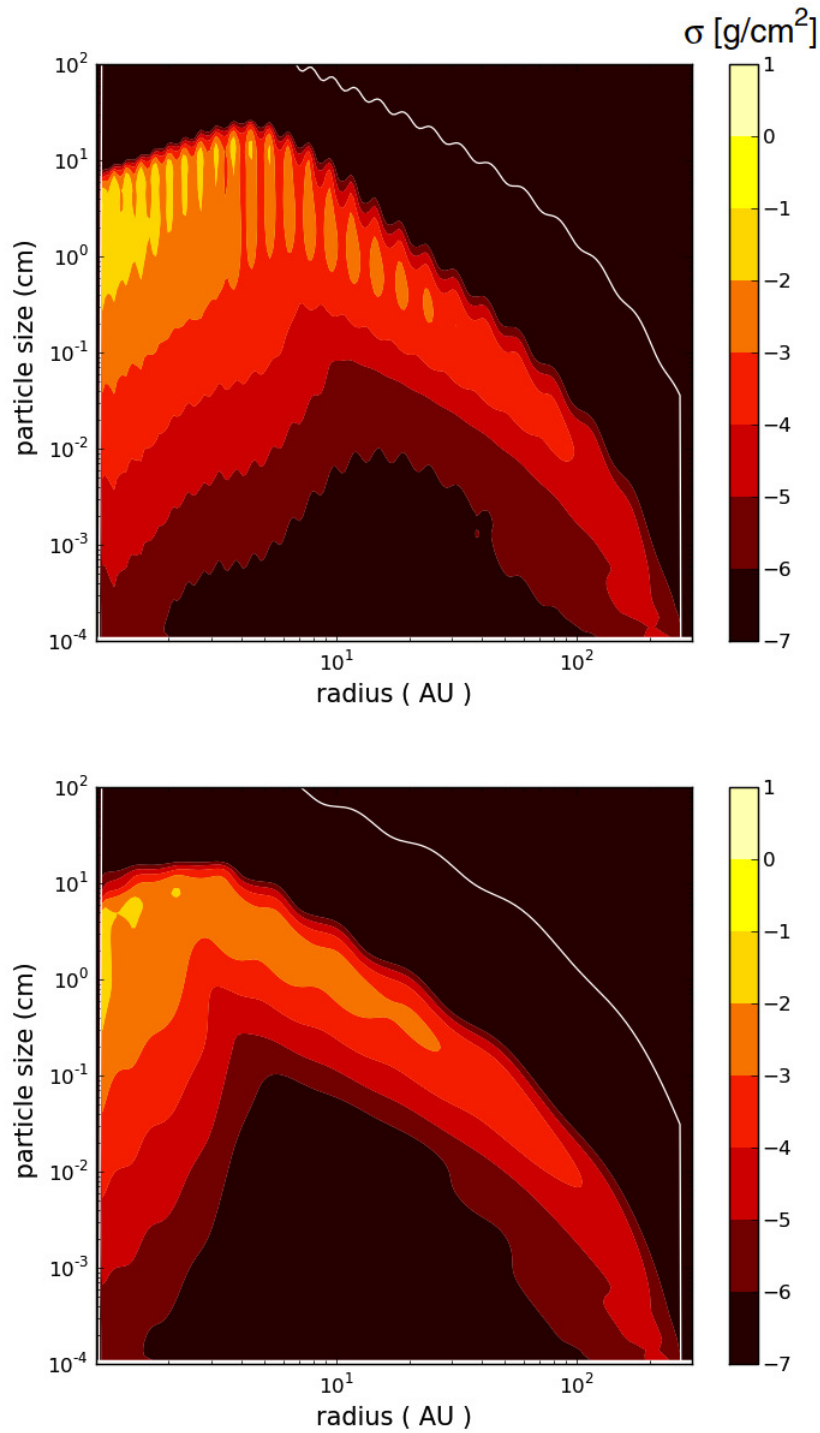


Figure 9.1: Vertically integrated dust density distribution at 1 Myr for $A = 0.1$ and $f = 1$ (top) and $A = 0.1$ and $f = 3$ (bottom). The solid white line shows the particle size corresponding to a Stokes number of unity

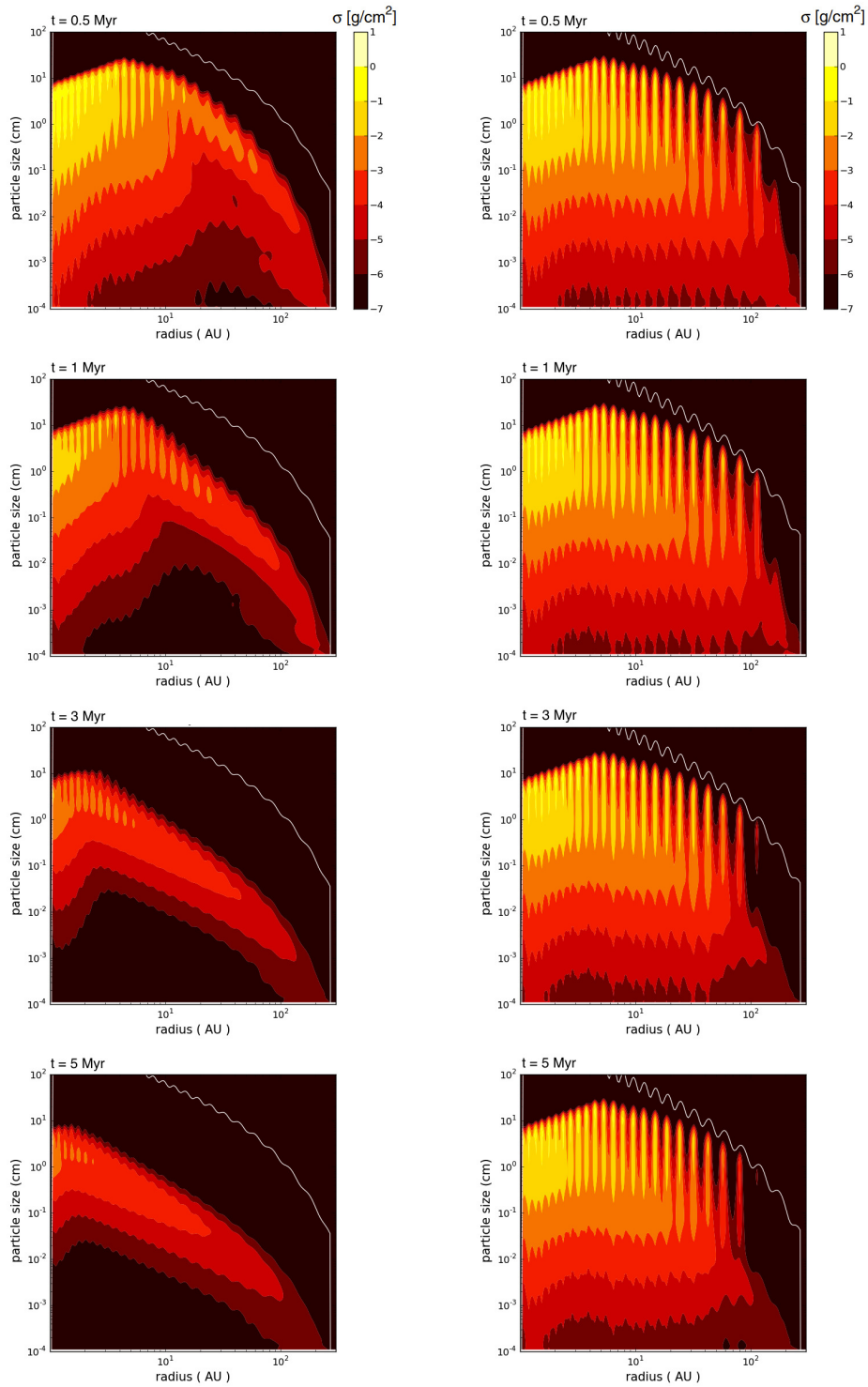


Figure 9.2: Vertically integrated dust density distribution with fixed value of length scale as $f = 1$, for $A = 0.1$ (left column) and $A = 0.3$ (right column) at different times 0.5 Myr, 1.0 Myr, 3.0 Myr and 5.0 Myr from top to bottom respectively. The solid white line shows the particle size corresponding to a Stokes number of unity.

Considering a perturbation for the surface gas density, given by:

$$\Sigma'(r) = \Sigma(r) \left(1 + A \cos \left[2\pi \frac{r}{L(r)} \right] \right), \quad (9.1)$$

where the unperturbed gas surface density $\Sigma(r)$ (Lynden-Bell & Pringle, 1974) is:

$$\Sigma(r) = \Sigma_0 \left(\frac{r}{r_c} \right)^{-\gamma} \exp \left(-\frac{r}{r_c} \right)^{2-\gamma}, \quad (9.2)$$

where r_c is the characteristic radius, taken to be 60AU, and γ is a power index equal to 1, which are the median values found from high angular resolution imaging in the sub-mm of disks in the Ophiucus star forming regions (Andrews & Williams, 2007b). The wavelength $L(r)$ of the sinusoidal perturbation depends on vertical disk scale-height $H(r)$ by a factor f as

$$L(r) = fH(r), \quad H(r) = \frac{c_s}{\Omega}. \quad (9.3)$$

where the isothermal sound speed c_s and the Keplerian angular velocity Ω are defined as

$$c_s^2 = \frac{k_B T}{\mu m_p}, \quad \Omega = \sqrt{\frac{GM_\star}{r^3}}. \quad (9.4)$$

with k_B being the Boltzmann constant, m_p the mass of the proton and μ is the mean molecular mass, which in proton mass units is taken as $\mu = 2.3$. For an ideal gas, the pressure is defined as

$$P(r) = c_s^2 \rho(r, z), \quad (9.5)$$

where $\rho(r, z)$ is the gas density, such that $\Sigma'(r) = \int_{-\infty}^{\infty} \rho(r, z) dz$. When the particles are large enough and they are not forced to move as the gas, they experience a head wind, because of the sub-Keplerian velocity of the gas and therefore they lose angular momentum and move inwards. In this case, the resulting drift velocity of the particles is given by (Weidenschilling, 1977):

$$u_{\text{drift}} = \frac{1}{\text{St}^{-1} + \text{St}} \frac{\partial_r P}{\rho \Omega} \quad (9.6)$$

where St denotes the Stokes number that describes the coupling of the particle to the gas. In general, the Stokes number is defined as the ratio between the eddy turn-over time ($1/\Omega$) and the stopping time. For larger bodies, the Stokes number is much greater than one, which implies that the particles are not affected by the gas drag, consequently they move on Keplerian orbits. When the particles are small, $\text{St} \ll 1$, they are strongly coupled to the gas. In the Epstein regime, where the ratio between the mean free path of the gas

molecules λ_{mfp} and the particle size, denoted by a , satisfies that $\lambda_{\text{mfp}}/a \geq 4/9$, the Stokes number is given by:

$$\text{St} = \frac{a\rho_s \pi}{\Sigma} \frac{\pi}{2}, \quad (9.7)$$

where ρ_s is the solid density of the dust grains, that is taken to be constant (see table 9.1). In this case particles are small enough to be in this regime. Parameterizing the radial variation of the sound speed via

$$c_s \propto r^{-q/2}, \quad (9.8)$$

where for a typical disk, the temperature is assumed to be a power law such that $T \propto r^{-q}$, which is an approximation of the temperature profile taken for this model. Therefore, the wavelength of the perturbation $L(r)$ scales as:

$$L(r) = fH(r) \propto fr^{(-q+3)/2}. \quad (9.9)$$

The pressure bumps have the same amplitude A and wavelength $L(r)$ than the density, because the over pressure is induced adding inhomogeneities to the gas surface density and parameterizing the temperature on the midplane by a power law (Nakamoto & Nakagawa, 1994). The model taken here can artificially imitate e.g. the case of zonal flows in protoplanetary disks (?), where over densities create pressure bumps. Or we can also mimic the case of Rossby wave instabilities where the viscosity drops, changing the density profile and causing a local inversion of the pressure gradient.

To constrain the values of the amplitude and wavelength of the perturbation, it is important to analyze the necessary conditions to have outwards movement of the dust particles and to study the Rayleigh stability of the disk. In this work, we only work with perturbations that allow to the disk to stay stable with time. The Rayleigh criterion establishes that for a rotating fluid system, in the absence of viscosity, the angular momentum must be transported outwards, which implies that

$$\frac{\partial}{\partial r}(rv_\phi) > 0, \quad (9.10)$$

For a typical α -turbulent disk, the viscous time scale is much greater than the time that the disk needs to recover the Rayleigh stability, this implies that the disk should remain quasi stable at all time. The angular velocity of equation (9.10) is given by:

$$v_\phi^2 = v_k^2 + \frac{r}{\rho} \frac{\partial P}{\partial r} = v_k^2(1 - 2\eta) \quad (9.11)$$

with

$$\eta = -\frac{1}{2r\Omega^2\rho} \frac{\partial P}{\partial r}. \quad (9.12)$$

The Rayleigh stability of the disk depends on the amplitude and the width of the bumps. In this case, we want to study the influence of the amplitude of the perturbation so we

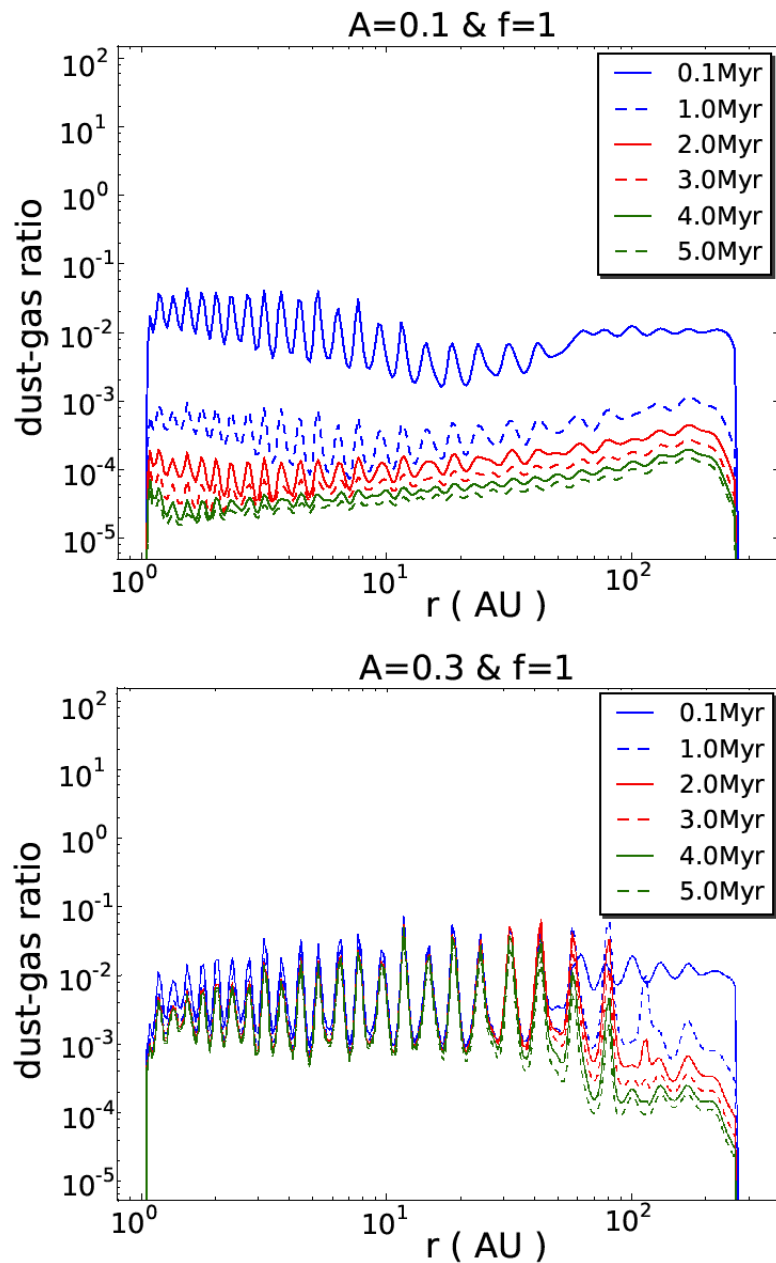


Figure 9.3: Dust to gas mass ratio at the disk midplane for different times of disk evolution and the parameter summarizing in Table 9.1: $A = 0.1$ and $f = 1$ (top) and $A = 0.3$ and $f = 1$ (bottom)

constrain the value of the wavelength of the perturbation, f equals to unity, such that the possible formed structures can be compared or detected with current or future observations. Taking the perturbed gas density of equation (9.1), it is possible to find the upper limit of the amplitude to satisfy the equation (9.10). This calculation lets the maximum value of the amplitude A to be at most $\sim 35\%$ of the aspect ratio of the disk H/r .

On the other hand, since the drift velocity is given by equation (9.6), to prevent the inwards drift, the value of η from equation (9.12) must be negative, this implies that the pressure gradient has to be positive for some regions of the disk, therefore this condition is fulfilled. Doing this calculation for the condition that $\eta < 0$, in order to retain particles, we get that the values of the amplitude A have to be at least equal to about 10% of the aspect ratio of the disk. Summarizing the upper and lower values of the amplitude should be $0.10 \lesssim A \lesssim 0.35$, when the width of the amplitude is constrained to be $f = 1$.

Taking into account the growth-fragmentation cycle and the existence of pressure bumps, the radial drift efficiency can be reduced if the bumps have favorable values for the amplitude and the length scale. When the particles grow by coagulation, they reach a certain size with velocities high enough to cause fragmentation (fragmentation barrier), the maximum value of the grain size is given by (Birnstiel et al., 2010b):

$$a_{\max} \simeq \frac{\Sigma}{\pi \alpha \rho_s} \frac{v_f^2}{c_s^2}, \quad (9.13)$$

where v_f is the fragmentation velocity. Laboratory experiments and theoretical work suggest that typical values for fragmentation velocities are of the order of few $m s^{-1}$ for silicate dust (see Blum & Wurm, 2008). Recent collision experiments (Güttler et al., 2010) and numerical simulations (Zsom et al., 2010) show that there is an intermediate regime where particles should bounce. In this work, we do not take into account this regime since there is still many open questions in this field. The fragmentation velocity is taken as $v_f = 10 m/s$. All the parameters used for this model are summarized in Table 9.1.

The dust grain distribution $n(m, r, z)$ is the number of particles per cubic centimeter per gram interval in particle mass, which depends on the grain mass, distance to the star r and height above the mid-plane z , such that

$$\rho(r, z) = \int_0^\infty n(m, r, z) \cdot m dm, \quad (9.14)$$

is the total dust volume density. The quantity $n(m, r, z)$ can change due to grain growth and distribution of masses via fragmentation. The vertically integrated dust surface density distribution per logarithmic bin is

$$\sigma(r, a) = \int_{-\infty}^\infty n(r, z, a) \cdot m \cdot a dz, \quad (9.15)$$

where mass and sized particles are connected via $m = 4\pi/3\rho_s a^3$. The total dust surface

density is then

$$\Sigma_d(r) = \int_0^\infty \sigma(r, a) d \ln a. \quad (9.16)$$

9.3 Results

9.3.1 Density distribution of dust particles

The simulations have been done with a disk of mass $0.05M_\odot$, with a surface density described by equation (9.1) from 0.1 AU to 300 AU, around a star with one solar mass. Figure (9.1) shows the vertically integrated dust density distribution, taking into account: coagulation, radial mixing, radial drift and fragmentation, after 1 Myr of the evolution of the protoplanetary disk. The solid white line shows the particle size corresponding to a Stokes number of unity.

Both plots of Figure (9.1) have the same amplitude of the sinusoidal perturbation $A = 0.1$. The factor f which describes the width of the perturbation, is taken to be $f = 1$ for the top plot, and $f = 3$ for the bottom plot of Figure (9.1). This result shows that: first, the amplitude $A = 0.1$ of the perturbation is not high enough to have a pressure gradient such that particles can be retained in the outer regions of the disk. Instead the dust particles are still affected by radial drift, they move inwards and the high relative velocities lead to reach the fragmentation velocity such that the particles do not grow over mm size particles in the outer regions. Second, taking a greater value of the factor f , that implies a longer wavelength for the perturbation, at the same amplitude, implies that the retention of particles is even weaker. We show that the trapping efficiency is higher when the wavelength of the perturbation is shorter, however if we want to compare these kind of perturbations with future observations (e.g. ALMA), the width of the perturbation has to be large enough to have detectable structures. In this case, due to the assumption of the presence of a bumpy surface density, will be regions on the disk where the dust accumulate. The separations of these ring structures depend of f , if the width of the perturbation is too short, so the rings will be very closed each other such that it would be very difficult to resolve them.

On the other hand, for longer widths, we should have therefore higher values of the amplitudes, however the disk becomes easily unstable when the amplitude goes up, this is the reason why we keep our results only for $f = 1$ and we take two different possible values for the amplitude.

Figure (9.2) compares the surface density distribution for two different values of the amplitude of the perturbation $A = 0.1$ and $A = 0.3$, at different times of evolution. Taking $A = 0.3$, we can notice that in the pressure bumps, there is high density of dust particles, even after 5 Myr of evolution for a maximum radius around 100 AU.

To break through the meter-size barrier, it is important to take into account the two sources of relative velocities: radial drift and turbulence. In the bumps the radial drift relative velocities are zero, but there are still relative velocities due to the turbulence.

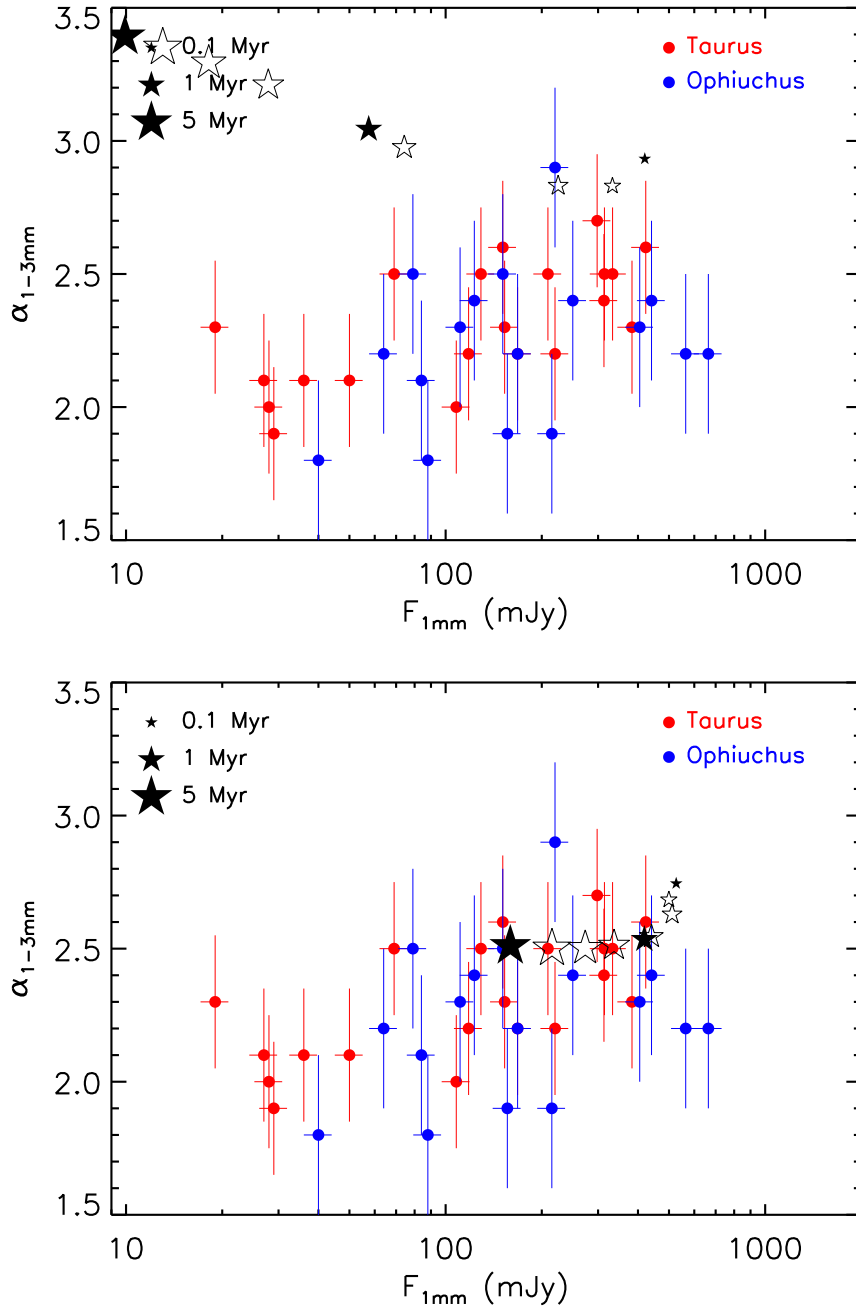


Figure 9.4: Comparison of the observed fluxes at mm-wavelengths of the Taurus (red dots) and the Ophiuchus (blue dots) star forming regions (Ricci et al., 2010a,b, 2011) with the results of the simulations at different times of the disk evolution (star-dots). Results for $A = 0.1$ (top) and $A = 0.3$ (bottom)

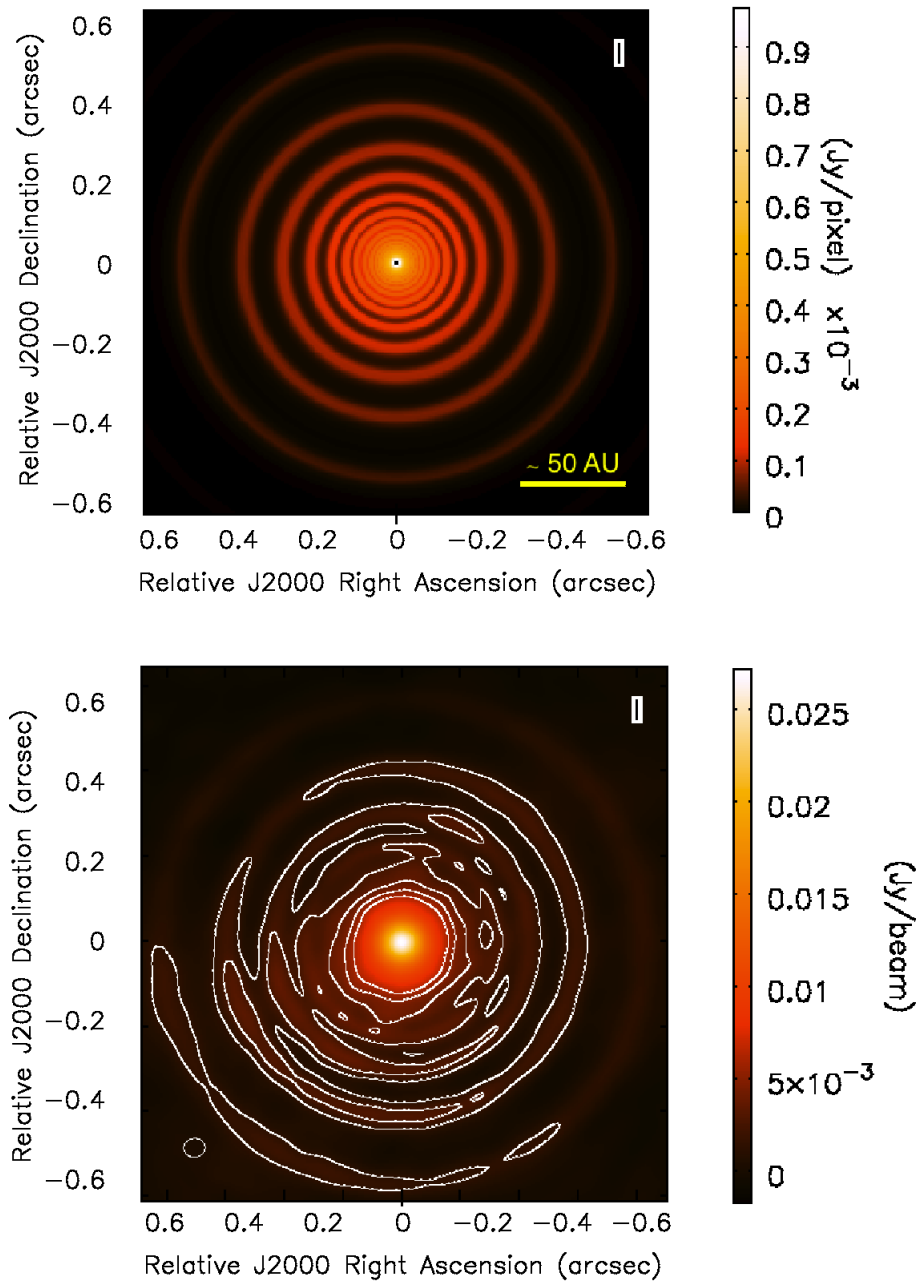


Figure 9.5: Disk image at 2 Myrs and observing wavelength of 0.45 mm, the amplitude of the perturbation is $A = 0.3$ and the factor $f = 1$ for: disk model with parameters of Table 9.1 (left) , simulated image using full configuration of ALMA (right) with a maximum value of baseline of around 3km and with an observing time of 4 hours.

Therefore, it is necessary get a constraint on the turbulence. The largest turbulent relative velocity between particles is given by (Ormel et al., 2007a),

$$\Delta u_{max} \simeq 2\alpha c_s^2 \quad (9.17)$$

Therefore, to break through the meter size barrier, we must have that

$$u_f > \sqrt{2\alpha} c_s. \quad (9.18)$$

This last condition is satisfied in the outer region of the disk when the conditions of the perturbation are $A \geq 0.3$ and $f = 1$. With the turbulence parameter fixed to $\alpha = 10^{-3}$ and with the low temperatures at the outer regions of the disk, $T \sim 10K$, the relative velocities due to the turbulence are lower than the taken fragmentation velocity, allowing to the particle to grow over mm sizes.

Figure 9.3 shows the radial dependence of the dust-to-gas ratio for different times of the simulation and two values for the perturbation amplitude. For $A = 0.1$ (top plot of Figure 9.3), we can see that the dust-to-gas ratio decreased significant after few Myrs of the dust evolution, this implies that the dust particles does not grow considerably. Due to fragmentation the dust particles collide and become even smaller. Then, because of the turbulence and radial drift, the dust particles mix and move inwards. Since the dust particles remain vary small, the dust-gas ratio decreases and become almost constant with time, which implies that the dust particles are small enough to be well coupled to the gas.

Whereas, due to the strong over pressures at $A = 0.3$ (bottom plot of Figure 9.3), the dust-to-gas ratio remains almost constant with time for $r < 100AU$, oscillating radially between 10^{-3} to 10^{-1} . This oscillating behavior, even after 5 Myr of dust evolution, is possible thanks to the fact that the particles are retained in the bumps and grow enough to make the dust-gas ration higher inside the bumps. Only around $\sim 100AU$ from the star, the dust to gas ratio decreases significantly. Summarizing, due to the presence of the pressure bumps with an amplitude $A = 0.3$, the dust-gas mass ratio increases locally with the dust evolution. This implies that the drift is counteracted by the positive local pressure gradient, allowing that the time scales for the growth are comparable with the disk evolution times, i. e. with the drift time scales.

9.3.2 Comparison to current observations

We compare the opacity index (or flux index) by the model explained above with observational data of Ricci et al. (2010a). A crude approximation of the flux is given by

$$F_\nu = \frac{M_{\text{dust}}}{d^2} \kappa_\nu B_\nu(T), \quad (9.19)$$

which depends on the mass of optically thin dust M_{dust} , the Planck function $B_\nu(T)$, the source distance d and the opacity κ_ν . Since dust is the dominant opacity source, it is fundamental to describe dust properties. The opacity, in the millimeter wavelength regime,

Table 9.2: Atmospheric conditions, total flux and rms for the simulated observations at 140pc and at different observing wavelengths. The pwv value takes into account the expected conditions for ALMA. The simulated images are using the full ALMA, but the antenna configuration is chosen in order to have the best conciliation between resolution and sensitivity.

Amplitude	Wavelength (mm)	Atmospheric conditions		Total Flux (Jy)	rms (Jy)
		pwv (mm)	τ_0		
A=0.3	0.45	0.5	0.60	6.9×10^{-1}	7.5×10^{-4}
	0.66	1.0	0.40	7.6×10^{-1}	3.8×10^{-4}
	1.00	1.5	0.20	2.2×10^{-1}	1.4×10^{-4}
	3.00	2.3	0.03	4.0×10^{-1}	2.0×10^{-5}
A=0.1	1.00	1.5	0.20	1.6×10^{-2}	1.3×10^{-5}

can be approximated by a power law $\kappa_\nu \propto \nu^\beta$, which means that in the Rayleigh-Jeans regime, where $h\nu \ll k_B T$, the flux is approximated to

$$F_\nu \propto \nu^{\beta+2} \propto \nu^{\alpha_{1-3mm}}. \quad (9.20)$$

The index α_{1-3mm} gives us information about the size distribution of the dust in the disk. When $\alpha_{1-3mm} \lesssim 3$, the dust particles have acquired millimeter sizes (Testi et al., 2001; Birnstiel et al., 2010b). The range of temperatures that we have been taken, allow to work on Rayleigh-Jeans regime.

Figure (9.4) shows the predicted fluxes and the spectral index for the results of the simulations at different times of the disk evolution, and samples of observations of the star forming regions of Taurus-Auriga and ρ -Oph. In Figure (9.4) it is possible to compare the effect on the flux and the spectral index for two different values of the amplitude of the perturbation $A = 0.1$ (top) and $A = 0.3$ (bottom). For $A = 0.1$ we can see that after several Myrs, the spectral indices are larger for modeled data because in this case, the particles cannot grow due to the rapid inward drift and the low pressure gradient, which confirms that an amplitude of about 10% of the aspect ratio of the disk is not enough in order to trap particles in the pressure bumps. However, for $A = 0.3$ the spectral indices decrease and the results from the simulations fall into the observed sample region, due to the high value of the amplitude for the perturbation, the pressure gradient is enough to counteract the radial drift and allow particles to grow locally in the pressure bumps. This allows to have values of $\alpha_{1-3mm} \lesssim 3$ that are in agreement with the observed presence of mm size particles in the outer regions of disks.

In the work from Birnstiel et al. (2010b), they compared between simulated grain size distributions and the mm spectral indices of the same set of observations of Taurus and the Ophiuchus star-forming regions. However, in their work, they did not take into account radial drift, therefore they restrict particles to stay artificially in the outer regions of the disk. They found that most of the observable fluxes are lower than the simulated

fluxes, and also that the spectral index $\alpha_{1-3\text{mm}}$ was higher than the observable $\alpha_{1-3\text{mm}}$. This evidences that, ignoring radial drift and with a smooth pressure, all larger grains in the outer disk would disappear quicker than observations indicate. In this work, taking the radial drift into account and the trapping of particles in pressure bumps, we get a better match between observable and simulated fluxes. Here our simulations, specially with $A = 0.3$ allow some particles to grow and reduce the fluxes and the spectral index for a better prediction of those observations.

9.3.3 Future observations with ALMA

The Atacama Large Millimeter/sub-millimeter Array (ALMA) will provide an increase in sensitivity and resolution to observe in more detail the structure and evolution of proto-planetary disks. With a minimum beam diameter of ~ 5 mas at 900GHz, ALMA will offer a resolution down to 2 AU for disks observed in Orion and sub-AU for disk in Taurus-Auriga (Cossins et al., 2010a). Using the Common Astronomy Software Applications (CASA) ALMA simulator (version 3.2.0), we run simulations to produce realistic ALMA observations of our model using the full configuration of ALMA of 54 antennas of 12-m each and other 12 antennas of 7-m each.

The simulated images were obtained in order to have simultaneously the most favorable values for the resolution and sensitivity that should be available with ALMA. The spatial resolution depends on the observing frequency and the maximum baseline of the array, we do not take the largest array because for very large baselines, the sensitivity could be not enough for the tiny regions that we will need to observe. Therefore, we used different antenna arrays depending on the observing frequency to get the best possible resolution with enough sensitivity. The sensitivity depends on the number of antennas, the bandwidth (which is taken as $\Delta\nu = 8\text{GHz}$ for continuum observations) and the total observing time that is fixed to four hours for each simulation. The sensitivity also depends on the atmospheric conditions, ALMA is located in Llano de Chajnantor Observatory, where the precipitable water vapor (pwv) varies between 0.5 mm and 2.0 mm depending on the observable frequency.

Figure (9.5) shows a comparison between the model image and a simulated image using the full configuration of ALMA with a maximum baseline of around 3 km and an observation total time of four hours. This image is for observing wavelength of 0.45mm (Band 9 of ALMA 620 – 750 GHz). It is important to note that the simulated images take into account the atmospheric conditions and the expected receiver noise based on technical information of the antennas, but the residual noise after data calibrations and its incertitudes are not considered. We can note (See Figure 9.5-right plot) that with one of the full configurations (max. baseline ~ 3 km), it is possible to distinguish some ring structures due to the fact that the dust has drifted considerably into the rings compared to the gas. The antenna configuration is chosen to have the optimal values of sensitivity and resolution at the same time as we have explained before. The contours are at 2, 4, 6, 8 the rms vale. These values are summarized in table 9.2.

In Figure 9.6 we note again the importance to have a high value of the amplitude of the

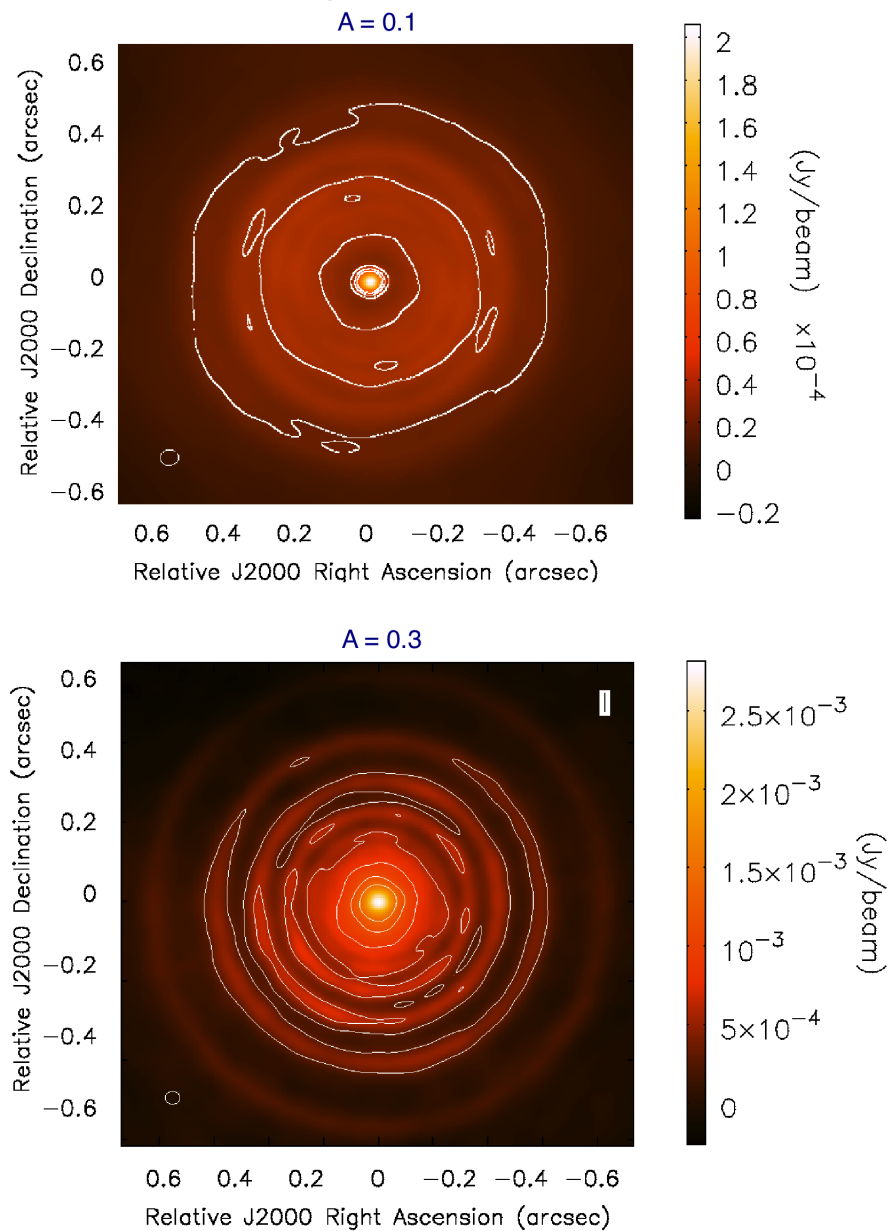


Figure 9.6: Comparison between the simulated images for an observing wavelength of 1 mm and 2 Myr of evolution, using full antenna configuration of ALMA for two different values of the amplitude of the perturbation: $A = 0.1$ (top) and $A = 0.3$ (bottom). The contour plots are at $\{2, 4, 6, 8\}$ the corresponding rms value (Table 9.2)

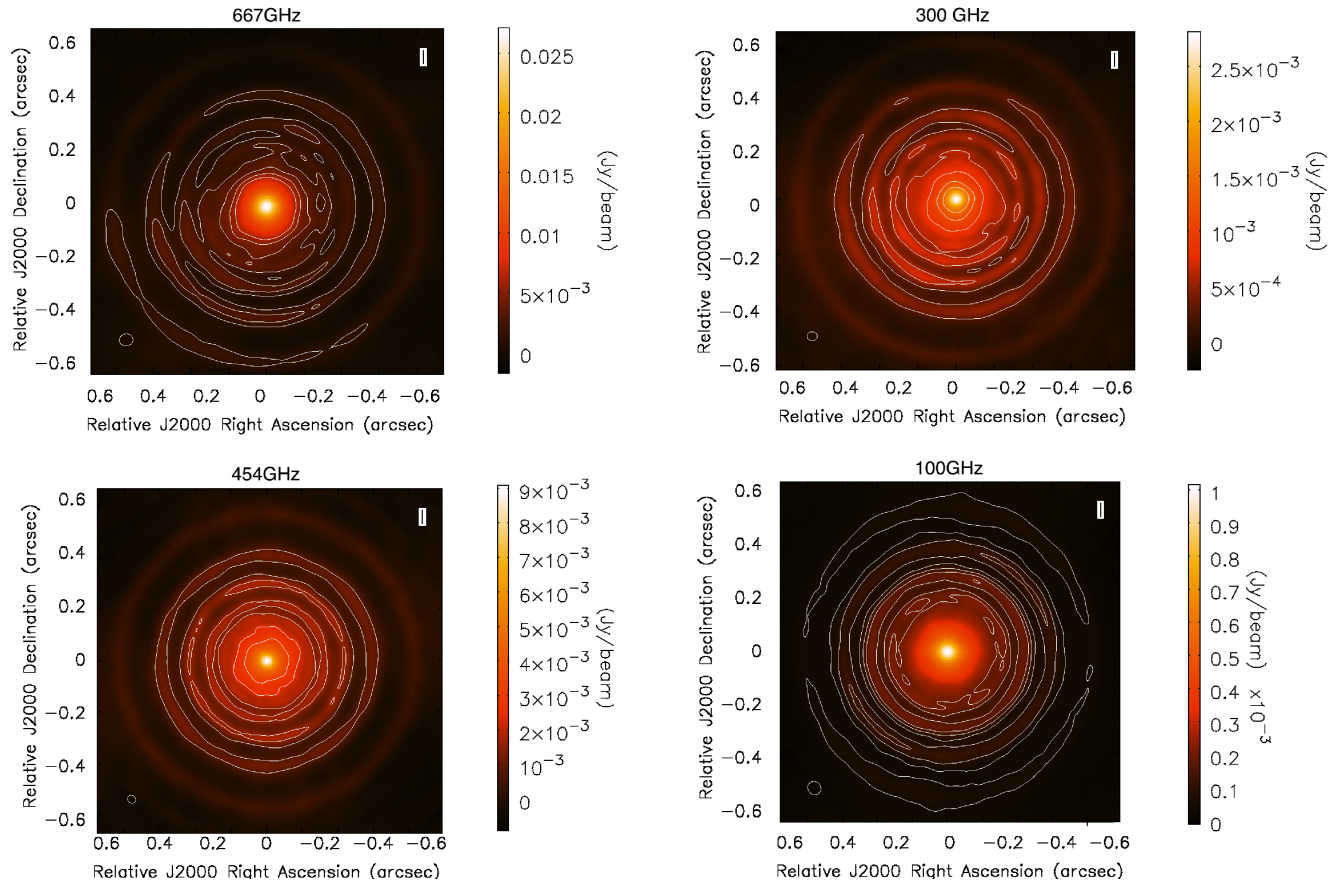


Figure 9.7:]

Disk simulated images with parameters of Table (9.1), $A = 0.3$ and $f = 1$ at 2 Myr of the disk evolution and for observing frequency of: 667 GHz with a maximum baseline of around 3 km (top left), 454 GHz (bottom right) with a maximum baseline of around 4 km, 300 GHz (top left) with a max. baseline of around 7 km and 100 GHz with a maximum baseline of 16 km (bottom right)

perturbation for future ALMA observations. Both images of the figure have been computed with the complete antenna configuration of ALMA for an observing wavelength of 1 mm and 2 Myr of the disk evolution. We can see that for $A = 0.1$ it is not possible to detect any structures around the star even considering a perfect data calibration. The contour plots are at $\{2, 4, 6, 8\}$ the corresponding rms value (see table 9.2).

Figure 9.7 compares the simulated images at different observing wavelengths using different antenna configurations of ALMA. For each image, the contour plots are at $\{2, 4, 6, 8\}$ the corresponding rms value. The antenna configuration is chosen by CASA depending on the expected resolution. The best image is obtained at 100 GHz and a maximum baseline of 16 km (most extended ALMA configuration), where it is possible to detect clearly the most external ring structure and some internal ring structures. Nevertheless, with more compact configurations at different frequencies it is still possible to detect some structures from the presence of the pressure bumps which allow the formation of mm-sized particles. However, it is important to take into account that the simulated images of figures 9.5, 9.6, 9.7 and 9.8 are considering a perfect data calibration after observations, for long baselines and high frequencies the calibration effects become more important.

Taking the ratio of the images at two different wavelengths and, we will have the values of the spectral index α_{1-3mm} , which indicates the location of mm-sized grains. With the full configuration of ALMA and a maximum value of the baseline of 12 km for both observing frequencies, some regions with large particles are distinguished. In Figure 9.8 is the spectral index of the model data (top plot) and the spectral index taking two simulated images at 0.45mm and 3.0mm, with a total observing time of four hours.

9.4 Conclusions

Theoretical models of dust evolution in protoplanetary disks show that the growth from sub-micron sized particles to larger objects is prevented basically by two phenomena: radial drift and fragmentation. Nevertheless, infrared and radio observations show that millimeter sized particles can survive under those circumstances in the outer regions of disks. Therefore, various theoretical efforts have been focused on explaining the survival of those bodies.

Taking into account strong inhomogeneities expected to be in the gas density profile (e.g. zonal flows, dead zone boundaries, etc), and using the coagulation/fragmentation and disk-structure models by Birnstiel et al. (2010a), we have investigated how the presence of pressure bumps can cause the reduction of radial drift, allowing the existence of millimeter sized grains and the agreement with observations. In this work, we assumed a sinusoidal function for the surface gas density to simulate pressure bumps. Future efforts will be focused on relating this work with some hydrodynamic effects like: the presence of zonal flows, vortices, baroclinic instabilities or dead zones.

The results presented suggest that the presence of pressure bumps with a width of the order of the disk scale-height and an amplitude of 30% of the aspect ratio of the disk, provide the necessary physical conditions for the survival of larger grains in a disk

with properties summarized in Table 9.1. Comparisons between the observed fluxes of the Taurus and Ophiuchus star forming regions with the results of the model presented ratify that the effect of the radial drift is reduced allowing particles to grow.

The simulated images using CASA ALMA simulator (version 3.2.0) show that, with different antenna configuration of the final ALMA stage, the ring structures, due to the presence of the pressure bumps, should be detectable. Future ALMA observations will have an important impact for understating the first stages of planet formation and it will be very important to investigate if the grain growth can be explained with the presence of these kind of inhomogeneities in the gas density profile.

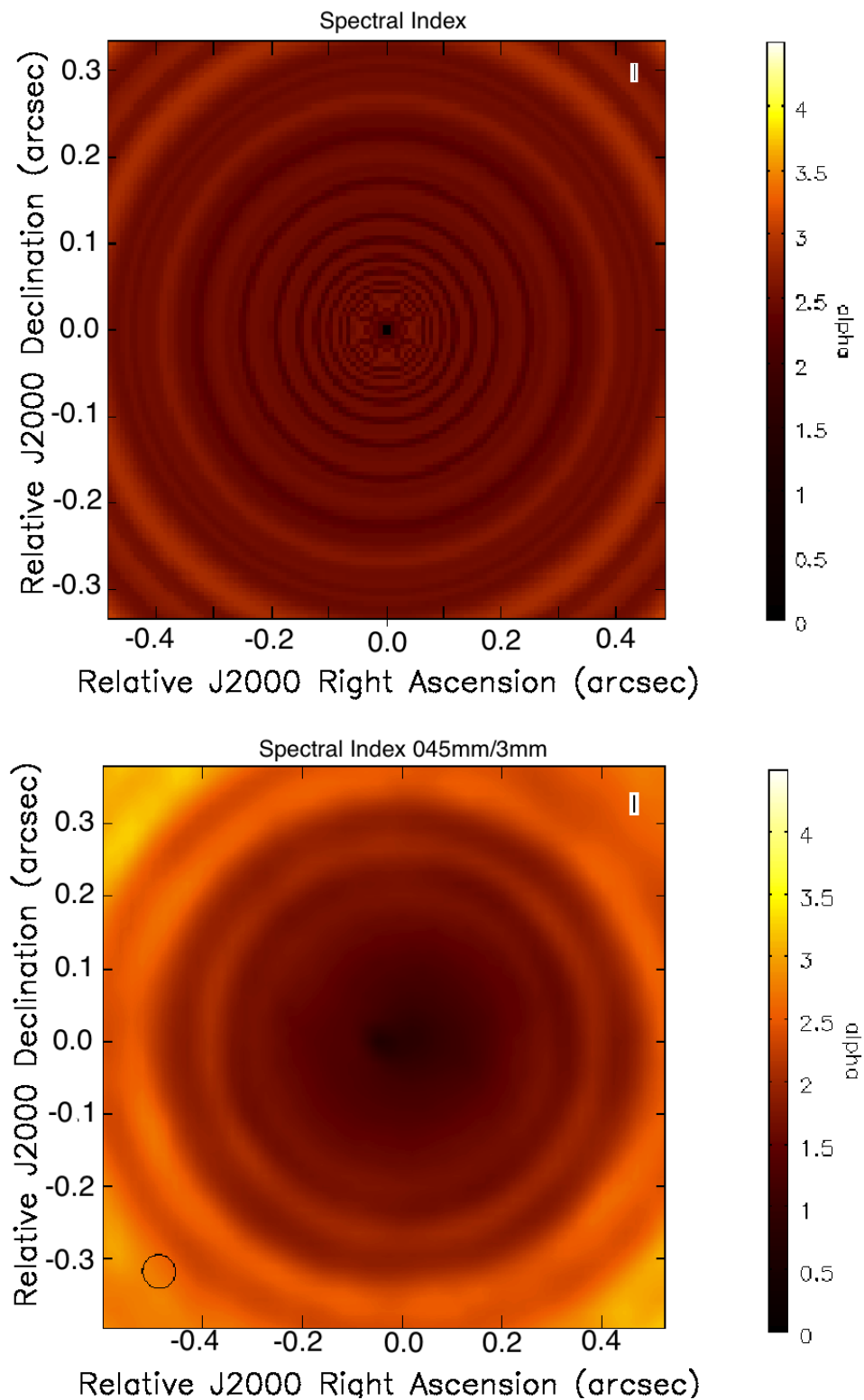


Figure 9.8:]

Spectral index α_{1-3mm} of the model data (top plot) and the spectral index taking two simulated images at 0.45mm and 3.0mm, with a time observation of four hours and using the full configuration (max. baseline of 12 km)

Chapter 10

Conclusions

In this final Chapter I summarize the main findings of this Thesis, and discuss some of possible follow-up investigations of this work.

In this project I obtained and analyzed new data in the millimetre for a sample of more than 50 young disks in three nearby star forming regions (Taurus, Ophiuchus, Orion); for all these sources I derived some of the main properties of dust particles, such as grain size and total mass; these observations have the potential to test models of early evolution of solid particles in protoplanetary disks, i.e. the first stages of planet formation in these systems. In my Thesis I have produced the first statistically sound and well populated dataset to study the grain growth process in disks. The results of my analysis indicate that nearly all the disks in the Class II evolutionary stage, no matter what their mass is or in which environment they are formed, contain dust grains with sizes of at least 1 mm in their outer regions. This shows that the formation of these large grains is very rapid, occurring before a young stellar object enters in the Class II stage, and also that these large solid particles are retained in the disk outer regions. I also showed how observations of young binary disk systems in the sub-mm and mm can be used to test the models of dust evolution and early growth of solids in disks.

I investigated the effect of possible optically thick regions in the disk midplane on the disk SED at sub-mm/mm wavelengths. Although the measured mm-fluxes can be potentially explained by disks with very small optically thick and dense regions, for the vast majority of the observed disks no physical processes proposed so far are capable to reproduce the low mm-spectral indices via a strong enough concentration of small ISM-like particles. The result of this analysis further strengthen the scenario for which the measured low spectral indices of protoplanetary disks at long wavelengths are due to the presence of large mm/cm-sized pebbles in the disk outer regions.

One of the strong aspects of my work has been the detailed comparison of the observations at millimetre wavelengths with the predictions of theoretical models for the evolution of solids in disks. Such comparison has been possible through a strong collaboration with one of the leading theoretical groups based in Heidelberg. We have been able to highlight the successes and shortcomings of current dust evolution models in protoplanetary disks.

In particular, we have shown that in the case radial drift of solids is completely neglected relatively massive disks can form mm pebbles in their outer regions and reproduce the mm-fluxes observed for the brightest disks. However, according to the same models, densities in the outer regions of less massive disks are not high enough to form pebbles and reproduce the low values of the mm-spectral indices of faint disks.

We have started to investigate a possible solution to this problem by considering a density structure in the disk which shows sinusoidal perturbations as suggested by MHD simulations of young disks. The first results show that 1) these structures have the potential to retain mm-sized solids in the disk outer regions (thus reducing the efficiency of radial drift of solids in a gaseous disk), 2) smaller particles are dragged inward by the viscous evolution of gas in the disk, and this results in a loss of flux at mm-wavelengths on a timescale of few Myr. This has the potential to explain the low mm-spectral indices observed for faint disks, and a deep investigation of this scenario is currently undergoing. Also, high angular resolution observations with ALMA in the near future will allow us to test the existence of these perturbations in the disk structure.

The results presented in my Thesis clearly identify the directions for future investigations in this area. On the observational side the next frontier is to resolve the spatial distribution of large grains in disks at high angular resolution. I am part of the EVLA Key Science Project called “Disks@EVLA: Grain growth and sub-structure in protoplanetary disks”. In this project, we will use the Expanded Very Large Array to observe at wavelengths between about 7 and 60 mm a sample of about 70 disks in nearby star forming regions. By combining these observations at long wavelengths with existing and future ones with ALMA in the sub-mm, we will measure the spatial variation of the mm-spectral index throughout the disk. This will constrain the spatial distribution of mm/cm-sized pebbles in the disk and test the predictions of evolutionary models of solids in protoplanetary disks.

Another interesting follow-up study will be the investigation of the process of grain growth over both time and mass of the central star. Multi-wavelength observations of young stellar objects at the earliest stages of disk formation (Class 0/I) will tell us how early mm/cm-sized pebbles, i.e. the building blocks of planetesimals, are formed in the disk. Observations of disks at more evolved stages, e.g. in transitional disks, will shed light onto the ability of the disk to retain large pebbles in the outer disk, and possibly on the physical mechanism which is halting the radial drift of solids in a gaseous disk. Observing disks around young very low mass stars or brown dwarfs, and around intermediate-mass, or more massive young stars (Herbig AeBe stars) will allow us to probe the presence of large grains in the extreme environments which are characteristic of these systems. The results of these observations, which are becoming possible with ALMA and EVLA, will guide the model development and ultimately constrain the initial phases of planetary systems formation.

Bibliography

- Adachi, I., Hayashi, C., & Nakazawa, K. 1976, *Prog. Theor. Phys.* 56, 1756
- Adams, F. C., Emerson, J. P., & Fuller, G. A. 1990, *ApJ* 357, 606
- Allen, L. E., & Strom, K. M. 1995, *AJ* 109, 1379
- Altenhoff, W. J., Thum, C., & Wendker, H. J. 1994, *A&A* 281, 161
- Andre, P. 2002, *Star Formation and the Physics of Young Stars*, ed. J Bouvier, JP Zahn, pp. 138. Les Ulis, Fr.: EDP Sci
- Andre, P., Ward-Thompson, D., Barsony, M. 1993, *ApJ* 406, 122
- Andrews, S. M., Wilner, D. J., Hughes, A. M., Qi, C., & Dullemond, C. P. 2010, *ApJ* 723, 1241
- Andrews, S. M., Wilner, D. J., Hughes, A. M., Qi, C., & Dullemond, C. P. 2009, *ApJ* 700, 1502
- Andrews, S. M., & Williams, J. P. 2007a, *ApJ* 671, 1800
- Andrews, S. M., & Williams, J. P. 2007b, *ApJ* 659, 705
- Andrews, S. M., & Williams, J. P. 2005, *ApJ* 631, 1134
- Ballesteros-Paredes, J., Klessen, R. S., Mac Low, M.-M., Vazquez-Semadeni, E. 2007, in Reipurth, B., Jewitt, D., Keil, K. (eds.), *Protostars & Planets V*. University of Arizona Press. Tucson. 2007. p. 63
- Banzatti, A., Testi, L., Isella, A., Natta, A., Neri, R., & Wilner, D. J. 2011, *A&A* 525, 12
- Baraffe, I., Chabrier, G., Allard, F. & Hauschildt, P. H. 1998, *A&A* 337, 403
- Barge, P., & Sommeria, J. 1995, *A&A* 295, L1

- Beckwith, S. V. W., Henning, Th., & Nakagawa, Y. 2000, in Mannings, V., Boss, A. P., Russell, S. S. (eds.), *Protostar & Planets IV*. Univ. of Arizona Press. Tucson 2000. p. 533
- Beckwith, S. V. W., & Sargent, A. I. 1991, *ApJ* 381, 250
- Beckwith, S. V. W., Sargent, A. I., Chini, R. S., & Guesten, R. 1990, *AJ* 99, 924
- Bertin, G., & Lodato, G. 2001, *A&A* 370, 342
- Bertout, C., Robichon, N., & Arenou, F. 1999, *A&A* 352, 574
- Bessell, M. S., & Brett J. M. 1988, *PASP* 100, 1134
- Birnstiel, T., Ormel, C. W., & Dullemond, C. P. 2011, *A&A* 525, 11
- Birnstiel, T., Ricci, L., Trotta, F., Dullemond, C. P., Natta, A., Testi, L., Dominik, C., Henning, Th., Ormel, C. W., & Zsom, A. 2010, arXiv1006:0940
- Birnstiel, T., Dullemond, C. P., & Brauer, F. 2010, *A&A* 513, 79
- Birnstiel, T., Dullemond, C. P., & Brauer, F. 2009, *A&A* 503, 5
- Blum, J., & Wurm, G. 2008, *ARA&A* 46, 21
- Brauer, F., Dullemond, C. P., & Henning, T. 2008a, *A&A* 480, 859
- Brauer, F., Henning, T., & Dullemond, C. P. 2008b, *A&A* 487, L1
- Brauer, F., Dullemond, C. P., Johansen, A., et al. 2007, *A&A* 469, 1169
- Bressert, E., Bastian, N., et al. 2010, *MNRAS* 409, L54
- Bruggeman, D. A. G. 1935, *Annalen der Physik* 416, 636
- Boss, A. P. 2010, *ApJL* 725, 145
- Boss, A. P. 2007, *ApJL* 661, 73
- Bouwman, J., Meeus, G., de Koter, A., Hony, S., Dominik, C., & Waters, L. B. F. M. 2001, *A&A* 375, 950
- Briceño, C., Luhman, K. L., Hartmann L., Stauffer, J. R., & Kirkpatrick, J. D. 2002, *ApJ* 580, 317
- Briceño, C., Hartmann, L., Stauffer, J. R., & Martin, E. L. 1998, *AJ* 115, 2074
- Brown, J. M., Blake, G. A., Qi, C., Dullemond, C. P., Wilner, D. J., & Williams, J. P. 2009, *ApJ* 704, 496

- Cai, K., Pickett, M. K., Durisen, R. H., & Milne, A. M. 2010, *ApJL* 716, 176
- Calvet, N., Muzerolle, J., Briceño, C., Hernández, J., Hartmann, L., Saucedo, J. L., & Gordon, K. D. 2004, *AJ* 128, 1294
- Calvet, N., D'Alessio, P., Hartmann, L., Wilner, D., Walsh, A., & Sitko, M. 2002, *ApJ* 568, 1008
- Calvet, N., & Gullbring, E. 1998, *ApJ* 509, 802
- Cardelli, J. A., Clayton G. C., & Mathis, J. S. 1989, *ApJ* 345, 245
- Carpenter, J. M. 2001, *AJ* 121, 2851
- Chiang, E., & Youdin, A. N. 2010, *AREPS* 38, 493
- Chiang, E. I., & Goldreich, P. 1997 *ApJ* 490, 368
- Cossins, P., Lodato, G., & Testi, L. 2010a, *MNRAS* 407, 181
- Cossins, P., Lodato, G., & Clarke, C. 2010b, *MNRAS* 401, 2587
- Cossins, P., Lodato, G., & Clarke, C. J. 2009, *MNRAS* 393, 1157
- Cutri, R. M. et al. 2003, 2MASS All Sky Catalog of point sources
- Da Rio, N., Robberto, M., Soderblom, D. R., Panagia, N., Hillenbrand, L. A., Palla, F., & Stassun, K. G. 2010, *ApJ* 722, 1092
- Davies, D. R. & Ryan, E. V. 1990, *Icarus* 83, 156
- Dent, W. R. F., Matthews, H. E., & Ward-Thompson, D. 1998, *MNRAS* 301, 1049
- Desch, S. J. 2007, *ApJ* 671, 878
- Dominik, C., Blum, J., Cuzzi, J. N., & Wurm, G., in Reipurth, B., Jewitt, D., Keil, K. (eds.), *Protostars & Planets V*. University of Arizona Press. Tucson. 2007. p. 783
- Dominik, C., & Tielens, A. G. G. M. 1997, *ApJ* 480, 647
- Draine, B. T. 2006, *ApJ* 636, 1114
- Draine, B. T. & Lee, H.-M. 1984, *ApJ* 285, 89
- Duchene, G. 2008, *NewAR* 52, 117
- Duchene, G., Bouvier, J., Bontemps, S., André, P., Motte, F. 2004, *A&A* 427, 651
- Dullemond, C. P., & Dominik, C. 2005, *A&A* 434, 971

- Dullemond, C. P., & Natta, A. 2003, *A&A* 405, 597
- Dullemond, C. P., Dominik, C., & Natta, A. 2001, *ApJ* 560, 957
- Dutrey, A., Guilloteau, S., Duvert, G., et al. 1996, *A&A*, 309, 493
- Eisner, J. A., Plambeck, R. L., Carpenter, J. M., Corder, S. A., Qi, C., & Wilner, D. 2008, *ApJ* 683, 304
- Fromang, S., & Nelson, R. P. 2005, *MNRAS* 364, 81L
- Furlan, E., Hartmann, L., Calvet, N., et al. 2006, *ApJS* 165, 568
- Galli, D., & Shu, F. H. 1993, *ApJ* 417, 220
- Gammie, C. F. 2001, *ApJ* 553, 174
- Gammie, C. F. 1996, *ApJ* 457, 355
- Goldreich, P., & Ward, W. R. 1973, *ApJ* 183, 1051
- Greene, T. P., Wilking, B. A., Andre, P., Young, E. T., & Lada, C. J. 1994, *ApJ* 434, 614
- Guilloteau, S., Dutrey, A., Pietu, V., & Boehler, Y. 2011, *A&A* 529, 105
- Gullbring, E., Calvet, N., Muzerolle, J., & Hartmann, L. 2000, *ApJ* 544, 927
- Gullbring, E., Hartmann, L., Briceño, C., & Calvet, N. 1998, *ApJ* 492, 323
- Güttler, C., Blum, J., Zsom, A., Ormel, C. W., & Dullemond, C. P. 2010, *A&A* 513, 56
- Hartigan, P., & Kenyon, S. J. 2003, *ApJ*, 583, 334
- Hartmann, L. 2001, *AJ*, 121, 1030
- Hartmann, L., Calvet, N., Gullbring, E., & D'Alessio, P. 1998, *ApJ* 495, 385
- Hayashi, C. 1981, *PThPS* 70, 35
- Henning, T., & Stognienko, R. 1996, *A&A* 311, 291
- Herbig, G. H. 1950, *ApJ* 111, 15
- Herczeg, C. J., & Hillenbrand L. A. 2008, *ApJ* 681, 594
- Herczeg, C. J., et al. 2009, in preparation
- Hernández, J., Hartmann, L., Megeath, T., Gutermuth, R., Muzerolle, J, et al., 2007, *ApJ* 662, 1067
- Hillenbrand, L. A. 1997, *AJ* 113, 1733

- Ho, P. T. P., Moran, J. M., & Lo, K. Y. 2004, ApJ 616, L1
- Hughes, M. A., Wilner, D. J., Qi, C., & Hogerheijde, M. R. 2008, ApJ 678, 1119
- Klahr, H. H., & Bodenheimer, P. 2003, ApJ 582, 869
- Klahr H & Henning T. 1997, Icarus 128, 213
- Kraus, S., Weigelt, G., Balega, Y. Y., Docobo, J. A., Hofmann, K.-H., Preibisch, T., Schertl, D., Tamazian, V. S., Driebe, T., et al. 2009, A&A 497, 195
- Isella, A., Carpenter, J. M., & Sargent, A. F. 2010, ApJ 714, 1746
- Isella, A., Carpenter, J. M., & Sargent, A. F. 2009, ApJ 701, 260
- Itoh, Y., et al. 2009, ApJ 620, 984
- Jensen, E. L. N., Dhital, S., Stassun, K. G., Patience, J., Herbst, W., Walter, F. M., Simon, M., & Basri, G. 2007, AJ, 134, 241
- Jensen, E. L. N., Koerner, D. W., & Mathieu, R.D. 1996, AJ, 111, 2431
- Joergensen, J. K., Bourke, T. L., Myers, P. C., Di Francesco, J., van Dishoeck, E. F., Lee, Chin-Fei, Ohashi, N., Schoeier, F. L., Takakuwa, S., Wilner, D. J., & Zhang, Q. 2007, ApJ 659, 479
- Johansen, A, Youdin, A., & Klahr, H. 2009, ApJ 697, 1269
- Johansen, A., & Youdin, A. 2007, ApJ 662, 627
- Johansen, A, & Klahr, H. 2005, ApJ 634, 1353
- Johnstone, D., & Bally, J. 1999, ApJ 510, L49
- Kenyon, S. J., & Hartmann L. 1995, ApJS 101, 117
- Kenyon, S. J., & Hartmann L. 1987, ApJ 323, 714
- Kessler-Silacci, J.; Augereau, J. C.; Dullemond, C. P., Geers, V., Lahuis, F., et al. 2006, ApJ 639, 275
- Kitamura, Y., Momose, M., Yokogawa, S., et al. 2002, ApJ 581, 357
- Klein, R., Apai, D., Pascucci, I., Henning, Th., & Waters, L. B. F. M. 2003, ApJ 593, 57
- Klahr, H. H., & Henning, T. 1997, Icarus, 128, 213
- Koerner, D. W., Chandler, C. J., & Sargent, A. I. 1995, ApJ 452, 69
- Kraus, S., Weigelt, G., Balega, Y. Y., et al. 2009, A&A 497, 195

- Kudo, T., Tamura, M., Kitamura, Y., Hayashi, M., Kokubo, E., Fukagawa, M., Hayashi, S. S., Ishii, M., Itoh, Y., Mayama, S., Momose, M., Morino, J., Oasa, Y., Pyo, T.-S., & Suto, H. 2008, *ApJL* 673, 67
- Kwon, W., Looney, L. W., Mundy, L. G., Chiang H., & Kemball, A. 2009, *ApJ* 696, 841
- Lada, C. J., 1987, *IAU Symposium 115: Star Forming Regions*, 115, 1
- Leggett, S. K. 1992, *ApJS* 82, 351
- Leinert, C., Zinnecker, H., Weitzel, N., Christou, J., Ridgway, S. T., Jameson, R., Haas, M., & Lenzen, R. 1993, *A&A* 278, 129
- Lombardi, M., Lada, C. J., & Alves, J. 2008, *A&A* 480, 785
- Lommen, D., van Dishoeck, E. F., Wright, C. M., Maddison, S. T., Min, M., Wilner, D. J., Salter, D. M., van Langevelde, H. J., Bourke, T. L., van der Burg, R. F. J., & Blake, G. A. 2010, *A&A* 515, 77
- Lommen, D., Maddison, S. T., Wright, C. M., van Dishoeck, E. F., Wilner, D. J., & Bourke, T. L. 2009, *A&A* 495, 869
- Lommen, D., Wright, C. M., Maddison, S. T., Jrgensen, J. K., Bourke, T. L., van Dishoeck, E. F., Hughes, A., Wilner, D. J., Burton, M., & van Langevelde, H. J. 2007, *A&A* 462, 211
- Lovelace, R. V. E., Li, H., Colgate, S. A., & Nelson, A. F. 1999, *ApJ* 513, 805
- Luhman, K. L., Allen, P. R., Espaillat, C., Hartmann, L., & Calvet, N. 2010, *ApJS* 186, 111
- Luhman, K. L., Stauffer, J. R., Muench, A. A., Rieke, G. H., Lada, E. A., Bouvier, J., & Lada, C. J. 2003, *ApJ* 593, 1093
- Luhman, K. L. 1999, *ApJ* 525, 466
- Lynden-Bell, D., & Pringle, J. E. 1974, *MNRAS* 168, 603
- Lyra, W., Johansen, A., Zsom, A., Klahr, H., & Piskunov, N. 2009, *A&A* 497, 869
- Malfait, K., Waelkens, C., Waters, L. B. F. M., Vandenbussche, B., Huygen, E., & de Graauw, M. S. 1998, *A&A* 332, 25
- Lynden-Bell, D., & Pringle, J. E. 1974, *MNRAS* 168, 603
- Mann, R. K., & Williams, J. P. 2010, *ApJ* 725, 430
- Mann, R. K., & Williams, J. P. 2009a, *ApJ* 699, L55

- Mann, R. K., & Williams, J. P. 2009b, *ApJ* 694, L36
- Mannings, V., & Emerson, J. P. 1994, *MNRAS* 267, 361
- Mathieu, R.D. 1994, *ARA&A* 32, 465
- Mathis, J. S., Rumpl, W., & Nordsieck, K. H. 1977, *ApJ* 217, 425
- Mayer, L., Quinn, T., Wadsley, J., & Stadel, J. 2004, *ApJ* 609, 1045
- Mayor, M., & Queloz, D. 1995, *Nature* 378, 355
- McCabe, C., Ghez, A. M., Prato, L., Duchene, G., Fisher, R. S., & Telesco, C. 2006, *ApJ* 636, 932
- McCaughrean, M. J., & O'Dell, R. C. 1996, *AJ* 111, 5
- McClure, M. K., Furlan, E., Manoj, P., Luhman, K. L., Watson, D. M., Forrest, W. J., Espaillat, C., et al. 2010, *ApJS* 188, 75
- Menten, K. M., Reid, M. J., Forbrich, J., & Brunthaler, A. 2007, *A&A* 474, 515
- Meru, F., & Bate, M. R. 2011, *MNRAS* 411, 1
- Meyer, M. R., Calvet, N., & Hillenbrand, L. A. 1997, *AJ* 114, 288
- Mezger, P. G., Schraml, J., & Terzian, Y. 1967, *ApJ* 150, 807
- Miyake, K., & Nakagawa, Y. 1993, *Icarus* 106, 20
- Momose, M., Ohashi, N., Kudo, T., Tamura, M., Kitamura, Y. 2010, *ApJ* 712, 397
- Mordasini, C., Klahr, H., Alibert, Y., Benz, W., & Dittkrist, K.-M. 2010, *ArXiv:1012.5281*
- Mordasini, C., Alibert, Y., & Benz, W. 2009, *A&A* 501, 1139
- Motte, F., Andre, P., & Neri, R. 1998, *A&A* 336, 150
- Mundy, L. G., et al. 1996, *ApJ* 464, L169
- Nakamoto, T., & Nakagawa, Y., 1994, *ApJ* 421, 640
- Nakagawa, Y., Nakazawa, K., & Hayashi, C., 1981, *Icarus* 45, 517
- Natta, A., Testi, L., Calvet, N., Henning, Th., Waters, R., & Wilner, D., in Reipurth, B., Jewitt, D., Keil, K. (eds.), *Protostars & Planets V*. University of Arizona Press. Tucson. 2007. p. 783
- Natta, A., Testi, L., & Randich, S. 2006, *A&A* 452, 245

- Natta, A., Testi, L., Neri, R., Shepherd, D. S., & Wilner, D. J. 2004, *A&A* 416, 179
- Natta, A., Grinin, V., & Mannings, V. 2000, *Protostars & Planets IV*, p. 559
- Ney, E. P., Strecker, D. W., & Gehrz, R. D. 1973, *AJ* 78, 1074
- O'Dell, C. R., & Wong, S. K. 1996, *AJ* 111, 846
- Ohashi, N., Hayashi, M., Kawabe, R., & Ishiguro, M. 1996, *ApJ* 466, 317
- Okuzumi, S., 2009, *ApJ* 698, 1122
- Ormel, C. W., Paszun, D., Dominik, C., & Tielens, A. G. G. M. 2009, *A&A* 502, 845
- Ormel, C. W., & Cuzzi, J. N. 2007, *A&A* 466, 413
- Ormel, C. W., Spaans, M., & Tielens, A. G. G. M. 2007, *A&A* 461, 215
- Paczyński, B. 1971, *ARA&A* 9, 183
- Padgett, D. L., Brandner, W., Stapelfeldt, K. R., Strom, S. E., Terebey, S., & Koerner, D. 1999, *AJ* 117, 1490
- Palla, F., & Stahler, S. W. 1999, *ApJ* 525, 772
- Panagia, N., & Felli, M. 1975, *A&A* 39, 1
- Perley, R. A. et al. 2011, *ApJL*, this volume
- Pinte, C., Fouchet, L., Ménard, F., Gonzalez, J.-F., & Duchêne, G. 2007, *A&A* 469, 963
- Pollack, J. B., Hubickyj, O., Bodenheimer, P., Lissauer, J. J., Podolak, M., & Greenzweig, Y. 1996, *Icarus* 124, 62
- Pollack, J. B., Hollenbach, D., Beckwith, S., Simonelli, D. P., Roush, T., & Fong, W. 1994, *ApJ* 421, 615
- Poppe, T., Blum, J., & Henning, T. 2000, *ApJ* 533, 454
- Ratzka, T., Köhler, R., & Leinert, Ch. 2005, *A&A* 437, 611
- Reipurth, B., & Zinnecker, H. 1993, *A&A* 278, 81
- Ricci, L., Mann, R. K., Testi, L., Williams, J. P., Isella, A., Robberto, M., Natta, A., & Brooks, K. J. 2011, *A&A* 525, 81
- Ricci, L., Testi, L., Natta, A., Neri, R., Cabrit, S., & Herczeg, G. J. 2010, *A&A* 512, 15 (R10)
- Ricci, L., Testi, L., Natta, A., & Brooks, K. J. 2010b, *A&A* 521, 66

- Ricci, L., Robberto, M., & Soderblom, D. R. 2008, *AJ* 136, 2136
- Rice, W. K. M., Lodato, G., & Armitage, P. J., 2005, *MNRAS* 364, 56
- Rice, W. K. M., Lodato, G., Pringle, J. E., Armitage, P. J., & Bonnell, I. A. 2004, *MNRAS* 355, 543
- Rice, W. K. M., Armitage, P. J., Bate, M. R., & Bonnell, I. A. 2003, *MNRAS* 339, 1025
- Rieke, G. H., & Lebofsky, M. J. 1985, *ApJ* 288, 618
- Rodmann, J., Henning, T., Chandler, C. J., Mundy, L. G., & Wilner, D. J. 2006, *A&A* 446, 211
- Safronov, V. S., & Zvjagina, E. V. 1969, *Icarus* 10, 109
- Salter, D. M., Kspal, A., Getman, K. V., Hogerheijde, M. R., van Kempen, T. A., Carpenter, J. M., Blake, G. A., Wilner, D. 2010, *A&A* 521, 32
- Sandstrom, K. M., Peek, J. E. G., Bower, G. C., Bolatto, A. D., & Plambeck, R. L. 2007, *ApJ* 667, 1161
- Sault, R. J., Teuben, P. J., & Wright, M. C. H. 1995, *ASPC* 77, 433
- Schaefer, G. H., Dutrey, A., Guilloteau, S., Simon, M., & White, R. J. 2009, *ApJ*, 710, 698
- Schmidt-Kaler T. 1982, in *Landolt-Bornstein Group VI, Vol. 2*, ed. K.-H. Hellwege (Berlin: Springer), 454
- Scholz, A., Jayawardhana, R., & Wood, K. 2006, *ApJ* 645, 1498
- Semenov, D., Henning, T., Helling, C., Ilgner, M., & Sedlmayr, E. 2003, *A&A*, 410, 611
- Shakura, N. I., & Sunyaev, R. A. 1973, *A&A* 24, 337
- Shu, F. H., Adams, F. C., & Lizano, S. 1987, *ARA&A* 25, 23
- Shuping, R. Y., Kassis, M., Morris, M., Smith, N., & Bally, J. 2006, *ApJ* 644, 71
- Shuping, R. Y., Bally, J., Morris, M., & Throop, H. 2003, *ApJ* 587, L109
- Semenov, D., Henning, T., Helling, C., Ilgner, M., & Sedlmayr, E. 2003, *A&A* 410, 611
- Shakura, N. I., & Sunyaev, R. A. 1973, *A&A* 24, 337
- Simon, M., Dutrey, A., & Guilloteau, S. 2000, *ApJ* 545, 1034
- Simon, M., Ghez, A. M., Leinert, Ch., Cassar, L., Chen, W. P., Howell, R. R., Jameson, R. F., Matthews, K., Neugebauer, G., & Richichi, A. 1995, *ApJ*, 443, 625

- Simon, M., Chen, W.-P., Howell, R. R., Benson, J. A., & Slowick, D. 1992, ApJ 384, 212
- Smith, N., Bally, J., Licht, D., & Walawender, J. 2005, AJ 192, 382
- Stratton J. A. 1941, *Electromagnetic Theory*, New York: McGraw-Hill
- Strom, K. M., Strom, S. E., Edwards, S., Cabrit, S., & Skrutskie, M. F. 1989, AJ 97, 1451
- Takeuchi, T., & Lin, D. N. C. 2005, ApJ 623, 482
- Tanaka, H., Himeno, Y., & Ida, S. 2005, ApJ 625, 414
- Terebey, S., Shu, F. H., & Cassen, P. 1984, ApJ 286, 529
- Testi, L., Natta, A., Shepherd, D. S., & Wilner, D. J. 2003, A&A 403, 323
- Testi, L., Natta, A., Shepherd, D. S., & Wilner, D. J. 2001, ApJ 554, 1087
- Throop, H. B., Bally, J., Esposito, L. W., & McCaughrean, M. J. 2001, Science 292, 1686
- Toomre, A. 1964, ApJ 139, 1217
- Valenti, J. A., Basri, G., & Johns, C. M. 1993, AJ 106, 2024
- Van Boekel, R., Waters, L. B. F. M., Dominik, C., Bouwman, J., de Koter, A., Dullemond, C. P., Paresce, F. 2003, A&A 400, 21
- Wallace, L., & Hinkle, K. 1997, ApJS 111, 445
- Warren, S. G. 1984, ApOpt 23, 1206
- Weidenschilling, S. J. 1977, MNRAS 180, 57
- Weingartner, J. C., & Draine, B. T. 2001, ApJ 548, 296
- Wiling, B. A., Gagné, M., & Allen, L. E. 2008, in *Handbook of Star Forming Regions: Volume II, The Southern Sky*, ed. Reipurth (San Francisco, CA: ASP), 351
- Williams, J. P., & Cieza, L. A. 2011, arXiv:1103.0556
- Williams, J. P., Andrews, S. M., & Wilner, D. J. 2005, ApJ 634, 495
- Wilner, D. J., D'Alessio, P., Calvet, N., Claussen, M. J., & Hartmann, L. 2005, ApJ 626, 109
- Wilner, D. J., Ho, P. T. P., Kastner, J. H., & Rodríguez, L. F. 2000, ApJ 534, L101
- Wolszczan, A., & Frail, D. A. 1992, Nature 355, 145
- Youdin, A. N. 2010, EAS 41, 187

Youdin, A. N., & Shu, F. H., 2002, ApJ 580, 494

Zsom, A., Ormel, C. W., Güttler, C., Blum, J., & Dullemond, C. P. 2010, A&A 513, 57

Zsom, A., & Dullemond, C. P. 2008, A&A 489, 931

Zubko, V. G., Mennella, V., Colangeli, L., & Bussoletti, E. 1996, MNRAS 282, 1321

Curriculum Vitae

Luca Ricci

European Southern Observatory
Karl-Schwarzschild-Str. 2
85748 Garching bei München, Germany
Office 503

Phone: (+49) 89-3200-6635
Email: lricci@eso.org
Homepage: <http://www.eso.org/~lricci>

Personal

Born December 17 1983, Ravenna, Italy. Italian Citizen.

Education

- **Ph.D. Astronomy**, ESO (European Southern Observatory) and Ludwig-Maximilians Munich University, expected date: September 29, 2011.
- **M.A. Astrophysics**, Milan University, Italy, summa cum laude, 2008.
- **B.S. Physics**, Milan University, Italy, summa cum laude, 2006.

Research Interests

Star and Planet Formation, Dust Processing in Protoplanetary Disks, Origin and Evolution of Protoplanetary Disks.

Refereed Publications

1. **L. Ricci**, T. Birnstiel, F. Trotta, L. Testi, C. P. Dullemond, & A. Natta, *Constraining the early evolution of solids with mm-data of protoplanetary disks: the impact of disk evolution and dust properties*, in preparation.
2. **L. Ricci**, L. Testi, F. Trotta, A. Natta, A. Isella, & D. J. Wilner, *The effect of local optically thick regions in the long-wave emission of young circumstellar disks*, in preparation.
3. M. Robberto, L. Spina, D. Apai, I. Pascucci, N. Da Rio, **L. Ricci**, C. Goddi, L. Testi, F. Palla, & F. Bacciotti, *An HST Imaging Survey of Low-Mass Stars in the Chamaeleon I Star Forming region*, submitted to AJ.
4. M. Reggiani, M. Robberto, D. R. Soderblom, M. R. Meyer, N. Da Rio, & **L. Ricci**, *On age in the Orion Nebula Cluster*, A&A in press (arXiv:1108.1015).
5. **L. Ricci**, L. Testi, J. Williams, R. K. Mann, & T. Birnstiel, *The mm-colors of a young binary disk system in the Orion Nebula Cluster*, ApJ Letters in press, to appear in the ApJL special issue on the early EVLA results (arXiv:1106.2150).
6. **L. Ricci**, R. K. Mann, L. Testi, J. P. Williams, A. Isella, M. Robberto, A. Natta, & K. J. Brooks, *The (sub-)millimeter SED of protoplanetary disks in the outskirts of the Orion Nebula Cluster*, A&A 525, 81, 2011 (arXiv:1010.1677).
7. **L. Ricci**, L. Testi, A. Natta, & K. J. Brooks, *Dust grain growth in rho-Ophiuchi protoplanetary disks*, A&A 521, 66, 2010 (arXiv:1008.1144).
8. T. Birnstiel, **L. Ricci**, F. Trotta, C. P. Dullemond, A. Natta, L. Testi, C. Dominik, T. Henning, C. W. Ormel, & A. Zsom, *Testing the theory of grain growth and fragmentation by millimeter observations of protoplanetary disks*, A&A Letters 516, 14, 2010 (arXiv:1006.0940).
9. **L. Ricci**, L. Testi, A. Natta, R. Neri, S. Cabrit, & G. J. Herczeg, *Dust properties of protoplanetary disks in the Taurus-Auriga star forming region from millimeter wavelengths*, A&A 512, 15, 2010 (arXiv:0912.3356).
10. M. Robberto, **L. Ricci**, N. Da Rio, & D. R. Soderblom, *Evidence for a photoevaporated circumbinary disk in Orion*, ApJ Letters 687, 83, 2008 (arXiv:0809.3208).
11. **L. Ricci**, M. Robberto, & D. R. Soderblom, *The Hubble Space Telescope/Advanced Camera for Surveys Atlas of protoplanetary disks in the Great Orion Nebula*, AJ 136, 2136, 2008 (arXiv:0808.3336).

Skills

Observing Experience

- Australian Telescope Compact Array (ATCA)
- Expanded Very Large Array (VLA/EVLA)
- Combined Array for Research in Millimeter Astronomy (CARMA)
- Atacama Pathfinder EXperiment (APEX)

Competitive Time Allocation

Awarded more than 600 hours of observing time for astronomical facilities at optical-NIR and sub-mm/mm-wavelengths (17 accepted proposals, PI for 14 of them), 2008–present:

1. *Investigating dust grain growth in very young stellar objects with ATCA*, 36 ATCA hours, PI.
2. *Investigating the large grains in the Fomalhaut debris disk with ATCA*, 18 ATCA hours, PI.
3. *Constraining the long wave emission of Southern Herbig Ae/Be with ATCA*, 24 ATCA hours, PI.
4. *Investigating grain growth in the disk of a young brown dwarf*, 24 EVLA hours, PI.
5. *Investigating the relation between disk and stellar mass with APEX/LABOCA*, 29 APEX hours, PI.
6. *Disks@EVLA: Grain growth and sub-structure in protoplanetary disks*, 360 EVLA hours, PI C. Chandler.
7. *Massive protoplanetary disks in the outskirts of the Orion Nebula*, 24 CARMA hours, PI.
8. *Dust properties in the Taurus-Auriga protoplanetary disks*, 30 CARMA hours, PI.
9. *Investigating gravitational instability in a massive protoplanetary disk in Orion*, 2 VLT/X-Shooter hours, PI.
10. *Investigating the first stages of planet formation in the Orion Nebula*, 8 ATCA hours, PI.
11. *Dust grain growth in Chamaeleon I protoplanetary disks*, 6 ATCA hours, PI.

12. *Mapping the dust grain growth in the protoplanetary disk around RY Tau*, 15 VLA hours, PI.
13. *Dust properties in a massive disk in the Orion Nebula*, 6 EVLA hours, PI.
14. *Dust properties of Ophiuchus protoplanetary disks*, 22 VLA hours, PI.
15. *A 850 μm survey of the outskirts of ρ -Oph Star Forming Region with APEX/LABOCA*, 29 APEX hours, PI.
16. *The protoplanetary disks in the rho-Oph star forming region*, 45 ATCA hours, PI.
17. *Dust properties in Classical T-Tauri disks*, 33 VLA hours, PI L. Testi.

Programming/Software

- IDL, Fortran, C, CASA, MIRIAD.